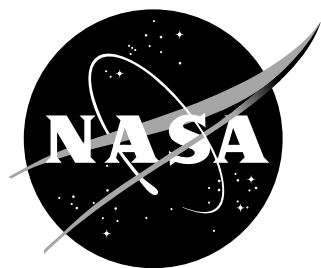NASA/TM–2019–220286

An Experimental Investigation of a Wing-Fuselage Junction Model in the NASA Langley 14- by 22-Foot Subsonic Tunnel

Michael A. Kegerise and Dan H. Neuhart
Langley Research Center, Hampton, Virginia

June 2019

NASA STI Program . . . in Profile

Since its founding, NASA has been dedicated to the advancement of aeronautics and space science. The NASA scientific and technical information (STI) program plays a key part in helping NASA maintain this important role.

The NASA STI program operates under the auspices of the Agency Chief Information Officer. It collects, organizes, provides for archiving, and disseminates NASA's STI. The NASA STI program provides access to the NTRS Registered and its public interface, the NASA Technical Reports Server, thus providing one of the largest collections of aeronautical and space science STI in the world. Results are published in both non-NASA channels and by NASA in the NASA STI Report Series, which includes the following report types:

- TECHNICAL PUBLICATION. Reports of completed research or a major significant phase of research that present the results of NASA Programs and include extensive data or theoretical analysis. Includes compilations of significant scientific and technical data and information deemed to be of continuing reference value. NASA counter-part of peer-reviewed formal professional papers but has less stringent limitations on manuscript length and extent of graphic presentations.

- TECHNICAL MEMORANDUM. Scientific and technical findings that are preliminary or of specialized interest, e.g., quick release reports, working papers, and bibliographies that contain minimal annotation. Does not contain extensive analysis.

- CONTRACTOR REPORT. Scientific and technical findings by NASA-sponsored contractors and grantees.

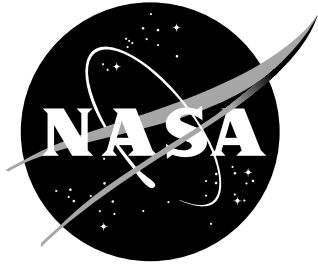- CONFERENCE PUBLICATION. Collected papers from scientific and technical conferences, symposia, seminars, or other meetings sponsored or co-sponsored by NASA.

- SPECIAL PUBLICATION. Scientific, technical, or historical information from NASA programs, projects, and missions, often concerned with subjects having substantial public interest.

- TECHNICAL TRANSLATION. English-language translations of foreign scientific and technical material pertinent to NASA's mission.

Specialized services also include organizing and publishing research results, distributing specialized research announcements and feeds, providing information desk and personal search support, and enabling data exchange services.

For more information about the NASA STI program, see the following:

- Access the NASA STI program home page at http://www.sti.nasa.gov

- E-mail your question to help@sti.nasa.gov

- Phone the NASA STI Information Desk at 757-864-9658

- Write to:
  NASA STI Information Desk
  Mail Stop 148
  NASA Langley Research Center
  Hampton, VA 23681-2199

An Experimental Investigation of a Wing-Fuselage Junction Model in the NASA Langley 14- by 22-Foot Subsonic Tunnel

Michael A. Kegerise and Dan H. Neuhart
Langley Research Center, Hampton, Virginia

Abstract

Current turbulence models, such as those employed in Reynolds-averaged Navier-Stokes CFD, are unable to reliably predict the onset and extent of the three-dimensional separated flow that typically occurs in wing-fuselage junctions. To critically assess, as well as to improve upon, existing turbulence models, experimental validation-quality flow-field data in the junction region is needed. In this report, we present an overview of experimental measurements on a wing-fuselage junction model that addresses this need. The experimental measurements were performed in the NASA Langley 14-by 22-Foot Subsonic Tunnel. The model was a full-span wing-fuselage body that was configured with truncated DLR-F6 wings, both with and without leading-edge extensions at the wing root. The model was tested at a fixed chord Reynolds number of 2.4 million, and angles-of-attack ranging from -10 degrees to +10 degrees were considered. Flow-field measurements were performed with a pair of miniature laser Doppler velocimetry (LDV) probes that were housed inside the model and attached to three-axis traverse systems. One LDV probe was used to measure the separated flow field in the trailing-edge junction region. The other LDV probe was alternately used to measure the flow field in the leading-edge region of the wing and to measure the incoming fuselage boundary layer well upstream of the leading edge. Both LDV probes provided measurements from which all three mean velocity components, all six independent components of the Reynolds-stress tensor, and all ten independent components of the velocity triple products were calculated. In addition to the flow-field measurements, static and dynamic pressures were measured at selected locations on the wings and fuselage of the model, infrared imaging was used to characterize boundary-layer transition, oil-flow visualization was used to visualize the separated flow in the leading- and trailing-edge regions of the wing, and unsteady shear stress was measured at limited locations using capacitive shear-stress sensors. Sample results from the measurement techniques employed during the test are presented and discussed.

Contents

Nomenclature

A	fringe gradient of the blue beam measurement volume
$\vec{b}_i$	unit vector along direction of laser beam i
B	systematic uncertainty
c	chord length at wing planform break
c_f	skin friction coefficient
C'	dynamic pressure calibration coefficient for the 14x22
d	outer diameter of the Preston tube
d_{ij}	fringe spacing for measurement volume formed by laser beams i and j
d_o	fringe spacing at the center of the blue beam measurement volume
d_r	diameter of the PMT receiving fiber
D	diameter of the LDV measurement volume
$\vec{e}_{ij}$	measure direction unit vector formed by beams i and j
f	frequency or focal length
f_{ij}	Doppler frequency from measurement volume formed be laser beams i and j
i	ith sample or ith laser beam
k	calibration coefficient for the 14x22 check standard probe
ℓ	length of the corner-flow separation
ℓ_e	effective length of the LDV measurement volume
M_∞	freestream Mach number
N	number of samples
p'	fluctuating pressure
p_o	total pressure
p_s	test section static pressure
p_v	vapor pressure
P	random uncertainty
q_∞	freestream dynamic pressure, $q_\infty = \rho_\infty U_\infty^2 / 2$
R	gas constant for air
Re_c	Reynolds number based on chord length at wing planform break
Re_s	Reynolds number based on distance along surface
RMS	root-mean-squared value
S_τ	static sensitivity of shear stress sensor
T	duration of a Doppler burst signal
T_a	air temperature
T_{dew}	dew point temperature
u	x component of velocity
u_{ij}	velocity component along the measurement direction unit vector, $\vec{e}_{ij}$
u_τ	friction velocity
U	total uncertainty
U_∞	freestream velocity
v	y component of velocity
V	shear stress sensor voltage
V_o	shear stress sensor voltage for wind-off conditions
w	z component of velocity or width of corner-flow separation
w_o	blue beam waist radius
x	distance along length of model from nose tip
y	distance toward starboard wing tip from model nose tip
y_o	y location of the fuselage surface
z	distance above model nose tip
z_o	z location of the wing surface

α	geometric model pitch angle
β	random value for uncertainty analysis by direct Monte Carlo simulation
Δ	pressure gradient parameter
Δp	difference between total pressure and static pressure at test-section inlet
Δp_p	Preston tube differential pressure
ϵ	random value for uncertainty analysis by direct Monte Carlo simulation
η	distance along bisector of blue-beam measurement volume
η_R	Rayleigh length
η_w	distance between the beam waist and the center of the blue beam measurement volume
θ	off-axis viewing angle of the LDV receiving optic
θ_{ij}	included angle between laser beams i and j
λ	wavelength of laser light
μ	dynamic viscosity at the air temperature
ν	kinematic viscosity at the air temperature
ρ	density at the air temperature
ρ_c	density at the air temperature corrected for compressibility
σ	standard deviation
τ_i	particle transit time through the measurement volume for the ith sample
τ_w	wall shear stress

Operators

$\bar{(\ )}$	mean value
$(\ )'$	fluctuating value

List of Tables

List of Figures

6

11

12

13

1 Introduction

Junction flows, such as those formed around a wing-fuselage or a wing-pylon intersection, are common features of practically all civil and military aircraft. Since these flows typically exhibit regions of flow separation that can adversely impact aircraft performance, there is a strong desire to accurately predict the behavior associated with them. For wing-fuselage junction flows in particular, the flow is often observed to separate in the corner-flow region near the wing trailing edge. However, the turbulence models currently employed in Reynolds-averaged Navier-Stokes CFD are unable to reliably predict the onset and extent of this separated corner flow. For example, CFD computations at past Drag Prediction Workshops have displayed large variations in the predictions of separation, skin friction, and pressure in the corner-flow region near the wing trailing edge [1]. To critically assess our existing turbulence models, as well as to improve upon them, experimental validation-quality flow-field data in the junction region is needed. To address that, NASA has developed a CFD validation experiment for a generic full-span wing-fuselage junction model at subsonic conditions. Rumsey *et al.* has previously reported on the detailed goals of this effort and has provided a history of its development [2,3]. The ultimate goal of this experiment is to provide a publicly-available high-quality flow field and surface data set with quantified boundary conditions, geometry, and measurement uncertainties. This data set should be suitable for use in CFD workshop environments and will help CFD practitioners validate and improve their predictive capabilities for turbulent separated corner flows.

Initially, a full-span wing-fuselage body with top-bottom/left-right symmetry and a symmetric-wing profile was desired for the junction flow CFD validation experiment. That would allow us to make measurements with the model both upright and inverted $180°$ so that geometric imperfections in the model and flow nonuniformities in the freestream would be exposed, and their impact on measurement uncertainty could be assessed [4,5]. Furthermore, we hoped that such a configuration would display fully-attached corner flow, incipient corner-flow separation, and a large corner-flow separation simply by varying the freestream Mach number or the model pitch angle. Several symmetric-wing profiles and a cambered wing profile (the DLR-F6) were analyzed via CFD, but none of them displayed all of the desired flow-separation conditions [2]. However, given the current limitations of the CFD turbulence models for separated flows, and our lack of trust in them, we decided to perform a couple of risk-reduction experiments on flow-visualization models to see whether or not corner-flow separation occurred in the trailing-edge region and if it did, to document its progression with model pitch angle.

The first risk-reduction experiment was conducted with a smaller-scale model in the Virginia Tech Stability Tunnel [2,6]. This full-span wing-fuselage junction model could be configured with five different wing designs, two of which were based on an NACA 0015 wing and a DLR-F6 wing. Oil-flow visualizations were used to document the surface topology in the corner-flow region. All of the wing configurations, except for the NACA 0015 wing, indicated corner-flow separation over the range of pitch angles considered ($-10°$ to $10°$). The NACA 0015 wing indicated a small corner-flow separation for pitch angles above $7.5°$. In terms of progression, the corner-flow separation increased in size with increasing pitch angle.

Since the first risk-reduction experiment was conducted at a relatively low chord Reynolds number of 0.62 million, fully-turbulent flow on the model was not realized for all model pitch angles, even with the use of boundary layer trip dots. In addition, it was expected that the onset and size of the corner-flow separation could be dependent on the Reynolds numbers. To address these concerns, a second risk-reduction experiment was conducted on a larger model in the NASA Langley 14- by 22-Foot Subsonic Tunnel [7]. The geometry of that model—and its five interchangeable wings— was the same as the small-scale model, but the chord Reynolds number of 2.4 million was equal to the desired Reynolds number for the CFD validation experiment. In addition, for this larger chord Reynolds number, turbulent flow on the fuselage and wing surfaces was achieved with boundary layer trip dots. As before, all of the wing configurations, except the NACA 0015 wing, indicated a corner-flow separation for all pitch angles considered ($-10°$ to $10°$). The NACA 0015 wing indi-

cated a corner-flow separation for pitch angles of $5°$ and above; however, it was very small in size. For all of the wing configurations, the corner-flow separation was observed to increase in size with increasing pitch angle.

While the NACA 0015 wing design did provide the desired progression from attached flow to separated flow, it was felt that the small extent of the corner-flow separation would be hard to probe experimentally and still achieve the desired spatial resolution. On the other hand, the DLR-F6 wing design did provide a progression from a small corner-flow separation to a large one that could be easily probed for flow-field measurements. Of course, the down side of the DLR-F6 wing was the loss of symmetry in the wing profile and with that, the ability to fully probe uncertainties due to geometric imperfections. Since neither wing design was optimal in terms of our original requirements, a decision was made and both wings were designed and built for the CFD validation experiment.

In late 2017 and early 2018, the junction flow CFD validation experiment was conducted in the NASA Langley 14- by 22-Foot Subsonic Tunnel and here, we provide an initial report out on that test entry. The primary objective of this first test entry was to perform flow-field measurements in the trailing-edge corner region of the wing-fuselage junction model using an internally mounted laser Doppler velocimetry (LDV) system. For this set of measurements, the junction model was configured with the DLR-F6 wing geometry. The LDV system provided measurements of all three velocity components and all six independent components of the Reynolds-stress tensor. A second internally mounted LDV system was alternately used to measure the flow field in the leading-edge region of the wing and to measure the incoming fuselage boundary layer well upstream of the leading edge. In addition to the flow-field measurements, static and dynamic pressures were measured at selected locations on the wings and fuselage of the model, infrared thermography was used to characterize boundary-layer transition, oil flow was used to visualize the separated flow in the leading- and trailing-edge regions of the wing, and unsteady shear stress was measured at limited locations using capacitive shear-stress sensors. Sample results from these measurement techniques will be presented and discussed in this report (with the exception of the static pressure results, which will be reported at a later time).

It should be noted that a concerted effort was also made to document the as-built, as-assembled, and as-tested geometry of the junction model using laser-based scanning techniques over the course of the test entry. In addition, the wind-tunnel test-section geometry was documented and measurements of the tunnel wall pressures, diffuser pressures, and boundary-layer rake pressures were acquired as boundary conditions during the test entry. An earlier test entry in the 14- by 22-Foot Subsonic Tunnel also attempted to characterize the test-section inflow using various measurement techniques [8]. The ultimate goal for this group of measurements is to provide documented boundary conditions and geometry so that an unambiguous comparison between CFD calculations and the experimental measurements can be made. These aspects of the junction flow CFD validation experiment are not included in this report and they will be documented at a later date.

In the next section, the experimental methods are presented and there, details of the wind-tunnel facility and the junction model are provided, along with the details of the model instrumentation. This is followed by a discussion of the data-analysis methods. Sample results for the experimental measurements are then presented and discussed, followed by a summary for the report.

2 Experimental Methods

2.1 Wind-Tunnel Facility

The experiment was performed in the Langley 14- by 22-Foot Subsonic Tunnel which is a closed-circuit, atmospheric-pressure wind tunnel capable of operating in an open, partially closed, or closed test-section mode. Raising and lowering the north and south walls and ceiling creates the various modes of tunnel geometry. The floor of the test section is formed by two model carts that are moved

to and from the test section front and back bays. The carts are raised and lowered on hydraulic lifts and transported along the floor under the test section on air pads. Once in place, the tunnel floor is fixed during testing. Measurements for this test were made in the closed test section mode. In this mode, the test section measures approximately 4.42 m high and 6.63 m wide, and the maximum freestream velocity is 103 m/s. Flow conditioning is provided by a flow-straightening honeycomb, four square-mesh screens with a mesh count of 10 per inch and 64% open area, and a tunnel contraction ratio of 9 to 1. This arrangement achieves a low test-section turbulence intensity of between 0.07 and 0.08 percent at a dynamic pressure (q_∞) of 2.87 kPa (60 psf)—but that does vary somewhat with dynamic pressure and location in the test section [9]. A planform view of the tunnel circuit is shown in Fig. 1 and further details about the tunnel can be found in Gentry *et al.* [10].

There are several key tunnel parameters that were monitored and measured during a wind-tunnel run. The total pressure was measured downstream of the mesh screens with a silicon pressure transducer (SPT) that has an absolute full-scale range of 137.9 kPa. The differential pressure between the total pressure and the static pressure at the test-section entrance was measured with an SPT that has a differential full-scale range of 6.9 kPa. The air temperature and the dew-point temperature—both of which were measured at the test-section entrance—were measured with a 4-wire RTD and a dew-point hygrometer, respectively. Using these four parameters, all other test conditions were calculated according to the equations documented by Boney [11].

Throughout all of the wind-tunnel runs, the tunnel controller held the chord Reynolds number, Re_c, at a constant value of 2.4 million to within $\pm 0.3\%$. Since the facility does not have a temperature controller, the air temperature increased over the course of a given run and therefore, the velocity was increased accordingly to maintain a constant chord Reynolds number. In addition, there were substantial changes in the nominal air temperature from day-to-day and over the course of the test entry due to prevailing outdoor conditions. As such, the nominal tunnel velocity was again adjusted to maintain the target chord Reynolds number. In general, the air temperature ranged from 275 to 308 K and the Mach number ranged from 0.175 to 0.205 over the course of the test entry.

2.2   Wing-Fuselage Junction Model

The model was a full-span wing-fuselage body fabricated from 6061-T6 aluminum. The overall length, height, and width of the fuselage was 4.839 m, 0.670 m, and 0.472 m, respectively, and the tip-to-tip wing span was 3.397 m. Port-side, starboard-side, and front-view images of the model installed in the 14x22 wind tunnel are shown in Figs. 2–4. Port- and starboard-side views of the model looking in the upstream direction are shown in Figs. 5 and 6. Here the images are annotated to show some of the test-section instrumentation, such as the ceiling and wall boundary-layer rakes. CAD drawings showing top, bottom, front, port, and starboard views of the junction-model assembly are shown in Figs. 7–11.

The model was painted with a black lusterless polyurethane paint suitable for both infrared imaging and oil-flow visualizations on the model surface. A coating thickness gauge, which uses eddy-current principles to measure the coating thickness on nonferrous metals, indicated a paint thickness on the order of 254 to 330 μm (10–13 mils).

The model was attached to a long sting that could be raised or lowered via a motorized sting mast to keep a reference point on the model near the center of the test section during a pitch-angle adjustment. The reference point was located approximately 2.448 m from the model nose tip (5.41 m from the test-section entrance) and on the fuselage centerline. Pitch angles for this test ranged from $-10°$ to $10°$ in increments of $2.5°$. Generally the nominal height of the reference point was 2.2098 m above the test-section floor; however, for pitch angles of $-10°$ and $-7.5°$, that height could not be reached due to geometrical constraints on the sting-mast height. As such, the height was reduced to 1.7907 m and 2.0574 m, respectively, for those two angles. The model sting was also motorized to allow for adjustments of the model roll angle, and over the course of this test, roll angles of $0°$ and $180°$ were considered. The pitch and roll angles of the model were measured with a pair of accelerometer-based model-attitude sensors that were located inside the model fuselage,

17

and both sensors had an accuracy of $\pm 0.01°$. Further details on the model-attitude sensors can be found in Finley and Tcheng [12]. To quantify vibration levels during a wind-tunnel run, the junction model was instrumented with accelerometers to measure three orthogonal components of acceleration. These sensors all had a nominal sensitivity of 5 g/V and were mounted inside the model to a fixture on the wing box.

The junction-model fuselage consists of two parts: the fuselage nose section and the fuselage main section. An exploded view of the fuselage nose-section assembly is shown in Fig. 12. The port and starboard sides of the fuselage nose section were designed to be flat so that flat instrumentation inserts could be used. The inserts were centered on the model centerline and 1168.4 mm from the nose-section tip. Different types of insert plates were used, depending on the objectives of a given run. For the LDV measurements the insert had an acrylic window. Other inserts were made for an unsteady pressure transducer, a MEMS capacitive shear-stress sensor, and a Preston tube, all of which were located in the center of a given insert plate. An additional insert plate with an array of static-pressure ports was also available. Removable hatches on the top and bottom of the fuselage nose-section provided internal access to the instrumentation. In Fig. 13, a CAD drawing of the port side of the fuselage nose section is shown with an LDV/traverse assembly in place. This assembly was mounted to a bridge piece located inside the nose-section. Further details on the LDV/traverse assembly with be presented in the following section.

During fabrication of the junction model, a second fuselage nose section was made with an extended length (2120.9 mm versus the 1511.3 mm length of the standard nose-section described above). The purpose of this extended nose section was to thicken the fuselage boundary layer at the wing-fuselage junction relative to that of the standard nose-section. This boundary-layer thickness is known to have some impact on the flow field in the junction region and would be a useful parametric for study. However, due to the time constraints of our test entry, this extended nose section was not tested, but may be the subject of future test entries.

An exploded view of the fuselage main section is shown in Fig. 14. This section has four removable inserts that were located on the flat sections of the fuselage sidewalls. On the port side, one insert was located upstream of the wing box, providing access to the leading-edge region of the wing. The other insert was located downstream of the wing box, providing access to the trailing-edge region of the wing. These inserts were mirrored on the starboard side of the fuselage main section. As with the fuselage nose section, several types of insert plates were used. Acrylic window inserts were used on the port side of the model to provide optical access for the LDV measurements. Solid inserts with static pressure ports were also used on this side of the model. An insert with a MEMS capacitive shear-stress sensor was used in the port-side leading-edge location. On the starboard side of the model, both inserts were instrumented with static pressure ports and unsteady pressure transducers. A large removable hatch on the top side of the fuselage main section and two smaller hatches on the bottom provided internal access to the instrumentation. Cabling for the instrumentation was routed through the model sting and through four PVC conduits arranged around the sting adaptor at the back end of the fuselage. Cables routed through the conduits were secured to the model sting and sting mast with duct tape and zip ties. In Fig. 15, a CAD drawing of the starboard side of the fuselage main section is shown with two LDV/traverse assemblies in place. These assemblies were mounted to bridge pieces located inside the main section. As stated earlier, further details on the LDV/traverse assemblies will be presented in the following section.

The junction model was configured with truncated DLR-F6 wings, both without and with a leading-edge extension (or fillet). The geometry of the wings is characterized by a leading-edge sweep angle of $27.1°$, dihedral, wash-out twist towards the wing tip, and a planform break located 759 mm from the fuselage side wall. The planform break chord length for the wings was 557.17 mm and this was used as the reference length when calculating the chord Reynolds number. Top views of the wing planform without the extension (hereafter referred to as the F6 wing) and the wing planform with the extension (hereafter referred to as the F6 wing with extension) are shown in Figs. 16 and 17. Root-section profiles for the wing are shown in Fig. 18. A removable insert around the leading-edge root region of the wing was used to switch between the two configurations. The

leading-edge extension at the wing root is simply a geometrical fairing intended to eliminate or minimize the development and influence of the horseshoe vortex that normally forms at the wing leading edge in the absence of the extension. Both port and starboard wings were instrumented with static pressure ports and the starboard wing was additionally instrumented with unsteady pressure transducers. Further details on that instrumentation will be provided in subsequent sections.

During fabrication of the junction model, a second set of wings with an NACA 0015 root section was also made. The purpose of this wing geometry was to provide a measurement case for CFD validation where separation did not occur in the corner-flow region of the wing trailing edge (specifically for pitch angles below $5°$) [7]. As with the extended fuselage section discussed above, time constraints prevented us from testing this wing configuration during our test entry.

To ensure a turbulent boundary layer on the fuselage and the upper and lower surfaces of the wing, trip-dot arrays were used to fix the transition location. The trip dots were applied to the model with a commercially-produced trip-dot tape that is available in a range of heights. Specific details for the trip-dot placement on the fuselage and wings, including trip-dot geometry, will be presented in the Results section below.

2.3   Laser Doppler Velocimetry Measurements

As shown in the previous section, a pair of miniature laser Doppler velocimetry (LDV) probes were located inside the model and each one was mounted to a three-axis traverse system. The LDV probes provided flow-field measurements of all three velocity components and all six independent components of the Reynolds stress. In addition, each probe has the capability to measure the particle position within the measurement volume and that feature can be used to achieve submeasurement-volume spatial resolution. During the test entry, both LDV probes were operated simultaneously and measurements were made only on the port side of the model. One probe was located near the trailing-edge of the wing and was used to measure upstream of and inside the separated corner flow. The other probe was alternately used to measure the flow field in the leading-edge region of the wing and to measure the incoming boundary layer on the fuselage nose section. Images of the LDV systems installed at the trailing-edge and the leading-edge of the port wing are shown in Figs. 19 and 20.

The LDV system consists of a photonics system that provides laser light to the LDV probe, a fiber-optic-based probe head with off-axis receiving optics, a set of photomultipliers to detect Doppler bursts, and a data acquisition computer with a high-speed A/D board and software for burst processing[1]. The photonics system, which resides in a cart located outside the test section, consists of the laser systems, discrete optics, and acousto-optical modulators (Bragg cells). Power supplies and water chillers for the lasers, as well as the Bragg cell frequency sources, also reside in the cart. A schematic diagram of the photonics system is shown in Fig. 21.

Laser light for the system was provided by three continuous-wave diode-pumped solid-state lasers with a power output of 1 W. Lasers 1 and 2 provided laser light with a wavelength of 532 nm and laser 3 provided laser light with a wavelength of 488 nm. The beam emitted from laser 1 was sent through a half-wave plate in a rotation mount before entering a polarizing beam splitter. This arrangement allowed us to adjust the relative power of the two beams emitted from the beam splitter. The first split beam (Beam 1, 0 MHz)[2] was passed into a polarization-maintaining (PM) fiber via a 5 mm focal length fiber-optic coupler. The second split beam was passed through a Bragg cell driven by a 200 MHz frequency source. Here the optical frequency of the output was downshifted (minus first order). This beam (Beam 2, -200 MHz) was then passed into a PM fiber via a 5 mm focal length fiber-optic coupler.

---

[1]The LDV system used in our study was a custom design delivered by Applied University Research, Inc. under a Phase III SBIR contract (80NSSC18P0088).

[2]The frequency associated with the beam label denotes the amount by which the optical frequency is shifted from the baseline value for the laser.

The beam emitted from laser 2 was also sent through a half-wave plate in a rotation mount before entering a polarizing beam splitter. The first split beam (Beam 3, 0 MHz) was passed into a PM fiber via a 5 mm focal length fiber-optic coupler. The second beam was passed through a second half-wave plate in a rotation mount before being divided again by another polarizing beam splitter. The first beam coming from the second beam splitter was passed into a Bragg cell driven by an 80 MHz frequency source and here the optical frequency of the output was downshifted (minus first order). The output of this Bragg cell was reflected off a mirror that directed the beam (Beam 4, -80 MHz) into a PM fiber via a 5 mm focal length fiber-optic coupler. The second split beam was passed to a Bragg cell driven by a 350 MHz frequency source and here the optical frequency of the output was upshifted (plus first order). The beam output from this Bragg cell (Beam 5, 350 MHz) was passed to a PM fiber via a 5 mm focal length fiber-optic coupler.

The beam emitted from laser 3 was passed through a half-wave plate in a rotation mount before entering a polarizing beam splitter. The first split beam (Beam 6, 0 MHz) was passed into a PM fiber via a 5 mm focal length fiber-optic coupler. The second split beam was passed through a Bragg cell driven by a 200 MHz frequency source and here the optical frequency was downshifted (minus first order). This beam (Beam 7, -200 MHz) was then passed into a PM fiber via a 5 mm focal length fiber-optic coupler.

All seven of the PM single-mode fibers were bundled together and passed through a 23 m cladded conduit that was run from the photonics cart to the back end of the junction model, through one of the PVC conduits in the model, and terminated at the LDV probe head. Along the way, the fiber conduit was secured to the test section floor, sting mast, and sting.

A photograph of the LDV probe head is shown in Fig. 22. The probe head measures 22.8 cm long by 8 cm high by 7.7 cm wide. Each of the PM single-mode fibers carried into the probe head terminate in ferrules that were mounted in collimating cylinders arranged with the pattern shown in Fig. 23. Each cylinder holds a fiber ferrule at the focus of an aspheric lens that collimates the laser light emitted from the fiber end and it also holds the orientation of the fiber end to maintain the polarization direction. The beams emitted from the collimating lenses were then focused by a transmitting lens to form four overlapping measurement volumes. For the current study, the LDV probe heads were fitted with 90 mm focal length transmitting lenses. The power of the laser beams emitted from the probe head were typically on the order 100 mW for beams 1–5 and 150 mW for beams 6 and 7.

The five green (532 nm) laser beams (beams 1–5) emitted from the probe head were crossed at their beam waists to form three measurement volumes: beams 1 and 2 with a frequency shift of -200 MHz, beams 3 and 4 with a frequency shift of -80 MHz, and beams 3 and 5 with a frequency shift of 350 MHz. Note that an additional measurement volume is formed due to the interference between beams 4 and 5 and has a frequency shift of 430 MHz. However, the burst signals from this measurement volume are redundant and were discarded during the processing steps. The optical frequency shift of one beam relative to the other in each measurement volume was used to set up traveling interference fringes that can be used to determine the direction of particle motion [13]. A stationary particle will produce a burst signal with a modulation frequency equal to the frequency shift. A particle moving with the fringes yields a lower frequency and movement against the fringes yields a higher frequency. For each of the three measurement volumes mentioned above, the nominal diameter and length of the measurement volume was 140 μm and 960 μm, respectively. The measurement directions defined by these three measurement volumes are nonorthogonal and therefore, it was necessary to form a linear transformation to convert the measured velocity components to an orthogonal body-fixed coordinate system. To that end, the beam unit vectors were measured via the method described in Appendix A. Those unit vectors were then used to calculate the measurement directions, the fringe spacings, and the linear-transformation as described in Section 3.1.

The two blue (488 nm) laser beams (beams 6 and 7) emitted from the probe head were crossed at the measurement volumes formed by the green laser beams. However, this crossing occurred before the beam waists of the blue beams and that produced a converging set of fringes along the bisector of the two interfering beams [14]. In other words, the fringe spacing becomes smaller along the length

20

of the measurement volume when moving away from the probe. Using the Doppler frequency measured with this converging fringe pattern and the velocity measured by the conventional green-beam measurement volumes (which have a uniform fringe pattern), the local fringe spacing of the converging fringe volume can be deduced and that in turn yields a measure of the particle position along the length of the measurement volume. Further details on the theory and development of this particle-position-resolving capability can be found in Lowe [15] and in several other references [16–18]. In Section 3.1, we will discuss the processing details used to calculate the particle positions and with that, discuss the method used to achieve submeasurement-volume spatial resolution.

Scattered light from particles moving through the measurement volume was collected with a 110 mm focal-length lens oriented at approximately 35° to the optical axis of the probe head (see Fig. 22). Light collected with that lens was then focused onto a multimode fiber with a diameter of 105 μm. The off-axis arrangement of the receiving optics reduces the effective length of the measurement volume. With front and back focal lengths equal to 110 mm, the effective length of the measurement volume is calculated as: $\ell_e = d_r/\sin\theta$, where d_r is the diameter of the receiving fiber and θ is the off-axis viewing angle [19]. For our configuration, the effective length of the measurement volume was approximately 180 μm.

The multimode receiving fiber was routed out of the model, through one of the PVC conduits, to an enclosure residing outside of the test section. The enclosure housed two photomultipliers—with associated power supplies and signal amplifiers—to measure the green light and blue light burst signals carried by the receiving fiber. The amplified signals from the photomultipliers were then sent to the inputs of an 8 bit, 1 GHz sample rate data acquisition card.

Burst signals from the LDV system were processed with proprietary software developed by Applied University Research, Inc. For our system, the software was configured to sample the two electronic signals from the photomultipliers. Burst detection for each channel was performed in the time domain and Doppler frequencies were extracted from the power-spectral densities of the sampled burst signals. Details on the burst processing algorithm can be found in Lowe [15]. The software allowed for adjustment to the sampling parameters for burst acquisition and to the validation criteria for detected bursts. Real-time displays of the sampled burst time series and spectra allowed us to assess the quality of the LDV signal and to make adjustments to the probe receiving-optic alignment as necessary. For the blue channel burst signals, a single Doppler frequency associated with the single measurement volume was present. For the green channel burst signals, three Doppler frequencies, associated with the three measurement volumes, were present. Here the frequency shift for each measurement volume was separated far enough apart in the frequency domain so that no signal ambiguity could occur for our flow conditions. The software saved several parameters to disk for post processing and included: the Doppler frequencies, a time stamp for each burst, the burst duration, validation criteria for each burst component, and coincidence information.

Seeding for the LDV measurements was provided by a smoke generator that uses a low-residue mineral oil and has an output volume of up to 800 m^3 per minute. The low-residue smoke allowed for longer run durations before signal levels were degraded due to deposition of residue on the optical windows. The smoke generator was placed in the wind tunnel settling chamber ahead of the honeycomb and it was necessary to run the generator continuously during a run so that adequate burst data rates could be maintained. Depending on where the measurement volume was located in the flow field, validated burst data rates on the order of 100 bursts/s to 500 bursts/s were achieved. The smoke generator produced a narrow distribution of particle sizes with a nominal diameter of 0.94 μm.

Optical access to the flow field was provided by 1 mm thick acrylic windows at three locations on the port side of the fuselage: one on the fuselage nose section, one in the wing leading-edge region, and one in the wing trailing-edge region. These windows had antireflection coatings on both sides and an antismudge coating on the outer surface that aided surface cleaning for removal of seeding residue. The thin windows were chosen so that refraction of the probe laser beams was minimal and did not alter the beam alignment. In fact, this was true even when the probe optical axis was tilted relative to the window surface normal. However, the window frames to which the thin

acrylic windows were bonded did require supporting ribs to help minimize deflections when under a pressure differential during a wind tunnel run. This compromise somewhat limited the regions of optical access for the LDV probes.

As stated earlier, the LDV probe measurement volume was positioned in the flow field with a three-axis traverse system. Each stage in this system was of a center-driven leadscrew design where the leadscrews were driven by servo motors. Linear encoders were used to measure the stage positions and to provide feedback to the stage controllers. Traverse motion was performed in a body-fixed coordinate system with origin at the model nose tip and with coordinate directions as shown in Fig. 24. With the model at a pitch angle of $0°$ for example, the x-coordinate is positive in the downstream direction, the y-coordinate is positive towards the starboard wing tip, and the z-coordinate is positive in the upward direction. The x-axis stage had a travel of 152.4 mm, a positional accuracy of 15 μm, and a bidirectional repeatability of ± 1 μm. The y-axis stage had a travel of 101.6 mm, a positional accuracy of 10 μm, and a bidirectional repeatability of ± 1 μm. The z-axis stage had the same specifications as the x-axis stage.

For the fuselage nose section, the traverse stages were configured as shown in Fig. 13. Here the probe optical axis was normal to the window surface. For the leading-edge region of the fuselage main section, the traverse stages were configured as shown in Fig. 15. Here also the probe optical axis was normal to the window surface. However, for a subset of measurements at this location, the probe was mounted on an adapter plate—between the probe and the y-axis stage—that tilted the probe in the x-y plane by $39°$ (Fig. 25). This allowed us to position the LDV measurement volume closer to the F6 wing leading edge. For the trailing-edge region of the fuselage main section, the traverse stages were configured as shown in Fig. 15. Here the probe optical axis was tilted downward by $10°$ in the y-z plane so that the measurement volume could be placed closer to the wing surface without clipping some of the probe beams. For all three stage assemblies a tungsten counterweight was used to balance the torque load placed on the x-axis stage by the other stages and the probe assembly. This was necessary to properly tune the x-axis servo motor for smooth operation.

Over the course of the test, one LDV probe/traverse assembly was alternately moved from the fuselage nose section to the leading-edge region of the fuselage main section. This required disassembly and reassembly of the traverse system and so each time the move was made, the probe beam unit vectors were remeasured and a new velocity-transformation matrix between the probe measurement directions and the body-fixed coordinate system was calculated. Similarly, the second LDV probe/traverse assembly at the wing trailing edge was periodically moved to different locations on the bridge piece to access a wider range of x-locations beyond that of the x-axis stage travel. When this move was made, the probe beam unit vectors were remeasured and a new velocity-transformation matrix was calculated.

When performing flow-field surveys with the LDV probe, it was necessary to locate the measurement volume relative to the window surface and to the wing surface. To that end, we used the following procedure. The laser for beams 1 and 2 was reduced to a power level of 60 mW and the lasers for the remaining beams were set to a power level of zero. Starting with the measurement volume inside the model, the y-axis stage was scanned through the window in 25 μm increments until is was positioned outside the model. At each point in the survey, scattered light received at the photomultiplier was recorded and the RMS voltage was calculated. An example for one of these window scans is shown in Fig. 26. The peak of this RMS voltage distribution denotes the location where the center of the measurement volume is at the outer window surface; *i.e.*, the light scattering is greatest at this location. For measurement-volume locations on either side of the window, the RMS voltage is indicative of the photomultiplier noise floor. To find the wing surface, the measurement volume was scanned down in the z-direction towards the wing surface and the photomultiplier RMS voltage was recorded for each point in the scan. An example for one of the wing-surface scans is shown in Fig. 27. Here again, the peak of the RMS voltage distribution denotes the location where the center of the measurement volume is at the wing surface. The window and wing-surface scans were performed before each profile measurement with the LDV system. Furthermore, these scans were performed at the desired flow conditions so that any deflections of the window and wing sur-

faces were accounted for. To find the x-locations of profile measurements, the probe measurement volume was positioned relative to reference marks on the windows that were at known locations from the model nose tip.

The LDV data were collected as a series of profile measurements using a comprehensive program that controlled the traverse motion, communicated with the burst-processing software, and collected tunnel parameters from the tunnel data system. Provisions were made in the software to pause the acquisition occasionally so that the burst-processing parameters could be optimized as conditions changed in a survey across the wing or fuselage boundary layer.

For the LDV probe positioned at the wing trailing edge, data were collected as a series of z-direction profiles at several (x, y)-locations. Each profile typically contained 30 z-locations with the first z-location 500 μm from the wing surface. Locations closer to the wing surface could not be achieved due to light-scattering noise and the inability to detect burst signals. For each location in a given profile, 30,000 samples were acquired. This probe was operated with the five green laser beams and a single photomultiplier channel—hereafter referred to as single-channel mode—to make three-component velocity measurements. Data from the blue channel were not collected with this probe and so particle positions within the measurement volume are not available for this data set. As such, the spatial resolution for measurements with this probe are dictated by the measurement volume diameter (140 μm) and effective length (180 μm). The (x, y)-locations for profile measurements in the trailing-edge region of the F6 wing at $\alpha = 5°$ are listed in Table 1. In Fig. 28 these locations are overlaid on an oil-flow image of the separated corner flow to provide a spatial reference. The (x, y)-locations for profile measurements in the trailing-edge region of the F6 wing with extension at $\alpha = 5°$ and $-2.5°$ are listed in Tables 2 and 3. Those locations are also overlaid on corresponding oil-flow images in Fig. 29.

For the LDV probe positioned in the fuselage nose section, data were collected as a series of y-direction profiles at $x = 1168.4$ mm and $z = 0$, ±30 mm, and ±60 mm. Each profile typically contained 30 y-locations with a logarithmic spacing between locations, and the first location from the surface of the window was 200 μm. As before, 30,000 samples were acquired at each location in a given profile. This probe was operated with both green and blue laser beams—hereafter referred to as dual-channel mode—to provide three components of velocity plus particle position. With these measurements, submeasurement-volume resolution was achieved for near-wall y-locations as will be discussed in Section 3.1. As with the other LDV probe measurements discussed above, profiles were obtained on the fuselage nose section for the F6 wing configuration at $\alpha = 5°$ and for the F6 wing with extension configuration at $\alpha = 5°$ and $-2.5°$.

For the LDV probe positioned at the leading edge, data were collected as a series of y-direction profiles, typically with 30 y-locations and 30,000 samples at each location. For the F6 wing configuration at $\alpha = 5°$, the (x, z)-locations at which profile measurements were made are listed in Table 4. Here the LDV probe was tilted 39° in the (x, y)-plane and was operated in the single-channel mode. The first measurement location for each profile was 500 μm off the surface of the fuselage. For the F6 wing with extension configuration at $\alpha = 5°$ and $-2.5°$, the (x, z)-locations at which profile measurements were made are listed in Table 5. Here the LDV probe was normal to the window surface and the probe was operated in both single-channel and dual-channel modes. The specific operating mode for each profile is also included in Table 5. For dual-channel mode, the first measurement location for each profile was 200 μm off the surface of the fuselage; otherwise it was 500 μm.

2.4   Infrared Imaging

Infrared (IR) imaging was used to determine the location of boundary-layer transition on the junction model. This method is based on the detection of surface temperature differences brought about by the increased heat-transfer rates that occur as the boundary layer transitions from laminar to turbulent flow. Although these surface temperature changes are small in low-speed flows, the current generation of IR cameras can resolve temperature differences on the order of tens of milliKelvins,

which is sufficient to reveal the transition location for our test conditions.

For the present experiment, three IR cameras were used. One IR camera was mounted behind a hole in the north wall of the test section to view the port side of the model fuselage. The other two IR cameras were mounted behind holes in the test-section ceiling to view the upper surfaces of the port and starboard wing planforms. Once IR imaging of the upper wing surfaces was completed, the two IR cameras were moved and mounted behind holes in the test-section floor to view the lower surfaces of the port and starboard wing planforms.

All three IR cameras had cooled Indium Antimonide (InSb) detectors that provide temperature measurements in the midwavelength infrared (MWIR) range of 3 to 5 μm. The resolution of the detectors was 1460 x 852 pixels with a pitch of 14 μm, and the noise equivalent temperature difference (NETD) of the detectors was less than 25 mK. Each camera was calibrated for a temperature range from -20 to 350 °C with an accuracy of ± 2 °C or 2% of reading. All cameras were fitted with 25 mm, $f/4.0$ lenses for a wide field of view, and each camera was connected to a host PC via a GigE Vision interface for camera control and image acquisition. Adjustments to the overall exposure and contrast of the acquired IR images were made during post processing.

2.5 Oil-Flow Visualization

Oil-flow visualizations were performed at selected locations on the port side of the junction model for a range of model pitch angles. In the trailing-edge region of the wing-fuselage junction, the oil-flow visualizations allowed us to observe the surface topology of the corner-flow separation and its progression with model pitch angle. Although these visualizations are generally regarded as qualitative in nature, here they were used to obtain approximate measurements of the length and width of the corner-flow separation. That information was then used to guide the selection of an (x, y)-grid of locations for z-direction profile measurements with the LDV system. In the leading-edge region of the wing-fuselage junction, the surface topology revealed by the oil-flow visualizations was used to guide the selection of (x, z)-locations for y-direction profile measurements with the LDV system. In both regions, the oil-flow visualizations provided useful context for the interpretation of velocity and unsteady-pressure measurements.

The oil-flow material was a mixture of 1 part titanium dioxide (TiO$_2$), 2 parts kerosene, and 0.3 parts oleic acid. The TiO$_2$, which serves as a pigment for the mixture, was white and contrasted well against the black painted model surface. The kerosene, which serves as a carrier liquid for the pigment, facilitated the flow visualization by moving under the influence of the local surface shear stress and then evaporated to leave a mean-flow pattern of pigment on the surface. The oleic acid, which serves as a dispersant, kept the TiO$_2$ from clumping. In addition, by increasing the proportion of oleic acid, the viscosity of the mixture could be increased, if needed.

Prior to a given run, the oil-flow material was applied to the model surface with foam paint brushes. The tunnel was then ramped up to the desired chord Reynolds number and a live video feed was used to determine when the oil-flow material stopped flowing. After the run, post-test imagery of the oil-flow visualization was acquired. Close-up images of the corner-flow separation at the wing trailing edge, the wing-leading edge region, and any other flow features of interest from a given run were acquired with a 12 megapixel digital SLR camera. Video recordings of the oil-flow development during a run were also saved. Approximate measurements of key flow features in the oil-flow visualizations were made with a ruler with 1 mm divisions.

2.6 Steady Pressure Measurements

The junction model was instrumented with 266 static pressure ports on the F6 wings and 247 static pressure ports on the fuselage. The inner diameter of each pressure port was 597–648 μm (0.0235–0.0255 inch). The locations of these static pressure ports are plotted on a CAD rendering of the junction model in Figs. 30 and 31. Electronically scanned pressure (ESP) modules, which were stowed inside the junction model, were used to measure the mean pressure at each port. The full

scale range of the modules was 6.89 kPa (1 psid) or 34.47 kPa (5 psid) depending on the expected pressure range of the ports connected to the module, and the modules were referenced to the ambient pressure in the control room of the wind-tunnel facility.

Additional mean pressure measurements were made at static pressure ports on the ceiling, the north wall and the south wall of the test section and on a pressure rail mounted to the floor of the first diffuser, just downstream of the test section. The mean total pressures from a set of boundary-layer rakes mounted to the ceiling, the north wall, and the south wall were also acquired.

Analysis of the steady pressures is still ongoing and as such, these results will not be presented in this report.

2.7 Unsteady Pressure Measurements

Unsteady pressure measurements were performed to gain insight to the dynamic nature of the surface pressure field in specific regions of the junction model. Twenty three MEMS piezoresistive pressure transducers were embedded in the starboard wing of the model at the locations listed in Table 6. These transducer locations are also plotted on a CAD rendering of the junction model in Figs. 30 and 31 to provide a spatial reference, and here we see that they were clustered near the wing trailing edge, in the corner-flow region. These differential pressure transducers had a full-scale range of 34.5 kPa (5 psid) and a nominal static sensitivity of 72.5 mV/kPa (550 mV/psid). Each of the sensors were referenced to the ambient pressure in the room below the wind tunnel test section. The active element of each sensor was covered by a screen with a 1 mm diameter hole in the center and the screen was set flush to the outer surface of the wing. The frequency response of the sensors was nominally flat from DC to approximately 20 kHz as reported in Hurst *et al.* [20]. The acceleration sensitivity of the transducers was 5.2×10^{-4} kPa/g equivalent; which for the acceleration levels measured during the test, produces equivalent pressures that are below the noise floor of the measurement system.

An additional thirty one MEMS pressure transducers were embedded in the fuselage of the model at the locations listed in Table 7 and plotted on the CAD rendering of the junction model in Figs. 30 and 31. Most of these sensors were located on the starboard side of the fuselage, but a select few were placed on the port side at mirrored locations to examine the symmetry in the unsteady pressure field. The full scale range, static sensitivity, reference pressure, and acceleration sensitivity of the fuselage sensors were the same as for the wing sensors. In contrast, the active element of each fuselage sensor was not covered by a screen and it was flush mounted with the outer surface of the fuselage. For this configuration, Hurst *et al.* [20] have shown that the frequency response for the sensors is extended to approximately 50 kHz. The spatial resolution for each fuselage pressure sensor was 0.5 mm by 0.5 mm.

The voltage signals from the pressure transducers were AC coupled at 0.25 Hz, preamplified, and then passed through an 8th-order low pass filter with a cutoff frequency of 40 kHz for anti-aliasing. The signals were then digitized with a 24-bit A-to-D converter at a sample rate of 100 kHz. Each channel was sampled simultaneously for a duration of 20 seconds, yielding a total of 2 million samples per channel.

All of the pressure transducers were calibrated *in situ* by applying a range of known pressures to the reference line of each sensor and recording the output voltage through the data acquisition system. A linear regression was then applied to each sensor calibration data set and the static sensitivity was set equal to the slope of the curve fit.

2.8 Shear-Stress Measurements

Wall shear stress measurements were made on the junction-model fuselage with MEMS capacitive shear stress sensors.[3] These sensors are a floating element device that provides time-resolved, one-dimensional direct mean and fluctuating wall shear stress measurements. Two different shear stress

---

[3]The shear-stress sensors used in our study were delivered by the Interdisciplinary Consulting Corp. (IC^2) under a Phase III SBIR contract (NNX16CS72P).

sensor models were used in our study. The first one had a full scale range of 50 Pa, a bandwidth of 1.4 kHz, a dynamic sensitivity of 47.4 mV/Pa, and sensing element dimensions of 2 mm by 0.4 mm. The second one had a full scale range of 300 Pa, a bandwidth of 5 kHz, a dynamic sensitivity of 1.84 mV/Pa, and sensing element dimensions of 1 mm by 0.2 mm. Both sensors were operated with the long dimension oriented in the x-direction of the body-fixed coordinate system and both had a sensor flushness of ± 25 μm (± 0.001 in).

Both sensors were used to make shear-stress measurements at two locations on the port side of the model fuselage. The first location was in the fuselage nose section at $x = 1168.4$ mm and $z = 0$ mm. The second location was near the wing leading edge at $x = 2001.37$ mm and $z = 46.56$ mm. Measurements at that location were made only for the F6 wing because the leading-edge extension of the other wing configuration covered that sensor location.

The shear-stress sensors were mounted in plexiglas plugs that were in turn mounted to the fuselage insert plates. A photo of a shear-stress sensor installed at the leading edge of the F6 wing is shown in Fig. 32. The sensor control units—which provide low-noise power to the sensor and condition the analog voltage signal from the sensor for output to the data acquisition system—were housed inside the model and were run off of battery power.

The voltage signal from the control unit of a given shear-stress sensor was split into AC and DC components. The AC signal was coupled at 0.25 Hz, preamplified and then passed through an 8th-order low pass filter with a cutoff frequency of either 1.5 kHz or 5 kHz depending on the bandwidth of a given sensor. The DC signal was also passed through an 8th-order low pass filter with a cutoff frequency of 20 Hz. Both signals were then digitized with a 24-bit A-to-D converter at a sample rate of 100 kHz for a duration of 20 seconds, yielding a total of 2 million samples per channel.

For comparison to the wall shear stress measured with the MEMS capacitive shear stress sensors, a Preston tube was used to measure the wall shear stress at $x = 1168.4$ mm, $z = 0$ mm for a pitch angle of $\alpha = 0°$. The Preston tube was a circular pitot tube resting on the surface of an aluminum plug that was mounted in a fuselage nose section insert plate on the port side of the model. Pressure ports located on either side of the Preston tube (± 5.08 mm) were used to measure the local undisturbed static pressure. A photo of the Preston tube installed in the fuselage nose section is shown in Fig. 33. The Preston tube was 7.62 mm long and had inner and outer diameters of 0.84 mm and 1.27 mm, respectively. The front opening of the Preston tube was polished to remove any burrs or cut marks that could affect the pressure reading. The nondimensional relationship between the Preston tube reading and the wall shear stress:

$$\frac{\tau_w d^2}{4\rho\nu^2} = F\left(\frac{\Delta p_p d^2}{4\rho\nu^2}\right) \tag{1}$$

and the calibration function $F(\cdot)$—which was determined experimentally by Patel in a fully developed turbulent pipe flow [21]—were used to calculate the wall shear stress. In Eq. 1, Δp_p is the difference between the Preston-tube reading and the local static pressure, d is the outer diameter of the Preston tube, ρ and ν are the fluid density and kinematic viscosity at the air temperature, and τ_w is the wall shear stress. A key assumption in the Preston-tube calibration is that the boundary layer under consideration obeys the law of the wall. If, however, the boundary layer develops under a pressure gradient, that assumption could be invalidated. For the junction model at a pitch angle of $0°$, CFD indicates that the boundary layer on the flat section of the fuselage is developing under a favorable pressure gradient in the vicinity of the Preston tube. Patel [21] provided guidelines for estimating the effect of pressure gradients on the Preston tube in terms of the pressure gradient parameter, $\Delta = \nu/(\rho u_\tau^3 dp/dx)$. For a favorable pressure gradient, he reported a maximum uncertainty in the Preston-tube calibration of 3% if $0 > \Delta > -0.005$ and $u_\tau d/\nu \leq 200$. For our test conditions, $\Delta \approx -0.00027$ and $u_\tau d/\nu \approx 195$, and so the Preston-tube calibration can still be applied with a reasonable uncertainty level.

3 Data Analysis Methods

3.1 LDV Data Processing

In this section, we describe the methods used to process the LDV data acquired in both single-channel and dual-channel modes. First, the unit vectors for each beam emitted by the LDV probe head were measured using the procedure described in Appendix A. This was performed each time the LDV probe/traverse assembly was moved to a new location in the model (for example, when moving the assembly from the fuselage nose section to the wing leading edge). A schematic for a pair of beam unit vectors and the associated measurement direction is shown in Fig. 34. Using the unit vectors for a pair of beams that form a measurement volume, the measurement direction unit vector was calculated from:

$$\vec{e}_{ij} = \frac{\left(\vec{b}_i \times \vec{b}_j\right) \times \left(\vec{b}_i + \vec{b}_j\right)}{\left\|\left(\vec{b}_i \times \vec{b}_j\right) \times \left(\vec{b}_i + \vec{b}_j\right)\right\|}, \tag{2}$$

where $\vec{b}_i$ and $\vec{b}_j$ are unit vectors along the direction of beam i and beam j, respectively. The included angle, θ_{ij}, between beam i and beam j is equal to $\arccos(\vec{b}_i \cdot \vec{b}_j)$ and the fringe spacing for the measurement volume formed by the beam pair is given as:

$$d_{ij} = \frac{\lambda}{2\sin\left(\theta_{ij}/2\right)}, \tag{3}$$

where λ is the wavelength of the laser light. The included angle and fringe spacing for each beam pair of the LDV probe positioned at the wing trailing edge are listed in Table 8, while those of the LDV probe positioned at the wing leading edge or in the fuselage nose section are listed in Table 9. Note that in both tables, no fringe-spacing value is provided for beam pair 6 & 7 because the fringe pattern is converging.

For single-channel mode, the five green laser beams of the LDV probe head form three overlapping measurement volumes: beams 1 & 2, beams 3 & 4, and beams 3 & 5. The measured Doppler frequencies from each of these measurement volumes were converted into velocities in the probe optical axes using:

$$u_{ij} = \vec{u} \cdot \vec{e}_{ij} = f_{ij}d_{ij}, \tag{4}$$

where u_{ij} is velocity along the measurement direction unit vector formed by beam i and beam j, $\vec{u}$ is the velocity vector, and f_{ij} is the associated Doppler frequency. The histograms of these velocity components were then calculated and the histogram-clipping routine of Ölçmen and Simpson [22] was applied for removal of noise and outliers. Briefly, that method fits parabolas to each side of the logarithm of the histogram ordinate and then discards data lying outside the intersection of the parabolas with the ordinate value, which corresponds to one occurrence of a velocity signal. Next, the nonorthogonal velocity components in the probe optical axes were converted to orthogonal velocity components in the body-fixed coordinate system according to:

$$\begin{bmatrix} u \\ v \\ w \end{bmatrix} = \begin{bmatrix} e_{12(x)} & e_{12(y)} & e_{12(z)} \\ e_{34(x)} & e_{34(y)} & e_{34(z)} \\ e_{35(x)} & e_{35(y)} & e_{35(z)} \end{bmatrix}^{-1} \begin{bmatrix} u_{12} \\ u_{34} \\ u_{35} \end{bmatrix}, \tag{5}$$

where $e_{ij(x)}$, $e_{ij(y)}$, and $e_{ij(z)}$ denote the x, y, and z components of the measurement direction unit vectors in the body-fixed coordinate system. Histograms of these transformed velocity components were calculated and once again the histogram-clipping routine was applied.

The processed velocity samples—which were sampled with random spacing in time—were then used to calculate several statistical moments. To account for velocity bias effects on the statistical moments, each sample was weighted by the particle transit time through the measurement volume

(or burst duration, which was recorded by the burst processor for each sample) [13]. With this weighting factor, the mean components of velocity were calculated as:

$$\overline{u} = \frac{\sum_i^N u_i \tau_i}{\sum_i^N \tau_i},$$ (6)

$$\overline{v} = \frac{\sum_i^N v_i \tau_i}{\sum_i^N \tau_i},$$ (7)

and

$$\overline{w} = \frac{\sum_i^N w_i \tau_i}{\sum_i^N \tau_i},$$ (8)

where τ_i is the transit time for a given sample i and N is the total number of samples. The Reynolds normal stress components were calculated as:

$$\overline{u'u'} = \frac{\sum_i^N (u_i - \overline{u})^2 \tau_i}{\sum_i^N \tau_i},$$ (9)

$$\overline{v'v'} = \frac{\sum_i^N (v_i - \overline{v})^2 \tau_i}{\sum_i^N \tau_i},$$ (10)

and

$$\overline{w'w'} = \frac{\sum_i^N (w_i - \overline{w})^2 \tau_i}{\sum_i^N \tau_i}.$$ (11)

Similarly, the Reynolds shear stress components were calculated as:

$$\overline{u'v'} = \frac{\sum_i^N (u_i - \overline{u})(v_i - \overline{v}) \tau_i}{\sum_i^N \tau_i},$$ (12)

$$\overline{u'w'} = \frac{\sum_i^N (u_i - \overline{u})(w_i - \overline{w}) \tau_i}{\sum_i^N \tau_i},$$ (13)

and

$$\overline{v'w'} = \frac{\sum_i^N (v_i - \overline{v})(w_i - \overline{w}) \tau_i}{\sum_i^N \tau_i}.$$ (14)

Triple products of the velocity components were also calculated as:

$$\overline{u'v'w'} = \frac{\sum_i^N (u_i - \overline{u})(v_i - \overline{v})(w_i - \overline{w}) \tau_i}{\sum_i^N \tau_i},$$ (15)

with similar relations for the other nine independent components: $\overline{u'u'u'}$, $\overline{v'v'v'}$, $\overline{w'w'w'}$, $\overline{u'u'v'}$, $\overline{u'u'w'}$, $\overline{u'v'v'}$, $\overline{u'w'w'}$, $\overline{v'v'w'}$, and $\overline{w'w'v'}$. In Eqs. 12–15, it is assumed that the u, v, and w velocities are available at the same instant in time and this was ensured by processing only coincident data.

As noted earlier in this report, 30,000 samples were typically collected at each measurement location in a flow-field survey. For the data rates that were achieved with our LDV system (100 to 500 samples/sec), many of the samples were statistically independent, being separated in time by at least two times the integral time scale. Running averages for the mean velocity and Reynolds stresses versus the sample count are shown in Fig. 35 for an example data set. Here it is observed that the number of samples collected are more than sufficient to achieve well-converged statistical

moments. The methods for estimating the uncertainties associated with these statistical moments are detailed in Appendix B.

For the dual-channel mode, an additional measurement volume associated with the blue laser beams of the LDV probe head overlaps those formed by the green laser beams: beams 6 & 7. Furthermore, this measurement volume has a converging set of fringes along the bisector of the two interfering beams. Using the measured Doppler frequency from the blue beams and the velocity vector measured with the green beams, the fringe spacing for a particle moving through the blue beam measurement volume was calculated as:

$$d_{67} = \frac{\vec{u} \cdot \vec{e}_{67}}{f_{67}}. \tag{16}$$

For noise reduction and outlier removal, histogram clipping was applied to the measured Doppler frequencies and the calculated fringe spacings. A simple model for the converging fringe pattern of the blue beams is given by [15]:

$$d_{67} = A\eta + d_o, \tag{17}$$

where η is the distance along the bisector of the two blue beams, d_o is the fringe spacing at the center of the measurement volume ($\eta = 0$), and A is the fringe gradient. Following Lowe *et al.* [18], the value for d_o was determined by placing the measurement volume in a region of the flow where the velocity gradient was zero; *e.g.*, outside the fuselage boundary layer. Assuming that particles are uniformly distributed and have an equal probability of passing through any point along the fringe gradient, the average fringe spacing at this location was set equal to d_o. The fringe gradient was calculated as:

$$A = \frac{d_o \eta_w}{[\eta_R^2 + (\eta_w/\cos(\theta_{67}/2)^2]}, \tag{18}$$

where η_w is the distance between the waist of the beam and the center of the measurement volume:

$$\eta_w = \frac{D}{2} \frac{\pi w_o}{\lambda}, \tag{19}$$

η_R is the Rayleigh length:

$$\eta_R = \frac{\pi w_o^2}{\lambda}, \tag{20}$$

D is the diameter of the measurement volume, w_o is the beam waist radius, and θ_{67} is the included angle between beams 6 and 7. Using Eqs. 17–20 and the calculated fringe spacings from Eq. 16, the position of a particle along the bisector of the measurement volume was calculated for each velocity sample.

Before calculating the statistical moments for the dual-channel data, additional processing steps were performed. First, it is important to recognize that the LDV probe was oriented normal to the window surface for dual-channel measurements. This means the measurement volume length was normal to the window surface and so particle positions within the measurement volume were measured along that direction. To aid the following discussion, consider the plot for the x-component of velocity shown in Fig. 36. This example profile was measured on the fuselage nose section at $x = 1168.4$ mm and $z = 0$ mm for $\alpha = 5°$. For each location in the profile, a colored point cloud of the particle velocity versus the particle position is shown. The circle symbols in the plot denote the mean velocity for each point cloud and are plotted against the location corresponding to the center of the measurement volume. For the first location in the survey, the center of the measurement volume was located 200 μm away from the wall. The corresponding point cloud (blue dots) shows particle positions distributed around the center of the measurement volume by $\approx \pm 100$ μm, which corresponds to the effective length of the measurement volume for our off-axis receiving optic. As we move away from the wall, subsequent point clouds overlap the previous one up until $y \approx 1$ mm. Beyond that, the point clouds no longer overlap.

The overlapping point clouds in the near-wall region of the profile were used to improve the spatial resolution of the statistical moments. To that end, a composite point cloud for the first nine measurement locations was created and is shown in Fig. 37 for our example data set. The point cloud was divided into fourteen linearly spaced bins with centers starting at $y = 150\ \mu$m and ending at $y = 670\ \mu$m, each with a bin width of 40 μm. The statistical moments for each bin were then calculated using Eqs. 6–15. While more bins and a smaller bin width could conceivably be used, the selected values were chosen so that sufficient samples were contained in each bin to ensure well-converged statistics with reasonable uncertainties. Generally, each bin contained approximately 5,000 to 10,000 samples for profile data collected in the dual-channel mode. The mean x-component of velocity is also shown in Fig. 37, where locations below $y = 0.7$ mm are bin averages derived from the composite point cloud. For locations above that, the mean velocity was calculated from the point cloud associated with each location. In that case, the spatial resolution of the statistical moments is dictated by the size of the measurement volume.

3.2   Processing of Unsteady Pressure and Shear-Stress Data

In this section, we describe the methods used to process the unsteady pressure time series and the shear stress data obtained with the MEMS capacitive shear stress sensors. For the voltage time series acquired with a given unsteady pressure transducer, the mean voltage was first calculated and subtracted. Next, the voltage time series were divided by the filter gain—which was equal to the product of the pre- and post-filter gains—and then divided again by the sensor static sensitivity as measured during the *in situ* calibration discussed in Section 2.7. The power spectral density (PSD) of the resulting pressure time series was then calculated via the Welch method using a block size of 10,000 points and a Hanning window with 50% overlap. With these parameters, 400 block averages were performed and the frequency resolution of the PSD was 10 Hz. In addition, the probability density function for the pressure time series was calculated with 100 bins distributed over a ± 5 standard deviation range. The broadband RMS pressure for the time series was also calculated. Due to the finite size of the unsteady pressure transducers, it is expected that spatial averaging of the unsteady pressure field will have some impact on the results calculated above [23–25]. However, no corrections were applied to the unsteady pressure results since the existing correction approaches may have limited validity.

For the AC coupled voltage time series acquired with a given shear-stress sensor, the mean voltage was calculated and subtracted (to remove any offset voltage associated with the data acquisition system) and the filter gain was divided out. The resulting time series was then divided by the sensor dynamic sensitivity to obtain the shear stress time series. The shear stress power spectral density, probability density function, and broadband RMS were than calculated using the same approach as for the unsteady pressure time series. The DC coupled voltage time series acquired with a given shear-stress sensor was averaged and the mean shear stress was calculated as:

$$\overline{\tau_w} = \frac{\overline{V} - \overline{V_o}}{S_\tau},\tag{21}$$

where S_τ is the sensor static sensitivity, $\overline{V}$ is the mean sensor voltage, and $\overline{V_o}$ is the mean sensor voltage at wind-off conditions. The wind-off voltage was measured prior to and after a given wind-tunnel run and the average value was used for $\overline{V_o}$. Unfortunately, due to the large changes in the test section air temperature over the course of a run, we were unable to obtain an accurate measurement of the mean shear stress. This is due to the temperature sensitivity of the wind-off voltage of the shear-stress sensors and therefore, we do not present values for the mean shear stress in this report. On the other hand, the dynamic sensitivity of the sensor is believed to have a much weaker dependence on the air temperature. Multiple measurements of the unsteady shear stress statistics over several runs were found to repeat, despite large changes in the air temperature from run-to-run. In light of that, we have better confidence in the unsteady shear stress data and will present some example results in this report.

4 Results

In this section, we present sample results for the various measurement techniques that were employed during the test entry. First, we present infrared images of the junction model and discuss the natural transition patterns that they revealed. We also present infrared images of the junction model with trip dots applied to fix the transition location. Next, we present oil-flow images of the trailing-edge corner-flow separation. This is followed by a presentation of LDV profile measurements on the fuselage nose section, in the leading-edge region of the wing, and in the trailing-edge corner region of the wing. The section finishes with sample results from the unsteady pressure measurements and shear-stress measurements.

4.1 Infrared Imaging Results

The model was initially configured with F6 wings and infrared imaging was used to determine the location of natural transition on the fuselage and the upper and lower surfaces of the wings. To determine the transition location on the fuselage, one IR camera with a 25 mm lens was placed behind an open hole in a tunnel sidewall panel to provide a port-side view of the model. Infrared images of the clean fuselage (no boundary layer trip dots) versus model pitch angle are shown in Fig. 38. In the images, dark tones correspond to lower (cooler) temperatures and lighter tones correspond to higher (warmer) temperatures. Since the model was cooler than the air temperature, the initially laminar boundary layer on the fuselage nose is marked by dark tones. Boundary-layer transition on the fuselage is then marked by the sudden shift towards lighter tones, where the increased heat transfer associated with the turbulent flow increases the fuselage temperature. It can be seen that the natural transition pattern is somewhat irregular and that the transition location changes slightly with model pitch angle. There is also a wedge of turbulent flow ahead of the natural transition location which was found to emanate from a small protuberance of paint near the lower side of the fuselage nose.

To ensure a consistent transition location for the fuselage boundary layer, trip dots were placed on the model at a nominal location of $x = 336$ mm from the fuselage nose tip. This location was chosen so that: 1) the trip dots were nominally positioned just downstream of the suction peak as determined from computed pressure distributions at our test conditions and 2) the local Reynolds number based on distance along the surface, Re_s, was greater than 100,000 to ensure fully effective trip dots [26]. The height of the trip dots was based on the roughness correlations of Braslow and Knox [27], and for our test conditions, the trip dots had a height of 289.4 ± 1.1 μm (0.0114 in). The trip dots were cylindrical in shape with a diameter of 1.16 ± 0.03 mm and had a center-to-center spacing of 2.47 ± 0.04 mm. Infrared images for the tripped fuselage versus model pitch angle are shown in Fig. 39. Here it is observed that the transition location is fixed at the trip dots and does not vary with model pitch angle.

The natural transition location on the upper surfaces of the port and starboard wings was determined with a pair of IR cameras positioned above the model behind openings in the test-section ceiling. Infrared images of the clean port and starboard F6 wings for a range of model pitch angles are shown in Figs. 40 and 42. Except for a few wedges of turbulent flow likely induced by imperfections in the painted surface, the overall transition pattern on the port and starboard wings is similar over the range of pitch angles considered. The darker tones near and along the length of the wing leading edges indicates that laminar flow prevails in this region. Although the fuselage boundary layer is turbulent near the wing root, it does not contaminate the wing leading edge because the attachment-line Reynolds number is too low to sustain turbulent flow. Initially, as the pitch angle is increased from $\alpha = -10°$, the transition location on the wing upper surface retreats, and then advances again, particularly in the region inboard of the wing planform break. From $\alpha = -2.5°$, the transition location rapidly advances forward along the entire wing span, and by $\alpha = 2.5°$, the transition location locks in to a distance from the wing leading edge that is nearly fixed with further increases in the pitch angle. This behavior suggests that a leading-edge separation bubble forms and

reattaches turbulent.

To eliminate the leading-edge separation bubble, trip dots with a height of 170.6 ± 2.5 μm (0.0067 in) were placed just upstream of the separation bubble along a line positioned at an arc-distance from the leading-edge equal to 1.6% of the local chord. These trip dots were also cylindrical in shape with a diameter of 1.27 ± 0.02 mm and had a center-to-center spacing of 2.53 ± 0.04 mm. The resulting IR images of the upper wing surfaces versus model pitch angle are shown in Figs. 41 and 43. For the two lowest model pitch angles, $-10°$ and $-7.5°$, the boundary layer was still laminar for some distance downstream of the trip dots. This is likely due to the fact that the trip dots are in a region of accelerated flow and therefore, due to the stabilizing effect of the favorable pressure gradient, are not fully effective. Once the model is moved to $\alpha = -5°$, it appears that, except for a few small streaks, transition was fixed at the trip dots and stays that way throughout the rest of the pitch-angle range.

The natural transition location on the lower surfaces of the port and starboard wings was determined with a pair of IR cameras positioned below the model behind open holes in the test-section floor. Infrared images of the clean lower surface F6 wings for a range of model pitch angles are shown in Figs. 44 and 46. As with the upper wing surfaces, the transition patterns on the lower surfaces of the port and starboard wings are similar. At $\alpha = -10°$, the transition location is very close to the wing leading edge in the region outboard of the wing planform break. Here, it is likely that a laminar separation bubble has formed on the lower surface and reattaches turbulent, and that persists until $\alpha = -5°$. Inboard of the wing planform break, the transition location retreats over this same pitch-angle range. At $\alpha = -2.5°$, the transition location has retreated along the entire wing span, but with further increases in the model pitch angle, the transition location begins to advance again.

To fix the transition location on the wing lower surfaces, trip dots with a height of 196.9 ± 1.3 μm (0.0078 in) were placed along a line positioned at an arc-distance from the leading-edge equal to 10% of the local chord. These trip dots were cylindrical in shape with a diameter of 1.24 ± 0.03 mm and had a center-to-center spacing of 2.42 ± 0.09 mm. The chord location for the trip dots was selected so that the local Reynolds number, Re_s, was greater than 100,000. The resulting IR images of the lower wing surfaces versus model pitch angle are shown in Figs. 45 and 47. For pitch angles of $\alpha = -5°$ and above, the transition location on the wing lower surfaces is fixed at the trip-dot location. For the lower pitch angles, $\alpha = -7.5°$ and $-10°$, the separation bubble that forms outboard of the wing planform break still causes the transition location to snap forward, very close to the leading edge. While this is suboptimal, it should be recalled that flow-field measurements with the LDV system were performed only at pitch angles of $-2.5°$ and $5°$ where a leading-edge separation bubble does not form on the lower-wing surfaces.

Infrared imaging for the F6 wing with leading-edge extension was not performed in this test entry. When switching from the F6 wing to the F6 wing with extension, the only model parts that changed were the removable inserts around the leading-edge root region (see Figs. 16 and 17). The trip dots on the remainder of the model were undisturbed and a new set of trip dots were placed on the leading-edge extensions of the port and starboard wings. On the basis of a previous risk-reduction experiment with a smaller-scale junction model, we can expect the turbulent boundary layer on the fuselage to contaminate the insert attachment line [7]. However, as we move outboard of the insert, the attachment line Reynolds number becomes too low to sustain turbulent flow and the attachment line is expected to relaminarize. Other than that difference, the tripped transition locations on the upper and lower wing surfaces of the F6 wing with extension are expected to remain the same as for the F6 wing.

4.2 Oil Flow Visualization Results

Oil-flow visualizations in the trailing-edge corner region of the F6 wing are shown in Fig. 48 for a range of model pitch angles. Here we observe the occurrence of separated flow and a progressive growth in the separated-flow region with increasing pitch angle. Measurements of the corner-flow

separation length, ℓ, and width, w, were made with a ruler with 1 mm divisions. Generally, the corner-flow separation is marked by a diffuse band of oil-flow material at the boundary of the separation. This is due to the unsteady nature of the corner-flow separation and the history of the oil-flow development as a run proceeds. As such, it is difficult to say precisely where the mean separation line is located. For this present study, we report the outer extent (length and width) of this band of oil-flow material,[4] and an example length and width measurement is annotated in Fig. 49. With this definition, it is likely that the true length and width bounding the mean separation line is less than what is reported here. While this is acceptable for identifying trends and in helping to guide the selection of survey regions for the LDV measurements, it is less suitable for exact comparison with other analyses, such as CFD calculations. Table 10 lists the separation lengths and widths on the F6 wing for the pitch angles considered. Uncertainty estimates are also included in the table and the uncertainty analysis from which they were derived is provided in Appendix B. Note that the oil-flow visualizations were performed only on the port side of the model since the unsteady pressure sensors on the starboard side precluded the use of oil flow.

Oil-flow visualizations in the trailing-edge corner region of the F6 wing with extension are shown in Fig. 50 for a range of model pitch angles. As before, we observe the occurrence of separated flow and a progressive growth in the separated-flow region with increasing pitch angle. Table 11 lists the separation lengths and widths, along with uncertainties, on the F6 wing with extension for the pitch angles considered.

4.3   LDV Measurements on the Fuselage Nose Section

In this section, we present examples of the measured velocity profiles on the port side of the fuselage nose section. A schematic of the measurement locations is shown in Fig. 51. The center of the window insert was located at $x = 1168.4$ mm, $z = 0$ mm and profile measurements were made there, as well as at two locations above ($z = 30$ mm, 60 mm) and two locations below ($z = -30$ mm, -60 mm). At each (x, z) location, the velocity profiles were acquired by traversing in the $-y$ direction, normal to the port side of the fuselage. In addition, the LDV probe was operated in the dual-channel mode for these measurements so that particle positions were available to improve the near-wall spatial resolution.

Mean velocity, Reynolds normal stress, and Reynolds shear stress profiles, on both linear and semilogarithmic scales, are shown in Figs. 52, 53, and 54 for three z-locations. For this data set, the model was configured with the F6 wing with extension and the model pitch angle was set to $\alpha = 5°$. Uncertainty bands are included in each profile plot and they represent the uncertainty for a 95% confidence level (see Appendix B for details on their calculation). The mean-velocity components were normalized by the freestream velocity and the Reynolds-stress components were normalized by the freestream velocity squared (this was done throughout all of the LDV profile plots in this report). The $\overline{u}$ component of mean velocity is similar to that of a zero-pressure-gradient (ZPG) turbulent boundary layer, with a distinct log region and a wake region. The $\overline{v}$ component of mean velocity is essentially zero across the boundary layer and the $\overline{w}$ component of mean velocity is positive, which reflects the fact that the model is pitched upward. For the z locations at which profile measurements were made, the mean-velocity profiles are the same to within the measurement uncertainty. The boundary layer thickness at this location on the model is approximately 13 mm.

The Reynolds normal stress profiles at this x-location (Fig. 53) are also similar in shape to those of a ZPG turbulent boundary layer and have similar anisotropy, with the $\overline{u'u'}$ component being the largest, followed by the $\overline{w'w'}$ component and then the $\overline{v'v'}$ component. The largest amplitude for the $\overline{u'u'}$ component occurs in the near-wall region, where turbulent production is expected to be largest. For the Reynolds shear stress profiles at this x location (Fig. 54), the $\overline{u'v'}$ component has a distribution similar to that of a ZPG turbulent boundary layer; but in the present case, the values are

---

[4]It is important to note that the length and width of the separation size were measured along the wing surface, which is not aligned with the body-fixed coordinate system.

positive as opposed to the negative values observed for the ZPG case. This is simply a reflection of our coordinate system, which has the y direction, and hence the v component of velocity, positive toward the port side of the fuselage. In contrast to a ZPG turbulent boundary layer, the $\overline{u'w'}$ and $\overline{v'w'}$ components of the Reynolds shear stress are nonzero across the boundary layer due to the spanwise mean-flow component. While the $\overline{u'v'}$ component is dominant across most of the boundary layer, the $\overline{u'w'}$ component becomes dominant in the near-wall region. As with the mean-velocity profiles, the Reynolds-stress profiles at the different z locations are the same to within the measurement uncertainty.

Mean-velocity, Reynolds normal-stress, and Reynolds shear-stress profiles for a model pitch angle of $\alpha = -2.5°$ are shown in Figs. 55, 56, and 57 for three z-locations. Here the model was configured with the F6 wing with extension. As with the previous case, the $\overline{u}$ component of mean velocity is similar to that of a ZPG turbulent boundary layer and the $\overline{v}$ component of mean velocity is essentially zero across the boundary layer. In contrast to the previous case, the $\overline{w}$ component of mean velocity is negative, which reflects the fact that the model is pitched downward. The Reynolds normal stress profiles are again similar to those for a ZPG turbulent boundary layer. The $\overline{u'v'}$ component of Reynolds shear stress (positive in our coordinate system) is also similar to that of a ZPG turbulent boundary layer and in the present case, it is the dominant component across the layer. The $\overline{u'w'}$ and $\overline{v'w'}$ components are nonzero and negative throughout the boundary layer and as before, this is due to the spanwise mean-flow component. As with the previous case, the mean-velocity and Reynolds-stress profiles for the different z locations are the same to within the measurement uncertainty.

Over the course of the test entry, profile measurements were repeated at selected locations on the model to assess any run-to-run variability that may exist. Three repeat profiles, acquired at $x = 1168.4$ mm, $z = 0$ mm, are shown in Fig. 58. For these measurements, the model was configured with the F6 wing with extension and set to a pitch angle of $\alpha = 5°$. The profile measurements were made over a period of days to weeks and the run-to-run profile points shown in the figure are generally within the measurement uncertainty.

In Fig. 59, repeat profile measurements at $x = 1168.4$ mm, $z = 0$ mm for the model configured with the F6 wing with extension (closed symbols) are compared to repeat profiles at the same location for the model configured with the F6 wing (open symbols). Uncertainty bands were not included in the plots for clarity. The data for the two cases presented in this plot were acquired three months apart and during that time, the fuselage nose section was removed and reassembled, and the LDV probe/traverse system was disassembled, reassembled, and the laser beam unit vectors were remeasured. Except for some minor differences in the $\overline{u'v'}$ component and in the other statistics very near the wall, the profiles are in good agreement and mostly within the measurement uncertainty. This suggests that the different wing leading-edge configurations have minimal, if any, effect on the velocity profiles measured at this location on the fuselage.

Triple products of the velocity components were also calculated and example profiles of the ten independent components are shown in Fig. 60. These profiles were measured at $x = 1168.4$ mm, $z = 0$ mm, and the model was configured with the F6 wing with extension and set at a pitch angle of $\alpha = 5°$. Note that the triple products were normalized by U_∞^3 and the amplitudes of the triple products are therefore very small. To reduce the number of decimal places on the abscissas of the plots, the normalized triple products were multiplied by 10^3. In Fig. 61, the triple product profiles at the same location on the model are compared for both wing configurations. Here the agreement is good except near the wall where there is increasing discrepancy for some of the components. For those near-wall points, the uncertainties are larger due to a fewer number of samples in the calculated statistics. Aside from those differences, it again appears that the wing leading-edge configuration has minimal effect on the boundary layer at this location on the fuselage.

4.4 LDV Measurements in the Wing Leading Edge Region

In this section, we present examples of the measured velocity profiles on the port side of the fuselage near the wing leading edge. Consider first the case where the model was configured with the F6 wing and the model pitch angle was set to $\alpha = 5°$. For these measurements, the LDV probe was mounted to a $39°$ tilt plate to avoid beam clipping when the measurement volume was close to the wing leading-edge (see Fig. 25). Here, the beam unit vectors were measured with the tilt adapter in place so that the calculated velocity transformation matrix accounts for the probe tilt automatically. In addition, the LDV probe was operated in the single-channel mode for these measurements and so particle positions within the measurement volume are not available for this data set.

A schematic of the measurement locations for this case is shown in Fig. 62 and it is superimposed on an oil-flow visualization of the flow in the leading-edge region. The surface pattern is characterized by a primary separation line and a secondary separation line further downstream and closer to the wing-leading edge. In the region between the secondary separation line (sometimes referred to as a line of low shear [28]) and the leading edge, oil-flow material is scrubbed away by a horseshoe vortex that is present in a mean sense. Velocity profiles were measured in two areas: first, profiles were measured at several x locations along a line located at $z = 93.3$ mm and second, profiles were measured at five locations along the root chord line projected forward of the wing leading edge (red dashed line in Fig. 62). The five locations along the chord line correspond to the same (x, z) locations of unsteady pressure sensors (sensors 27–31) on the starboard side of the model. For each (x, z) location, the velocity profiles were acquired by traversing in the $-y$ direction, normal to the port side of the fuselage. To aid the following discussion, schematics of the hypothesized mean flow in the leading-edge region are shown in Fig. 63.

Example mean velocity and Reynolds-stress profiles at four x locations along a line at $z = 93.3$ mm are plotted in Figs. 64, 65, and 66. The first location at $x = 1983.4$ mm (Fig. 64a) is upstream of the primary separation line (see Fig. 62) and here, the mean flow is directed up and around the separated-flow region. The $\overline{v}$ component of mean velocity at this location is slightly negative, indicating a weak flow directed away from the fuselage.

The mean-velocity profiles at $x = 2008.4$ mm display inflections, deficits, and excesses that suggest the presence of a vortex. To support that, consider the schematics in Fig. 63. In Fig. 63a, a top view looking down on the wing-fuselage junction shows a hypothesized mean horseshoe vortex in the junction region. The horizontal line cutting through the vortex corresponds to the location of the LDV survey at $x = 2008.4$ mm. Near the fuselage, the vortex opposes the oncoming flow. That accounts for the near-wall deficit in the $\overline{u}$ profile of Fig. 64b. At further distances from the wall, towards the center of the vortex, the $\overline{u}$ component of velocity induced by the vortex becomes smaller, providing less opposition to the oncoming flow. That is manifested as an increase in the $\overline{u}$ velocity above the deficit. Moving further out, above the center of the vortex at roughly 5–6 mm, the velocity induced by the vortex adds to the oncoming flow to further increase the $\overline{u}$ velocity. Eventually, as the y location exits the vortex, the $\overline{u}$ profile becomes more uniform.

From Fig. 63a, the $\overline{v}$ component of velocity induced by the vortex is always negative and away from the fuselage. More specifically, the $\overline{v}$ velocity is zero at the wall, increases negatively away from the wall, and peaks near the vortex centerline. Past that, the $\overline{v}$ velocity decreases and eventually approaches zero. This behavior is borne out in the $\overline{v}$ profile of Fig. 64b.

Consider next the schematic in Fig. 63b, which provides an end view looking upstream at the hypothesized mean flow. The approaching flow has a positive $\overline{w}$ component. Near the fuselage, the vortex adds to the $\overline{w}$ component of velocity until the point on the profile where the vortex centerline is reached. At that point, the vortex neither adds nor subtracts to the vertical flow. Further away from the wall, the vortex opposes the flow, subtracting from the $\overline{w}$ component of velocity. The $\overline{w}$ profile in Fig. 64b supports the hypothesized mean flow. The $\overline{w}$ profile bulges out near the wall where the vortical flow adds to the $\overline{w}$ component. Further away from the wall, the $\overline{w}$ profile peaks and then diminishes as the vertical velocity induced by the vortex decreases and then opposes the approaching vertical flow.

The mean velocity profiles at $x = 2053.4$ mm and $x = 2093.4$ mm (Figs. 64c and d) indicate a region of increasing $\overline{u}$ velocity where the flow is accelerating around the wing leading edge. This is also a region where CFD calculations show minimum static pressures on the upper surface of the wing root (not presented in this report). The $\overline{v}$ component of velocity for both profiles is zero near the wall and then increases with increasing distance from the surface, indicating that the flow is moving toward the wall in this region. As we move from $x = 2053.4$ mm to $x = 2093.4$ mm, the $\overline{w}$ component of velocity decreases as the flow becomes more oriented in the x direction.

The Reynolds normal-stress and shear-stress profiles at the four x locations along the line at $z = 93.3$ mm are shown in Figs. 65 and 66, respectively. The most notable feature in both plots is that the Reynolds stresses have significantly larger magnitudes at $x = 2008.4$ mm where the profile passes through the horseshoe vortex.

Example mean-velocity and Reynolds-stress profiles at the five locations along the root chord line projected ahead of the wing leading edge (see Fig. 62) are shown in Figs. 67, 68, and 69. Note that these profiles contain an increasing number of y locations with increasing x position. That difference is due to the accumulation of seeding material on the window over the course of a wind-tunnel run, particularly near the secondary separation line (see Fig. 70). The accumulation of seeding material on the window introduced flare noise that degraded the LDV signal to the point that bursts could no longer be detected without stopping the run and cleaning the window. As such, several of the profiles were abbreviated and have fewer y locations. As we moved downstream, towards the wing leading edge, the accumulation was not as significant, allowing for the acquisition of more profile points before the window required cleaning.

Considering the mean velocity profiles at $x = 1993.4$ mm, $z = 47.3$ mm (Fig. 67a), the negative $\overline{u}$ velocity near the wall and the negative $\overline{v}$ velocity throughout the profile suggest that a horseshoe vortex is present in the mean, with its center located downstream of the profile location. This scenario is sketched in Fig. 71, where a hypothesized mean vortex is located near the fuselage-wing junction. Considering next the mean velocity profiles at $x = 1998.5$ mm and $z = 46.8$ mm (Fig. 67b), the negative $\overline{u}$ near the wall and the positive $\overline{v}$ velocity throughout the profile suggest the presence of a horseshoe vortex; but in this case, the center is upstream of the profile location as sketched in Fig. 71. The subsequent mean velocity profiles (Figs. 67c–e) for $\overline{u}$ and $\overline{v}$ have a similar character to those shown in Fig. 67b. For all five locations, the $\overline{w}$ velocity profile is positive due to the positive model pitch angle and the associated upflow.

The Reynolds normal-stress profiles (Fig. 68) peak near the horseshoe vortex center (except for the x location closest to the wing leading edge) and then continuously diminish as the leading edge is approached. Similar characteristics are also observed in the Reynolds shear-stress profiles (Fig. 69).

The turbulent separated flow around wing-fuselage junctions can often display low-frequency, chaotic oscillations between two flow states and this behavior was first identified by Devenport and Simpson [28]. The first state is a back-flow mode where the horseshoe vortex that forms upstream of the wing leading edge induces a strong wall jet that penetrates far upstream. The second state is a zero-flow mode and occurs when the reverse flow produced by the horseshoe vortex is too weak to penetrate upstream and is instead ejected upward, away from the wall. These states manifest themselves as bimodal (double-peaked) probability density functions (PDFs) of velocity measurements at certain locations in the flow field. For the profile measurements made in the leading-edge region of the F6 wing at $\alpha = 5°$, only two locations were found to display bimodal PDFs: one was at $x = 1993.4$ mm, $z = 47.3$ mm and the other was at $x = 2008.4$ mm, $z = 93.3$ mm. For both of these locations, the mean-flow profiles cut through a portion of the mean horseshoe vortex (recall the above discussion and see Figs. 67a and 64b).

Probability density functions for the u component of velocity at $x = 1993.4$ mm, $z = 47.3$ mm are shown in Fig. 72 for several y locations above the wall. At the first two y locations off the wall, the PDFs display a bi-modal character, where the peak at negative velocities denotes the back-flow mode and the peak at low positive velocities denotes the zero-flow mode. For y locations further from the wall, the zero-flow mode diminishes until a single mode is present in the PDFs. Meanwhile, the mean u velocity increases from negative to positive values.

Probability density functions for the u component of velocity at $x = 2008.4$ mm, $z = 93.3$ mm are shown in Fig. 73 for several y locations above the wall. Here again, the near-wall PDFs display a bimodal character; but in this case, the PDFs are shifted towards positive values presumably by the accelerating flow around the leading edge. Therefore, the back-flow mode shows up as a peak near zero velocity and the zero-flow mode shows up as a peak around $u/U_\infty \approx 0.5$. In other words, the strong wall jet produced during the back-flow mode is counteracted by the oncoming flow to produce a velocity near zero, and the low-velocity flow produced during the zero-flow mode adds to the oncoming flow to produce a positive velocity. As the y location increases, the relative values of the bimodal peaks in the PDFs are reversed and by ≈ 7 mm from the wall, the PDFs display a single mode.

Example triple products of the velocity components at $x = 2009.1$ mm, $z = 45.8$ mm are shown in Fig. 74. This location is closest to the wing leading edge (see Fig. 62) and is at the same (x, z) location as an unsteady pressure sensor (sensor 31) on the starboard side of the model. In comparison to the triple-product values of the boundary layer on the fuselage nose section (Fig. 60), these values in the separated flow region are considerably larger.

For the remainder of this section, we present measured velocity profiles in the leading-edge region of the F6 wing with leading-edge extension. Model pitch angles of $5°$ and $-2.5°$ were considered for these measurements. The LDV probe head was oriented normal to the window surface and was operated in the single-channel mode for most of the measurements in this region. At the few locations indicated in Table 5, the probe was operated in dual-channel mode so that finer spatial resolution near the wall could be achieved.

A schematic of the measurement locations for the F6 wing with extension is shown in Fig. 75 and it is superimposed on an oil-flow visualization in the leading-edge region with the model at a pitch angle $\alpha = 5°$. In contrast to the F6 wing, there does not appear to be a strong horseshoe vortex and multiple separation lines ahead of the wing leading edge. Instead, there is a single separation line that emanates from a stagnation region below the wing chord line (the red dashed line in Fig. 75). This separation line lies much closer to the wing leading edge due to the weaker adverse pressure gradient imposed by the wing leading-edge extension that tapers into the fuselage almost tangentially. Velocity profiles were measured along a pair of lines located at $z = 98.05$ mm and $z = 6.2$ mm. In addition, profile measurements were made at $x = 1904.2$ mm, $z = 71.2$ mm and at a location further upstream ($x = 1859.2$ mm, $z = 55.05$ mm) to characterize the approaching flow. As before, the velocity profiles were acquired by traversing in the $-y$ direction, normal to the port side of the fuselage.

Mean-velocity and Reynolds-stress profiles at four locations along the $z = 98.05$ mm line are shown in Figs. 76, 77, and 78. Here, the model was set to a pitch angle of $5°$. The $\overline{u}$ profiles along the line are similar and do not change significantly as the leading edge is approached. The $\overline{v}$ profiles are essentially zero across the boundary layer while the $\overline{w}$ profiles are positive, reflecting the fact that the model is at a positive pitch angle. The $\overline{w}$ velocity also increases slightly as the leading edge is approached and this is due to the oncoming flow being directed up and around the leading edge. The Reynolds normal-stress profiles for the same four locations at $z = 98.05$ mm are shown in Fig. 77. The $\overline{v'v'}$ and $\overline{w'w'}$ components do not vary much at these four locations; however, the $\overline{u'u'}$ component does display some near-wall attenuation with increasing x location. The Reynolds shear-stress profiles, which are shown in Fig. 78, do not vary significantly for the first three x locations. At the last x location, the $\overline{u'w'}$ component is attenuated near the wall and above $y \approx 12$ mm, it becomes negative until $y \approx 23.8$ mm.

Mean-velocity and Reynolds-stress profiles along a line at $z = 6.2$ mm are shown in Figs. 79, 80, and 81. Here, the $\overline{u}$ component of velocity decreases as the x location moves into the stagnation region indicated by the oil-flow visualization (see Fig. 75). The $\overline{v}$ component of velocity becomes more negative as we move into the stagnation region, indicating flow directed away from the fuselage surface. The $\overline{w}$ component of velocity remains positive; but near the wall, it decreases slightly with increasing x location. For the Reynolds normal-stress profiles along the $z = 6.2$ mm line (Fig. 80), the $\overline{u'u'}$ component displays growth as we move into the stagnation region. The $\overline{v'v'}$ and

$\overline{w'w'}$ components are also slightly increased over the range of x locations shown. This behavior is consistent with the results of Bradshaw [29] where an adverse pressure gradient increased all three components of the Reynolds normal stress. For the Reynolds shear-stress profiles along the $z = 6.2$ mm line (Fig. 81), the $\overline{u'v'}$ and $\overline{u'w'}$ components are also enhanced as we move into the stagnation region, but the $\overline{v'w'}$ component is relatively constant.

An example for the triple products of the velocity components at $x = 1919.2$ mm, $z = 6.2$ mm is shown in Fig. 82. Here, the approaching boundary layer is exposed to an adverse pressure gradient as it moves into the stagnation region indicated in the oil-flow visualization (Fig. 75). Distinct variations in the triple-product profiles are observed for this location, but the amplitudes are less than what was observed for the F6 configuration at a location very close to the wing leading edge (Fig. 74).

Profile measurements of the mean velocity, the Reynolds normal stress, and the Reynolds shear stress at $x = 1859.2$ mm, $z = 55.05$ mm and $\alpha = 5°$ are shown in Figs. 83, 84, and 85, respectively. In these figures, three data sets—acquired over the course of several days—were plotted to demonstrate the repeatability of the measurements. In general, the repeat profiles are observed to be the same to within the measurement uncertainty.

A schematic of the measurement locations for the F6 wing with extension at $\alpha = -2.5°$ is shown in Fig. 86. As before, the locations are superimposed on an oil-flow visualization of the wing leading-edge region. In this case, the flow approaches the wing leading edge, nearly along the chord line, and then splits almost evenly around the upper and lower surfaces of the wing. Velocity profiles were measured at the same locations as for the $\alpha = 5°$ case and they were acquired by traversing in the $-y$ direction.

Mean-velocity and Reynolds-stress profiles at four locations along the $z = 98.05$ mm line are shown in Figs. 87, 88, and 89 for $\alpha = -2.5°$. The $\overline{u}$ velocity profiles display a slight decrease in the value near the wall as the x location increases. The $\overline{v}$ velocity profiles display increasingly negative values with increasing x location, specifically near the edge of the boundary layer. The $\overline{w}$ velocity profiles are observed to progress from slightly negative values in the freestream (Fig. 87a) to increasingly positive values across the boundary layer as the flow approaches the wing and is directed up and around the leading edge. The Reynolds normal-stress profiles for the same four locations at $z = 98.05$ mm are shown in Fig. 88. As with the $\alpha = 5°$ case, the $\overline{v'v'}$ and $\overline{w'w'}$ components do not vary significantly over these four x locations; but in contrast to the $\alpha = 5°$ case, the $\overline{u'u'}$ component displays a slight increase and development of a peak away from the wall. The Reynolds shear-stress profiles in Fig. 89 display vary little change over the four measurement locations at $z = 98.05$ mm.

Mean-velocity and Reynolds-stress profiles at four locations along the $z = 6.2$ mm line are shown in Figs. 90, 91, and 92 for $\alpha = -2.5°$. Both the $\overline{u}$ and $\overline{v}$ components show slight decreases with increasing x location. The $\overline{w}$ component is negative and becomes increasingly negative with increasing x location as the flow is directly down and around the wing leading edge. The Reynolds normal-stress profiles are shown in Fig. 91 and here, the $\overline{u'u'}$ component is observed to increase slightly and develop a peak away from the wall as the x location increases. The $\overline{v'v'}$ component changes only slightly and the $\overline{w'w'}$ component indicates some attenuation near the wall with increasing x location. The Reynolds shear-stress profiles shown in Fig. 92 change only slightly with increasing x location. In particular, both the $\overline{u'v'}$ and $\overline{u'w'}$ components display a slight attenuation very close to the wall. The $\overline{v'w'}$ component is essentially zero across the boundary layer for these four measurement locations.

4.5   LDV Measurements in the Wing Trailing-Edge Corner-Flow Region

In this section, we present examples of the measured velocity profiles on the port side of the model in the wing trailing edge corner region. Here, the profile measurements were made by traversing in the z direction, up from the wing surface for a range of (x, y) locations. The LDV probe was

operated in the single-channel mode for these measurements and so particle positions within the measurement volume are not available for this data set.

Consider first the case where the model was configured with the F6 wing and the model pitch angle was set to $\alpha = 5°$. Example profiles for this data set are presented at three x locations: the first is at $x = 2747.6$ mm, which is upstream of the corner separation; the second is at $x = 2852.6$ mm, which is at the beginning of the corner separation; and the third is at $x = 2892.6$ mm, which is located in the corner separation (the relation of these x locations to the corner separation is shown in Fig. 28).

Mean-velocity profiles in the corner-flow region of the F6 wing at $x = 2747.6$ mm and $\alpha = 5°$ are shown in Fig. 93. Here, the velocity profiles are plotted at six spanwise locations (y locations) and for reference, the fuselage surface is at $y = -236.1$ mm. The z_o in the ordinate label denotes the z location of the wing surface and those values are listed in Table 1. At the last two spanwise locations shown (Figs. 93e and f), the profiles extend over a smaller range of z values. This is due to support ribs on the optical windows that blocked some of the probe laser beams and thereby prevented measurements. For $z - z_o$ locations of ≈ 20 mm and above, the variations in the mean velocity profiles are indicative of the fuselage boundary layer. As we move outboard along the wing span to larger $-y$ values, the $\overline{u}$ component increases towards the local freestream value. The $\overline{v}$ component is zero in this region and the $\overline{w}$ component is negative as the flow moves down along the contour of the wing surface. At $y = -256.1$ mm, the measured profile is near the edge of the fuselage boundary layer. For $z - z_o$ locations below ≈ 20 mm, the variations in the mean velocity components are indicative of the merged fuselage and wing boundary layers. An interesting feature of these profiles is the negative $\overline{v}$ component near the wall, which indicates flow away from the fuselage. This may be the result of secondary flow induced by Reynolds shear-stress gradients along the bisector plane between the wing and fuselage surfaces [30]. However, more detailed analysis is required to support this explanation.

The corresponding Reynolds normal-stress profiles at $x = 2747.6$ mm are shown in Fig. 94. Similar to the mean-velocity profiles, the Reynolds normal-stress variations above $z - z_o \approx 20$ mm are indicative of the fuselage boundary layer. All three components are observed to decay towards the freestream levels as the y location moves out along the wing span. Below $z - z_o \approx 20$ mm, the normal-stress variations are driven by the interaction of the merged wing and fuselage boundary layers. By $y = -286.1$ mm, however, the normal-stress profiles are beginning to look like those of the wing boundary layer by itself.

The corresponding Reynolds shear-stress profiles at $x = 2747.6$ mm are shown in Fig. 95. Again, the shear-stress variations above $z - z_o \approx 20$ mm are indicative of the fuselage boundary layer. The $\overline{u'v'}$ component remains positive for most of the y locations and then decays to zero as we move beyond the fuselage boundary layer. In the fuselage boundary layer, both the $\overline{u'w'}$ and $\overline{v'w'}$ components are finite and negative and then decay to zero as we exit the fuselage boundary layer. Below $z - z_o \approx 20$ mm, where the wing and fuselage boundary layers are merged, there are significant variations in the components of Reynolds shear stress. As the y location moves out of the merged boundary-layer region, the shear-stress profiles begin to represent those of the wing boundary layer alone. Here, however, the $\overline{u'v'}$ and $\overline{v'w'}$ components remain nonzero presumably due to spanwise velocity gradients.

Mean velocity profiles at $x = 2852.6$ mm are shown in Fig. 96. Recall that these profile measurements were made near the beginning of the corner-flow separation. The character of the mean velocity profiles at this location are similar to those at $x = 2747.6$ mm, well upstream of the separated flow. Relative to the mean flow at the upstream location, the $\overline{u}$ component has decreased as the corner flow developed through an adverse pressure gradient to the $x = 2852.6$ mm location. In addition, the spanwise component of velocity near the wall has increased for y locations at and beyond -246.1 mm. In part, that may be due to an upstream influence of the separated-flow region that tends to direct the approaching flow away from the fuselage.

The corresponding Reynolds normal-stress profiles at $x = 2852.6$ mm are shown in Fig. 97. The variations in the normal-stress profiles are similar to the upstream location in that variations above

$z - z_o \approx 20$ mm are driven by the fuselage boundary layer and those below are driven by the merged wing and fuselage boundary layers. At $y = -286.1$ mm, the normal-stress profiles are indicative of the wing boundary layer. The corresponding Reynolds shear-stress profiles at $x = 2852.6$ mm are shown in Fig. 98 and also have a similar character to the shear-stress profiles at the upstream location.

Mean-velocity profiles at $x = 2892.6$ mm are shown in Fig. 99. Recall that these profile measurements are beyond the beginning of the corner-flow separation and that some of the profiles are located in the separated-flow region. At the first two y locations ($y = -236.6$ mm and -239.1 mm), the near-wall values of $\overline{u}$ are negative, indicating reversed flow in the mean. Here also, the near wall $\overline{w}$ values are positive, indicating that the flow moves upstream along the contour of the wing surface. At distances further outboard ($y = -243.1$ mm and -246.1 mm), the profiles are still inside the separated-flow region (as indicated by the oil-flow visualization in Fig. 28), but there is no longer reversed flow in the mean.

The corresponding Reynolds normal-stress profiles at $x = 2892.6$ mm are shown in Fig. 100. For the profiles at $y = -236.6$ mm and -239.1 mm, the normal stresses peak near the inflection point in the $\overline{u}$ profile and have the character of a free shear layer. As we move further outboard, that peak shifts towards the wall. By $y = -286.1$ mm, we are well outside the separated-flow region and the fuselage boundary layer, and the profiles are more indicative of the wing boundary layer.

The corresponding Reynolds shear-stress profiles at $x = 2892.6$ mm are shown in Fig. 101. For the profiles at $y = -236.6$ mm and -239.1 mm, the $\overline{u'w'}$ component displays large negative values that peak away from the wall near the peaks in the Reynolds normal-stress profiles. The peak in this component shifts towards the wing surface as we move outboard. The $\overline{u'v'}$ component displays a peak at the same location as the $\overline{u'w'}$ component, but it is positive at $y = -236.6$ mm and then decays and becomes negative as we move across the separated-flow region. Meanwhile, the $\overline{v'w'}$ component displays a peak at the same location and it is slightly negative at $y = -236.6$ mm and then grows and becomes positive as we move across the separated-flow region. Outside the separated-flow region, the $\overline{v'w'}$ component decays to near zero.

Next, we consider the case where the model was configured with the F6 wing with leading-edge extension at a model pitch angle of $5°$. Example profiles for this data set are presented at the same three x locations as for the F6 wing configuration: $x = 2747.6$ mm, 2852.6 mm, and 2892.6 mm. The relation of these x locations to the corner separation is shown in Fig. 29a.

Mean-velocity profiles at $x = 2747.6$ mm and $\alpha = 5°$ are shown in Fig. 102. Recall from the previous section that the leading-edge extension eliminates the horseshoe vortex and the associated bimodal oscillations. In addition, the initial development of the corner flow is modified by the change in the leading-edge geometry. Despite those differences, the mean-velocity profiles at $x = 2747.6$ mm are remarkably similar to those for the F6 wing at the same x location. That is also true for the Reynolds normal-stress and Reynolds shear-stress profiles shown in Figs. 103 and 104, respectively.

Mean-velocity profiles at $x = 2852.6$ mm and $\alpha = 5°$ are shown in Fig. 105. These profile measurements were made a few millimeters downstream of the start of the corner-flow separation as indicated by the oil-flow visualization (see Fig. 29a). The mean-velocity profiles are similar in character to those at the upstream x location; but due to the adverse pressure gradient imposed on the flow, the $\overline{u}$ component is reduced. For the profiles at $y = -236.6$ mm and -237.1 mm, the $\overline{u}$ velocity at the first measurement location above the wing surface is near zero. However, the instantaneous values of u near the wall are highly unsteady, with both negative and positive values that indicate periods of reversed and attached flow. This behavior manifests as bimodal probability density functions for the u component of velocity as shown in Fig. 106. Here, the near wall PDFs indicate that the instantaneous values of the velocity can be negative at times despite the fact that the mean velocity is near zero or increasingly positive as $z - z_o$ is increased. The Reynolds normal-stress profiles, which are shown in Fig. 107, indicate significant differences relative to the upstream x location, particularly near the wing-fuselage corner where the profiles are influenced by the separated flow. The Reynolds shear-stress profiles, which are shown in Fig. 108, also display differences relative to the upstream x location.

Mean-velocity profiles at $x = 2892.6$ mm are shown in Fig. 109. This x location is beyond the beginning of the corner separation and at the first two y locations (-237.1 mm and -239.1 mm) there, the $\overline{u}$ and $\overline{w}$ profiles indicate reversed flow near the wall. Further outboard, the $\overline{u}$ component is positive throughout the profile and by $y = -266.1$ mm, the profile measurement is out of the separated-flow region. The corresponding Reynolds normal-stress profiles are shown in Fig. 110. Similar to the F6 wing configuration, the normal stress profiles near the fuselage peak at the inflection point in the $\overline{u}$ profile and then that peak moves towards the wall as we move outboard on the wing. The normal-stress profiles at $y = -266.1$ mm are at a location out of the separated-flow region are are more characteristic of the wing boundary layer. The corresponding Reynolds shear-stress profiles are shown in Fig. 111. These profiles share similar characteristics to those discussed earlier for the F6 wing at the same x location (see Fig. 101).

Consider the final case where the model was configured with the F6 wing with leading-edge extension and set to a pitch angle of $-2.5°$. Example mean-velocity and Reynolds-stress profiles for the data set are presented at three x locations: $x = 2757.6$ mm (Figs. 112, 113, and 114), $x = 2887.6$ mm (Figs. 115, 116, and 117), and $x = 2922.6$ mm (Figs. 118, 119, and 120). Note that these locations are different than those for the case where the model was at $\alpha = 5°$, but they are at similar locations *relative* to the corner-flow separation: the first one is well upstream of the separation, the second one is near the beginning of separation, and the third one is within the separated-flow region. Figure 29b shows the relation of these x locations to the corner-flow separation. In general, many of the features for these mean-velocity and Reynolds-stress profiles are similar to those for the $\alpha = 5°$ case; therefore, a plot-by-plot description is not provided here.

To give a sense of the measurement repeatability, repeat profiles for the mean velocity (Fig. 121), the Reynolds normal stress (Fig. 122), and the Reynolds shear stress (Fig. 123) within the separated-flow region at $x = 2892.6$ mm, $y = -239.1$ mm are presented. For this data set, the model was configured with the F6 wing with extension and set to a pitch angle of $5°$. In the plots, each velocity statistic is represented by a different symbol and the different colors for each symbol represent the different repeat profiles. Five repeat profiles were acquired at this location over the course of a month. During that period, the LDV probe/traverse assembly was moved to a new location on the bridge piece inside the model (but one in which the traverse travel was sufficient to reach the same x location on the model). Since this could slightly alter the angles between the probe laser beams and the window-surface normal, the beam unit vectors were remeasured after moving the assembly and a new velocity transformation matrix was calculated. In general, the scatter in the statistics at a given $z - z_o$ location appears to be random and most of the scatter can be accounted for by the estimated measurement uncertainties (uncertainty limits are not shown in the plots to improve clarity).

Tunnel conditions for the above repeat data set are shown in Fig. 124. Recall that the chord Reynolds number was held constant during a wind-tunnel run by the tunnel controller and this is reflected by the tight clustering of data points around $Re_c = 2.4$ million. However, the air temperature from one run to another, and even within a given run, is observed to vary. As a result, the tunnel controller adjusted the freestream velocity to maintain the chord Reynolds number at a nominal value. To account for that velocity variation, the velocity statistics presented throughout the report were normalized, as appropriate, by the freestream velocity. For each of the repeat profile measurements, the model pitch angle was nominally set to $5°$ and that target was held to within $\pm 0.03°$ for the data shown here. For the repeat profile measurements discussed above, we did not observe any correlation with the slight variations in Re_c or α from one survey to another. In other words, the variations in the statistics from one run to another appear random and do not correlate with the small variations in the test conditions.

A limited number of repeat profile measurements were made with the model inverted (or rolled by $\phi = 180°$). These repeat profiles were made at the same spatial locations in the body fixed coordinate system as for the model upright repeat profiles ($\phi = 0°$); however, with the model inverted, the measurements are effectively made in a different spatial region of the 14x22 test section. Presumably, this would expose any nonuniformity or flow angularity in the freestream flow. However, given the limited amount of data we have collected, any difference that may exist between the

upright and inverted profile data at a given location in the model flow field cannot be attributed to a specific cause. In addition, the inverted model is not geometrically similar to the upright model: this is because the sting-mast position is fixed to the test-section floor and the model deformation due to gravity is different (and unquantified) in the inverted position. These limitations should be kept in mind when viewing the following example. Repeat mean velocity, Reynolds normal stress, and Reynolds shear stress profiles at $x = 2892.6$ mm, $y = -239.1$ mm and $\alpha = 5°$ for the F6 wing with leading-edge extension are shown in Fig. 125, 126, and 127. In the figures, the closed symbols denote 5 repeat profiles acquired with the model upright, while the open symbols denote 3 repeat profiles acquired with the model inverted. For the inverted case, there is a clear and repeatable shift in the $\overline{u}$ and $\overline{w}$ components of mean velocity, relative to the upright case, that is larger than the estimated measurement uncertainty. The Reynolds stresses also show a shift, but to a lesser extent.

As mentioned above, we cannot say what precisely is responsible for the difference between the model upright and inverted profiles at this location in the flow field. To allay concerns that the LDV probe/traverse system moved or deflected after the model was inverted, the beam unit vectors were remeasured with the model inverted. Whether the profile data were processed with these beam unit vectors or those measured in the upright configuration, the results were essentially the same. Also, after acquiring repeat profiles with the model inverted, the model was returned to the upright configuration and an additional repeat profile was acquired. That profile was found to be within the uncertainty of previous profiles acquired in the upright configuration. In light of these results, the difference in the upright and inverted profiles appears to be related to a change in the flow field rather than an obvious, unaccounted measurement error.

One possible explanation for the difference between the upright and inverted profiles could be related to flow angularity in the freestream. While the geometric pitch angle is the same for the two configurations, the actual angle-of-attack would be different if there was flow angularity in the freestream. Because the separated corner flow is sensitive to the model angle-of-attack, we would then be measuring a slightly different flow field when the model is inverted versus when it is upright. To support this conjecture, freestream flow angularity measurements would be required. However, an argument against this conjecture is provided by the repeat profiles acquired for the $\alpha = -2.5°$ case at $x = 2887.6$ mm, $y = -239.1$ mm (Figs. 128, 129, and 130), where the profiles for the upright and inverted configurations were generally the same to within the measurement uncertainty.

Example triple-product profiles of the velocity components at $x = 2892.6$ mm, $y = -239.1$ mm are shown in Fig. 131. Here, the model was configured with the F6 wing with extension and set to a pitch angle of $5°$. Uncertainty bands are shown for each data point in the profiles and they denote the estimated 95% confidence level. For the same location and model configuration, five repeat measurements of the triple products are presented in Fig. 132. Most of the repeat profiles are the same to within the measurement uncertainty.

4.6   Unsteady Pressure Results

Unsteady pressure data were collected from 23 pressure transducers on the starboard wing and 31 pressure transducers on the fuselage for model pitch angles ranging from $-10°$ to $10°$ in $2.5°$ increments. The locations of the pressure transducers are listed in Tables 6 and 7 and the details on the sensors—including the acquisition of voltage time series from them—were previously discussed in Section 2.7. Details on the processing of the voltage times series from the sensors were discussed in Section 3.2. Data were collected for both the F6 wing and the F6 wing with leading-edge extension. In this section, sample results are presented for both wing configurations at a limited number of sensor locations.

Broadband RMS pressures for a portion of the sensors on the starboard F6 wing are shown in Fig. 133. These sensors were located near the trailing-edge corner of the wing. For a given pitch angle, each symbol marks the (x, y) location of the sensor and the color represents the broadband RMS. The symbol for sensor 2 at $x = 2866.92$ mm, $y = 244.81$ mm is missing because that sensor was damaged at some point during the installation into the wing. For a few of the pitch angles,

the sensor symbols are overlaid on a corresponding image of the oil-flow visualization (obtained on the port side of the model and mirror imaged) to provide a spatial reference. The fuselage surface is located at $y = 236.1$ mm and the wing trailing edge is located at $x = 2961.9$ mm. As the model pitch angle is increased, the corner separation moves upstream and it expands outboard along the wing span to envelope an increasingly larger number of pressure sensors. As that occurs, the broadband RMS pressure for sensors within the separated-flow region increases and it continues to increase up to the largest model pitch angle.

The power spectral densities (PSDs) of the unsteady pressure at $x = 2902.94$ mm, $y = 244.81$ mm (sensor 4) are shown in Fig. 134 for a range of model pitch angles. Included in the plot is a wind-off PSD to show the sensor noise floor. The broad peak at about $f = 16.6$ kHz appears in both the wind-off and wind-on spectra and does not appear to be a flow-induced characteristic; rather, it is believed to be a characteristic of the in-line amplifier of the unsteady pressure transducer (in fact, all of the sensors have this preamplifier and display a similar peak). The narrowband peaks at ≈ 12 kHz and 36 kHz are due to electronic noise. For pitch angles up to $-5°$, the PSD are nearly the same and for these angles the sensor lies upstream of the corner separation. Once we move to higher pitch angles and the corner separation passes over the sensor, there is an increase in spectral energy and a shift towards lower frequencies.

The power spectral densities of the unsteady pressure at $x = 2956.94$ mm, $y = 262.79$ mm (sensor 13) are shown in Fig. 135 for a range of model pitch angles. This sensor is located further outboard than the previous one and is near the trailing edge of the wing. As with the previous sensor, the PSD are nearly the same for pitch angles up to $-5°$ and after that, the PSD display broadband energy growth, primarily at lower frequencies, as the separated-flow region moves outboard over the sensor. There is little change in the PSD at high frequencies (~ 10 kHz) as the pitch angle is increased.

In Figs. 136–139, the PSDs along a streamwise row of sensors at $y = 262.79$ mm are shown for pitch angles of $-2.5°$, $0°$, $2.5°$, and $5°$. At $\alpha = -2.5°$ (Fig. 136), the last two sensors in the row are influenced by the corner separation and display a slight reduction in high-frequency energy. With increasing pitch angle, more of the sensors in the row are influenced by the growing corner separation and they display an increase in broadband energy and a general shift towards lower frequencies with increasing x location.

The broadband RMS pressures for a portion of the sensors on the starboard F6 wing with extension are shown in Fig. 140. As with the F6 wing, a larger number of sensors are enveloped by the corner separation as it grows in length and width with increasing model pitch angle. As that occurs, the broadband RMS pressures for sensors within the corner separation increase and continue to increase up to the largest pitch angle. The corresponding PSDs for sensors located at $x = 2902.94$ mm, $y = 244.81$ mm (sensor 4) and $x = 2956.94$ mm, $y = 262.79$ mm (sensor 13) are shown for a range of pitch angles in Figs. 141 and 142, respectively. As with the F6 wing, the broadband energy grows and shifts towards lower frequencies as the separated-flow region grows in size and sweeps over the sensors with increasing pitch angle. In Figs. 143–146, the PSDs along a streamwise row of sensors at $y = 262.79$ mm are shown for pitch angles of $-2.5°$, $0°$, $2.5°$, and $5°$. The trends in the PSDs with increasing pitch angle and x location are similar to those for the F6 wing.

Consider next the unsteady pressure sensor at $x = 1993.44$ mm, $z = 47.32$ mm (sensor 27), which is on the starboard side of the fuselage and in the leading-edge region of the F6 wing. It is also near the secondary separation line indicated by the oil-flow visualization shown in Fig. 62. The power spectral densities of the unsteady pressure measured at this location are shown in Fig. 147 for a range of model pitch angles. The spectra are broadband in character and the amplitude of the spectra initially decrease with increasing pitch angle up to $\alpha = -2.5°$ and then increase with increasing pitch angle. To see that trend more clearly, the broadband RMS pressure for this sensor is plotted as a function of model pitch angle in Fig. 148. A minimum in the broadband RMS pressure is observed at $\alpha = -2.5°$ and for this pitch angle, the flow on the fuselage is expected to approach the leading-edge region nearly along the chord line, stagnate, and then split almost equally around

the wing leading edge. Note that two data sets are shown in Fig. 148: one where the pressures were acquired at progressively increasing pitch angles ($+\alpha$ sweep) and one where the pressures were acquired at progressively decreasing pitch angles ($-\alpha$ sweep). The RMS pressures for both data sets collapse and there is no apparent hysteresis in the unsteady pressure at this location.

Probability density functions of the unsteady pressure measured at $x = 1993.44$ mm, $z = 47.32$ mm (sensor 27) for a range of model pitch angles are shown in Fig. 149. Here, the unsteady pressure displays a bimodal PDF for pitch angles of $5°$ and above. This is associated with the chaotic oscillations of the horseshoe vortex in the leading-edge region of the F6 wing and the presence of two bistable flow states as described earlier in Section 4.4. This is also the same (x, z) location where bimodal PDFs were observed in the u component of velocity measured with LDV on the port side of the model at $\alpha = 5°$ (see Fig. 72). For model pitch angles below $5°$, bimodal PDFs are not observed for the unsteady pressure at this location. This does not necessarily imply the absence of bimodal oscillations in the flow field for these pitch angles; rather, the bimodal oscillations are fairly localized and this sensor may not be at the proper location to measure them.

For comparison, consider the sensor at $x = 1921.89$ mm, $z = 54.46$ mm (sensor 24), which is on the starboard side of the fuselage and in the leading-edge region of the F6 wing with extension. More specifically, this sensor is located on the root chord line projected forward of the leading edge and is just a few millimeters upstream of the leading edge. Recall that the purpose of the leading-edge extension was to eliminate the horseshoe vortex and the associated bimodal oscillations. As a result, there is a 1-to-2 orders of magnitude drop in the spectral amplitudes of the unsteady pressures near the leading edge (Fig. 150) relative to those of sensor 27 for the F6-wing configuration where bimodal oscillations were present (Fig. 147). The broadband RMS pressures (Fig. 151) are also an order-of-magnitude lower. Probability density functions for the sensor at $x = 1921.89$ mm, $z = 54.46$ mm (sensor 24) are shown in Fig. 152 for a range of pitch angles. For this sensor location, no bimodal oscillations are observed and the PDFs are nearly Gaussian.

4.7 Shear Stress Results

In this section, we present examples of the unsteady shear stress measurements made on the fuselage at $x = 1168.4$ mm, $y = -236.1$ mm, and $z = 0$ mm. Note that the MEMS capacitive shear stress sensors used for these measurements provide only a single component of the shear-stress vector, and in the present case, the sensor was oriented to measure the x component of shear stress; *i.e.*, the component along the length of the fuselage. Power spectral densities of the x component of shear stress for a range of model pitch angles are shown in Fig. 153. Here, PSDs for two models of capacitive shear stress sensors (model CS-D50 with a bandwidth of 1.4 kHz and model CS-A05 with a bandwidth of 5 kHz) and data for two test entries in the 14x22 (T638 and T640, separated by a month) are shown. In addition, the shear-stress data for the two test entries were collected with different test protocols. In test T638, the time series data from the shear stress sensors were collected at each model pitch angle as the pitch angle was increased from $-10°$ to $10°$ ($+\alpha$ sweep) and then decreased from $10°$ to $-10°$ ($-\alpha$ sweep) over the course of a run. In that case, the $+\alpha$ sweep and $-\alpha$ sweep PSDs are observed to collapse and there are no obvious hysteresis effects. In test T640, the time series data from the shear stress sensors were collected at each pitch angle during a different run, with the model pitch angle preset to the desired value prior to a given run. The shear stress PSDs measured during test entry T640 were found to be in good agreement with those measured during T638.

Example probability densities for the x component of shear stress measured at $x = 1168.4$ mm, $y = -236.1$ mm, and $z = 0$ mm for a range of model pitch angles are shown in Fig. 154. For this data set, the shear stress sensor bandwidth was 5 kHz (sensor model CS-A05). A Gaussian distribution (dashed line) is included in the plots for comparison. For the pitch angles considered, the PDFs for the x component of shear stress indicate a positively skewed signal. This characteristic is consistent with previous measurements in turbulent flat-plate boundary layers, where the unsteady shear stress was inferred from near-wall hot-wire measurements in the viscous sublayer [31].

As discussed earlier in Section 3.2, we were unable to obtain accurate measurements of the mean shear stress with the MEMS capacitive shear stress sensor due to the temperature sensitivity of the wind-off output voltage and the large changes in the air temperature over the course of a run in the 14x22. As such, those mean shear stress measurements are not reported. We did, however, measure the x component of mean shear stress with a Preston tube at $x = 1168.4$ mm, $y = -236.1$ mm, $z = 0$ mm for a model pitch angle of $\alpha = 0°$. From that measurement, the skin-friction coefficient was found to be $c_f = \tau_w/q_\infty = 0.0026 \pm 0.0001$.

5 Summary

In this report, we have presented the experimental details of and sample results for a recent CFD validation experiment on a full-span wing-fuselage junction model. This model geometry—which was designed in coordination with CFD subject matter experts from government, industry, and academia—exhibits a separated corner-flow region near the wing trailing edge that current RANS models are unable to reliably predict. The ultimate goal of this experimental effort is to provide a publicly-available high-quality flow field and surface data set with quantified boundary conditions, geometry, and measurement uncertainties. It is expected that this data set will be suitable for use in CFD workshop environments and will help CFD practitioners validate and improve their predictive capabilities for turbulent separated corner flows.

The primary objective of this first test entry with the junction model was to perform flow-field measurements with internally mounted laser Doppler velocimetry (LDV) systems. The flow-field measurements were focused in three regions on the port side of the junction model: 1) the boundary layer on the fuselage, well upstream of the wing leading edge; 2) the boundary layer in the vicinity of the wing leading edge; and 3) the corner-flow region near the wing trailing edge. For the corner-flow region in particular, profile measurements were acquired upstream of the corner-flow separation, near the beginning of separation, and within the separated-flow region. All three components of mean velocity and all six independent components of the Reynolds-stress tensor were calculated from the LDV measurements. In addition, all ten independent triple products of the velocity components were calculated. Sample results for these flow-field measurements were presented and the general features associated with them were discussed. Sample infrared images were presented to show the natural and tripped states of the boundary layer on the junction model. Oil-flow visualizations of the wing trailing edge region showed the progressive growth in the corner-flow separation with increasing model pitch angle and measurements of the length and width of the separated-flow region were documented. Sample results from the unsteady pressure measurements in the trailing edge corner region and in the leading-edge region of the wing-fuselage junction were presented and discussed. Finally, sample measurements of the unsteady shear stress on the fuselage nose section were presented.

References

1. Vassberg, J. C.; Tinoco, E. N.; Mani, M.; Brodersen, O. P.; Eisfeld, B.; Wahls, R. A.; Morrison, J. H.; Zickuhr, T.; Laflin, K. R.; and Mavriplis, D. J.: Abridged Summary of the Third AIAA Computational Fluid Dynamics Drag Prediction Workshop. *Journal of Aircraft*, vol. 45, no. 3, May–June 2008, pp. 781–798.

2. Rumsey, C. L.; Neuhart, D. H.; and Kegerise, M. A.: The NASA Juncture Flow Experiment: Goals, Progress, and Preliminary Testing (Invited). AIAA Paper 2016-1557, January 2016.

3. Rumsey, C. L.; and Morrison, J. H.: Goals and Status of the NASA Juncture Flow Experiment. AVT Specialists Meeting on Progress and Challenges in Validation Testing for CFD, STO-MP-AVT-246-03, September 2016.

4. Aeschliman, D. P.; and Oberkampf, W. L.: Experimental Methodology for Computational Fluid Dynamics Code Validation. *AIAA Journal*, vol. 36, no. 5, May 1998.

5. Rhode, M. N.; and Oberkampf, W. L.: Estimation of Uncertainties for a Model Validation Experiment in a Wind Tunnel. *Journal of Spacecraft and Rockets*, vol. 54, no. 1, January–February 2017.

6. Kuester, M. S.; Borgoltz, A.; and Devenport, W. J.: Experimental Visualization of Juncture Separation Bubbles at Low- to Moderate-Reynolds Numbers. AIAA Paper 2016-3880, June 2016.

7. Kegerise, M. A.; and Neuhart, D. H.: Wind Tunnel Test of a Risk-Reduction Wing/Fuselage Model to Examine Juncture-Flow Phenomena. NASA TM 219348, 2016.

8. Rumsey, C. L.; Carlson, J. R.; Hannon, J. A.; Jenkins, L. N.; Bartram, S. M.; Pulliam, T. H.; and Lee, H. C.: Boundary Condition Study for the Juncture Flow Experiment in the NASA Langley 14x22-Foot Subsonic Wind Tunnel. AIAA Paper 2017-4126, June 2017.

9. Neuhart, D. H.; and McGinley, C. B.: Free-Stream Turbulence Intensity in the Langley 14- by 22-Foot Subsonic Tunnel. NASA TP 213247, 2004.

10. Gentry, G. L.; Quinto, F. P.; Gatlin, G. G.; and Applin, Z. T.: The Langley 14- by 22-Foot Subsonic Tunnel. NASA TP 3008, 1990.

11. Boney, A. D.: Data Reduction Functions for the Langley 14- by 22-Foot Subsonic Tunnel. NASA TM 218513, 2014.

12. Finley, T.; and Tcheng, P.: Model Attitude Measurements at NASA Langley Research Center. AIAA Paper 92-0763, January 1992.

13. Albrecht, H. E.; Borys, M.; Damaschke, N.; and Tropea, C.: *Laser Doppler and Phase Doppler Measurement Techniques*. Springer, Berlin, Germany, 2003.

14. Miles, P. C.: Geometry of the Fringe Field Formed in the Intersection of Two Gaussian Beams. *Applied Optics*, vol. 35, no. 30, October 1996, pp. 5887–5895.

15. Lowe, K. T.: Design and Application of a Novel Laser-Doppler Velocimeter for Turbulence Structural Measurements in Turbulent Boundary Layers. Ph.D. Thesis, Virginia Polytechnic Institute and State University, 2006.

16. Lowe, K. T.; and Simpson, R. L.: An Advanced Laser-Doppler Velocimeter for Full-Vector Particle Position and Velocity Measurements. *Meas. Sci. Technol.*, vol. 20, 2009, pp. 1–16.

17. Brooks, D. R.; and Lowe, K. T.: Development and Application of a Compact Spatially Resolving Vector Laser Velocimeter for Near Surface Flow Measurements. *16th Int. Symp. on Applications of Laser Techniques to Fluid Mechanics*, Lisbon, Portugal, 2012.

18. Lowe, K. T.; Byun, G.; Neuhart, D. H.; and Simpson, R. L.: Auto-Calibration of Spatially-Resolving Laser-Doppler Veocimeters. AIAA Paper 2013-0044, January 2013.

19. Fingerson, L. M.; Adrian, R. J.; Menon, R. K.; and Kaufman, S. L.: Data Analysis, Laser Doppler Velocimetry and Particle Image Velocimetry. *TSI Short Course Text*, 1991.

20. Hurst, A. M.; Olsen, T. R.; Goodman, S.; VanDeWeert, J.; and Shang, T.: An Experimental Frequency Response Characterization of MEMS Piezoresistive Pressure Transducers. ASME Paper GT2014-27159, June 2014.

21. Patel, V. C.: Calibration of the Preston Tube and Limitations on its use in Pressure Gradients. *Journal of Fluid Mechanics*, vol. 23, 1965, pp. 185–208.

22. Ölçmen, S. M.; and Simpson, R. L.: An Experimental Study of a Three-Dimensional Pressure-Driven Turbulent Boundary Layer. *Journal of Fluid Mechanics*, vol. 290, 1995, pp. 225–262.

23. Corcos, G. M.: Resolution of Pressure in Turbulence. *J. Acoust. Soc. Am.*, vol. 35, no. 2, February 1963, pp. 192–199.

24. Schewe, G.: On the Structure and Resolution of Wall-Pressure Fluctuations Associated with Turbulent Boundary-Layer Flow. *Journal of Fluid Mechanics*, vol. 134, 1983, pp. 311–328.

25. Lueptow, R. M.: Transducer Resolution and the Turbulent Wall Pressure Spectrum. *J. Acoust. Soc. Am.*, vol. 97, no. 1, January 1995, pp. 370–378.

26. Braslow, A. L.; Hicks, R. M.; and Harris, R. V.: Use of Grit-Type Boundary-Layer-Transition Trips on Wind-Tunnel Models. NASA TN D-3579, September 1966.

27. Braslow, A. L.; and Knox, E. C.: Simplified Method for Determination of Crictial Height of Distributed Roughness Particles for Boundary-Layer Transition at Mach Numbers from 0 to 5. NASA TN 4363, September 1958.

28. Devenport, W. J.; and Simpson, R. L.: Time-Dependent and Time-Averaged Turbulence Structure Near the Nose of a Wing-Body Junction. *Journal of Fluid Mechanics*, vol. 210, 1990, pp. 23–55.

29. Bradshaw, P.: The Turbulence Structure of Equilibrium Boundary Layers. *Journal of Fluid Mechanics*, vol. 29, no. 4, 1967, pp. 625–645.

30. Gessner, F. B.: The Origin of Secondary Flow in Turbulent Flow along a Corner. *Journal of Fluid Mechanics*, vol. 58, no. 1, 1973, pp. 1–25.

31. Khoo, B. C.; Chew, Y. T.; and Teo, C. J.: Near-Wall Hot-Wire Measurements Part II: Turbulence Time Scale, Convective Velocity and Spectra in the Viscous Sublayer. *Experiments in Fluids*, vol. 31, 2001, pp. 494–505.

32. Coleman, H. W.; and Steele, W. G.: *Experimentation and Uncertainty Analysis for Engineers*. Wiley Interscience, New York, NY, 1999.

33. White, F. M.: *Viscous Fluid Flow*. McGraw–Hill, New York, NY, 1991.

34. Hemsch, M. J.; and Houlden, H. P.: Repeatability Modeling for Wind-Tunnel Measurements: Results for Three Langley Facilities. AIAA Paper 2014–0096, January 2014.

35. Shinpaugh, K. A.; Simpson, R. L.; Wicks, A. L.; Ha, S. M.; and Fleming, J. L.: Signal-Processing Techniques for Low Signal-to-Noise Ratio Laser Doppler Velocimetry Signals. *Experiments in Fluids*, vol. 12, 1992, pp. 319–328.

36. Benedict, L. H.; and Gould, R. D.: Towards Better Uncertainty Estimates for Turbulence Statistics. *Experiments in Fluids*, vol. 22, 1996, pp. 129–136.

Appendix A. Measurement of LDV Beam Unit Vectors

In this section, we describe the procedure used to measure the unit vectors for each laser beam emitted by the LDV probe head. These unit vectors were then used in subsequent calculations to process the LDV data as described in Section 3.1. A printed paper target with a known scale was first mounted to a bracket that was placed outside of and in front of a window on the junction-model fuselage. The LDV measurement volume was then positioned at a known y location (y_1) inside the model and the probe laser beams were projected onto the target. A digital SLR camera, fitted with a 105 mm lens, was then used to acquire an image of the probe laser beam pattern on the target. The LDV measurement volume was then moved to a second known y location (y_2) outside of the model and beyond the surface of the target. Here, a second image of the probe laser beam pattern on the target was captured. For both images, the laser power was set to a low level ($\approx 10\%$ of the maximum power) and the camera lens was fitted with an orange filter to cut back on the intensity of the laser light scattered by the target. A photograph of the measurement setup is shown in Fig. 155 and example images of the laser-beam pattern on the calibration target with the measurement volume at two different y locations are shown in Fig. 156. Note that the vertical shift in the laser-beam pattern for this example is due to the downward tilt of the LDV probe by $10°$ in the y–z plane. Since the images of the target were acquired with the camera at an angle to the target surface normal, there is perspective distortion in the images. Therefore, the images were preprocessed with a dewarping routine to remove the perspective distortion and subsequently cropped at four corners defined by fiducial marks on the calibration target. Examples of these preprocessed images (converted to gray-scale images) are shown in Fig. 157.

For a given preprocessed image, the next step was to find the (x, z) location for each laser-beam center. The origin of the coordinate system for these beam centers was located at the top left corner of the image, with x positive toward the right side of the image and z positive toward the bottom of the image. For a given laser beam, a rectangular region of interest (ROI) around the beam image was selected. The contrast of the ROI was then increased by saturating the bottom 1% and the top 1% of all pixel intensity values. The ROI was then converted to a binary image based on a threshold. A noise reduction step was then applied to the ROI in which all objects containing fewer than 50 connected pixels were removed from the image. Finally, the centroid of the connected object in the binary ROI image (the area of white pixels) was calculated to give the laser-beam center relative to the origin of the ROI; i.e., relative to the upper left corner. An example of these ROI processing steps is shown in Fig. 158 and here, the red plus symbol in images 1 and 4 denotes the calculated beam center location. Because we know the location of the origin for the ROI, the beam-center location can then be referenced to the origin of the full image that contains all of the probe laser beam images. The uncertainty in the beam-center location measured with this image-processing approach was estimated using simulated images of the Gaussian beam profile on the target and direct Monte Carlo simulation. In general, the 95% confidence interval for the measured beam center location was less than ± 1 pixel.

At this point, the laser-beam center locations are in units of pixels and need to be converted to physical units. To that end, a line of pixels passing through the grid on an image of the target (for example, the image in Fig. 157a) was selected and a spectrum for this line of intensity values was calculated. The fundamental frequency component of this spectrum corresponds to the inverse spacing of the the grid lines on the target in units of 1/pixels. Using that value, and the known target grid spacing of 5 mm, a scale factor in units of mm/pixel was calculated. This scale factor was subsequently used to convert the laser beam center locations to physical units. An example of the pixel intensity values for a line passing through the grid on an image of the target and the corresponding spectrum for that line of pixels is shown in Fig. 159. In this particular example, the scale factor was calculated to be 0.0159 mm/pixel.

Finally, for a given laser beam, the beam center location in the first image (x_1, y_1, z_1) and the beam center location in the second image (x_2, y_2, z_2) were used to calculate the unit vector of the

laser beam as:

$$\vec{b} = \frac{\Delta x \vec{i} + \Delta y \vec{j} + \Delta z \vec{k}}{\sqrt{\Delta x^2 + \Delta y^2 + \Delta z^2}}, \tag{22}$$

where $\Delta x = x_1 - x_2$, $\Delta y = y_2 - y_1$, and $\Delta z = z_1 - z_2$. It is important to note that the beam unit vectors as defined in this section are measured in an orthogonal coordinate system that is rotated about the x axis of the body-fixed coordinate system by $180°$. Therefore, once the velocity components were calculated as described in Section 3.1, they were rotated back to the body-fixed coordinate system.

Appendix B. Uncertainty Analysis

B.1. Uncertainty Analysis for the Wind Tunnel Test Conditions

During a given wind-tunnel run, several key tunnel parameters were monitored and measured. The settling chamber total pressure, p_o, was measured with a Mensor 2500 DPG with a full scale range of 2880 psfa and a systematic (bias) uncertainty of 0.01% of full scale ($B_{p_o} = 0.288$ psfa) as per the manufacturer's specifications. The differential pressure between the total pressure and the static pressure at the test-section entrance, Δp, was measured with a Mensor 2500 DPG with a full scale range of 144 psfd and a systematic uncertainty of 0.01% of full scale ($B_{\Delta p} = 0.0144$ psfd) as per the manufacturer's specifications. The air temperature, T_a, and the dew-point temperature, T_{dew}, were both measured at the test-section entrance with a Vigilant hygrometer and the systematic uncertainties in these temperatures were $B_{T_a} = 0.36$ °F and $B_{T_{dew}} = 0.36$ °F. Each of the systematic uncertainties for these measured variables was assumed to be a 95% confidence estimate.

The remaining test conditions were calculated using the data-reduction equations presented in the report by Boney [11]. For the present study, the freestream velocity, u_∞, the freestream Mach number, M_∞, and the chord Reynolds number, Re_c, were calculated from those equations. To estimate the systematic uncertainties for these variables, uncertainty analysis by direct Monte Carlo simulation (DMCS) was utilized [32]. In that analysis, each of the input parameters (p_o, Δp, T_a, and T_{dew}) are perturbed by a random value drawn from a normal distribution with a 2σ value equal to that of the corresponding systematic uncertainty. Here, it was assumed that the systematic uncertainties for the four input parameters were uncorrelated. The perturbed input parameters were then applied to the data-reduction equations to calculate the flow conditions of interest. This process was repeated 100,000 times to yield distributions in the calculated values. The systematic uncertainties for each of the calculated values were then set equal to the 2σ value of each respective distribution. As with the input variables, the systematic uncertainties in the calculated variables are 95% confidence estimates.

The specific data-reduction equations used to calculate the desired test conditions were as follows. First, the vapor pressure was calculated from:

$$p_v = 12.7654 \exp\left[\frac{9.72334 T_{dew} - 311.147}{0.555556 T_{dew} - 223.192}\right] \quad \text{(psf)}, \tag{23}$$

and the tunnel air density (uncorrected for compressibility) was calculated from:

$$\rho = \frac{p_o - 0.3789 p_v}{R(T_a + 459.67)} \quad \text{(slugs/ft}^3), \tag{24}$$

where $R = 1716.229$ (ft · lb)/(slug · °R) is the gas constant for air. The air viscosity was calculated from Sutherland's correlation:

$$\mu = \frac{0.0002672}{(T_a + 459.67) + 198.72}\left(\frac{T_a + 459.67}{518.69}\right)^{1.5} \quad \text{(slugs/ft · s)}. \tag{25}$$

The Sutherland correlation itself was assumed to have systematic uncertainty of 2% [33] and therefore, the viscosity values were also perturbed by a random value from a normal distribution with 2σ equal to 2% of μ during the DMCS. The test section static pressure was calculated from:

$$p_s = p_o - C'k\Delta p \qquad (26)$$

where C' is a dynamic pressure calibration coefficient for the 14x22 and k is a calibration coefficient for the check standard probe used to calibrate the 14x22 [34]. Based on unpublished calibration data from the facility, the systematic uncertainty in the product $C'k$ was assumed to be 2%, and it was perturbed by a random value from a normal distribution with 2σ equal to 2% of $C'k$ during the DMCS. The tunnel air density corrected for compressibility was calculated as:

$$\rho_c = \rho \left(\frac{p_o}{p_s}\right)^{-0.7143}, \qquad (27)$$

and the freestream Mach number was calculated as:

$$M_\infty = \sqrt{5\left(\left(\frac{p_o}{p_s}\right)^{2/7} - 1\right)}. \qquad (28)$$

The tunnel dynamic pressure was calculated as:

$$q_\infty = 3.5p_o\left((1-\lambda)^{5/7} - 1 + \lambda\right), \qquad (29)$$

where $\lambda = (p_o - p_s)/p_o$. The freestream velocity was then calculated as:

$$u_\infty = \sqrt{\frac{2q_\infty}{\rho_c}}, \qquad (30)$$

and the chord Reynold number was calculated as:

$$Re_c = \frac{\rho_c u_\infty c}{\mu}. \qquad (31)$$

Note that no wall or blockage corrections were applied to the test conditions calculated from the above equations. For further details on the 14x22 data-reductions equations, see Boney [11]. Using nominal values for p_o, Δp, T_a, and T_{dew} in the DMCS, the systematic uncertainties for the freestream velocity, the freestream Mach number, and the chord Reynolds number were found to be $B_{u_\infty} = 0.01u_\infty$, $B_{M_\infty} = 0.01M_\infty$, and $B_{Re_c} = 0.022Re_c$.

During a flow-field survey with the LDV system, a fixed number of samples were acquired over a period of time (generally on the order of a minute) at each point in the survey and with that, the tunnel test conditions were also acquired, but at a lower sample rate on the order of tens of Hz (note that the test-condition samples were not synchronized in time with the LDV data samples over the sample period). The test-condition samples were then used to calculate the mean test conditions for each point in the flow-field survey and they were also used to estimate the random uncertainty in those mean values. For example, the random uncertainty in the mean velocity (with 95% confidence) was calculated as:

$$P_{\overline{u_\infty}} = \frac{2S_{u_\infty}}{\sqrt{N}}, \qquad (32)$$

where S_{u_∞} is the standard deviation of the sample population for u_∞ and N is the number of statistically independent samples. In general, the test-condition samples were considered to be statistically independent since the intersample time was greater than twice the integral time scale derived from unpublished hot-wire measurements in the freestream of the 14x22. Similar equations were used to

calculate the random uncertainty for the mean Mach number, $P_{\overline{M_\infty}}$, the random uncertainty for the mean chord Reynolds number, $P_{\overline{Re_c}}$, and the random uncertainty for the mean air temperature, $P_{\overline{T_a}}$.

The total uncertainties for the mean values of u_∞, M_∞, Re_c, and T_a at each point in a flow-field survey were than calculated as:

$$U_{\overline{u_\infty}} = \sqrt{B_{u_\infty}^2 + P_{\overline{u_\infty}}^2}, \tag{33}$$

$$U_{\overline{M_\infty}} = \sqrt{B_{M_\infty}^2 + P_{\overline{M_\infty}}^2}, \tag{34}$$

$$U_{\overline{Re_c}} = \sqrt{B_{Re_c}^2 + P_{\overline{Re_c}}^2}, \tag{35}$$

and

$$U_{\overline{T_a}} = \sqrt{B_{T_a}^2 + P_{\overline{T_a}}^2}, \tag{36}$$

where the fact that $B_{u_\infty} = B_{\overline{u_\infty}}$, $B_{M_\infty} = B_{\overline{M_\infty}}$, $B_{Re_c} = B_{\overline{Re_c}}$, and $B_{T_a} = B_{\overline{T_a}}$ was used since averaging to obtain the mean does not reduce the systematic uncertainty [32].

B.2. Uncertainty Analysis for the LDV measurements

In this section, we provide an uncertainty analysis for the velocity measurements obtained with the LDV system. We start first with an uncertainty analysis for the instantaneous values of the velocity components, and then we present an uncertainty analysis for the various statistical moments calculated from those values. For each sample obtained with the LDV system, the three Doppler frequencies associated with the three nonorthogonal measurement directions (as defined by the five green laser beams) are measured. Then, Eqs. 22, 2, 3, 4, and 5 are used to calculate the three orthogonal velocity components in the body-fixed coordinate system. For convenience, these data-reduction equations are repeated below. The unit vector for each laser beam emitted by the probe is given as:

$$\vec{b}_i = \frac{\Delta x \vec{i} + \Delta y \vec{j} + \Delta z \vec{k}}{\sqrt{\Delta x^2 + \Delta y^2 + \Delta z^2}}, \tag{37}$$

where the subscript $i = 1, 2, \cdots, 5$ denotes the five green laser beams of the LDV probe. The measurement direction unit vector was calculated from:

$$\vec{e}_{ij} = \frac{\left(\vec{b}_i \times \vec{b}_j\right) \times \left(\vec{b}_i + \vec{b}_j\right)}{\left\|\left(\vec{b}_i \times \vec{b}_j\right) \times \left(\vec{b}_i + \vec{b}_j\right)\right\|}, \tag{38}$$

where $\vec{b}_i$ and $\vec{b}_j$ are unit vectors along the direction of beam i and beam j, respectively. The included angle, θ_{ij}, between beam i and beam j is equal to $\arccos(\vec{b}_i \cdot \vec{b}_j)$ and the fringe spacing for the measurement volume formed by the beam pair is given as:

$$d_{ij} = \frac{\lambda_{ij}}{2\sin\left(\theta_{ij}/2\right)}, \tag{39}$$

where λ_{ij} is the wavelength of the laser light for the beam pair. The measured Doppler frequencies were converted into velocities in the probe optical axes using:

$$u_{ij} = \vec{u} \cdot \vec{e}_{ij} = f_{ij} d_{ij}, \tag{40}$$

where u_{ij} is the velocity along the measurement direction unit vector formed by beam i and beam j, $\vec{u}$ is the velocity vector, and f_{ij} is the associated Doppler frequency. Finally, the nonorthogonal

velocity components in the probe optical axes were converted to orthogonal velocity components in the body-fixed coordinate system according to:

$$
\begin{bmatrix} u \\ v \\ w \end{bmatrix} = \begin{bmatrix} e_{12(x)} & e_{12(y)} & e_{12(z)} \\ e_{34(x)} & e_{34(y)} & e_{34(z)} \\ e_{35(x)} & e_{35(y)} & e_{35(z)} \end{bmatrix}^{-1} \begin{bmatrix} u_{12} \\ u_{34} \\ u_{35} \end{bmatrix},
\tag{41}
$$

where $e_{ij(x)}$, $e_{ij(y)}$, and $e_{ij(z)}$ denote the x, y, and z components of the measurement direction unit vectors in the body-fixed coordinate system.

The uncertainty in the velocity components for a given sample was determined by applying direct Monte Carlo simulation (DMCS) to the above data-reduction equations. To that end, the uncertainties in the input values to the data-reduction equations were first estimated. Those input values include the three measured Doppler frequencies (f_{12}, f_{34}, and f_{35}), the laser wavelengths for each beam pair (λ_{12}, λ_{34}, and λ_{35}) and the spatial measurements (Δx, Δy, and Δz) on the calibration target for each probe laser beam.

The Doppler frequency measurements introduce random uncertainties that are due to the signal-processing technique that is applied to the LDV burst signal. The burst-processing software uses an FFT with zero-padding to calculate the power spectral density (PSD) of the burst signal and then applies a Gaussian interpolation to find the peak of each Doppler component in the PSD. In that case, the worst-case frequency uncertainty for each component is [35]:

$$
P_{f_{12}} = \frac{0.1}{T} \approx \frac{0.1 \, \|\vec{u}\|}{D},
\tag{42}
$$

$$
P_{f_{34}} = \frac{0.1}{T} \approx \frac{0.1 \, \|\vec{u}\|}{D},
\tag{43}
$$

and

$$
P_{f_{35}} = \frac{0.1}{T} \approx \frac{0.1 \, \|\vec{u}\|}{D},
\tag{44}
$$

where T is the duration of the burst signal, D is the diameter of the measurement volume, and $\vec{u}$ is the velocity vector of the particle. The random uncertainties of the three Doppler frequencies are considered to be uncorrelated in the DMCS.

Uncertainty in the laser wavelength contributes a systematic uncertainty to the data-reduction equations. Laser beams 1 & 2 are sourced from a single laser that provides 532 nm laser light with a wavelength uncertainty of $B_{\lambda_{12}} = 3$ nm, as per the manufacturer's data sheet. Laser beams 3, 4 & 5 are sourced from a second laser that provides 532 nm laser light, also with a wavelength uncertainty of 3 nm. In this case, the wavelength uncertainty associated with beam pair 3 & 4 is $B_{\lambda_{34}} = 3$ nm and that for beam pair 3 & 5 is $B_{\lambda_{35}} = 3$ nm. Since a single laser provides laser light for beams 3, 4, & 5, the systematic uncertainties $B_{\lambda_{34}}$ and $B_{\lambda_{35}}$ are correlated, and that fact is used in the DMCS. However, the systematic uncertainty $B_{\lambda_{12}}$ is uncorrelated with $B_{\lambda_{34}}$ and $B_{\lambda_{35}}$ since it is related to a different laser system.

As discussed in Appendix A, the measured probe beam center locations on image 1 and 2 of the calibration target were used to calculate the beam unit vectors. The uncertainties in these measurements ultimately contribute systematic uncertainties to the data-reduction equations. For each laser beam in the probe, the uncertainty in $\Delta x = x_1 - x_2$ and $\Delta z = z_1 - z_2$ were nominally $B_{\Delta x} = 23 \, \mu$m and $B_{\Delta z} = 23 \, \mu$m, respectively, while the uncertainty in $\Delta y = y_2 - y_1$ was nominally $B_{\Delta y} = 14 \, \mu$m. Each one of these measurements were considered to be uncorrelated.

With the uncertainties as defined above, each of the input parameters to the data-reduction equations were perturbed by a random value drawn from a normal distribution with a 2σ value equal to that of the corresponding uncertainty. The perturbed input parameters were then applied to the data-reduction equations (Eqs. 37 to 41) to yield the three velocity components (u, v, and w). This process was repeated 10,000 times to yield distributions in the calculated velocity components and

the uncertainties for each component were then set equal to the 2σ value of each respective distribution. Tables 12 and 13 present the results of this analysis for LDV probes 1 and 2, respectively. Here, the results are broken down into the different uncertainty sources, where the uncertainty for a given source (for example, the uncertainty due to the Doppler frequency measurement) was generated by running the DMCS on that source acting alone. The total uncertainty was generated by running the DMCS with all uncertainty sources acting simultaneously. Figures 160 and 161 present the results of the analysis as a bar chart, and show the relative magnitudes of the different uncertainty sources. For both LDV probes, the largest uncertainties are associated with the v component of velocity.

B.2.1. Uncertainty Analysis for the Statistical Moments

For a given point in the flow-field surveys, a fixed number of samples, N, were collected with the LDV system and these were then used to calculate a number of statistical moments. The $\overline{u}$ component of mean velocity was calculated as:

$$\overline{u} = \frac{\sum_i^N u_i \tau_i}{\sum_i^N \tau_i}, \tag{45}$$

with similar equations for the $\overline{v}$ and $\overline{w}$ components of mean velocity. The $\overline{u'u'}$ component of Reynolds normal stress was calculated as:

$$\overline{u'u'} = \frac{\sum_i^N (u_i - \overline{u})^2 \tau_i}{\sum_i^N \tau_i}, \tag{46}$$

with similar equations for the $\overline{v'v'}$ and $\overline{w'w'}$ components, and the $\overline{u'v'}$ component of Reynolds shear stress was calculated as:

$$\overline{u'v'} = \frac{\sum_i^N (u_i - \overline{u})(v_i - \overline{v}) \tau_i}{\sum_i^N \tau_i}, \tag{47}$$

with similar equations for the $\overline{u'w'}$ and $\overline{v'w'}$ components. Finally, the $\overline{u'v'w'}$ triple product of the velocity components was calculated as:

$$\overline{u'v'w'} = \frac{\sum_i^N (u_i - \overline{u})(v_i - \overline{v})(w_i - \overline{w}) \tau_i}{\sum_i^N \tau_i}, \tag{48}$$

with similar equations for the other nine independent components: $\overline{u'u'u'}$, $\overline{v'v'v'}$, $\overline{w'w'w'}$, $\overline{u'u'v'}$, $\overline{u'u'w'}$, $\overline{u'v'v'}$, $\overline{u'w'w'}$, $\overline{v'v'w'}$, and $\overline{w'w'v'}$. These equations can be viewed as data-reduction equations where the inputs are the sequences of the velocity components u_i, v_i, and w_i with $i = 1, 2, \cdots, N$. The measurement uncertainties associated with those samples—which were estimated in the above discussion—propagate through the data-reduction equations and produce uncertainties in the calculated statistical moments. To estimate those uncertainties, a DMCS was performed. To that end, each sample in the data sequence was expressed as:

$$u_i = u_{i(MEAS)} + \epsilon_{i(u)} + \beta_{i(u)}, \tag{49}$$

$$v_i = v_{i(MEAS)} + \epsilon_{i(v)} + \beta_{i(v)}, \tag{50}$$

and

$$w_i = w_{i(MEAS)} + \epsilon_{i(w)} + \beta_{i(w)}, \tag{51}$$

where $u_{i(MEAS)}$, $v_{i(MEAS)}$, and $w_{i(MEAS)}$ are the measured velocity components of a given sample; $\epsilon_{i(u)}$, $\epsilon_{i(v)}$, and $\epsilon_{i(w)}$ are random values drawn from normal distributions with 2σ values of P_u, P_v, and P_w, respectively; and $\beta_{i(u)}$, $\beta_{i(v)}$, and $\beta_{i(w)}$ are random values drawn from normal distributions with 2σ values of B_u, B_v, and B_w, respectively. The P values represent the random

uncertainties for each velocity component due to the random uncertainties in the Doppler frequency measurements. The B values represent the systematic uncertainties for each velocity component due to all of the systematic uncertainty sources associated with each respective component (in a root-sum-square sense). The P and B values used in the DMCS are given in Tables 12 or 13, with the specific values depending on the LDV probe under consideration in the analysis.

As a practical matter, it is important to recognize that each $\epsilon_{i(u)}$, $\epsilon_{i(v)}$, and $\epsilon_{i(w)}$ value in the sample sequence was produced with a random-number generator with a zero-mean, unit-variance normal distribution and then scaled by $P_u/2$, $P_v/2$, and $P_w/2$, respectively. In this way, the random perturbations are uncorrelated from one sample to the next and they are also uncorrelated from one velocity component to the other. The perturbations associated with the systematic uncertainties in the measurement samples ($\beta_{i(u)}$, $\beta_{i(v)}$, and $\beta_{i(w)}$) were handled differently. Consider the perturbation for the u_i component, $\beta_{i(u)}$. A single random number was produced with a random-number generator with a zero-mean, unit-variance normal distribution, and then scaled by $B_u/2$ and added to all samples in the sample sequence. In this way, the perturbations are correlated from one sample to the next. This was done to account for the fact that the systematic uncertainty is common to all of the samples in a given sequence. The same procedure was also applied to the v_i and w_i sample sequences. Note that, here, separate random-number generators were used for each velocity component and therefore the perturbations are uncorrelated from one component to the other.

With the sample sequences for each velocity component perturbed as described above, the statistical moments in Eqs. 45–48 where calculated. This was then repeated 5,000 times to yield distributions in each of the statistical moments and the uncertainty for each one was estimated as the 2σ value for each respective distribution.

In addition to the uncertainties calculated above, there are uncertainties in the statistical moments that are due to sampling of the random process associated with the turbulent flow. Benedict and Gould [36] have developed formulas to estimate these uncertainties for a number of turbulence statistics and here, we list those pertinent to the present study. For the $\overline{u}$ component of mean velocity, the uncertainty can be estimated by:

$$U_{\overline{u}} = 2\left(\frac{\overline{u'^2}}{N_e}\right)^{1/2},\tag{52}$$

with similar equations for the $\overline{v}$ and $\overline{w}$ components. For the $\overline{u'u'}$ component of Reynolds normal stress, the uncertainty can be estimated by:

$$U_{\overline{u'u'}} = 2\left(\frac{\overline{u'^4} - (\overline{u'^2})^2}{N_e}\right)^{1/2},\tag{53}$$

with similar equations for the $\overline{v'v'}$ and $\overline{w'w'}$ components, and for the $\overline{u'v'}$ component of Reynolds shear stress, the uncertainty can be estimated by:

$$U_{\overline{u'v'}} = 2\left(\frac{\overline{u'^2v'^2} - (\overline{u'v'})^2}{N_e}\right)^{1/2},\tag{54}$$

with similar equations for the $\overline{u'w'}$ and $\overline{v'w'}$ components. For triple products such as $\overline{u'u'u'}$, the uncertainty can be estimated by:

$$U_{\overline{u'u'u'}} = 2\left(\frac{\overline{u'^6} - (\overline{u'^3})^2 - 6(\overline{u'^4})(\overline{u'^2}) + 9(\overline{u'^2})^3}{N_e}\right)^{1/2},\tag{55}$$

and for triple products such as $\overline{u'u'v'}$, the uncertainty can be estimated by:

$$U_{\overline{u'u'v'}} = 2\left(\frac{\overline{u'^4v'^2} - (\overline{u'^2v'})^2 + (\overline{u'^2})^2\overline{v'^2} + 8\overline{u'^2}(\overline{u'v'})^2 - 2\overline{u'^2}(\overline{u'^2v'^2}) - 4(\overline{u'v'})\overline{u'^3v'}}{N_e}\right)^{1/2}.$$

(56)

For the $\overline{u'v'w'}$ triple product, there is no explicit formula for the uncertainty estimate. Instead, the uncertainty for that triple product was estimated by using the jackknife resampling algorithm described by Benedict and Gould [36]. When calculating the uncertainty estimates from Eqs. 52–56, the statistical moments in those equations, $(\bar{\cdot})$, were estimated from the sample population. The parameter N_e in the above equations denotes the number of statistically independent samples in the sample sequence. For LDV data, N_e is generally less than the total number of samples collected in a data sequence, N. For the samples in the data sequence to be independent, the data rate must be less than $1/2\tau$, where τ is the integral time scale of the quantity being measured [13]. LDV data, however, is sampled at a variable rate, and therefore some of the samples are spaced too closely in time for them to be statistically independent. To estimate N_e from a sequence of N samples, the integral time scale of the quantity being measured was estimated and then the number of samples spaced by 2τ in time were counted and set equal to N_e.

The total uncertainty for each statistical moment was finally estimated as the root-sum-square of the uncertainty calculated from the DMCS described above and the uncertainty due to sampling of the turbulent random process as calculated from the equations listed above. The analysis was applied to each point in the flow-field surveys that were conducted over the course of the test. As such, the uncertainties in the statistical moments are unique to each point in the flow-field surveys.

All of the statistical moments presented in this report were made nondimensional with u_∞ as the velocity scale. For example, the $\overline{u}$ was nondimensionalized as:

$$\hat{\overline{u}} = \frac{\overline{u}}{u_\infty}.$$

(57)

Assuming that the uncertainties for $\overline{u}$ and u_∞ are uncorrelated, the uncertainty for $\hat{\overline{u}}$ was calculated as:

$$U_{\hat{\overline{u}}}^2 = \left(\frac{\partial\hat{\overline{u}}}{\partial\overline{u}}\right)^2 U_{\overline{u}}^2 + \left(\frac{\partial\hat{\overline{u}}}{\partial u_\infty}\right)^2 U_{u_\infty}^2,$$

(58)

or upon evaluating the derivatives:

$$U_{\hat{\overline{u}}}^2 = \left(\frac{1}{u_\infty^2}\right) U_{\overline{u}}^2 + \left(\frac{\overline{u}^2}{u_\infty^4}\right) U_{u_\infty}^2.$$

(59)

Similar expressions were used for the $\hat{\overline{v}}$ and $\hat{\overline{w}}$ components. The $\overline{u'v'}$ component of Reynolds stress was nondimensionalized as:

$$\hat{\overline{u'v'}} = \frac{\overline{u'v'}}{u_\infty^2},$$

(60)

and the uncertainty for that component was calculated as:

$$U_{\hat{\overline{u'v'}}}^2 = \left(\frac{\partial\hat{\overline{u'v'}}}{\partial\overline{u'v'}}\right)^2 U_{\overline{u'v'}}^2 + \left(\frac{\partial\hat{\overline{u'v'}}}{\partial u_\infty}\right)^2 U_{u_\infty}^2,$$

(61)

or upon evaluating the derivatives:

$$U_{\hat{\overline{u'v'}}}^2 = \left(\frac{1}{u_\infty^4}\right) U_{\overline{u'v'}}^2 + \left(4\frac{(\overline{u'v'})^2}{u_\infty^6}\right) U_{u_\infty}^2.$$

(62)

55

Similar expressions were used for the remaining five independent components of the Reynolds-stress tensor. Finally the $\overline{u'u'v'}$ triple-product component was nondimensionalized as:

$$\overline{u'\hat{u}'v'} = \frac{\overline{u'u'v'}}{u_\infty^3},$$ (63)

and the uncertainty for that component was calculated as:

$$U_{\overline{u'\hat{u}'v'}}^2 = \left(\frac{\partial \overline{u'\hat{u}'v'}}{\partial \overline{u'u'v'}}\right)^2 U_{\overline{u'u'v'}}^2 + \left(\frac{\partial \overline{u'\hat{u}'v'}}{\partial u_\infty}\right)^2 U_{u_\infty}^2,$$ (64)

or upon evaluating the derivatives:

$$U_{\overline{u'\hat{u}'v'}}^2 = \left(\frac{1}{u_\infty^6}\right) U_{\overline{u'u'v'}}^2 + \left(9\frac{\left(\overline{u'u'v'}\right)^2}{u_\infty^8}\right) U_{u_\infty}^2.$$ (65)

Similar expressions were used for the remaining 9 independent components of the velocity triple products. The uncertainties in the nondimensionalized statistical moments as defined by these equations were evaluated with the uncertainties in the statistical moments and the freestream velocity as estimated with the approaches discussed earlier.

B.2.2. Uncertainty Analysis for the LDV Measurement Volume Position

The x location of the LDV measurement volume (MV) was positioned in the flow field relative to reference marks on the windows of the junction model that were at known distances from the model nose apex (the origin of the body-fixed coordinate system). The x uncertainty in locating the MV relative to those reference marks was estimated to be equal to the MV diameter, 140 μm. In addition, the x-axis stage positioning accuracy and repeatability were 15 μm and 1 μm as per the manufacturer's data sheet. The total uncertainty in the x location was then estimated as the root-sum-square of these three uncertainty sources and is equal to $U_x = 140.8$ μm.

The y location of the LDV measurement volume was positioned in the flow field at locations relative to the surface of the junction model optical windows (at $y_o = -236.1$ μm in the body-fixed coordinate system). The y uncertainty in locating the MV at the window surface was estimated to be equal to 25 μm when using the wall-locating procedure discussed in Section 2.3. In addition, the y-axis stage positioning accuracy and repeatability were 10 μm and 1 μm as per the manufacturer's data sheet. The total uncertainty in the y location was then estimated as the root-sum-square of these three uncertainty sources and is equal to $U_y = 27$ μm.

For LDV measurements on the nose section and upstream of the wing leading edge, the z location of the MV was positioned in the flow field relative to reference marks on the junction model windows that were at known distances from the model nose apex. Here, the z uncertainty in locating the MV relative to those reference marks was estimated to be equal to the MV diameter, 140 μm. The z-axis stage positioning accuracy and repeatability were 15 μm and 1 μm as per the manufacturer's data sheet. The total uncertainty in the z location was then estimated as the root-sum-square of these three uncertainty sources and is equal to $U_z = 140.8$ μm.

For the LDV measurement in the trailing-edge corner region of the wing-fuselage junction, the z location of the MV was positioned in the flow field relative to the local position of the wing surface, z_o (which varies from one (x,y) location to another). The z uncertainty in locating the MV volume at the local wing surface was estimated to be equal to 25 μm when using the wall-locating procedure discussed in Section 2.3. In addition, the z-axis stage positioning accuracy and repeatability were 15 μm and 1 μm as per the manufacturer's data sheet. The total uncertainty in the z location was then estimated as the root-sum-square of these three uncertainty sources and is equal to $U_z = 29$ μm.

B.3. Uncertainty in the Corner-Flow Separation Size

In this section, we provide an uncertainty analysis for the measurements of the corner-flow separation width and length that were obtained from oil-flow visualizations. For the width measurement, the distance between the fuselage and the outer edge of the collection of oil-flow pigment at the trailing-edge boundary of the corner separation was measured with a ruler that had 1 mm divisions. Therefore, the systematic measurement uncertainty was 0.5 mm. Due to time constraints in the test schedule, we did not have the opportunity to perform repeated oil-flow visualizations for a given model pitch angle. As such, we were unable to estimate a random uncertainty in the width measurement from the current oil-flow images. However, in our past risk reduction experiment with a smaller-scale junction model [7], we were able to perform multiple oil-flow runs at fixed conditions, and from those, we estimated the random uncertainty in the corner separation width measurement. From that data, we found a random uncertainty that was approximately 16% of the measured corner-flow separation width. Given that the present oil-flow formulation and methodology was the same as that used during the risk-reduction experiment, we assumed a similar random uncertainty for the present data. The total uncertainty for the width measurement was then calculated as the root-sum-square of the systematic and random uncertainties.

The length of the corner-flow separation along the wing root was also measured with a ruler. However, due to the diffuse collection of oil-flow pigment at the wing root, it was more difficult to identify where the corner-flow separation began and so, by observation, the systematic uncertainty in the length measurement was approximately 2 mm. From the risk-reduction experiment [7], the random uncertainty was found to be approximately 13% of the measured corner-flow separation length and that was assumed to apply in the present study. As before, the total uncertainty for the length measurement was then calculated as the root-sum-square of the systematic and random uncertainties.

Table 1: Locations of profile measurements in the trailing-edge region of the F6 wing for $\alpha = 5°$. All locations are in the body-fixed coordinate system with origin at the model nose tip and z_o denotes the wing-surface location.

x (mm)	y (mm)	z_o (mm)
2747.6	-236.6	16.66
2747.6	-237.1	16.76
2747.6	-239.1	17.07
2747.6	-243.1	17.70
2747.6	-246.1	18.16
2747.6	-256.1	19.74
2747.6	-286.1	24.43
2832.6	-236.6	-3.15
2832.6	-237.1	-3.07
2832.6	-239.1	-2.74
2832.6	-241.1	-2.44
2832.6	-243.1	-2.11
2832.6	-246.1	-1.60
2832.6	-256.1	0.03
2832.6	-286.1	4.90
2852.6	-236.6	-8.56
2852.6	-237.1	-8.46
2852.6	-239.1	-8.13
2852.6	-243.1	-7.47
2852.6	-246.1	-6.99
2852.6	-256.1	-5.33
2852.6	-286.1	-0.38
2872.6	-236.6	-14.33
2872.6	-237.1	-14.25
2872.6	-239.1	-13.92
2872.6	-241.1	-13.59
2872.6	-243.1	-13.26
2872.6	-246.1	-12.75
2872.6	-256.1	-11.07
2872.6	-266.1	-9.42
2872.6	-286.1	-6.07
2892.6	-236.6	-20.60
2892.6	-239.1	-20.17
2892.6	-241.1	-19.84
2892.6	-243.1	-19.48
2892.6	-246.1	-18.97
2892.6	-251.1	-18.14
2892.6	-256.1	-17.30
2892.6	-266.1	-15.60
2892.6	-286.1	-12.22

Table 1: Continued. Locations of profile measurements in the trailing-edge region of the F6 wing for $\alpha = 5°$. All locations are in the body-fixed coordinate system with origin at the model nose tip and z_o denotes the wing-surface location.

x (mm)	y (mm)	z_o (mm)
2922.6	-236.6	-30.63
2922.6	-239.1	-30.20
2922.6	-246.1	-29.01
2922.6	-256.1	-27.28
2922.6	-266.1	-25.55
2922.6	-286.1	-22.12
2952.6	-239.1	-40.61
2952.6	-246.1	-39.40
2952.6	-256.1	-37.67
2952.6	-266.1	-35.92

Table 2: Locations of profile measurements in the trailing-edge region of the F6 wing with extension for $\alpha = 5°$. All locations are in the body-fixed coordinate system with origin at the model nose tip and z_o denotes the wing-surface location.

x (mm)	y (mm)	z_o (mm)
2747.6	-237.1	16.75
2747.6	-239.1	17.06
2747.6	-246.1	18.16
2747.6	-266.1	21.30
2822.6	-237.1	-0.51
2822.6	-239.1	-0.20
2832.6	-236.6	-3.15
2832.6	-237.1	-3.07
2832.6	-239.1	-2.74
2832.6	-241.1	-2.44
2832.6	-246.1	-1.60
2832.6	-266.1	1.65
2842.6	-237.1	-5.72
2842.6	-239.1	-5.41

Table 2: Continued. Locations of profile measurements in the trailing-edge region of the F6 wing with extension for $\alpha = 5°$. All locations are in the body-fixed coordinate system with origin at the model nose tip and z_o denotes the wing-surface location.

x (mm)	y (mm)	z_o (mm)
2852.6	-236.6	-8.56
2852.6	-237.1	-8.46
2852.6	-239.1	-8.13
2852.6	-241.1	-7.80
2852.6	-246.1	-6.99
2852.6	-266.1	-3.68
2872.6	-236.6	-14.33
2872.6	-239.1	-13.92
2872.6	-241.1	-13.59
2872.6	-243.1	-13.26
2872.6	-246.1	-12.75
2872.6	-256.1	-11.07
2892.6	-237.1	-20.50
2892.6	-239.1	-20.17
2892.6	-246.1	-18.97
2892.6	-251.1	-18.14
2892.6	-256.1	-17.30
2892.6	-266.1	-15.60
2922.6	-237.1	-30.56
2922.6	-239.1	-30.20
2922.6	-246.1	-29.01
2922.6	-256.1	-27.28
2922.6	-266.1	-25.55
2922.6	-276.1	-23.85
2922.6	-286.1	-22.12
2952.6	-237.1	-40.94
2952.6	-239.1	-40.61
2952.6	-246.1	-39.40
2952.6	-256.1	-37.67
2952.6	-266.1	-35.92
2952.6	-286.1	-32.44

Table 3: Locations of profile measurements in the trailing-edge region of the F6 wing with extension for $\alpha = -2.5°$. All locations are in the body-fixed coordinate system with origin at the model nose tip and z_o denotes the wing-surface location.

x (mm)	y (mm)	z_o (mm)
2757.6	-237.1	14.55
2757.6	-239.1	14.88
2757.6	-241.1	15.19
2757.6	-246.1	15.98
2757.6	-266.1	19.13
2869.6	-237.1	-13.36
2869.6	-239.1	-13.03
2875.6	-237.1	-15.16
2875.6	-238.1	-15.01
2875.6	-239.1	-14.83
2875.6	-246.1	-13.67
2875.6	-266.1	-10.31
2881.6	-237.1	-17.02
2881.6	-239.1	-16.69
2887.6	-237.1	-18.90
2887.6	-238.1	-18.75
2887.6	-239.1	-18.57
2887.6	-241.1	-18.24
2887.6	-246.1	-17.37
2899.6	-237.1	-22.78
2899.6	-238.1	-22.61
2899.6	-239.1	-22.45
2899.6	-241.1	-22.10
2899.6	-246.1	-21.26
2899.6	-256.1	-19.56
2911.6	-237.1	-26.80
2911.6	-238.1	-26.62
2911.6	-239.1	-26.47
2911.6	-241.1	-26.11
2911.6	-246.1	-25.25
2911.6	-256.1	-23.55
2922.6	-237.1	-30.56
2922.6	-239.1	-30.20
2922.6	-241.1	-29.87
2922.6	-246.1	-29.01
2922.6	-251.1	-28.14
2922.6	-256.1	-27.28

Table 3: Continued. Locations of profile measurements in the trailing-edge region of the F6 wing with extension for $\alpha = -2.5°$. All locations are in the body-fixed coordinate system with origin at the model nose tip and z_o denotes the wing-surface location.

x (mm)	y (mm)	z_o (mm)
2952.6	-239.1	-40.61
2952.6	-241.1	-40.26
2952.6	-246.1	-39.40
2952.6	-251.1	-38.53
2952.6	-256.1	-37.67
2952.6	-266.1	-35.92

Table 4: Locations of profile measurements in the leading-edge region of the F6 wing for $\alpha = 5°$. All locations are in the body-fixed coordinate system with origin at the model nose tip and y_o denotes the fuselage surface location.

x (mm)	z (mm)	y_o (mm)
1983.4	93.3	-236.1
1993.4	93.3	-236.1
1998.4	93.3	-236.1
2003.4	93.3	-236.1
2008.4	93.3	-236.1
2018.4	93.3	-236.1
2023.4	93.3	-236.1
2028.4	93.3	-236.1
2033.4	93.3	-236.1
2038.4	93.3	-236.1
2043.4	93.3	-236.1
2048.4	93.3	-236.1
2053.4	93.3	-236.1
2058.4	93.3	-236.1
2063.4	93.3	-236.1
2093.4	93.3	-236.1
1993.4	47.3	-236.1
1998.4	46.9	-236.1
2001.2	46.5	-236.1
2004	46.2	-236.1
2009	45.7	-236.1

Table 5: Locations of profile measurements in the leading-edge region of the F6 wing with extension for $\alpha = 5°$ and $-2.5°$. All locations are in the body-fixed coordinate system with origin at the model nose tip and y_o denotes the fuselage surface location. The LDV operating mode used for each profile location is also listed.

x (mm)	z (mm)	y_o (mm)	LDV Operating Mode
1864.2	98.05	-236.1	Single
1869.2	98.05	-236.1	Single
1874.2	98.05	-236.1	Single
1879.2	98.05	-236.1	Single
1884.2	98.05	-236.1	Single
1889.2	98.05	-236.1	Single
1894.2	98.05	-236.1	Single
1899.2	98.05	-236.1	Single
1904.2	98.05	-236.1	Single
1909.2	98.05	-236.1	Single
1914.2	98.05	-236.1	Single
1921.2 (1921.1 for $\alpha = -2.5°$)	98.05	-236.1	Single
1904.2	71.2	-236.1	Dual
1859.2	55.05	-236.1	Dual
1864.2	6.2	-236.1	Single
1879.2	6.2	-236.1	Single
1904.2	6.2	-236.1	Single
1919.2	6.2	-236.1	Single

Table 6: Locations of the MEMS pressure transducers on the F6 wing of the junction model.

Sensor ID	x (mm)	y (mm)	z (mm)
0	2830.93	244.81	-3.96
1	2848.94	244.81	-6.60
2	2866.92	244.81	-13.08
3	2884.93	244.81	-19.53
4	2902.94	244.81	-25.63
5	2920.92	244.81	-31.85
6	2938.93	244.81	-38.23
7	2956.94	244.81	-41.40
8	2866.92	262.79	-9.86
9	2884.93	262.79	-16.10
10	2902.94	262.79	-22.28
11	2920.92	262.79	-28.45
12	2938.93	262.79	-34.67
13	2956.94	262.79	-38.10
14	2902.94	280.80	-19.08
15	2920.92	280.80	-25.30
16	2938.93	280.80	-31.42
17	2956.94	280.80	-35.05
18	2938.93	298.81	-28.12
19	2956.94	298.81	-32.26
20	2956.94	415.09	-11.68
21	2956.94	469.09	-2.29
22	2956.94	560.10	13.72

Table 7: Locations of the MEMS pressure transducers on the junction-model fuselage.

Sensor ID	x (mm)	y (mm)	z (mm)
23	1904.21	236.10	56.18
24	1917.60	236.10	54.86
25	1921.89	236.10	54.46
26	1904.21	220.22	194.06
27	1993.44	236.10	47.32
28	1998.50	236.10	46.81
29	2001.27	236.10	46.56
30	2004.06	236.10	46.28
31	2009.11	236.10	45.80
32	1993.44	220.22	194.06
33	1993.44	220.22	-194.06
34	2319.86	220.22	194.06
35	2319.86	236.10	104.98
36	2831.85	220.22	194.06
37	2962.91	220.22	194.06
38	2962.91	236.10	23.04
39	2962.91	236.10	-23.04
40	2962.91	236.10	-66.04
41	2962.91	220.22	-194.06
42	2831.85	236.10	2.01
43	2867.91	236.10	-7.92
44	2903.98	236.10	-19.13
45	2939.80	236.10	-31.47
46	2957.83	236.10	-38.05
47	2975.86	236.10	-44.60
48	1168.40	220.22	194.06
49	1168.40	236.10	0.00
50	1168.40	-220.22	194.06
51	1168.40	-236.10	0.00
52	2319.86	-220.22	194.06
53	2319.86	-236.10	104.98

Table 8: Included angle and fringe spacing for each beam pair of the LDV probe positioned at the wing trailing edge.

Beam Pair	Included Angle	Fringe Spacing (μm)
1 & 2	$5.29 \pm 0.03°$	5.77 ± 0.03
3 & 4	$6.40 \pm 0.03°$	4.77 ± 0.02
3 & 5	$7.54 \pm 0.02°$	4.05 ± 0.01
6 & 7	$18.67 \pm 0.05°$	n/a

Table 9: Included angle and fringe spacing for each beam pair of the LDV probe positioned at the wing leading edge or in the fuselage nose.

Beam Pair	Included Angle	Fringe Spacing (μm)
1 & 2	$5.48 \pm 0.04°$	5.57 ± 0.04
3 & 4	$7.22 \pm 0.02°$	4.23 ± 0.01
3 & 5	$6.96 \pm 0.01°$	4.38 ± 0.01
6 & 7	$18.19 \pm 0.08°$	n/a

Table 10: Measured widths and lengths (with uncertainties) of the corner-flow separation for the F6 wing (port side).

α (degrees)	w (mm)	U_w (mm)	ℓ (mm)	U_ℓ (mm)
-2.5	18.5	3.0	76.5	10.1
0	25.0	4.0	93.0	12.3
2.5	31.0	5.0	102.0	13.4
5	36.5	5.9	116.0	15.2

Table 11: Measured widths and lengths (with uncertainties) of the corner-flow separation for the F6 wing with leading-edge extension (port side).

α (degrees)	w (mm)	U_w (mm)	ℓ (mm)	U_ℓ (mm)
-2.5	22.0	3.6	81.0	10.7
0	29.5	4.7	89.0	11.7
2.5	38.0	6.1	104.0	13.7
5	42.5	6.8	118.5	15.5
10	54.0	8.7	152.0	19.9

Table 12: Breakdown of uncertainty sources for a single, instantaneous velocity measurement with LDV probe 1.

Uncertainty Source	u (m/s)	v (m/s)	w (m/s)
Doppler frequency measurement (random uncertainty)	$P_u = 0.0026 \, \|\vec{u}\|$	$P_v = 0.0153 \, \|\vec{u}\|$	$P_w = 0.0029 \, \|\vec{u}\|$
Laser wavelength uncertainty (systematic uncertainty)	$B_u = 0.0054 \, \|\vec{u}\|$	$B_v = 0.0069 \, \|\vec{u}\|$	$B_w = 0.0013 \, \|\vec{u}\|$
Beam unit vector measurement (systematic uncertainty)	$B_u = 0.0028 \, \|\vec{u}\|$	$B_v = 0.0266 \, \|\vec{u}\|$	$B_w = 0.0049 \, \|\vec{u}\|$
Total uncertainty	$U_u = 0.0067 \, \|\vec{u}\|$	$U_v = 0.0315 \, \|\vec{u}\|$	$U_w = 0.0058 \, \|\vec{u}\|$

Table 13: Breakdown of uncertainty sources for a single, instantaneous velocity measurement with LDV probe 2.

Uncertainty Source	u (m/s)	v (m/s)	w (m/s)
Doppler frequency measurement (random uncertainty)	$P_u = 0.0027 \, \|\vec{u}\|$	$P_v = 0.0157 \, \|\vec{u}\|$	$P_w = 0.0044 \, \|\vec{u}\|$
Laser wavelength uncertainty (systematic uncertainty)	$B_u = 0.0054 \, \|\vec{u}\|$	$B_v = 0.0068 \, \|\vec{u}\|$	$B_w = 0.0020 \, \|\vec{u}\|$
Beam unit vector measurement (systematic uncertainty)	$B_u = 0.0025 \, \|\vec{u}\|$	$B_v = 0.0240 \, \|\vec{u}\|$	$B_w = 0.0062 \, \|\vec{u}\|$
Total uncertainty	$U_u = 0.0065 \, \|\vec{u}\|$	$U_v = 0.0295 \, \|\vec{u}\|$	$U_w = 0.0079 \, \|\vec{u}\|$
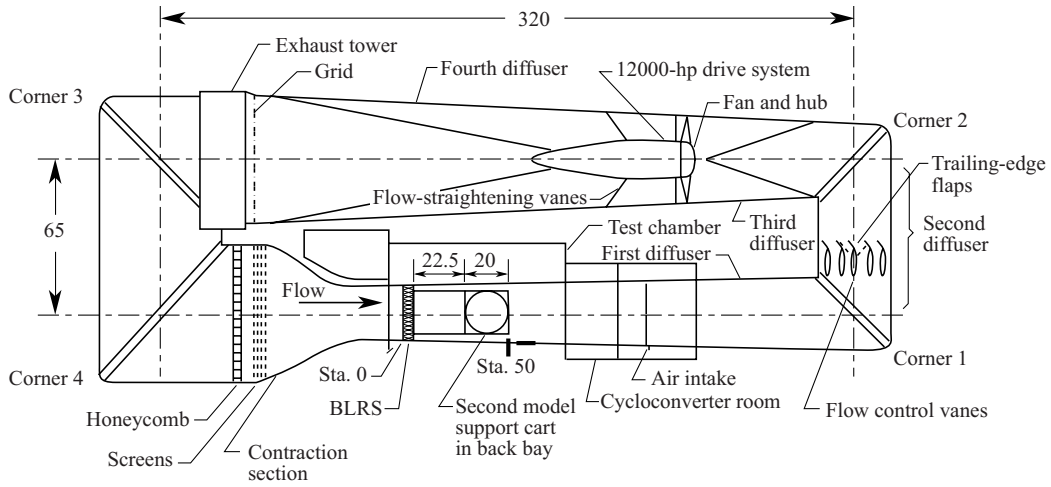
Figure 1: NASA Langley 14- by 22-Foot Subsonic Tunnel circuit (all dimensions are in feet).

Figure 2: Port-side image of the wing-fuselage junction model installed in the 14- by 22-Foot Subsonic Wind Tunnel.
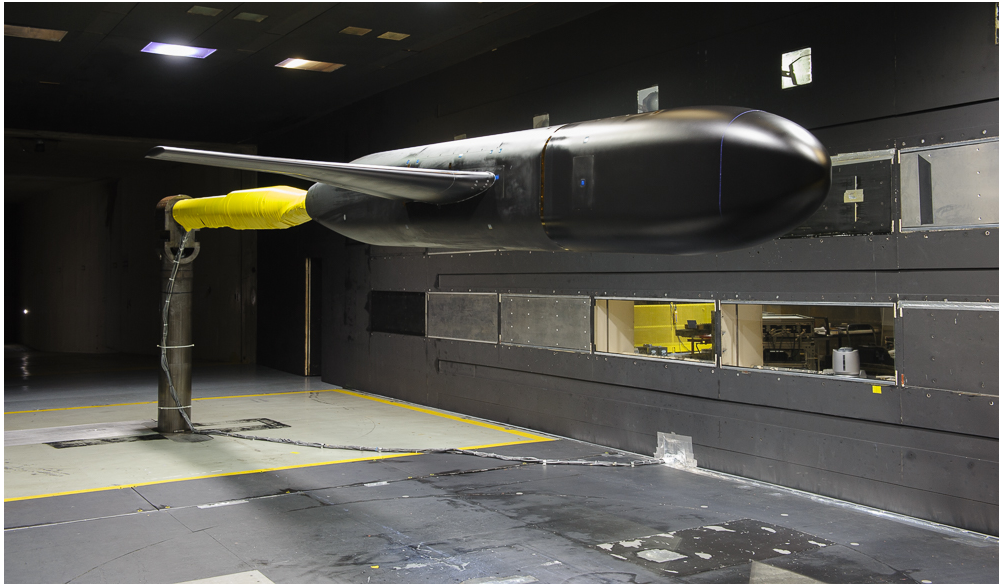
Figure 3: Starboard-side image of the wing-fuselage junction model installed in the 14- by 22-Foot Subsonic Wind Tunnel.

Figure 4: Front-view image of the wing-fuselage junction model installed in the 14- by 22-Foot Subsonic Wind Tunnel.
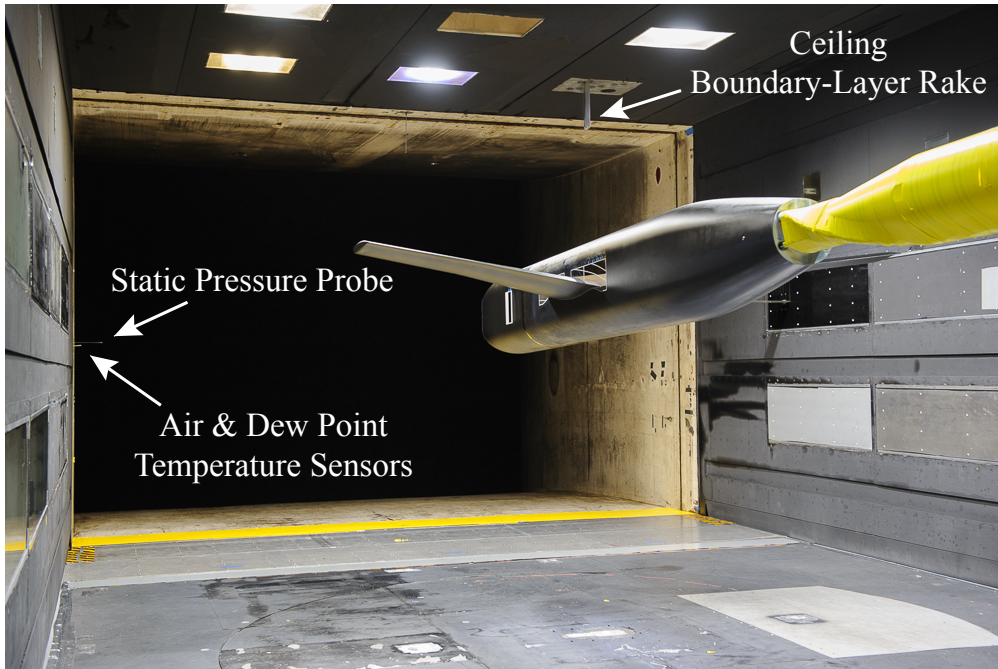
Figure 5: Port-side view of wing-fuselage junction model looking in the upstream direction.
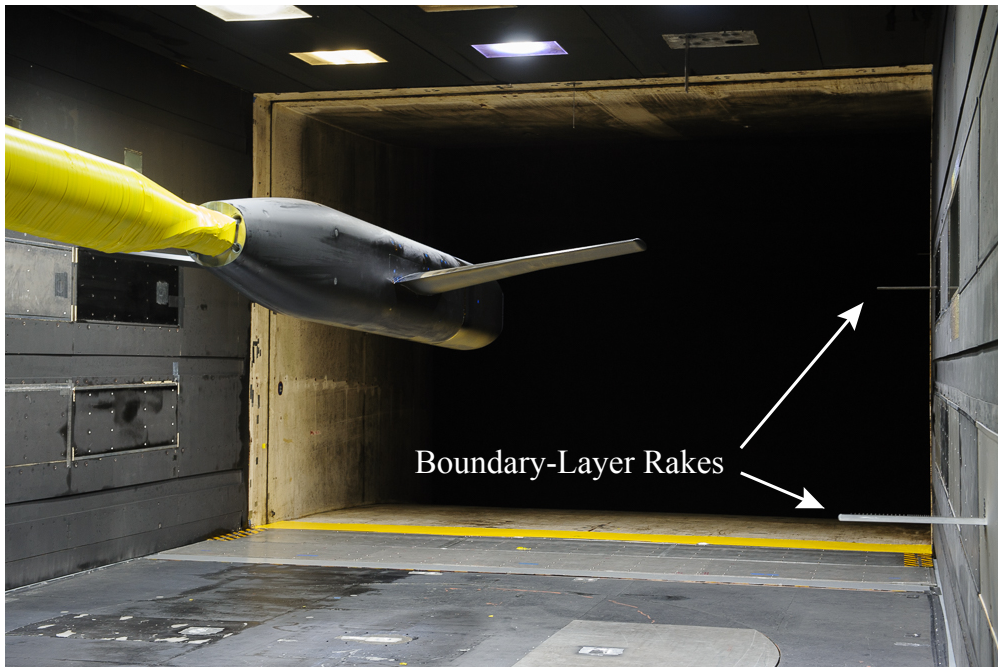
Figure 6: Starboard-side view of wing-fuselage junction model looking in the upstream direction.
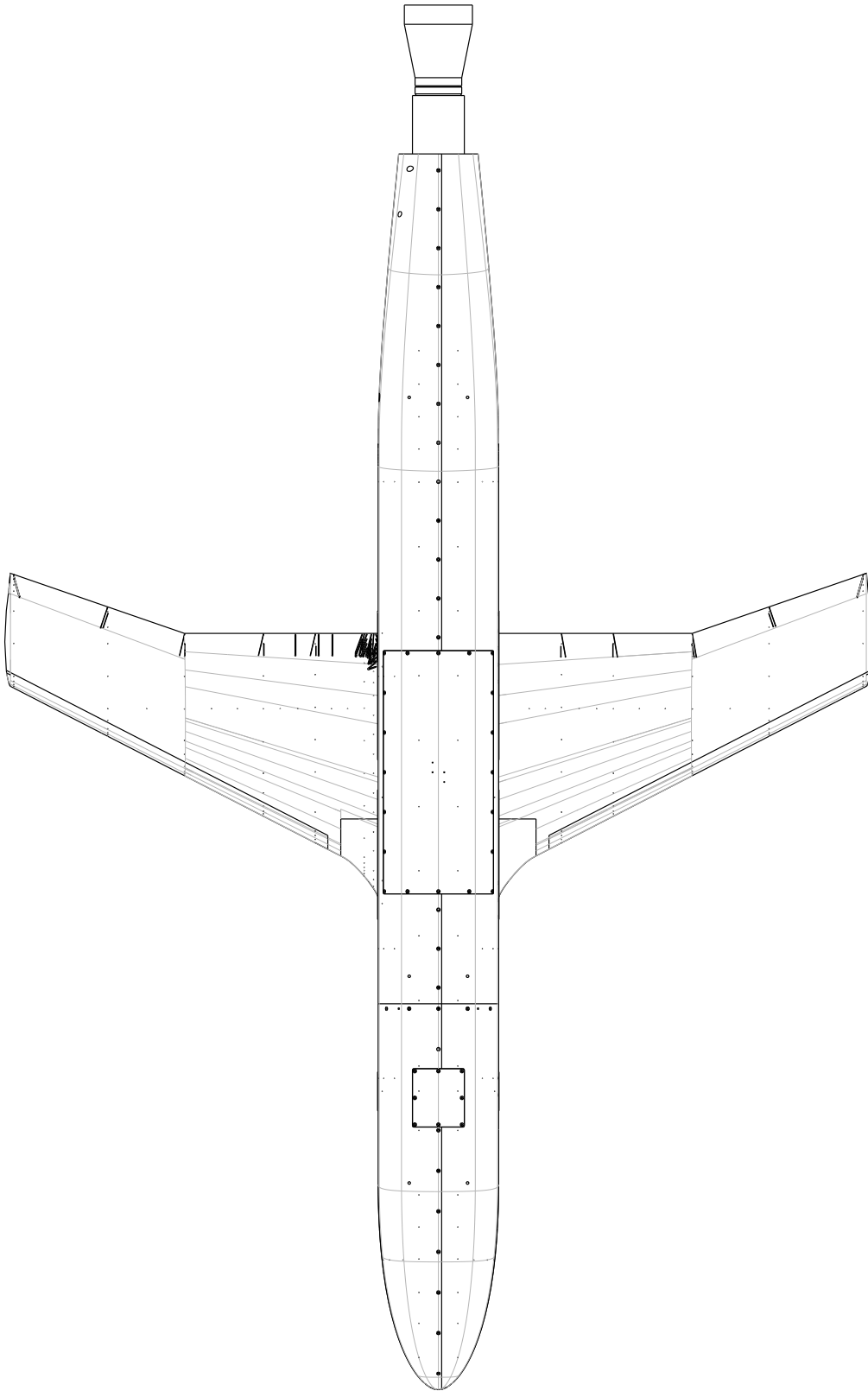
Figure 7: Top view of the wing-fuselage junction model assembly.
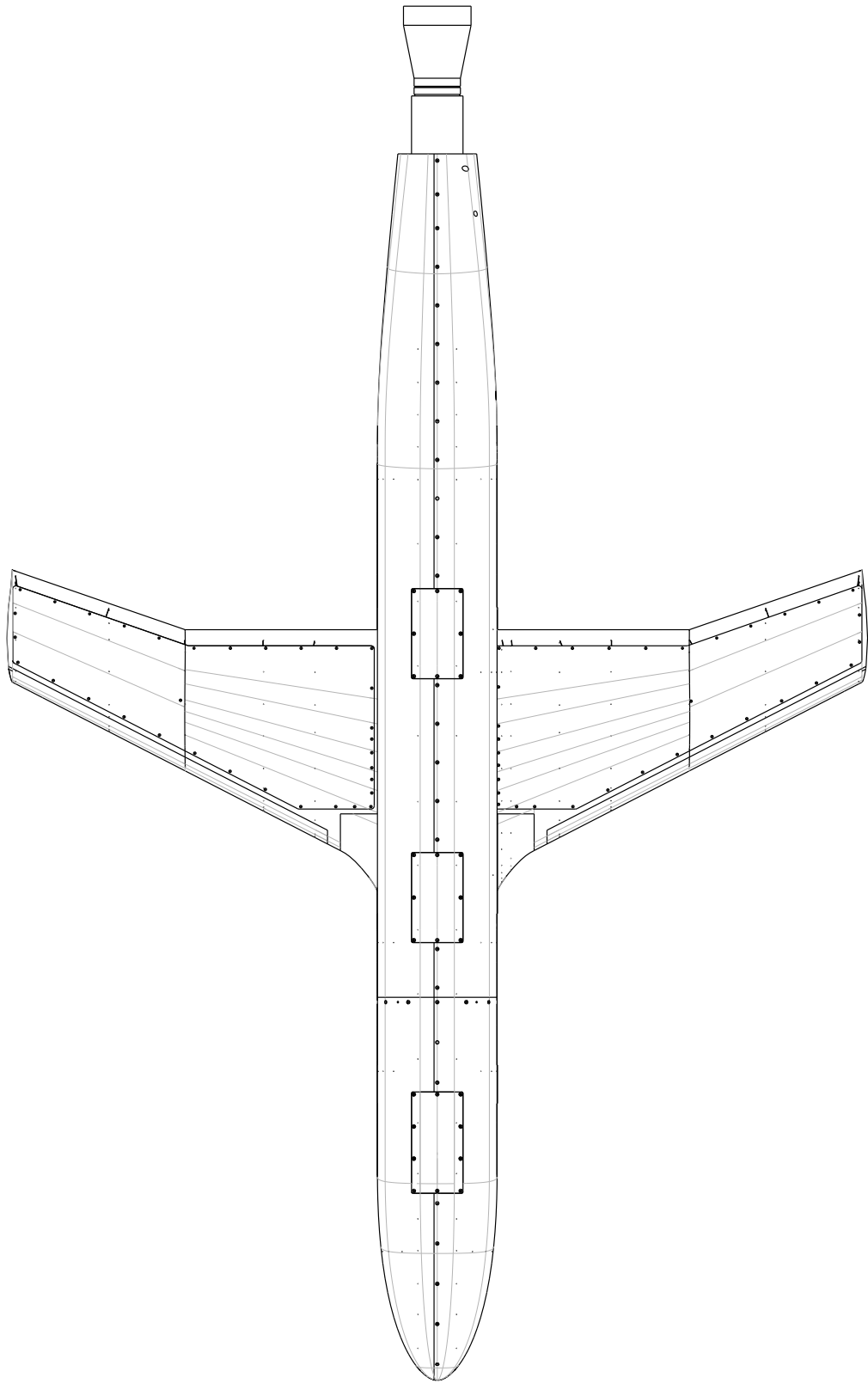
Figure 8: Bottom view of the wing-fuselage junction model assembly.
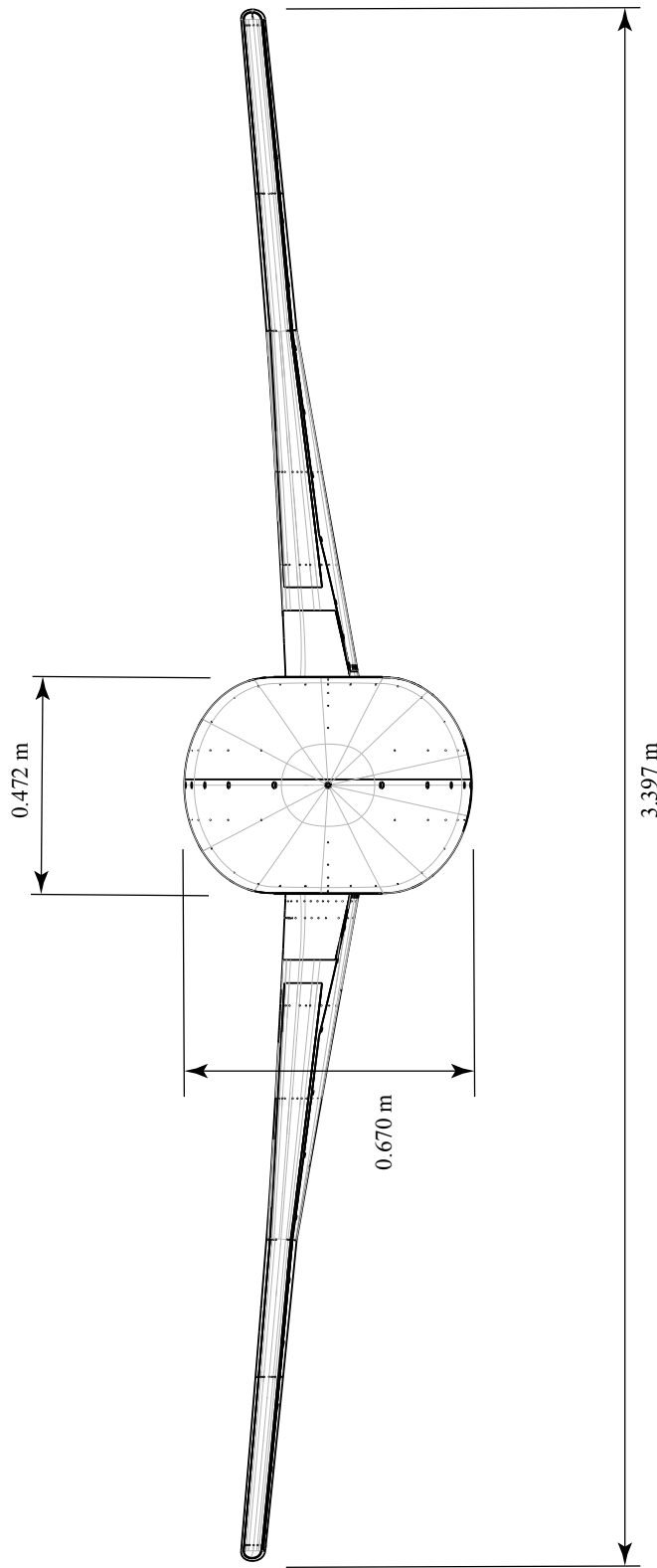
Figure 9: Front view of the wing-fuselage junction model assembly.
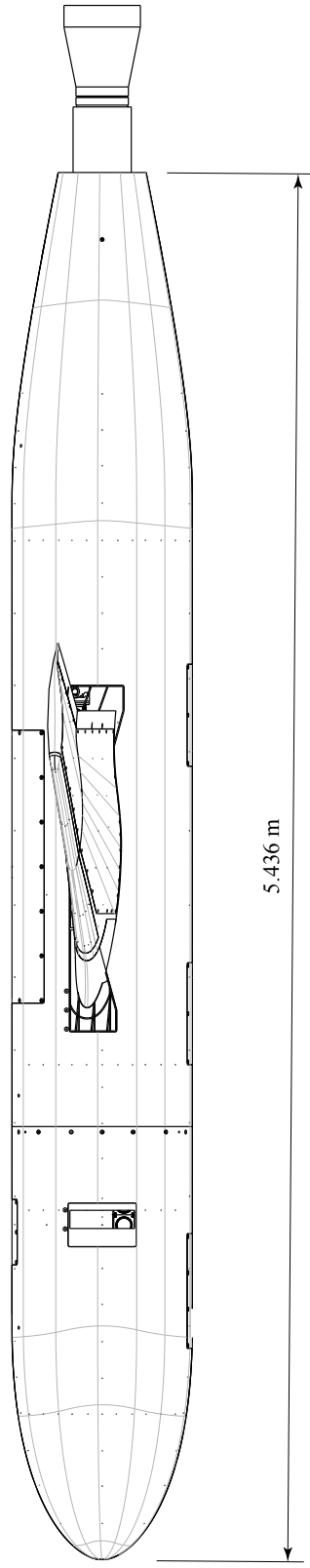
Figure 10: Port-side view of the wing-fuselage junction model assembly.

5.436 m
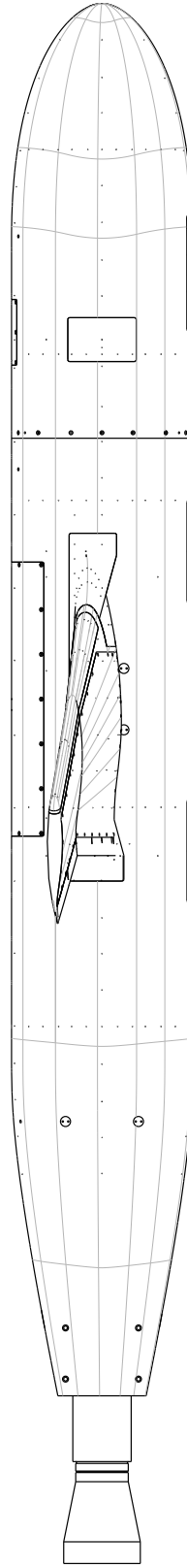
Figure 11: Starboard-side view of the wing-fuselage junction model assembly.
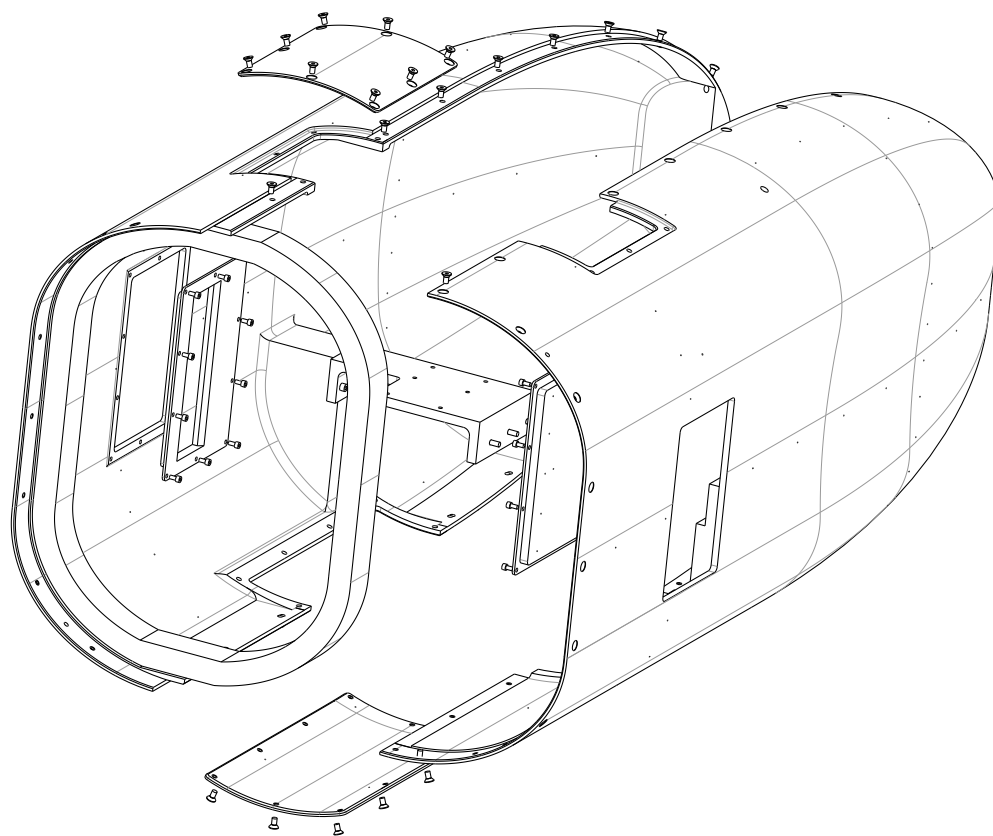
Figure 12: Exploded view of fuselage nose-section assembly.
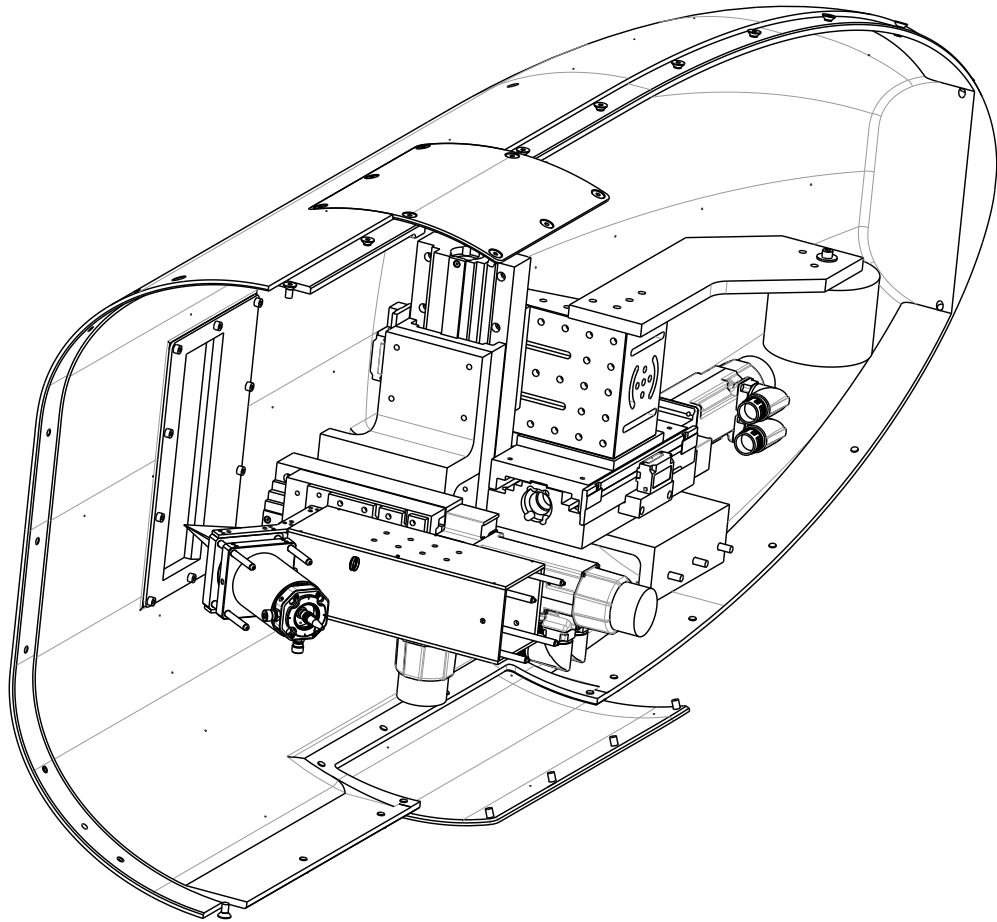
Figure 13: Port side of fuselage nose section with LDV/traverse assembly.
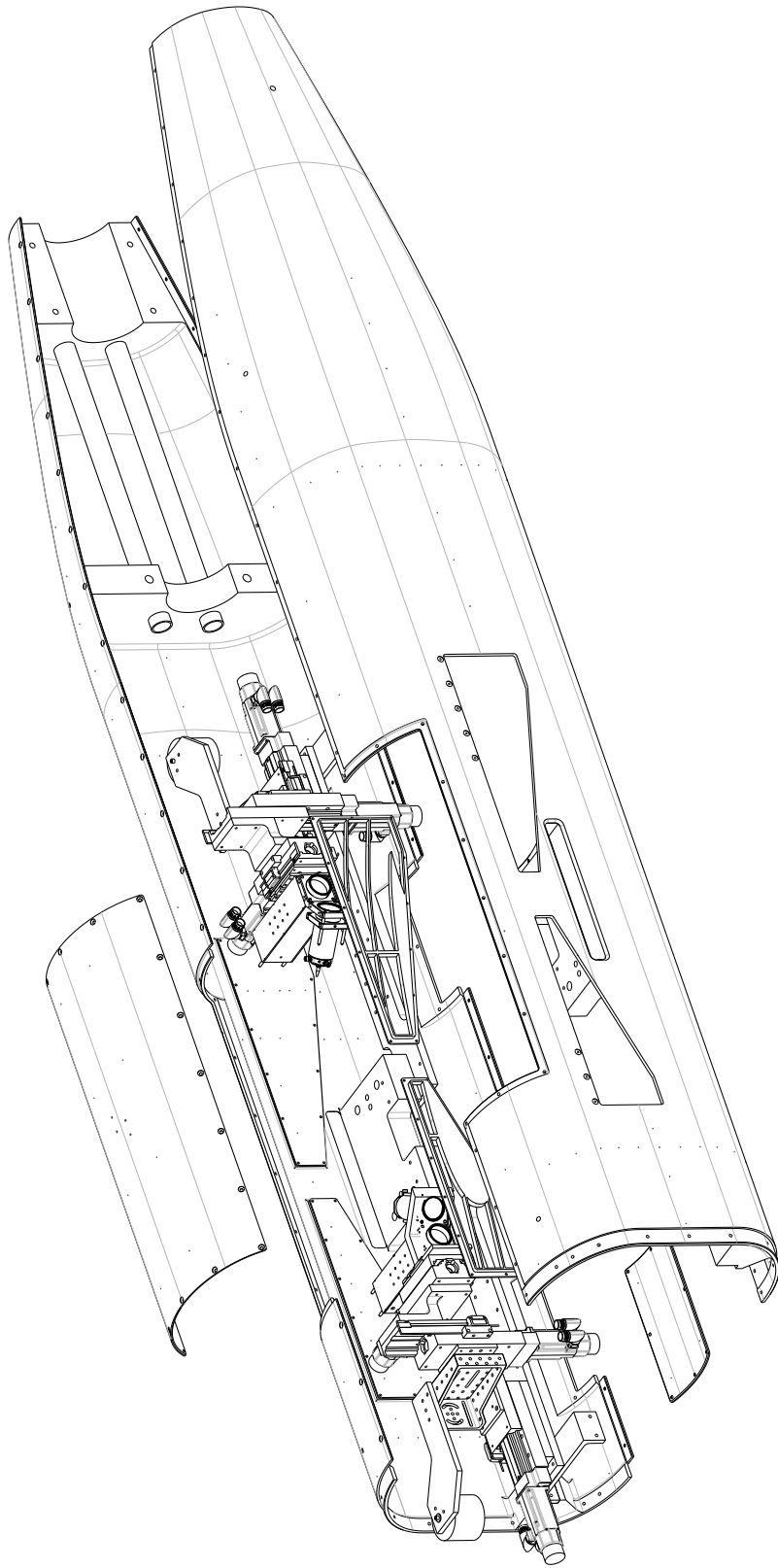
Figure 14: Exploded view of fuselage main-section assembly.
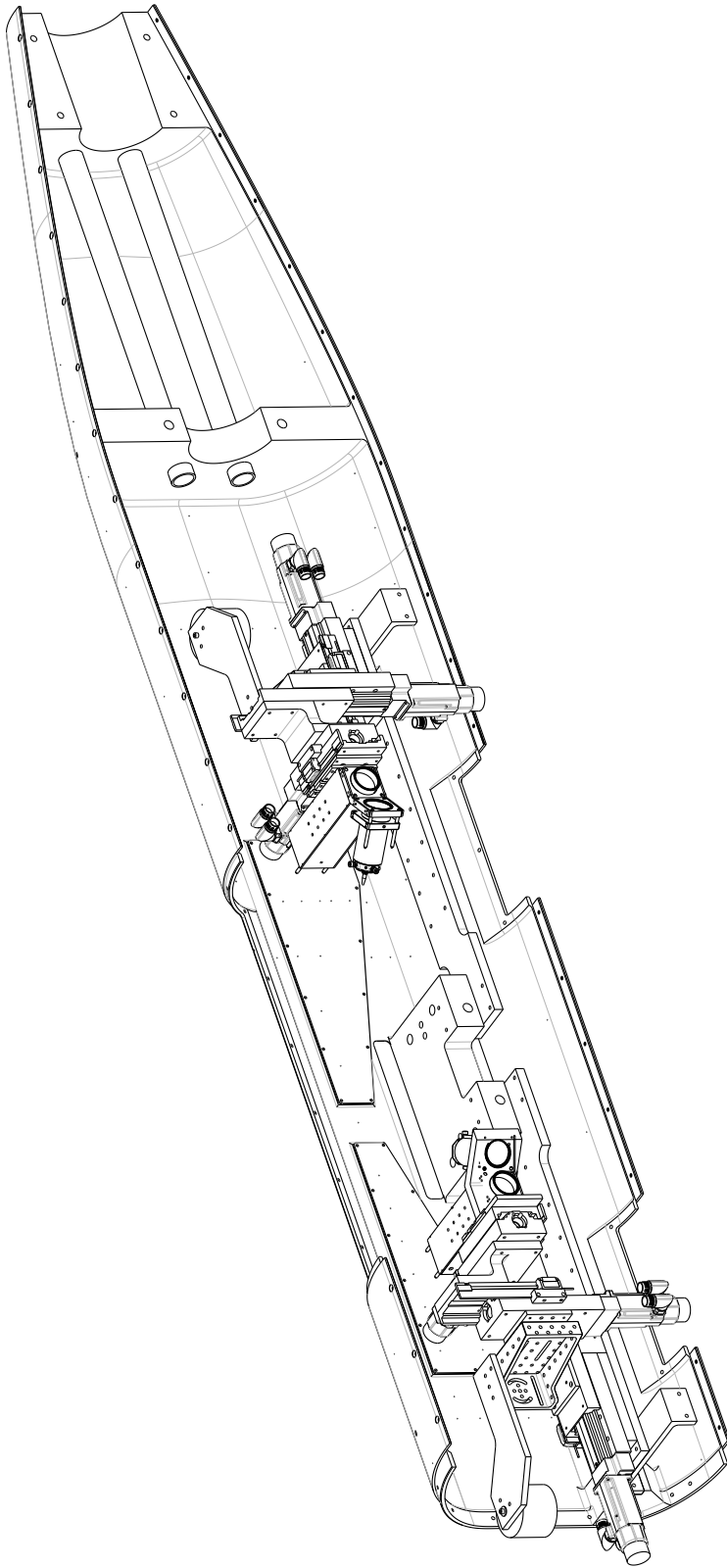
Figure 15: Starboard side of fuselage main section with LDV/traverse assembly.
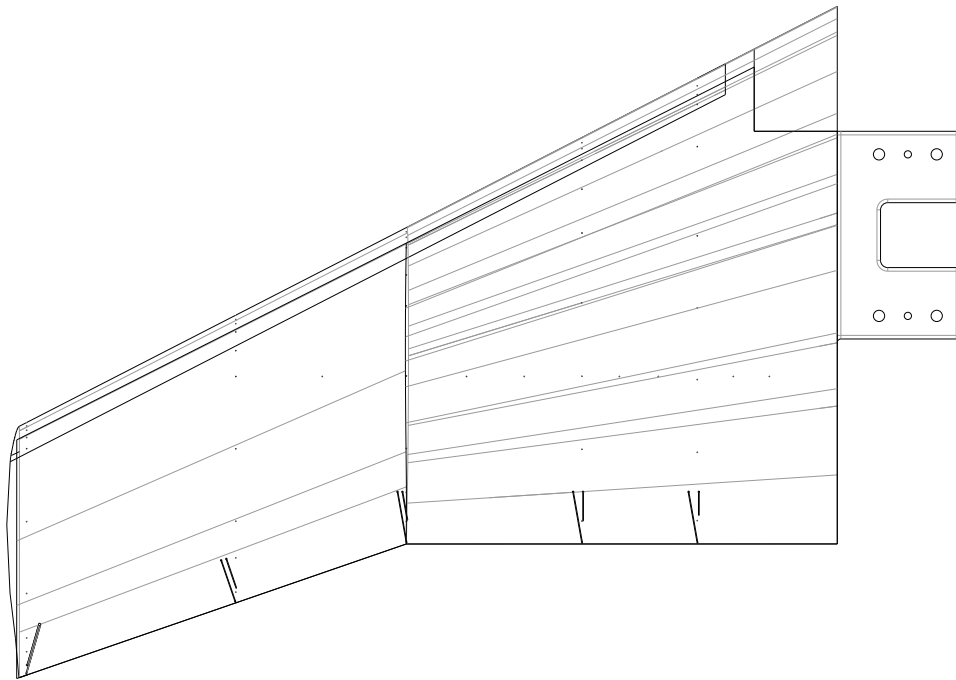
Figure 16: Top view of the F6 port-wing planform.
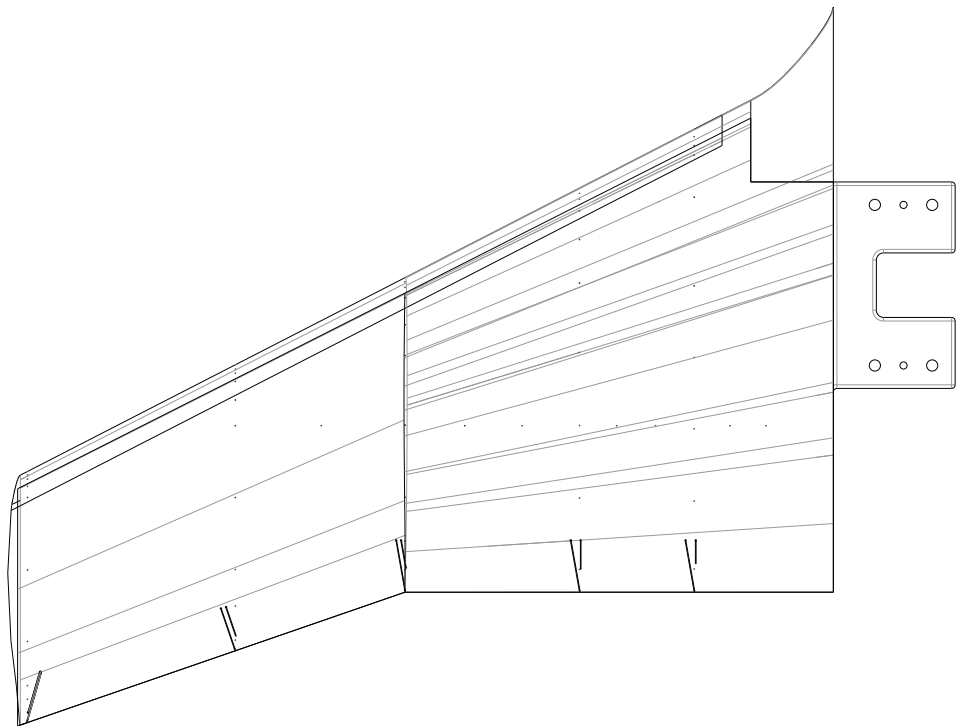
Figure 17: Top view of the F6 port-wing planform with leading-edge extension.
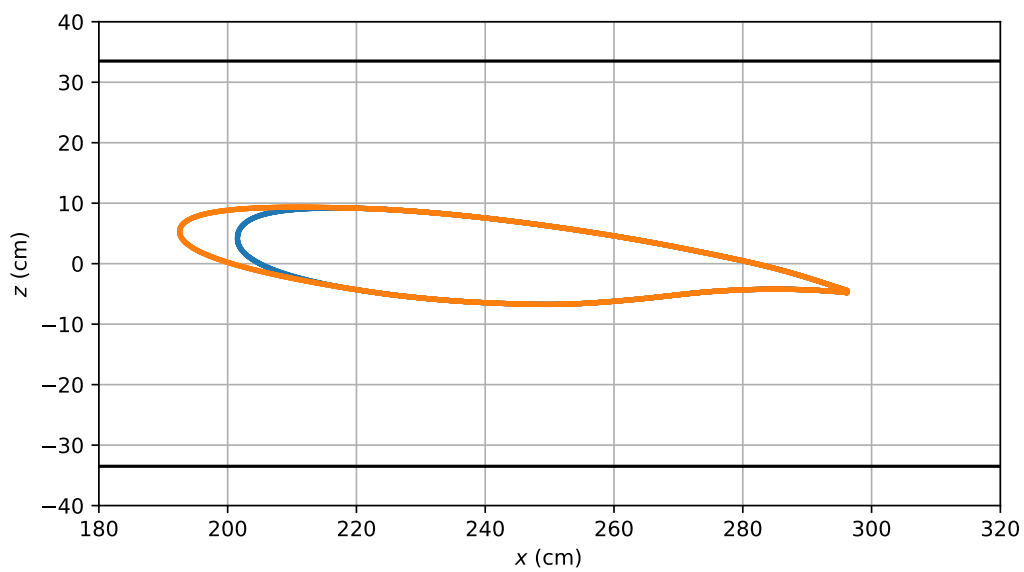
Figure 18: Root-section profiles for the F6 wing (blue) and the F6 wing with extension (orange). The solid black lines denote the top and bottom of the fuselage
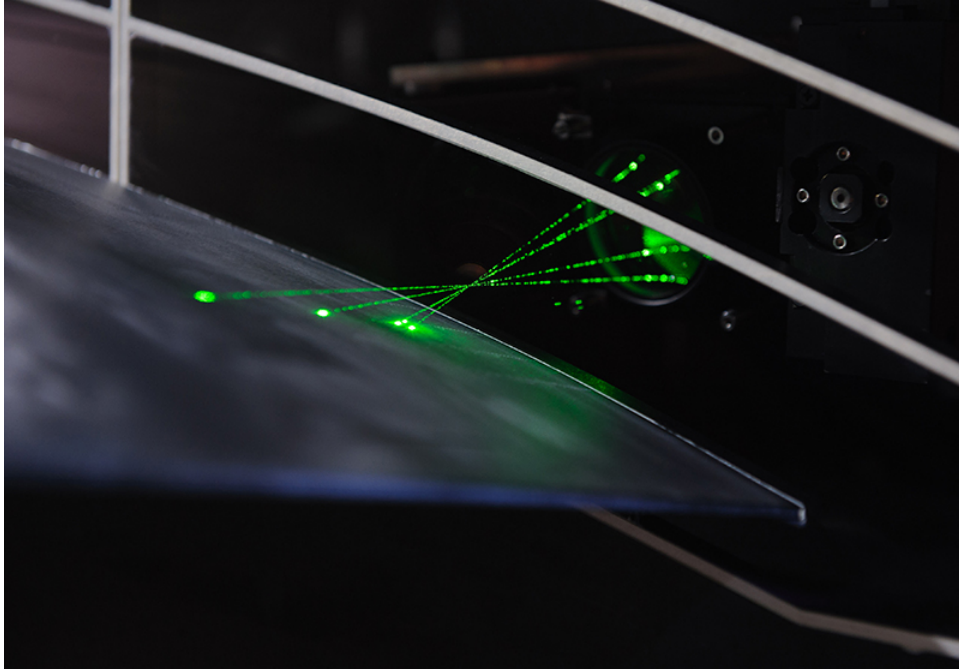
Figure 19: LDV system located near the wing trailing edge.
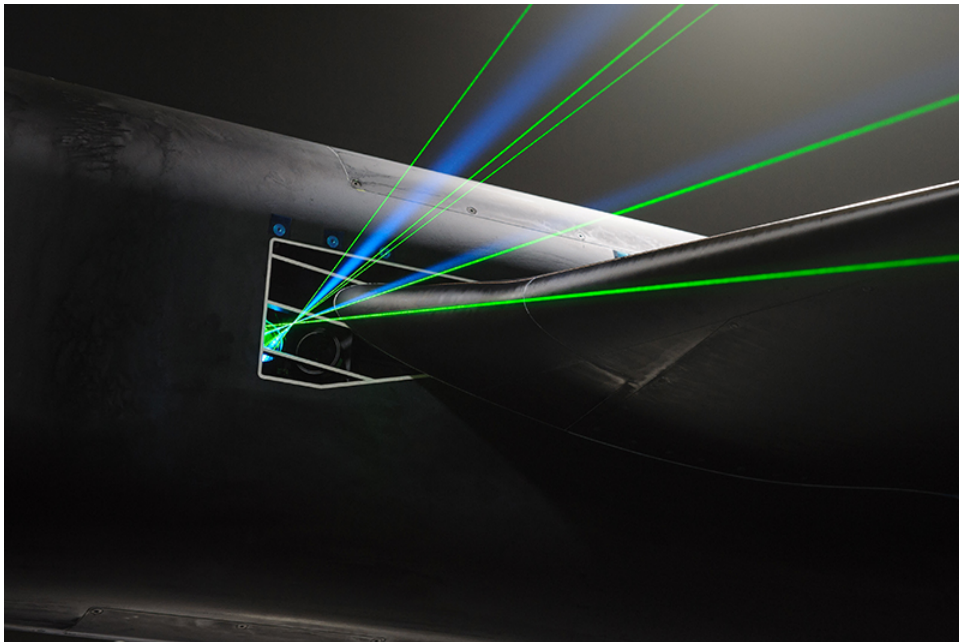
Figure 20: LDV system located near the wing leading edge.
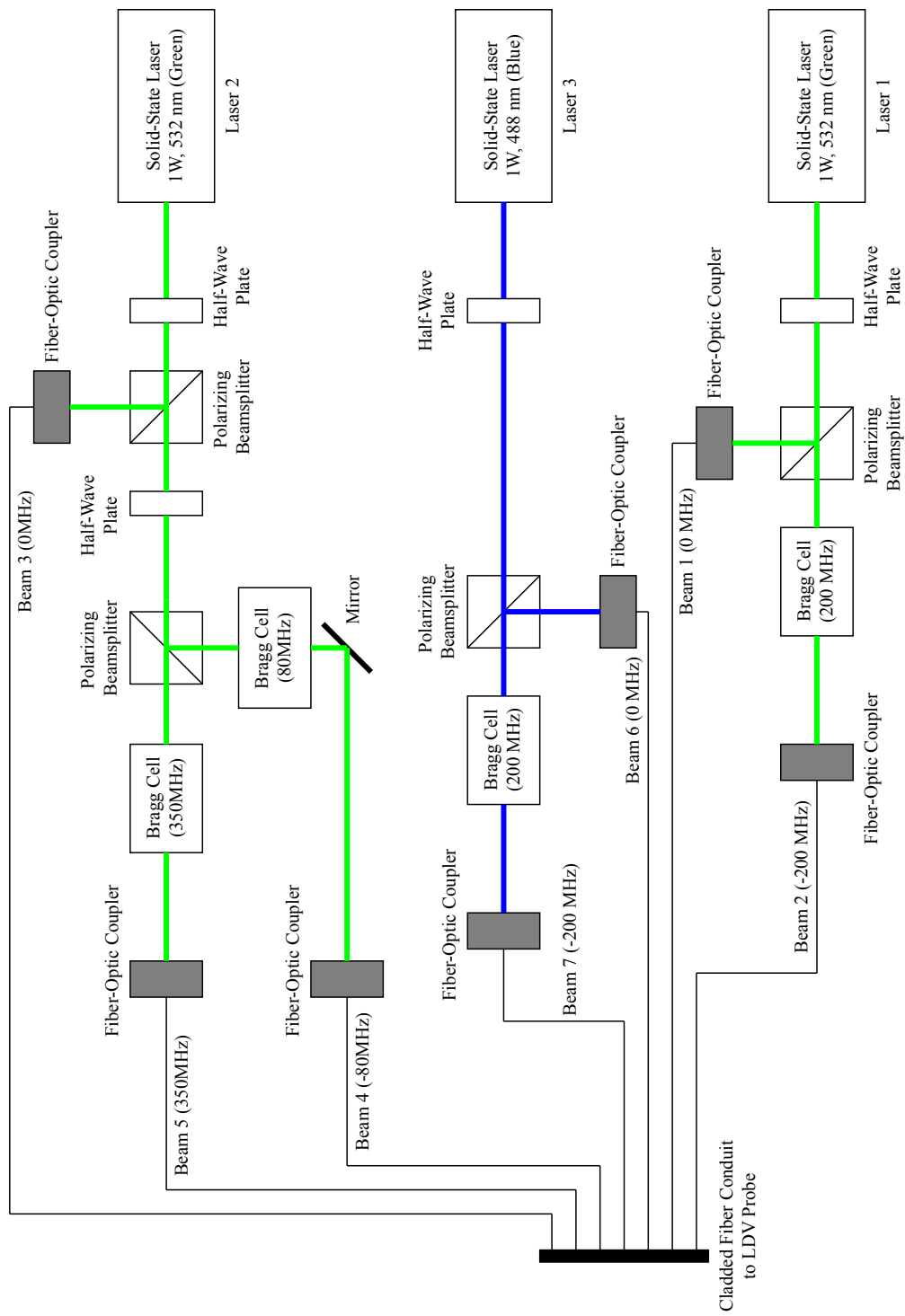
Figure 21: Schematic diagram of the photonics system showing the lasers, discrete optical components, and acoustic-optic modulators.
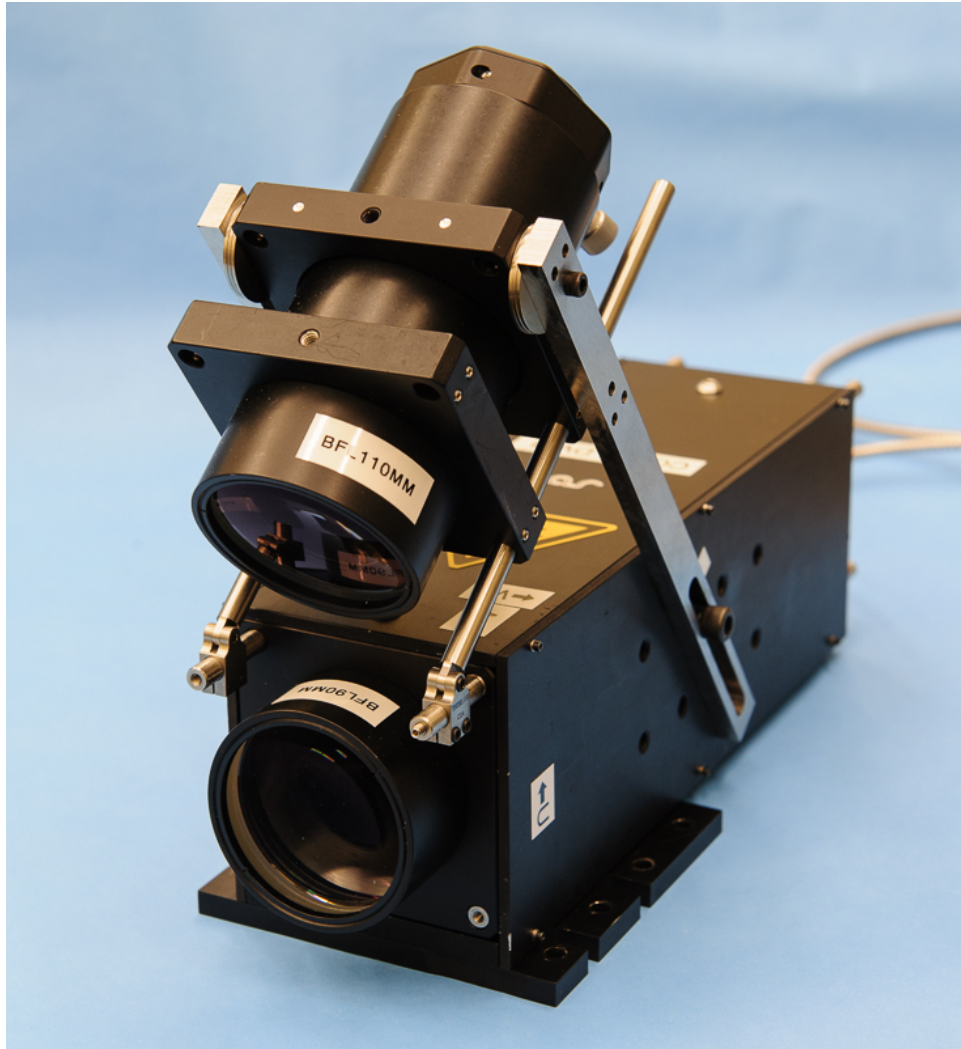
Figure 22: Photograph of the LDV probe head with off-axis receiving optics.

Y, V   Z, W

4"   10"

X, U

Z, W
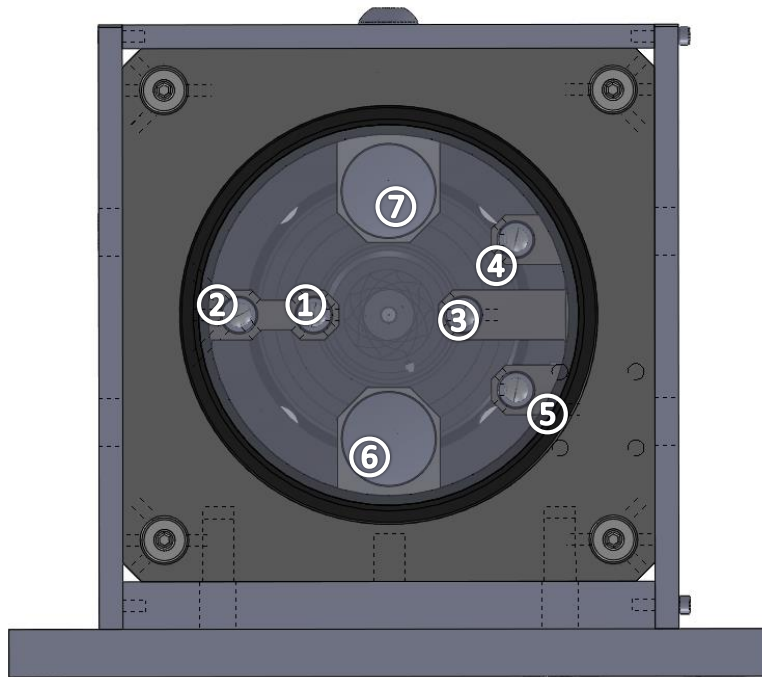
Figure 23: Front view of the LDV probe head with annotated locations for the collimating lenses of the seven laser beams. Beams 1 (0 MHz) and 2 (-200 MHz) were produced by laser 1 (532 nm). Beams 3 (0 MHz), 4 (-80 MHz), and 5 (350 MHz) were produced by laser 2 (532 nm). Beams 6 (0 MHz) and 7 (-200 MHz) were produced by laser 3 (488 nm).
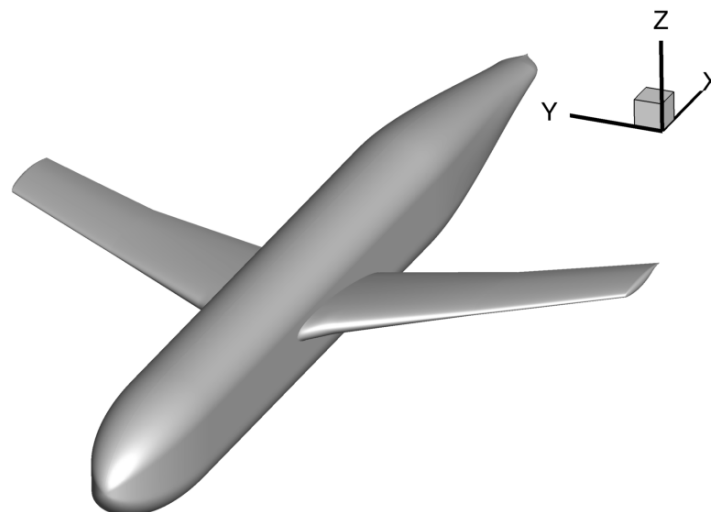
Figure 24: Body-fixed coordinate system for the junction model. The origin of coordinate system is located at the model nose tip.
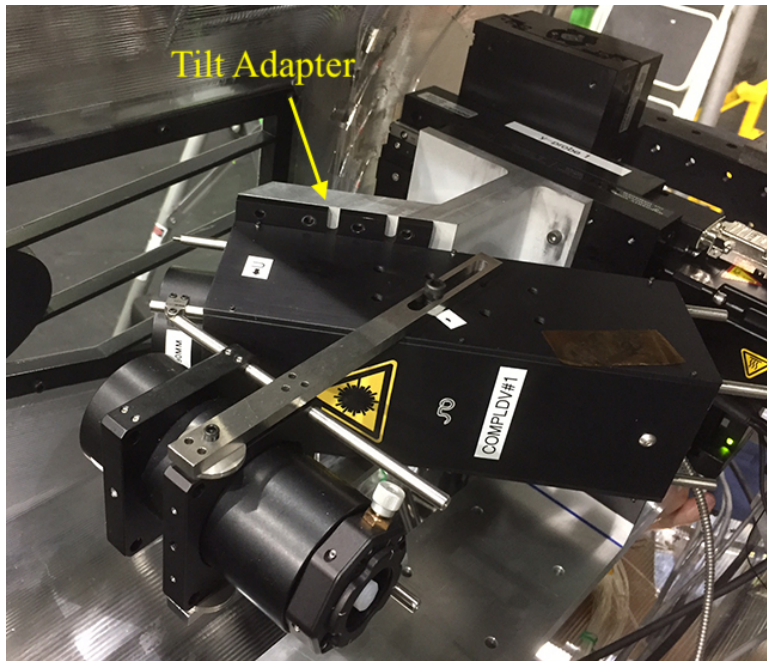
Figure 25: Photograph of an LDV probe head mounted to a 39° tilt adapter so that measurements could be made closer to the F6 wing leading edge without clipping the probe laser beams or blocking the receiving optics.
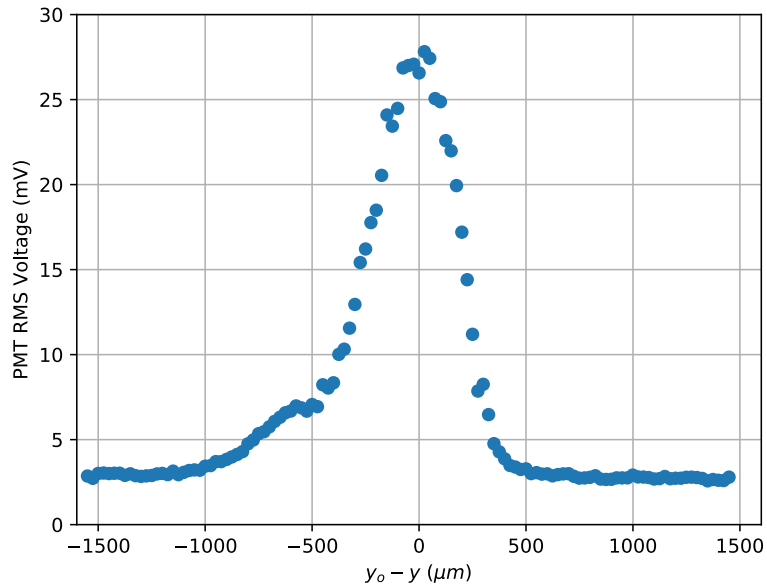
Figure 26: Photomultiplier RMS voltage as the LDV measurement volume is scanned through the fuselage optical window in the y direction. y_o denotes the surface of the window and for positive $y_o - y$ values, the center of the measurement volume is outside the model fuselage.
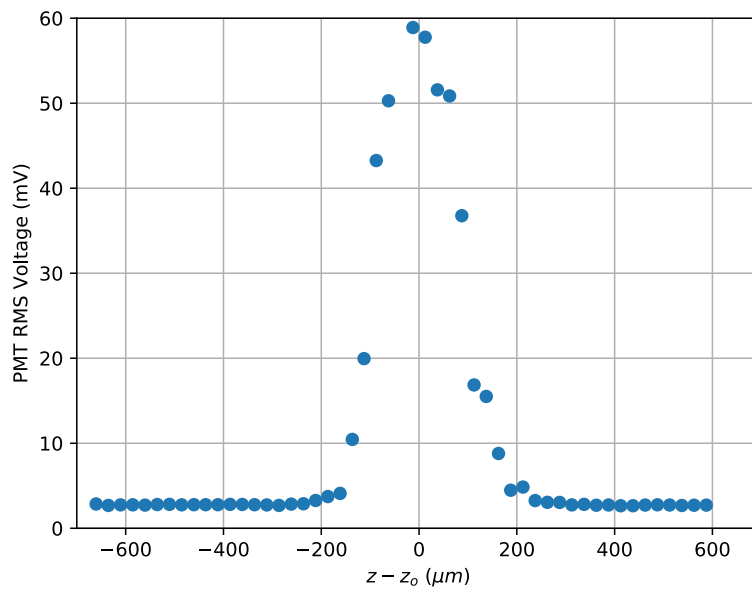
Figure 27: Photomultiplier RMS voltage as the LDV measurement volume is scanned down towards the wing surface in the z direction. z_o denotes the surface of the wing and for positive values of $z - z_o$, the center of the measurement volume is above the wing surface.
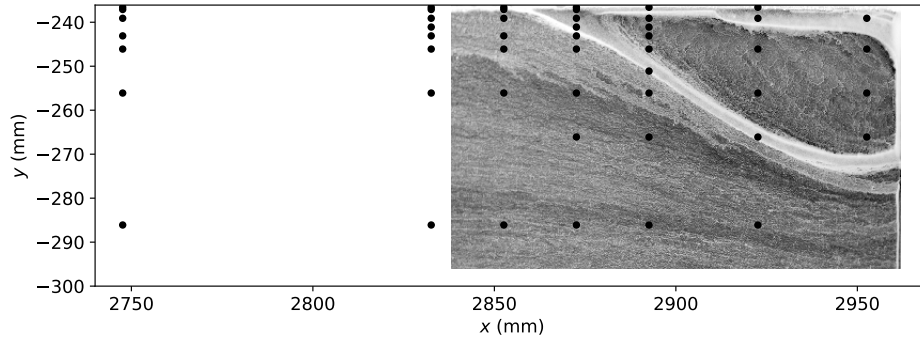
Figure 28: Locations of z-direction LDV surveys in the corner-flow region of the F6 wing. The black circles denote the (x, y)-locations of the profiles and those locations are superimposed on an image of the oil-flow visualization at $\alpha = 5°$.
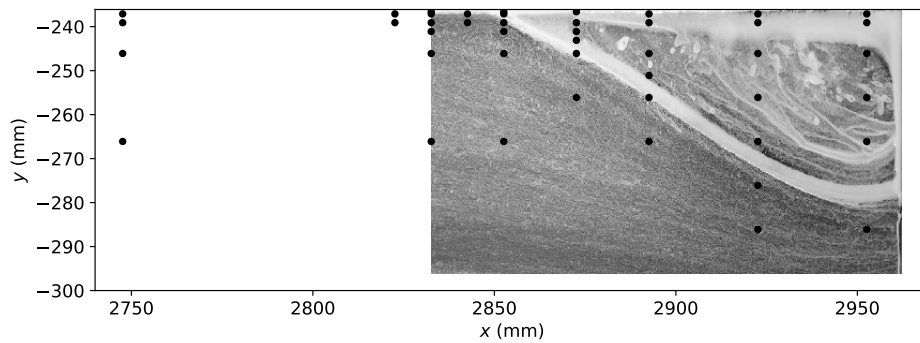
(a) $\alpha = 5°$.
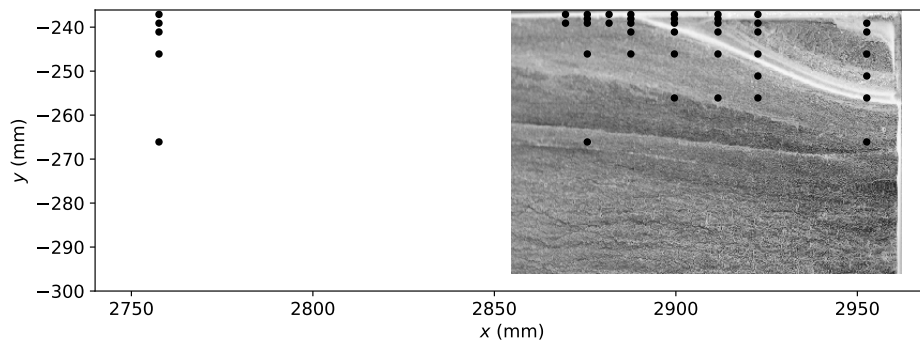
(b) $\alpha = -2.5°$.

Figure 29: Locations of z-direction LDV surveys in the corner-flow region of the F6 wing with extension. The black circles denote the (x, y)-locations of the profiles and those locations are superimposed on images of the oil-flow visualizations for the two pitch angles considered.
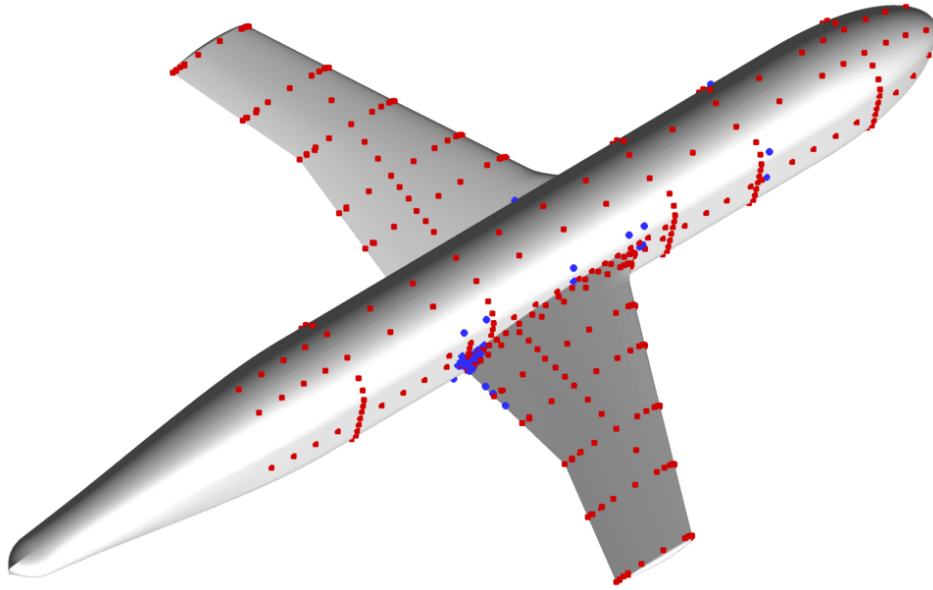
Figure 30: Static pressure port (red squares) and unsteady pressure transducer (blue circles) locations on the junction model configured with the F6 wing with extension.
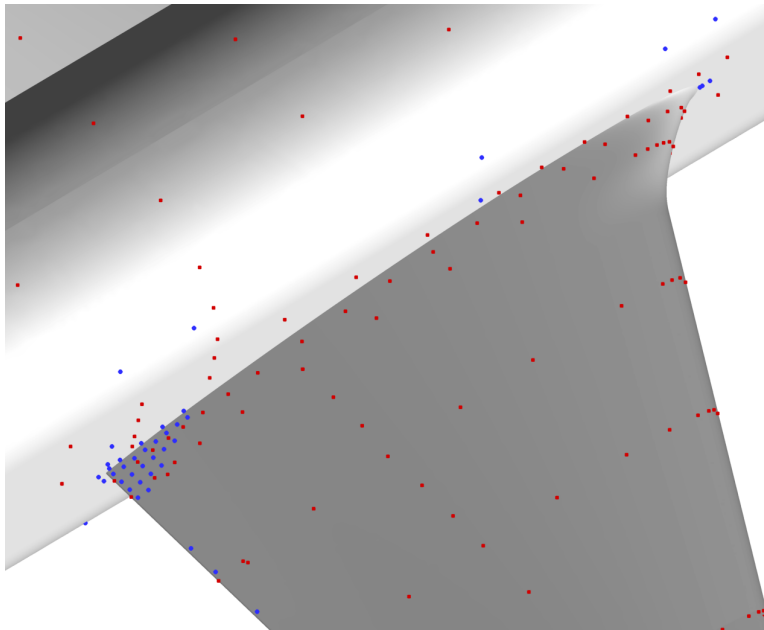
Figure 31: Static pressure port (red squares) and unsteady pressure transducer (blue circles) locations near the starboard wing root of the junction model configured with the F6 wing with extension.
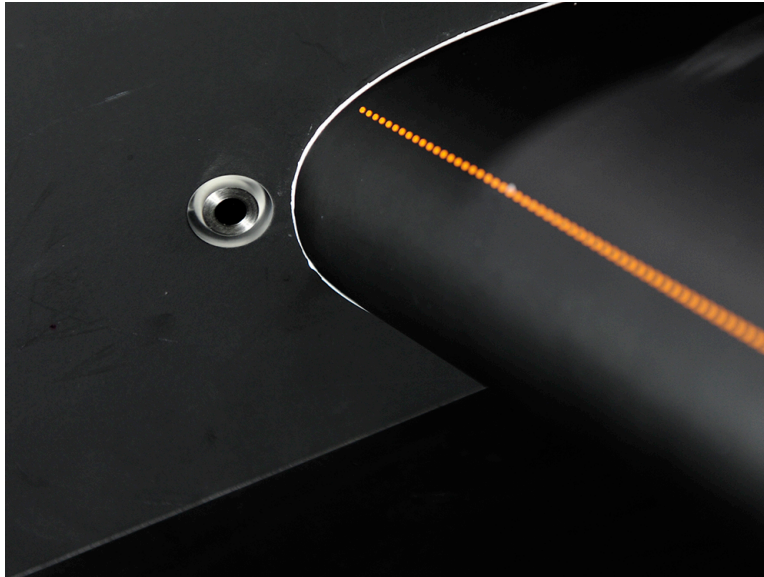
Figure 32: Photo of a MEMS capacitive shear stress sensor installed near the leading edge of the F6 wing.
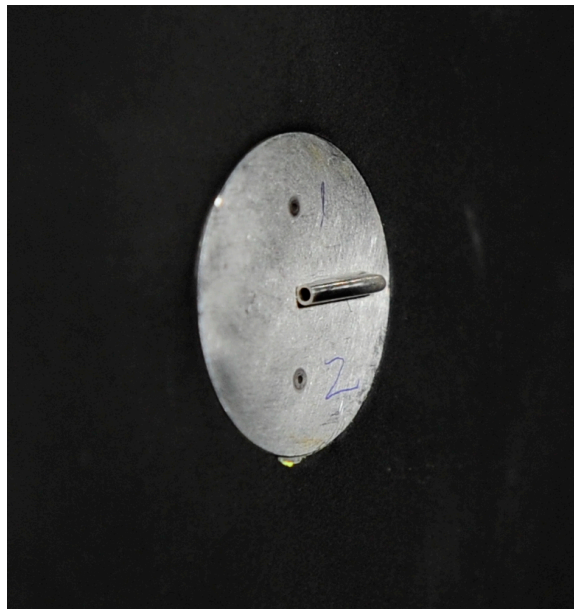
Figure 33: Close-up photo of a Preston tube installed in the fuselage nose section.
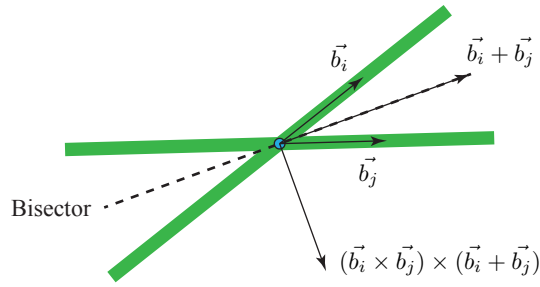
Figure 34: Schematic of a pair of LDV probe beams that form a measurement volume and the associated measurement direction.
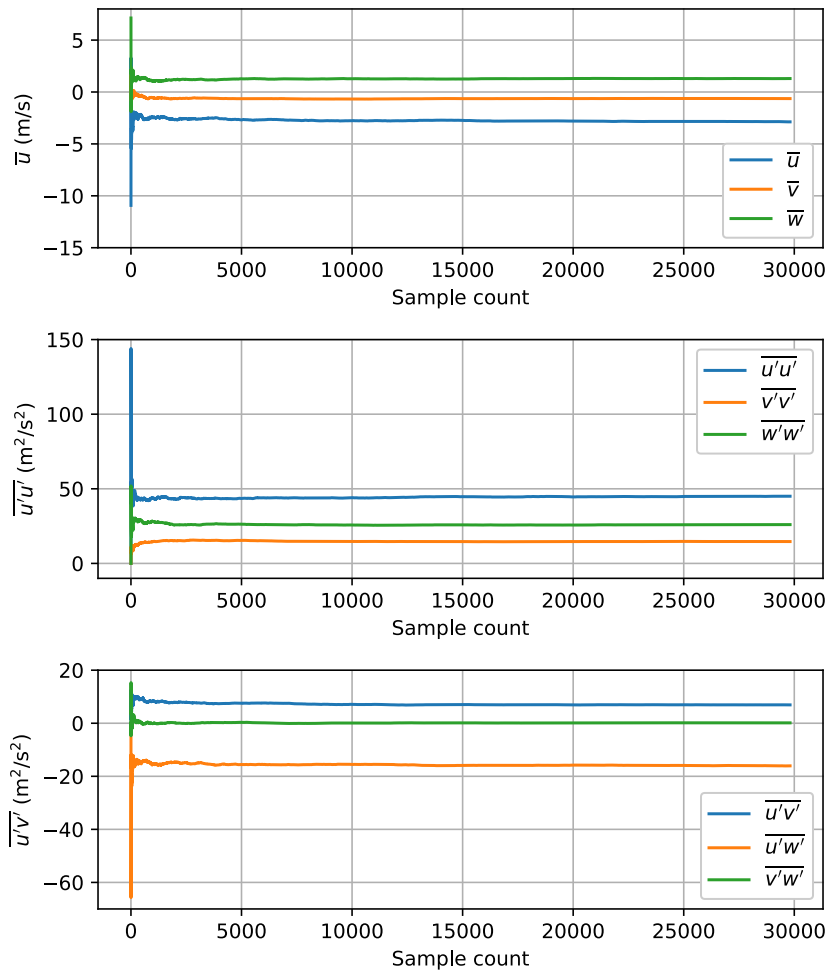
Figure 35: Running averages of mean velocity and Reynolds stresses versus sample count. Data were acquired at $x = 2892.6$ mm, $y = -239.1$ mm, and $z = -17.1$ mm for $\alpha = 5°$.
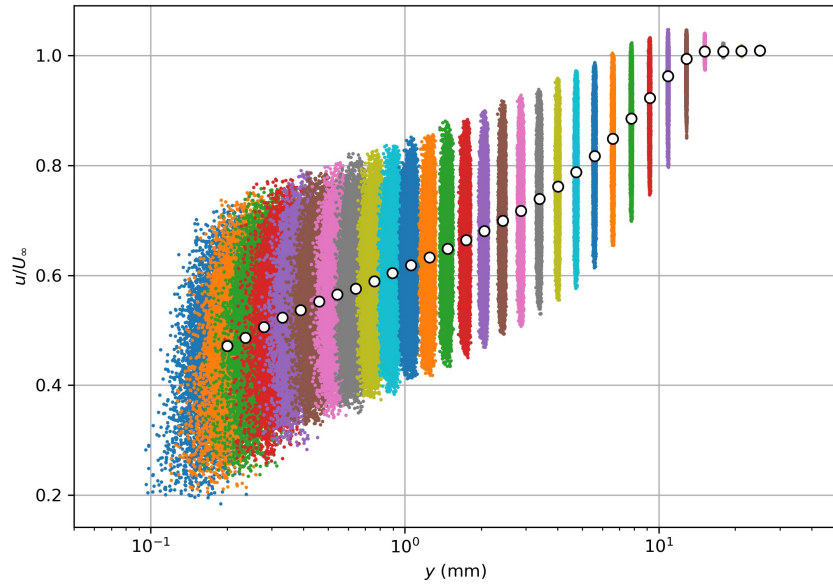
Figure 36: X-component velocity profile measured in the dual-channel mode at $x = 1168.4$ mm and $z = 0$ mm for $\alpha = 5°$. Point clouds of the particle velocity versus particle position are shown for each survey location in the profile as a different color. The circle symbols denote the average velocity of each point cloud and are plotted against the location of the center of the measurement volume.
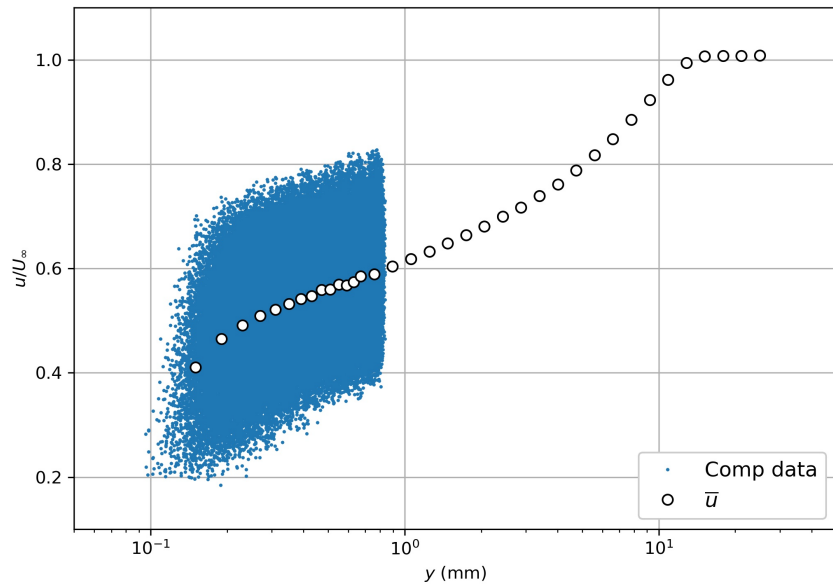
Figure 37: X-component velocity profile measured in the dual-channel mode at $x = 1168.4$ mm and $z = 0$ mm for $\alpha = 5°$. A composite point cloud of the particle velocity versus particle position for the first nine survey locations is shown and the circle symbols denote the average velocities. Locations below $y = 0.7$ mm are bin averages derived from the point cloud.

(a) $\alpha = -10.0°$ (b) $\alpha = -7.5°$ (c) $\alpha = -5.0°$

(d) $\alpha = -2.5°$ (e) $\alpha = 0.0°$ (f) $\alpha = 2.5°$

(g) $\alpha = 5.0°$ (h) $\alpha = 7.5°$ (i) $\alpha = 10.0°$
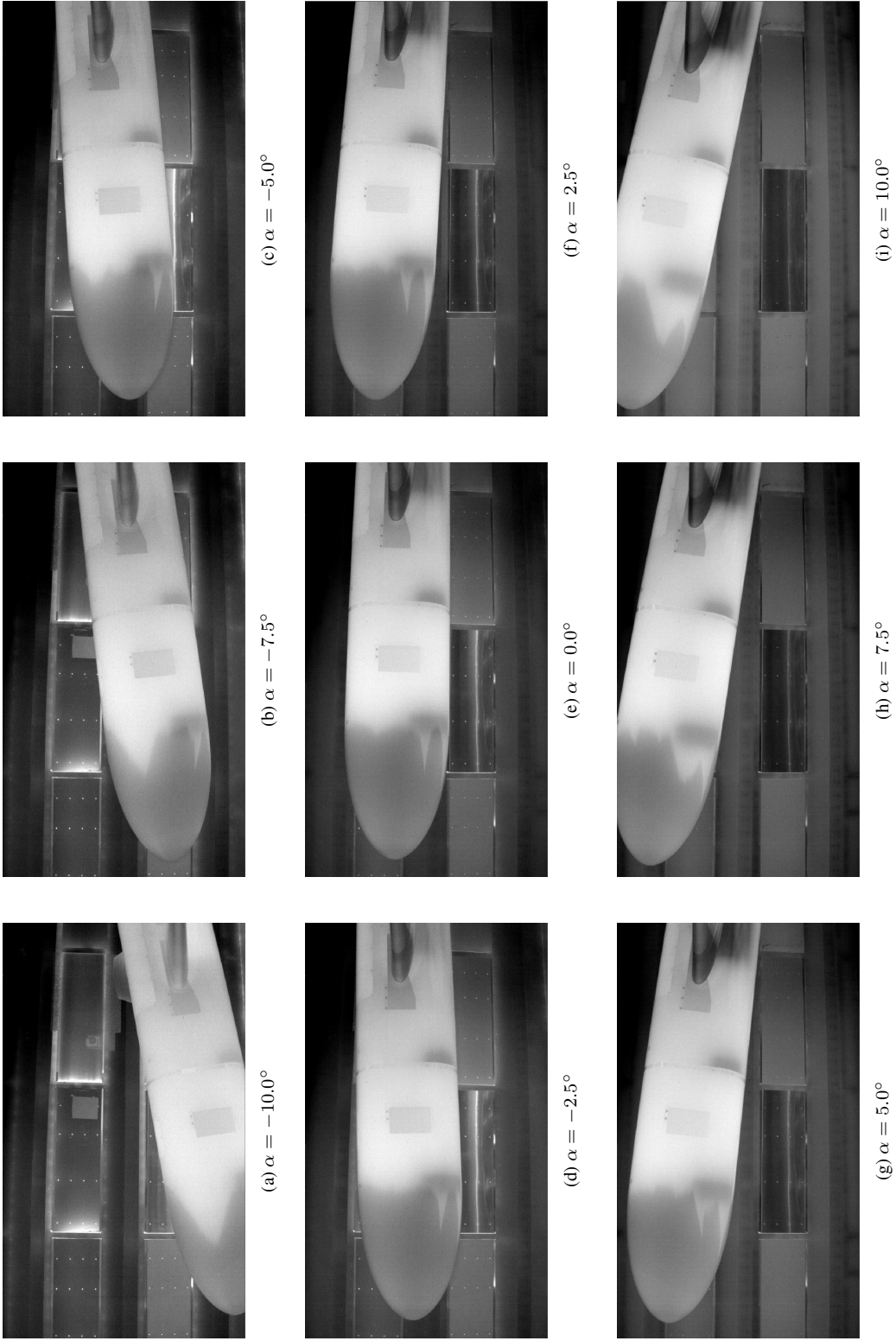
Figure 38: Infrared images of the fuselage port side versus model pitch angle. The model was clean (no trip elements). F6 wing geometry at $Re_c = 2.4 \times 10^6$.

(a) $\alpha = -10.0°$ (b) $\alpha = -7.5°$ (c) $\alpha = -5.0°$

(d) $\alpha = -2.5°$ (e) $\alpha = 0.0°$ (f) $\alpha = 2.5°$

(g) $\alpha = 5.0°$ (h) $\alpha = 7.5°$ (i) $\alpha = 10.0°$
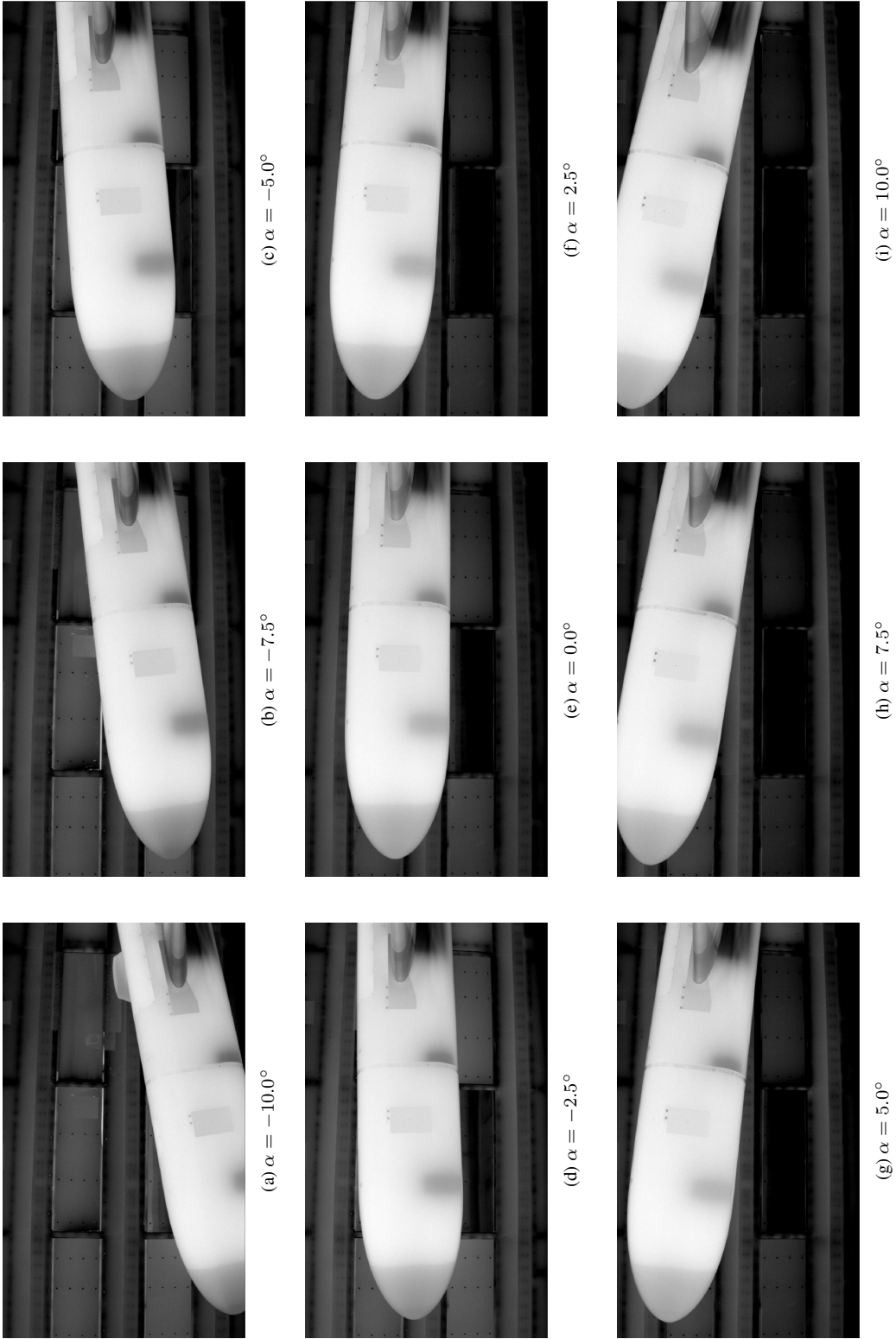
Figure 39: Infrared images of the fuselage port side versus model pitch angle. The fuselage boundary layer was tripped with 289.4 μm trip dots located at a nominal distance of $x = 336$ mm from the model nose tip. F6 wing geometry at $Re_c = 2.4 \times 10^6$.

(a) $\alpha = -10.0°$ (b) $\alpha = -7.5°$ (c) $\alpha = -5.0°$

(d) $\alpha = -2.5°$ (e) $\alpha = 0.0°$ (f) $\alpha = 2.5°$

(g) $\alpha = 5.0°$ (h) $\alpha = 7.5°$ (i) $\alpha = 10.0°$
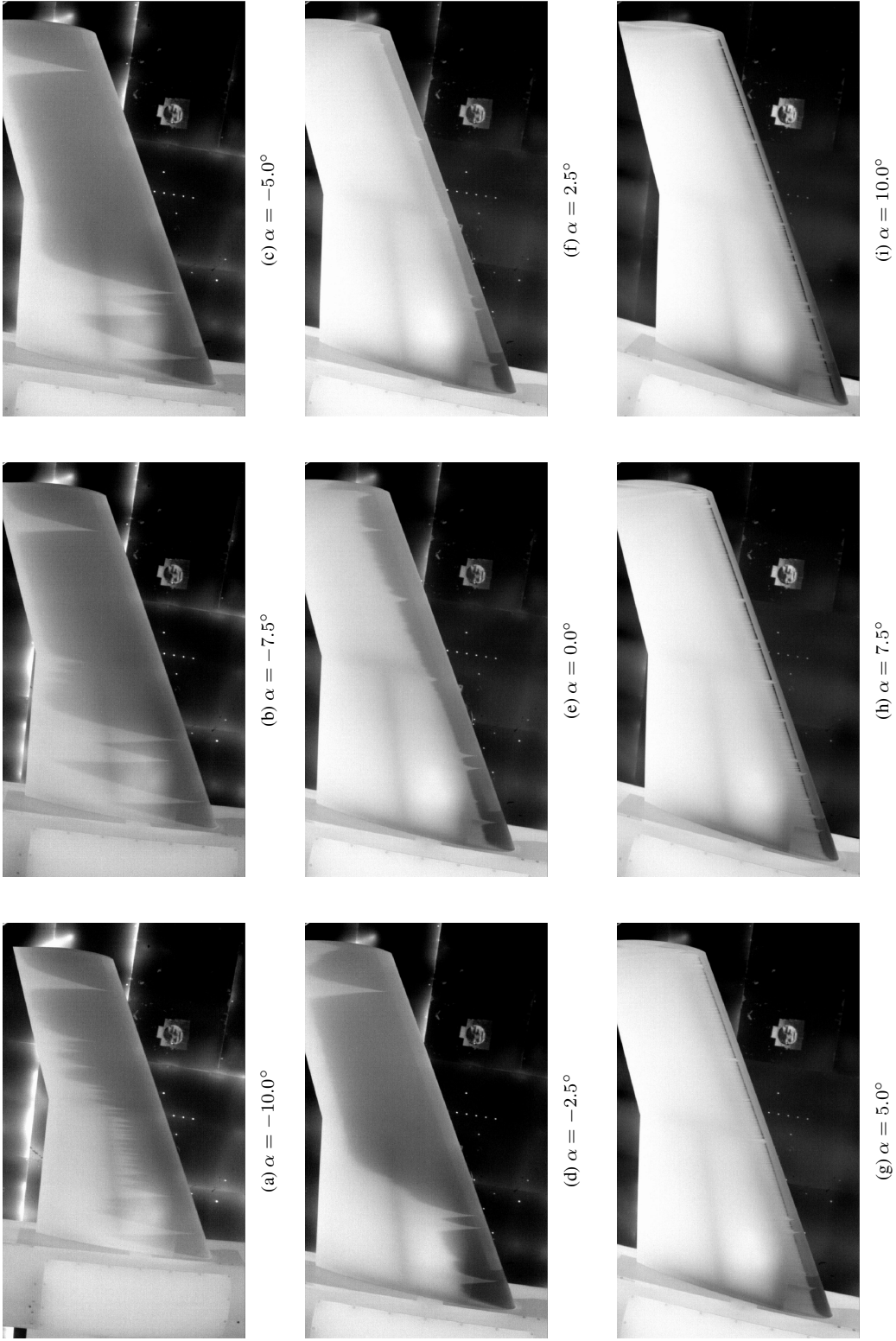
Figure 40: Infrared images of the upper surface of the port-side wing versus model pitch angle. The wing surface was clean (no trip elements). F6 wing geometry at $Re_c = 2.4 \times 10^6$.

94

(a) $\alpha = -10.0°$
(b) $\alpha = -7.5°$
(c) $\alpha = -5.0°$
(d) $\alpha = -2.5°$
(e) $\alpha = 0.0°$
(f) $\alpha = 2.5°$
(g) $\alpha = 5.0°$
(h) $\alpha = 7.5°$
(i) $\alpha = 10.0°$
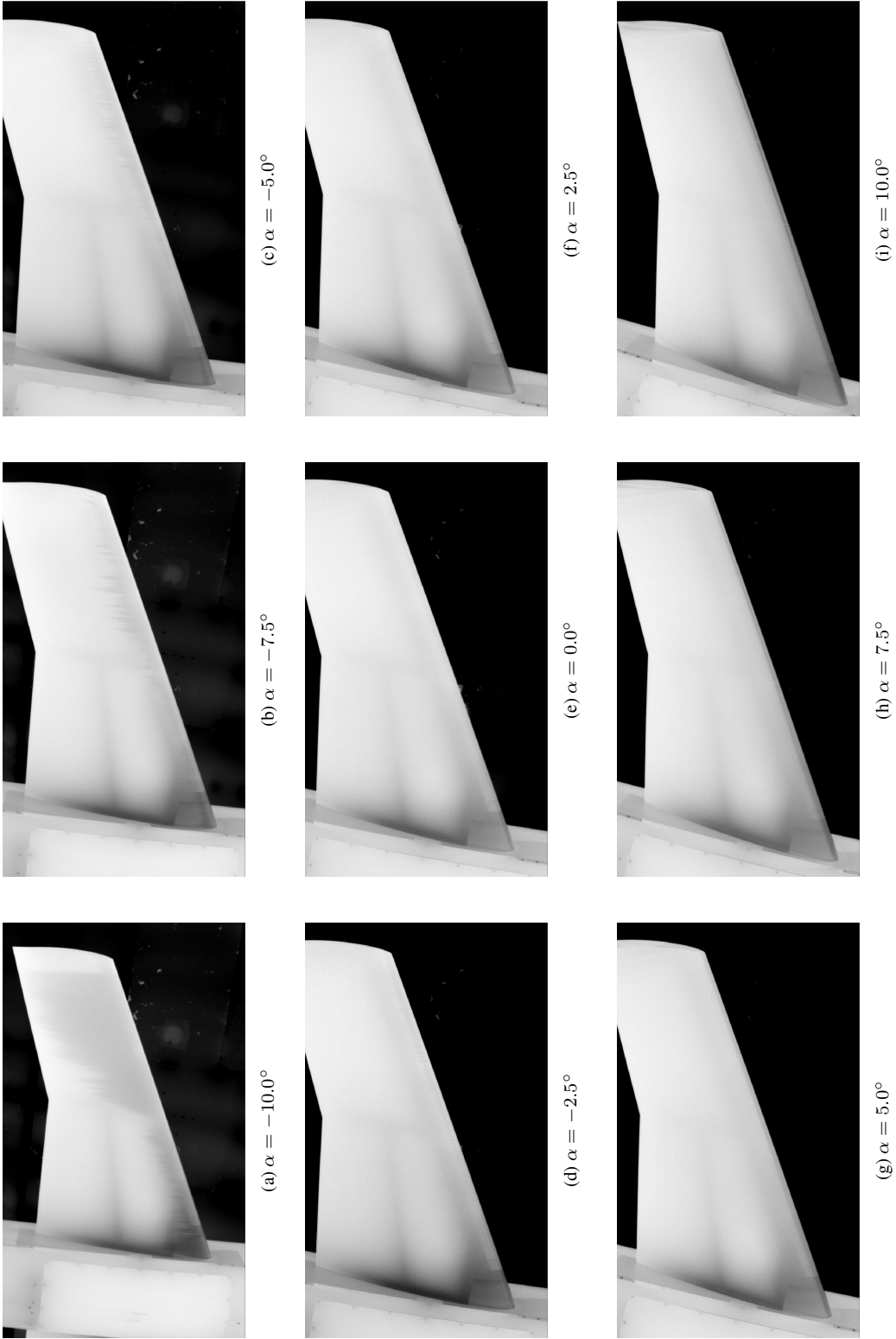
Figure 41: Infrared images of the upper surface of the port-side wing versus model pitch angle. The wing surface was tripped at approximately 1.6% chord with 170.6 μm trip dots. F6 wing geometry at $Re_c = 2.4 \times 10^6$.

95
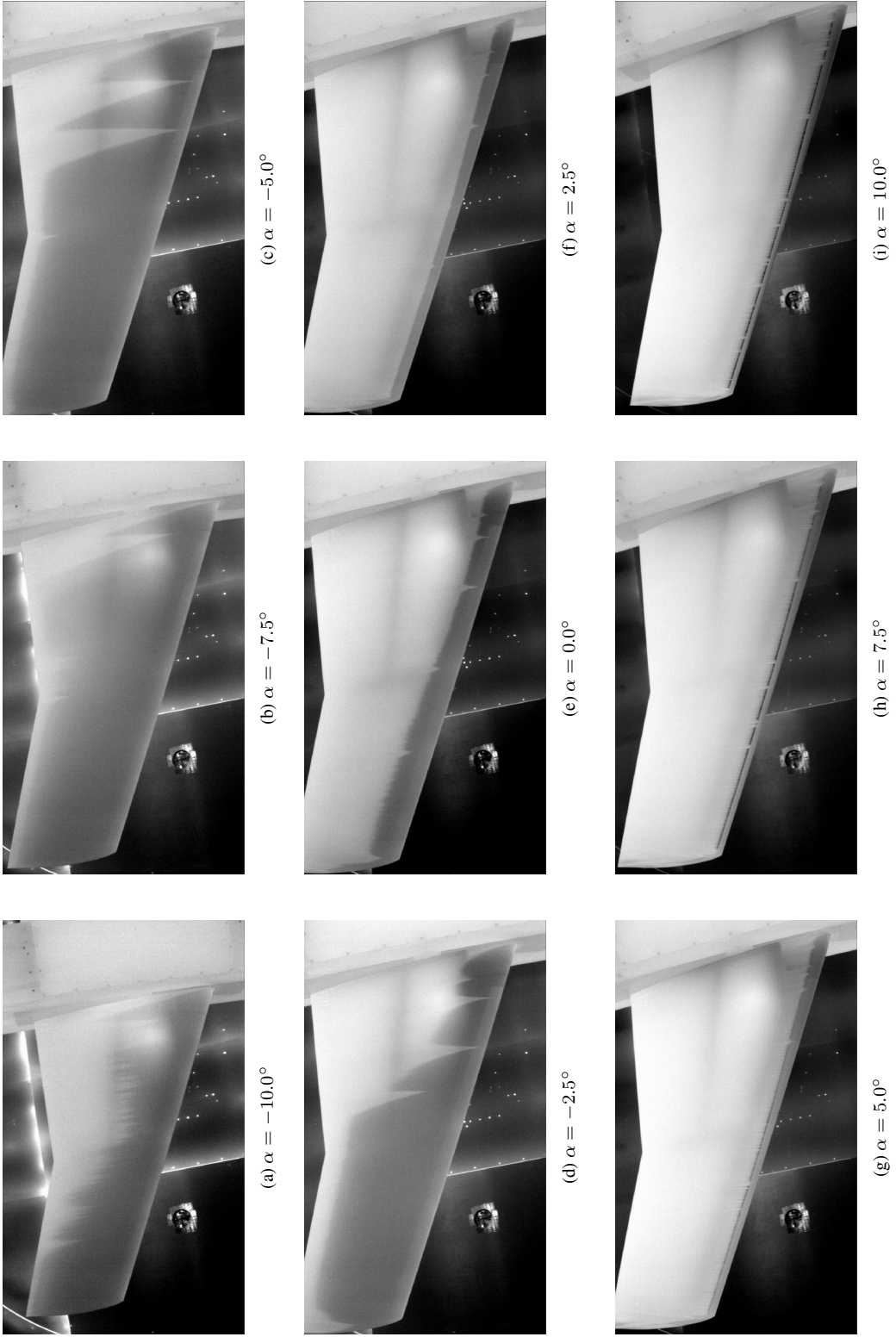
Figure 42: Infrared images of the upper surface of the starboard-side wing versus model pitch angle. The wing surface was clean (no trip elements). F6 wing geometry at $Re_c = 2.4 \times 10^6$.

(a) $\alpha = -10.0°$

(b) $\alpha = -7.5°$

(c) $\alpha = -5.0°$

(d) $\alpha = -2.5°$

(e) $\alpha = 0.0°$

(f) $\alpha = 2.5°$

(g) $\alpha = 5.0°$

(h) $\alpha = 7.5°$

(i) $\alpha = 10.0°$

(a) $\alpha = -10.0°$ (b) $\alpha = -7.5°$ (c) $\alpha = -5.0°$

(d) $\alpha = -2.5°$ (e) $\alpha = 0.0°$ (f) $\alpha = 2.5°$

(g) $\alpha = 5.0°$ (h) $\alpha = 7.5°$ (i) $\alpha = 10.0°$
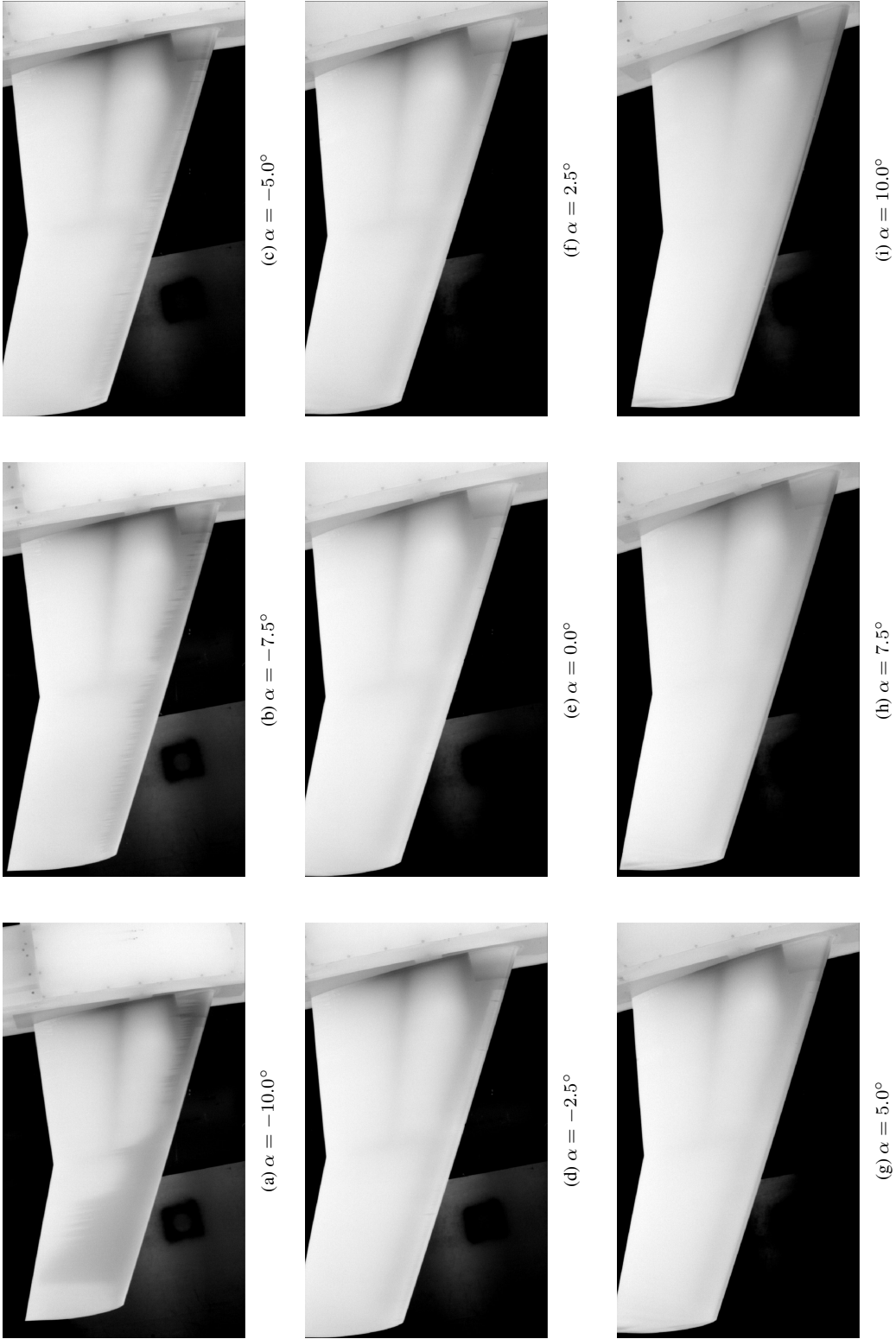
Figure 43: Infrared images of the upper surface of the starboard-side wing versus model pitch angle. The wing surface was tripped at approximately 1.6% chord with 170.6 μm trip dots. F6 wing geometry at $Re_c = 2.4 \times 10^6$.

(a) $\alpha = -10.0°$ (b) $\alpha = -7.5°$ (c) $\alpha = -5.0°$

(d) $\alpha = -2.5°$ (e) $\alpha = 0.0°$ (f) $\alpha = 2.5°$

(g) $\alpha = 5.0°$ (h) $\alpha = 7.5°$ (i) $\alpha = 10.0°$
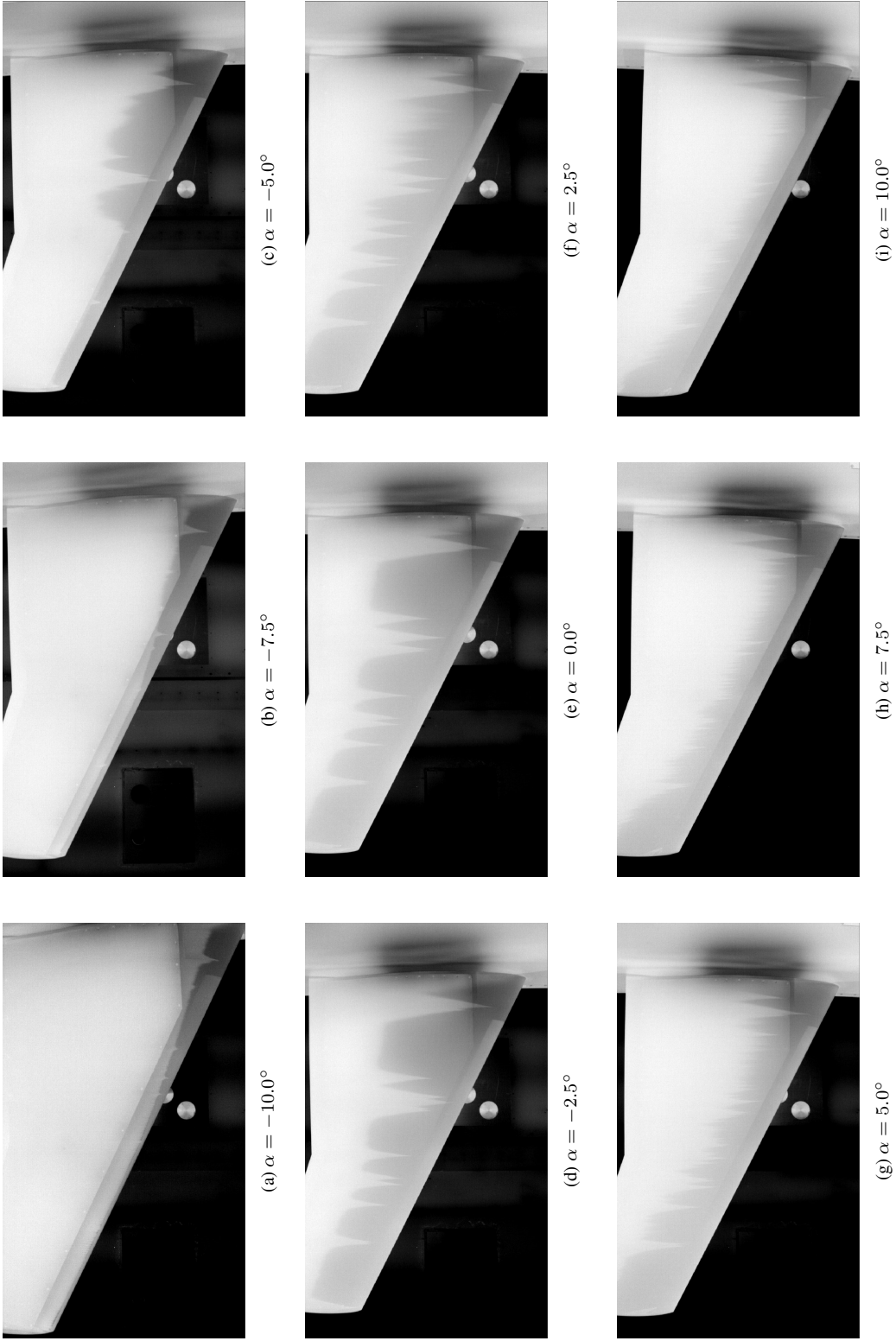
Figure 44: Infrared images of the lower surface of the port-side wing versus model pitch angle. The wing surface was clean (no trip elements). F6 wing geometry at $Re_c = 2.4 \times 10^6$.
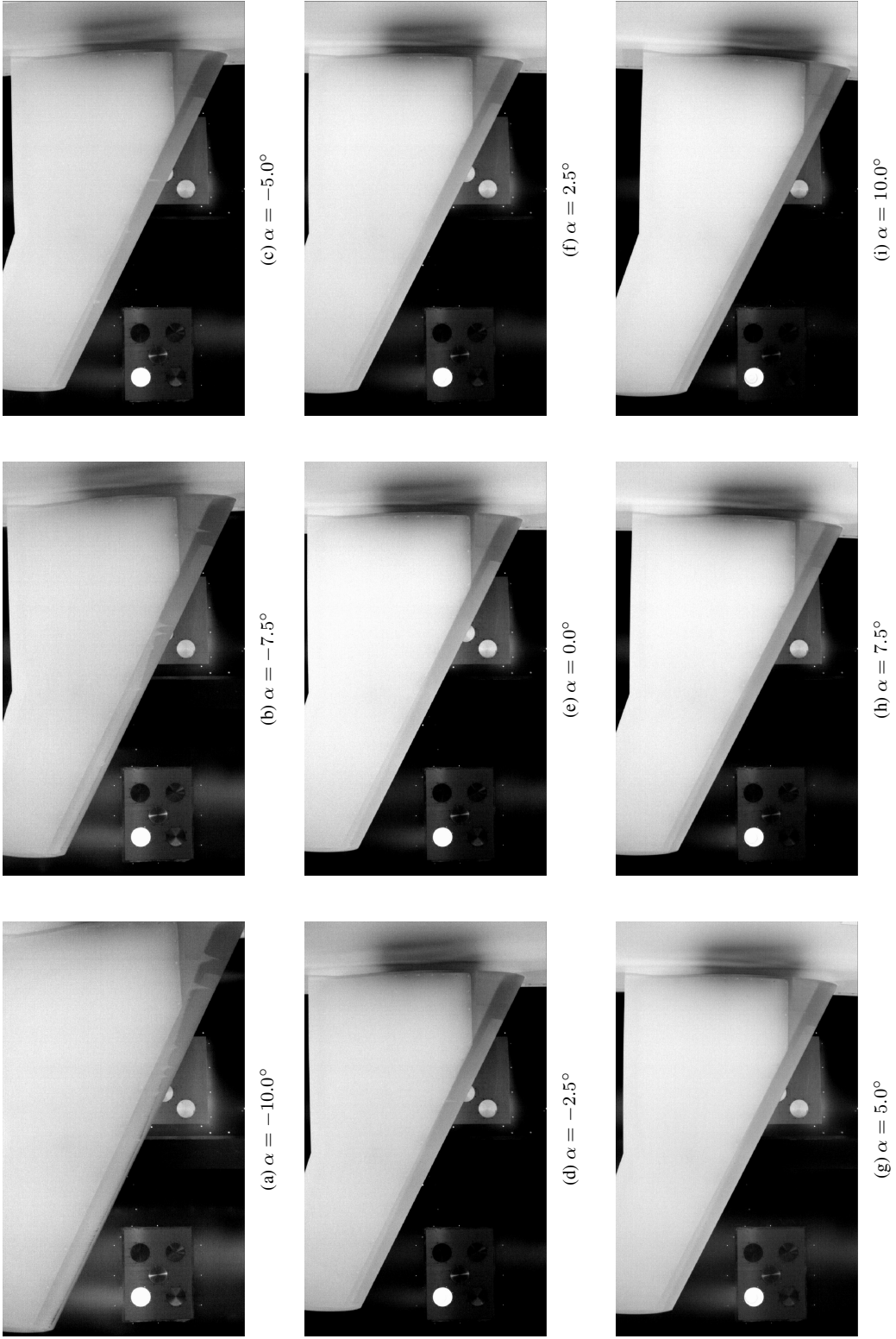
Figure 45: Infrared images of the lower surface of the port-side wing versus model pitch angle. The wing surface was tripped at approximately 10% chord with 196.9 μm trip dots. F6 wing geometry at $Re_c = 2.4 \times 10^6$.

(a) $\alpha = -10.0°$

(b) $\alpha = -7.5°$

(c) $\alpha = -5.0°$

(d) $\alpha = -2.5°$

(e) $\alpha = 0.0°$

(f) $\alpha = 2.5°$

(g) $\alpha = 5.0°$

(h) $\alpha = 7.5°$

(i) $\alpha = 10.0°$

(a) $\alpha = -10.0°$ (b) $\alpha = -7.5°$ (c) $\alpha = -5.0°$

(d) $\alpha = -2.5°$ (e) $\alpha = 0.0°$ (f) $\alpha = 2.5°$

(g) $\alpha = 5.0°$ (h) $\alpha = 7.5°$ (i) $\alpha = 10.0°$
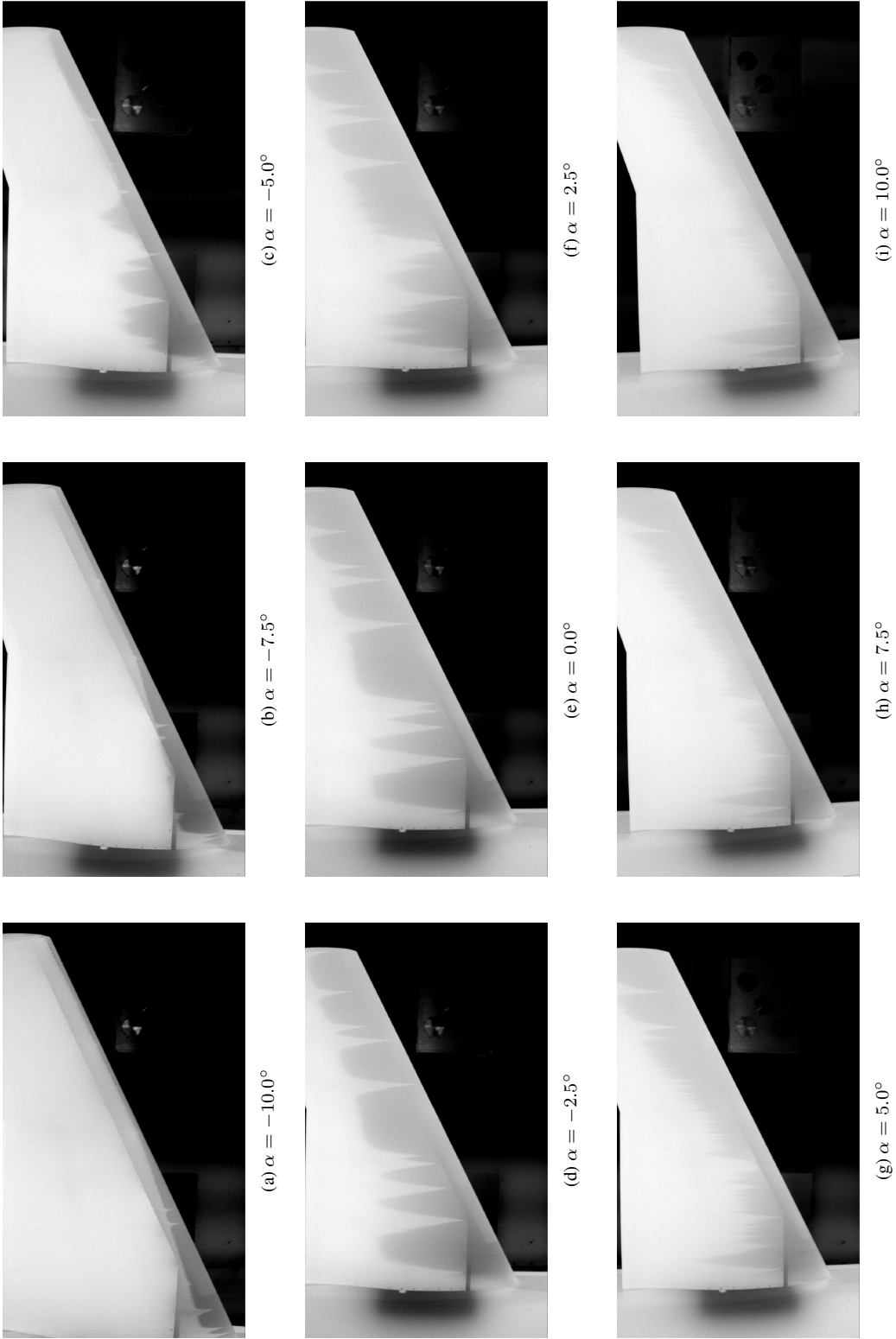
Figure 46: Infrared images of the lower surface of the starboard-side wing versus model pitch angle. The wing surface was clean (no trip elements). F6 wing geometry at $Re_c = 2.4 \times 10^6$.

(a) $\alpha = -10.0°$

(b) $\alpha = -7.5°$

(c) $\alpha = -5.0°$

(d) $\alpha = -2.5°$

(e) $\alpha = 0.0°$

(f) $\alpha = 2.5°$

(g) $\alpha = 5.0°$

(h) $\alpha = 7.5°$

(i) $\alpha = 10.0°$
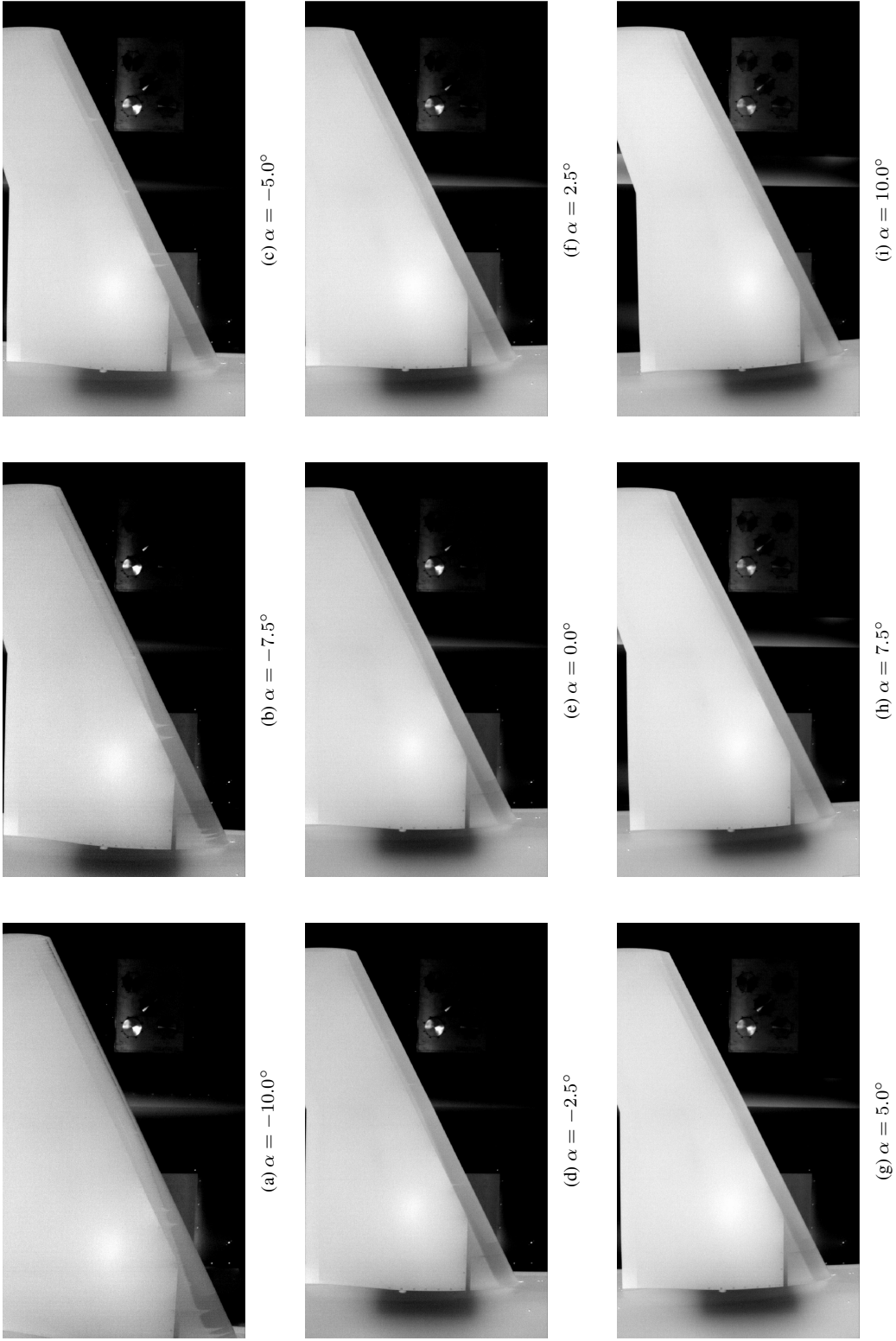
Figure 47: Infrared images of the lower surface of the starboard-side wing versus model pitch angle. The wing surface was tripped at approximately 10% chord with 196.9 μm trip dots. F6 wing geometry at $Re_c = 2.4 \times 10^6$.

(a) $\alpha = -2.5°$

(b) $\alpha = 0.0°$

(c) $\alpha = 2.5°$

(d) $\alpha = 5.0°$
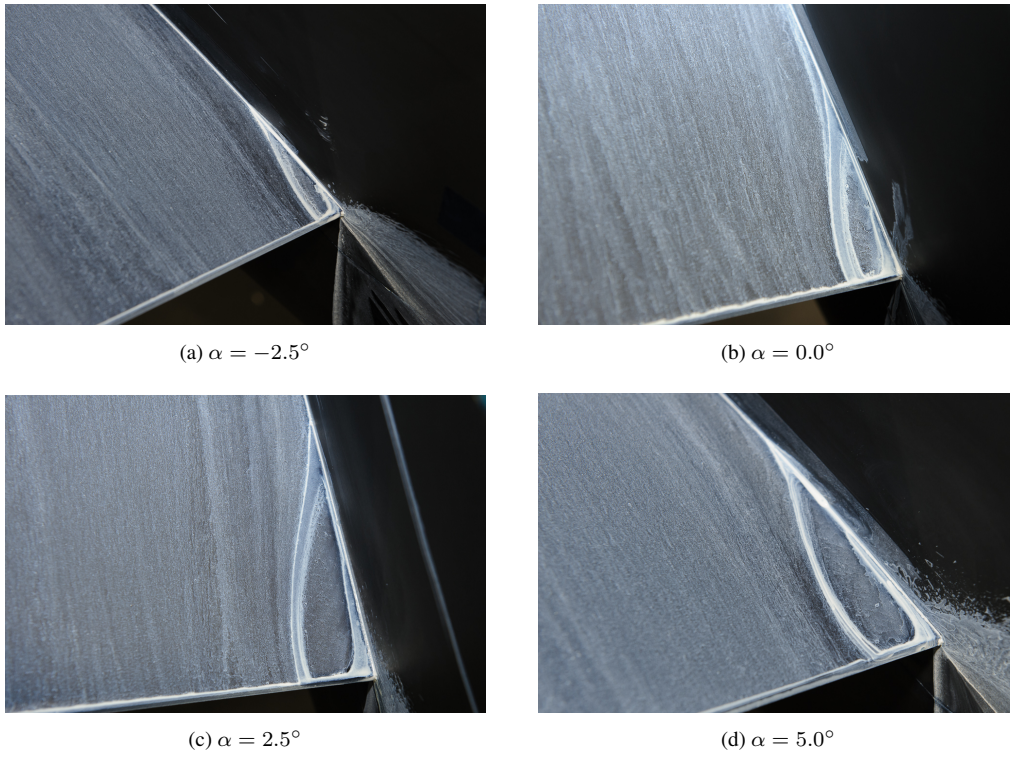
Figure 48: Oil-flow visualizations in the trailing-edge corner of the F6 wing (port side) versus model pitch angle.
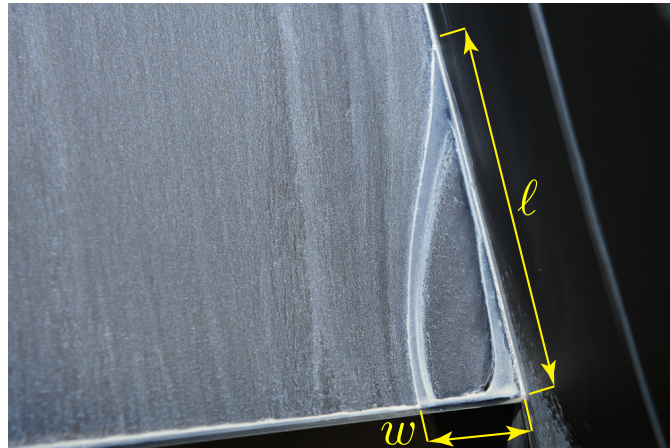
Figure 49: Definition of corner flow separation length, ℓ and width, w, from an example oil-flow visualization (F6 wing, $\alpha = 2.5°$, $Re_c = 2.4 \times 10^6$).

(a) $\alpha = -2.5°$

(b) $\alpha = 0.0°$

(c) $\alpha = 2.5°$

(d) $\alpha = 5.0°$

(e) $\alpha = 10.0°$
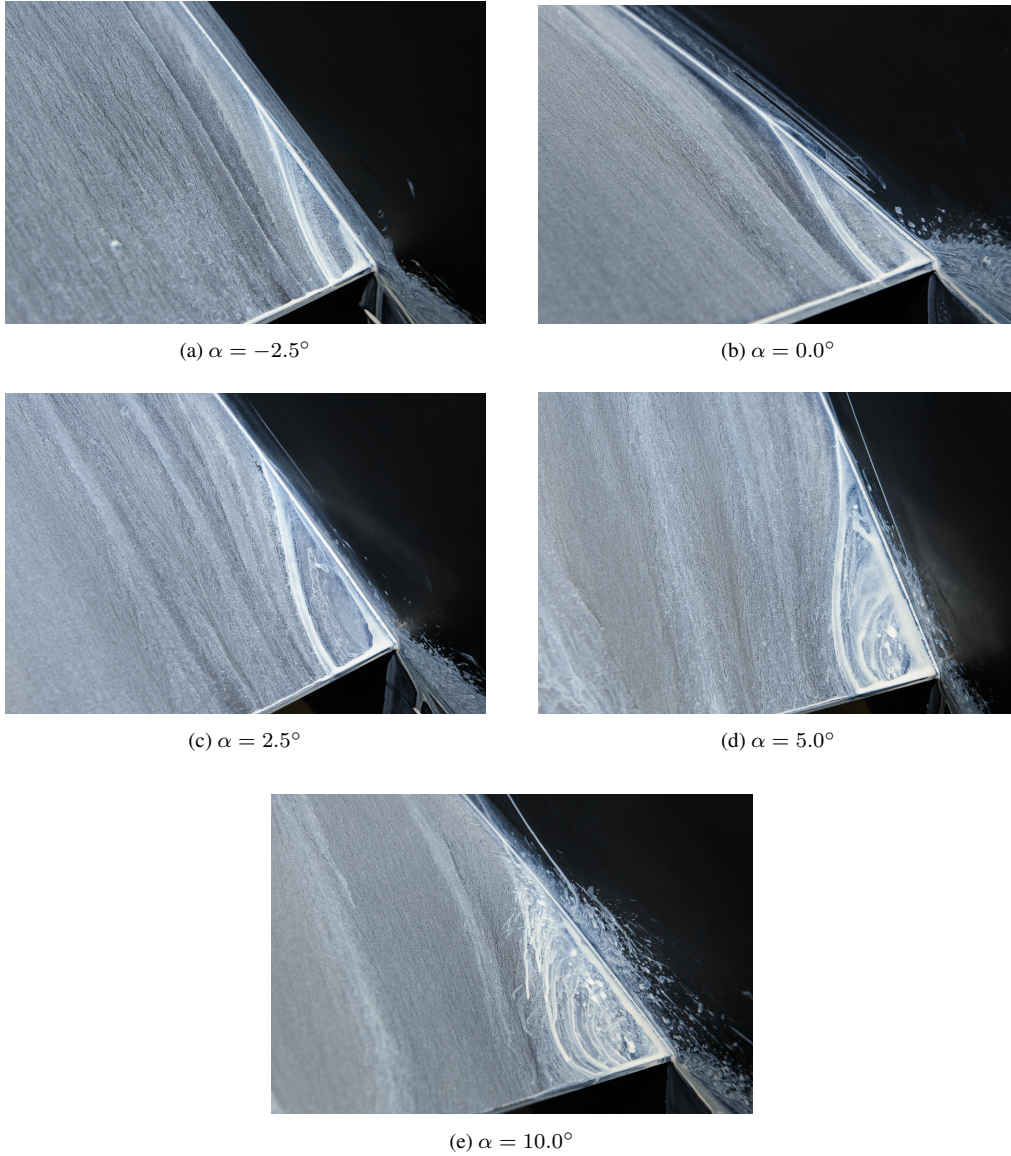
Figure 50: Oil-flow visualizations in the trailing-edge corner of the F6 wing with leading-edge extension (port side) versus model pitch angle.
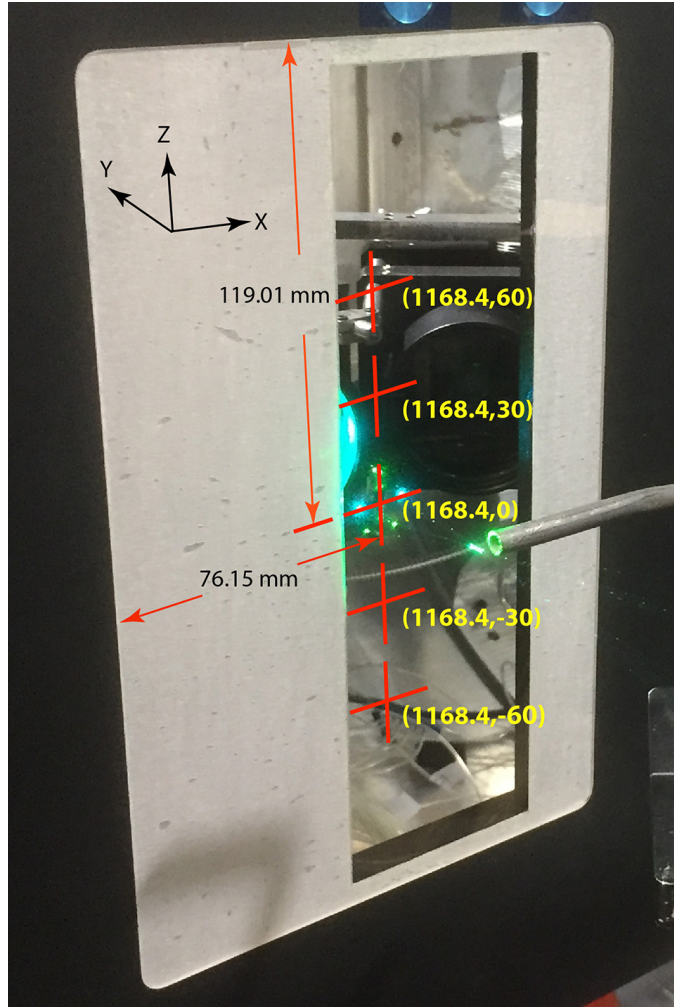
Figure 51: Schematic of the LDV measurement locations on the port side of the fuselage nose section. Dimensions are in millimeters. A small seeder jet is visible in the image.

(a) $z = 60$ mm

(b) $z = 60$ mm

(c) $z = 0$ mm

(d) $z = 0$ mm

(e) $z = -60$ mm

(f) $z = -60$ mm
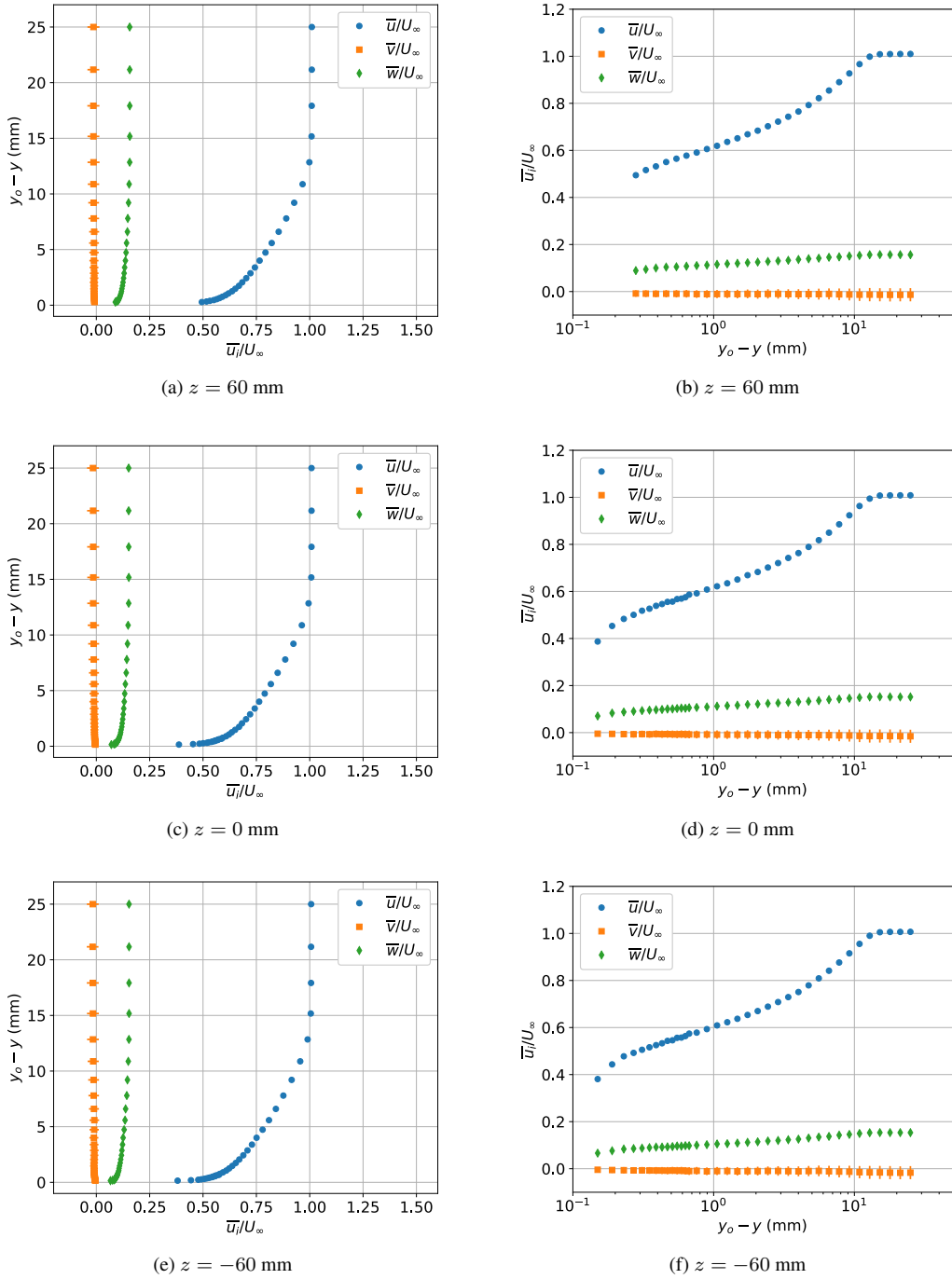
Figure 52: Mean velocity profiles (on both linear and semilogarithmic scales) on the fuselage nose section of the junction model at $x = 1168.4$ mm and $\alpha = 5°$. The model was configured with the F6 wing with leading-edge extension for these measurements.

105

(a) $z = 60$ mm

(b) $z = 60$ mm

(c) $z = 0$ mm

(d) $z = 0$ mm

(e) $z = -60$ mm

(f) $z = -60$ mm
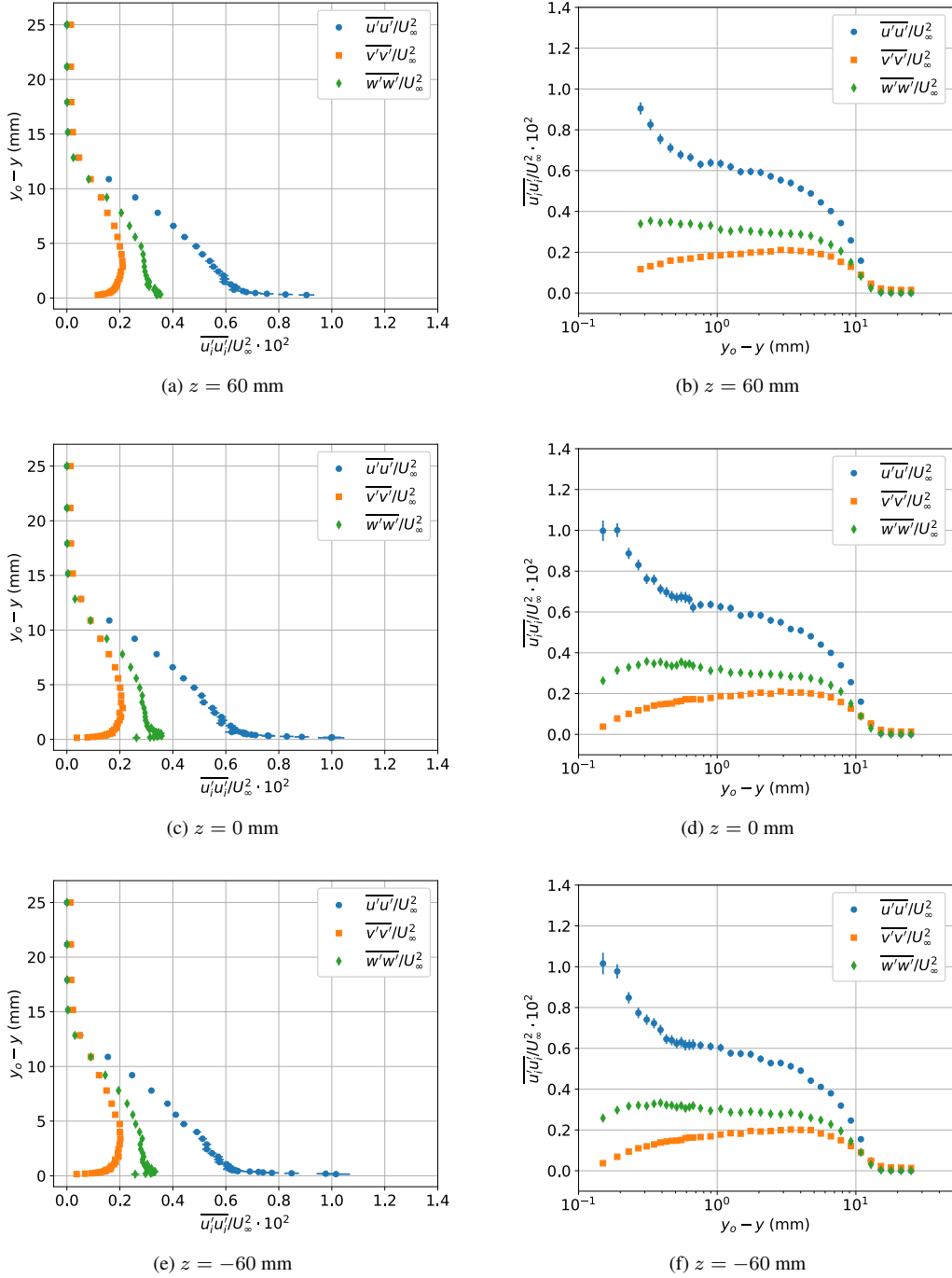
Figure 53: Reynolds normal stress profiles (on both linear and semilogarithmic scales) on the fuselage nose section of the junction model at $x = 1168.4$ mm and $\alpha = 5°$. The model was configured with the F6 wing with leading-edge extension for these measurements.

106

(a) $z = 60$ mm

(b) $z = 60$ mm

(c) $z = 0$ mm

(d) $z = 0$ mm

(e) $z = -60$ mm

(f) $z = -60$ mm
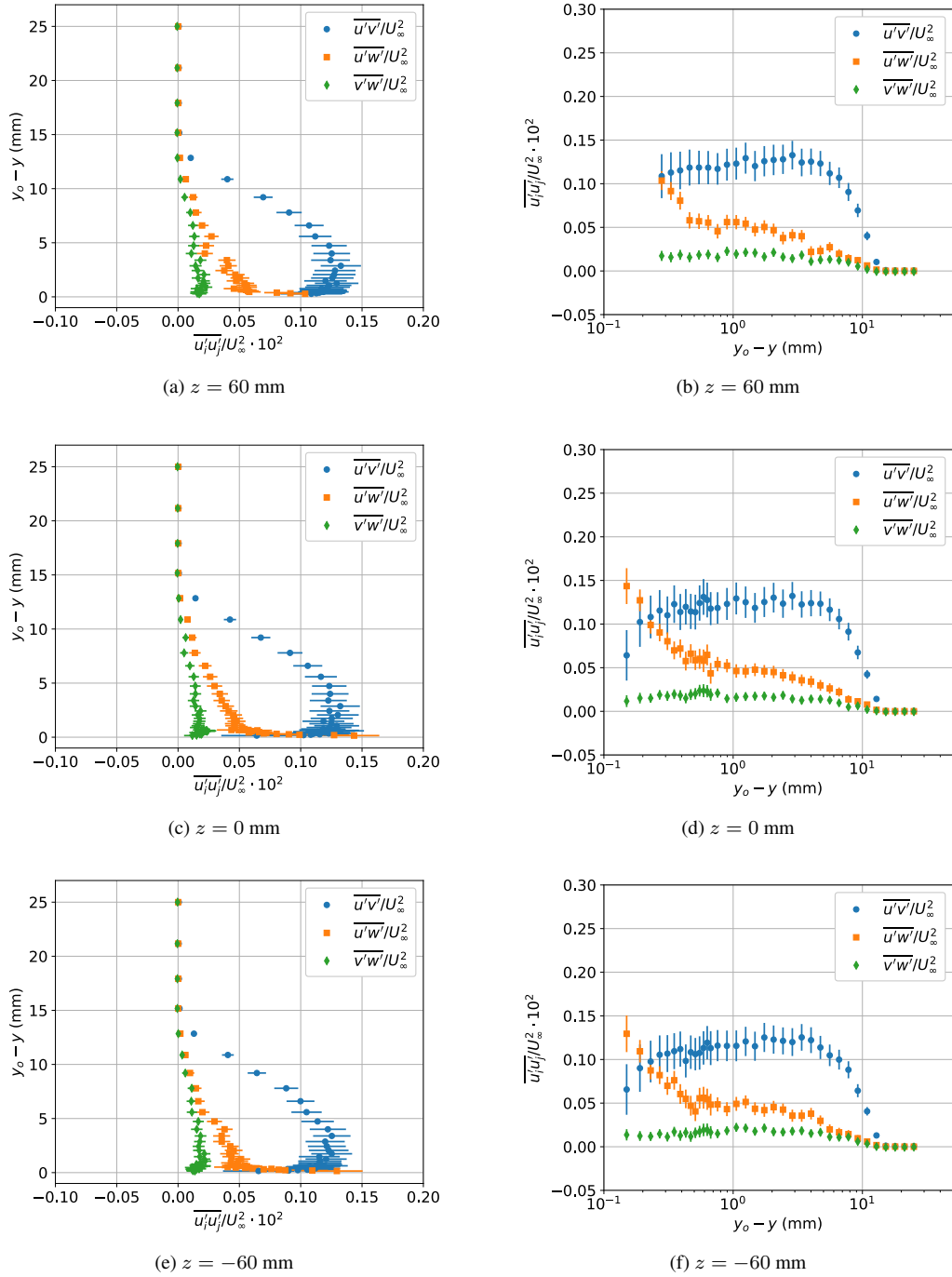
Figure 54: Reynolds shear stress profiles (on both linear and semilogarithmic scales) on the fuselage nose section of the junction model at $x = 1168.4$ mm and $\alpha = 5°$. The model was configured with the F6 wing with leading-edge extension for these measurements.

(a) $z = 60$ mm

(b) $z = 60$ mm

(c) $z = 0$ mm

(d) $z = 0$ mm

(e) $z = -60$ mm

(f) $z = -60$ mm
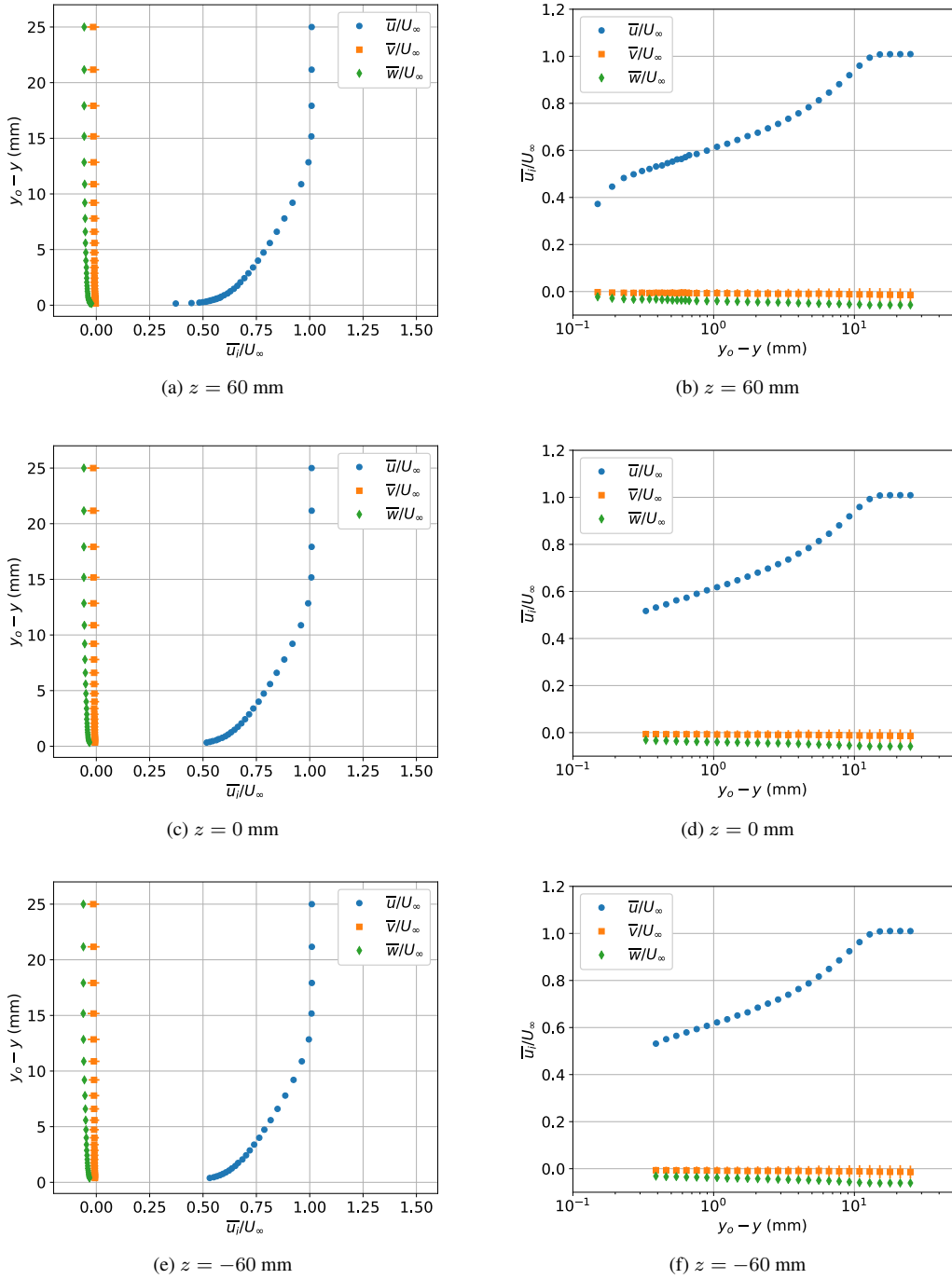
Figure 55: Mean velocity profiles (on both linear and semilogarithmic scales) on the fuselage nose section of the junction model at $x = 1168.4$ mm and $\alpha = -2.5°$. The model was configured with the F6 wing with leading-edge extension for these measurements.

108

(a) $z = 60$ mm

(b) $z = 60$ mm

(c) $z = 0$ mm

(d) $z = 0$ mm

(e) $z = -60$ mm

(f) $z = -60$ mm
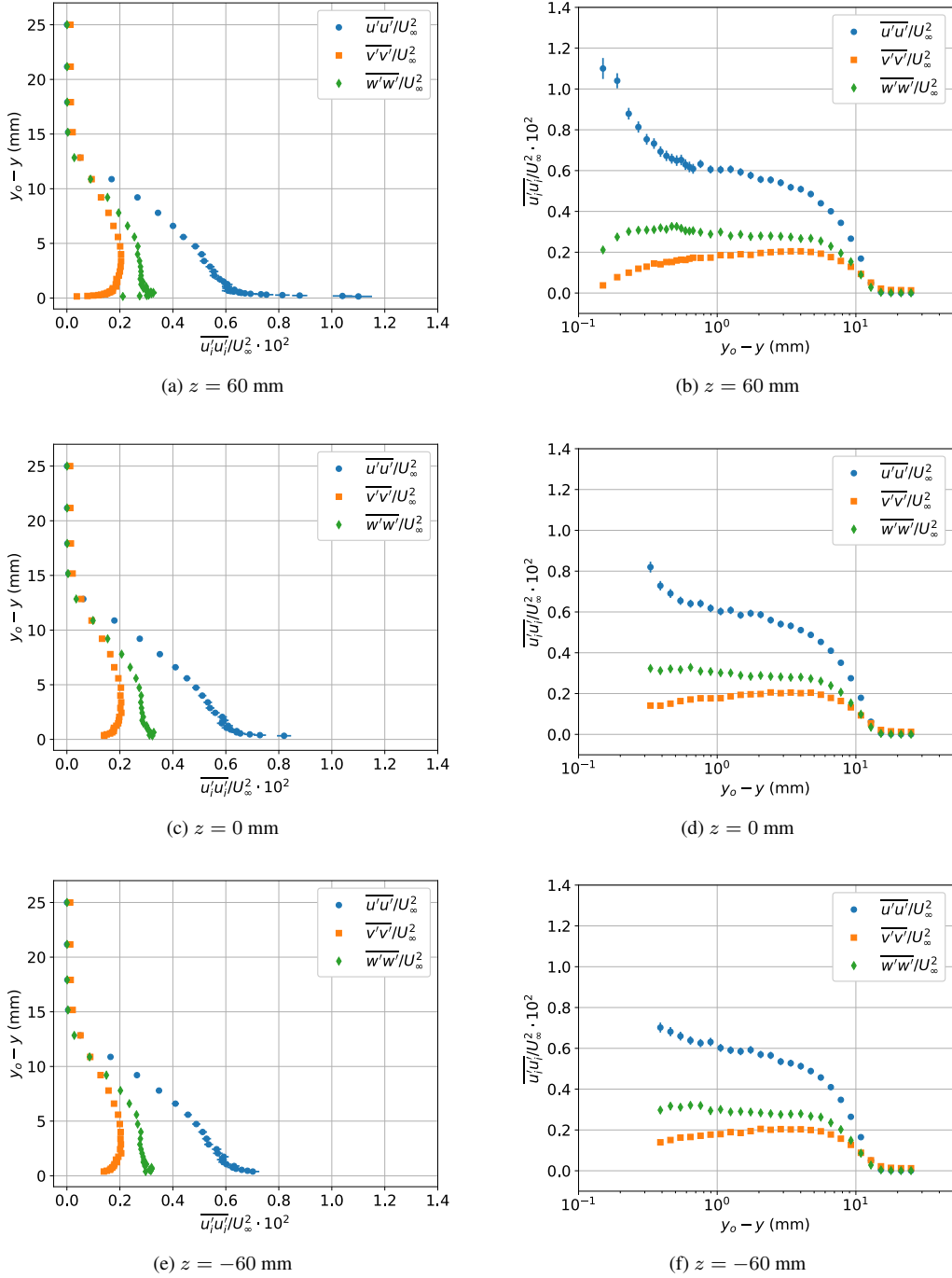
Figure 56: Reynolds normal stress profiles (on both linear and semilogarithmic scales) on the fuselage nose section of the junction model at $x = 1168.4$ mm and $\alpha = -2.5°$. The model was configured with the F6 wing with leading-edge extension for these measurements.
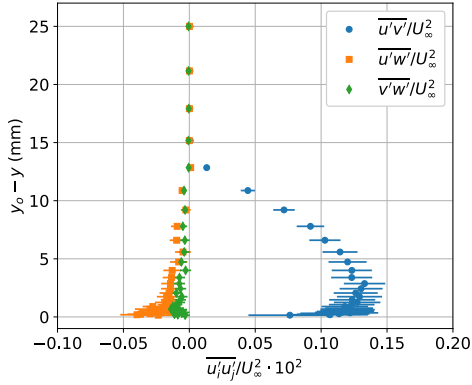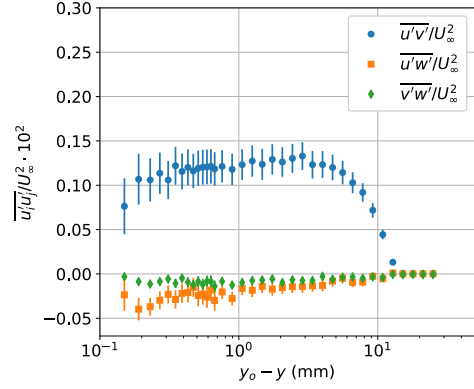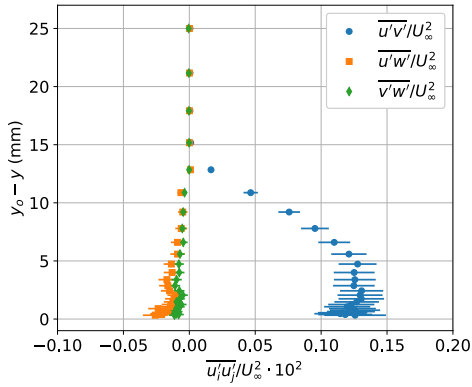
(a) $z = 60$ mm

(b) $z = 60$ mm

(c) $z = 0$ mm
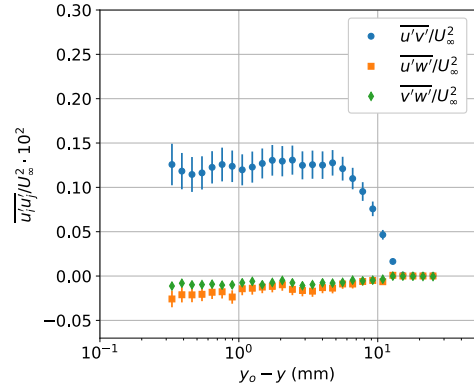
(d) $z = 0$ mm
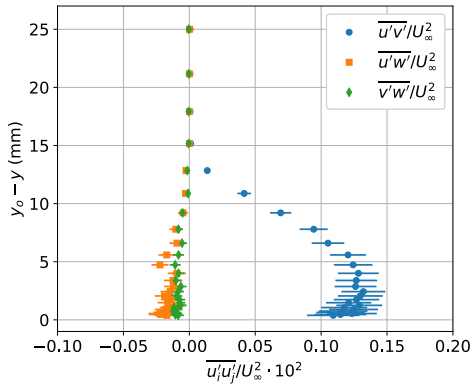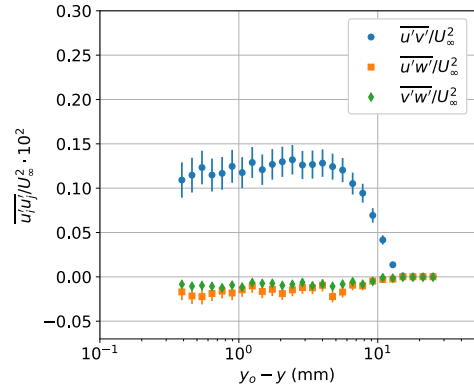
(e) $z = -60$ mm

(f) $z = -60$ mm

Figure 57: Reynolds shear stress profiles (on both linear and semilogarithmic scales) on the fuselage nose section of the junction model at $x = 1168.4$ mm and $\alpha = -2.5°$. The model was configured with the F6 wing with leading-edge extension for these measurements.
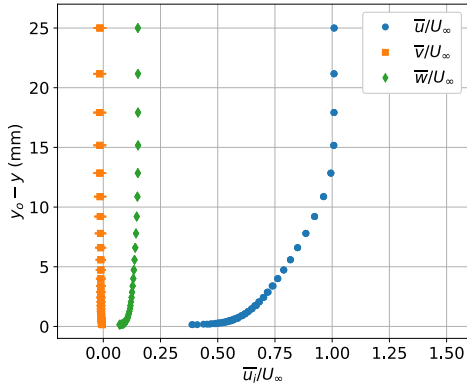
(a) Mean velocity.
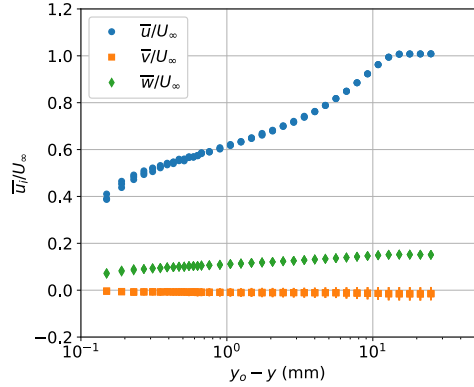
(b) Mean velocity
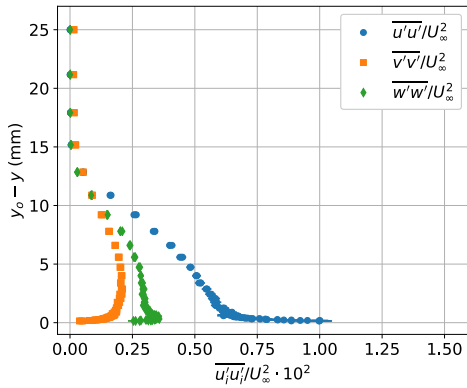
(c) Reynolds normal stress
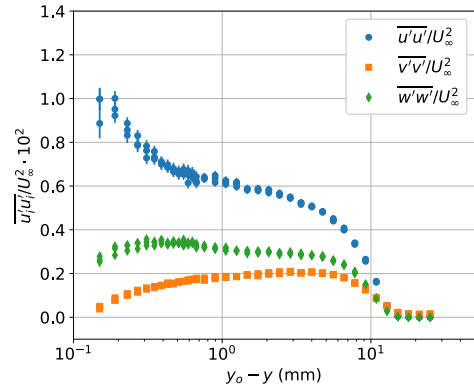
(d) Reynolds normal stress
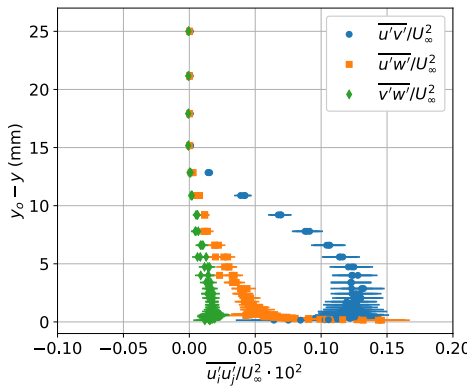
(e) Reynolds shear stress
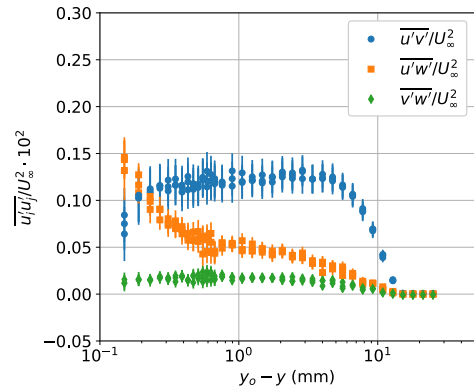
(f) Reynolds shear stress

Figure 58: Repeat measurements of the mean velocity and Reynolds-stress profiles (on both linear and semilogarithmic scales) on the fuselage nose section of the junction model at $x = 1168.4$ mm, $z = 0$ mm, and $\alpha = 5°$. The model was configured with the F6 wing with leading-edge extension for these measurements.

111
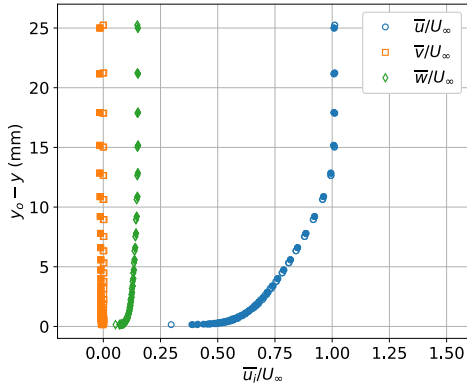
(a) Mean velocity.

(b) Mean velocity

(c) Reynolds normal stress
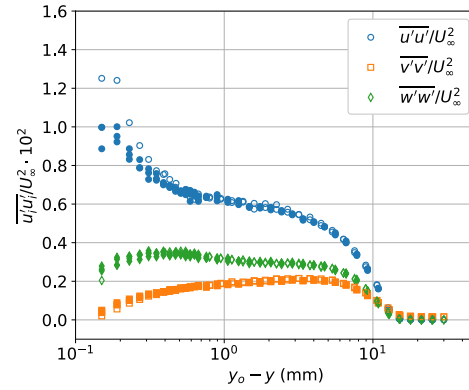
(d) Reynolds normal stress
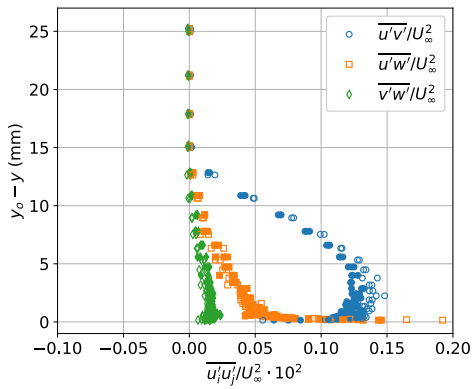
(e) Reynolds shear stress
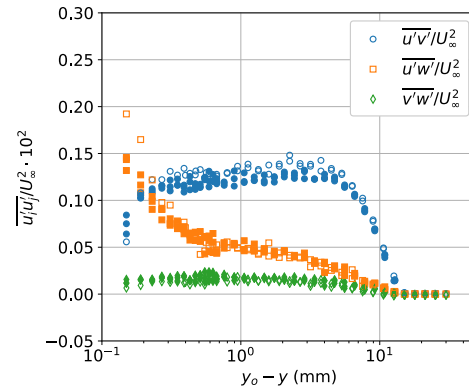
(f) Reynolds shear stress

Figure 59: Repeat measurements of the mean velocity and Reynolds-stress profiles (on both linear and semilogarithmic scales) on the fuselage nose section of the junction model at $x = 1168.4$ mm, $z = 0$ mm, and $\alpha = 5°$. Open symbols denote profiles for the model configured with F6 wing and closed symbols denote profiles for the model configured with F6 wing with leading-edge extension.
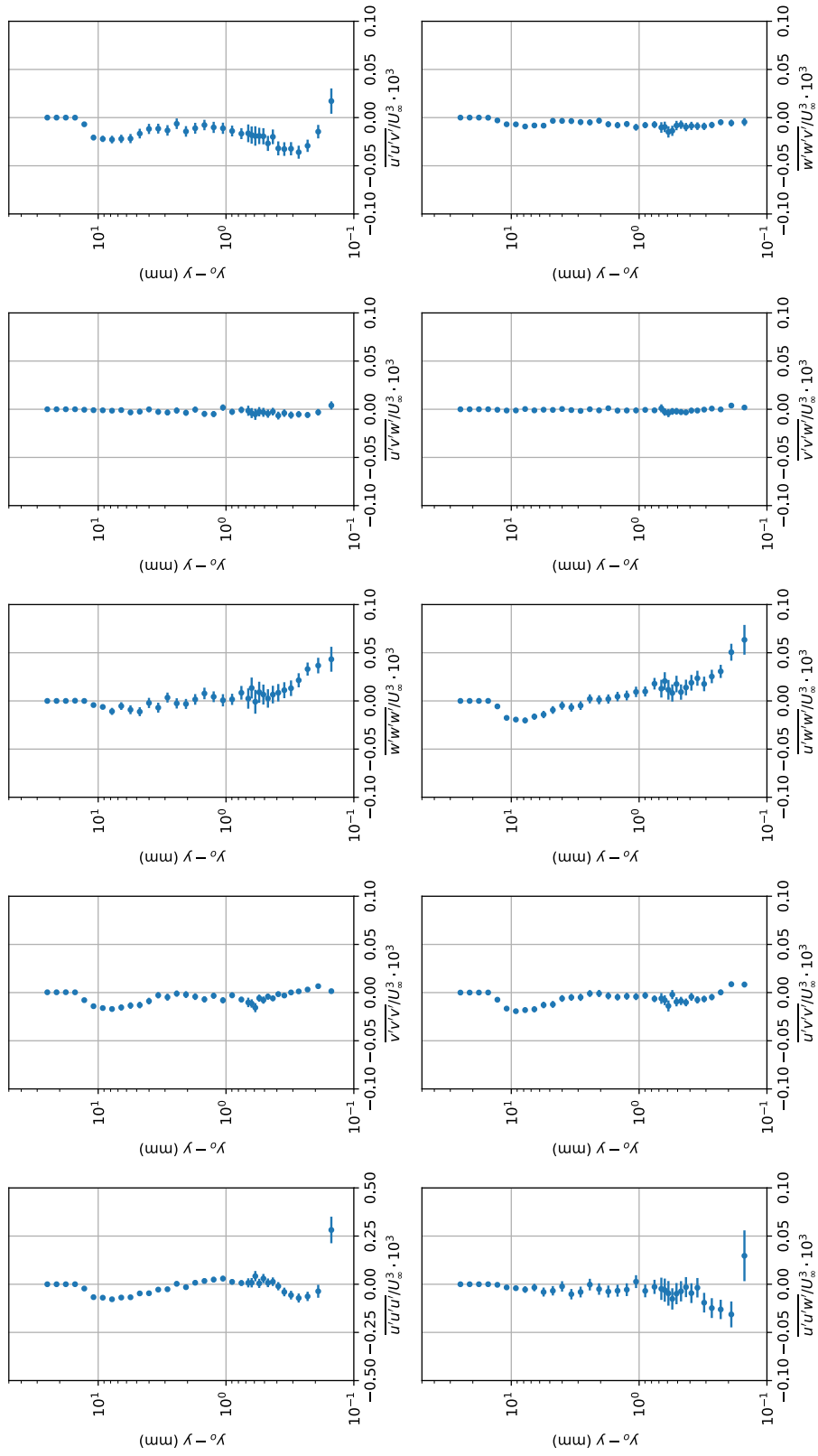
Figure 60: Triple products of the velocity components on the fuselage nose section of the junction model at $x = 1168.4$ mm, $z = 0$ mm, and $\alpha = 5°$. The model was configured with the F6 wing with leading-edge extension for these measurements
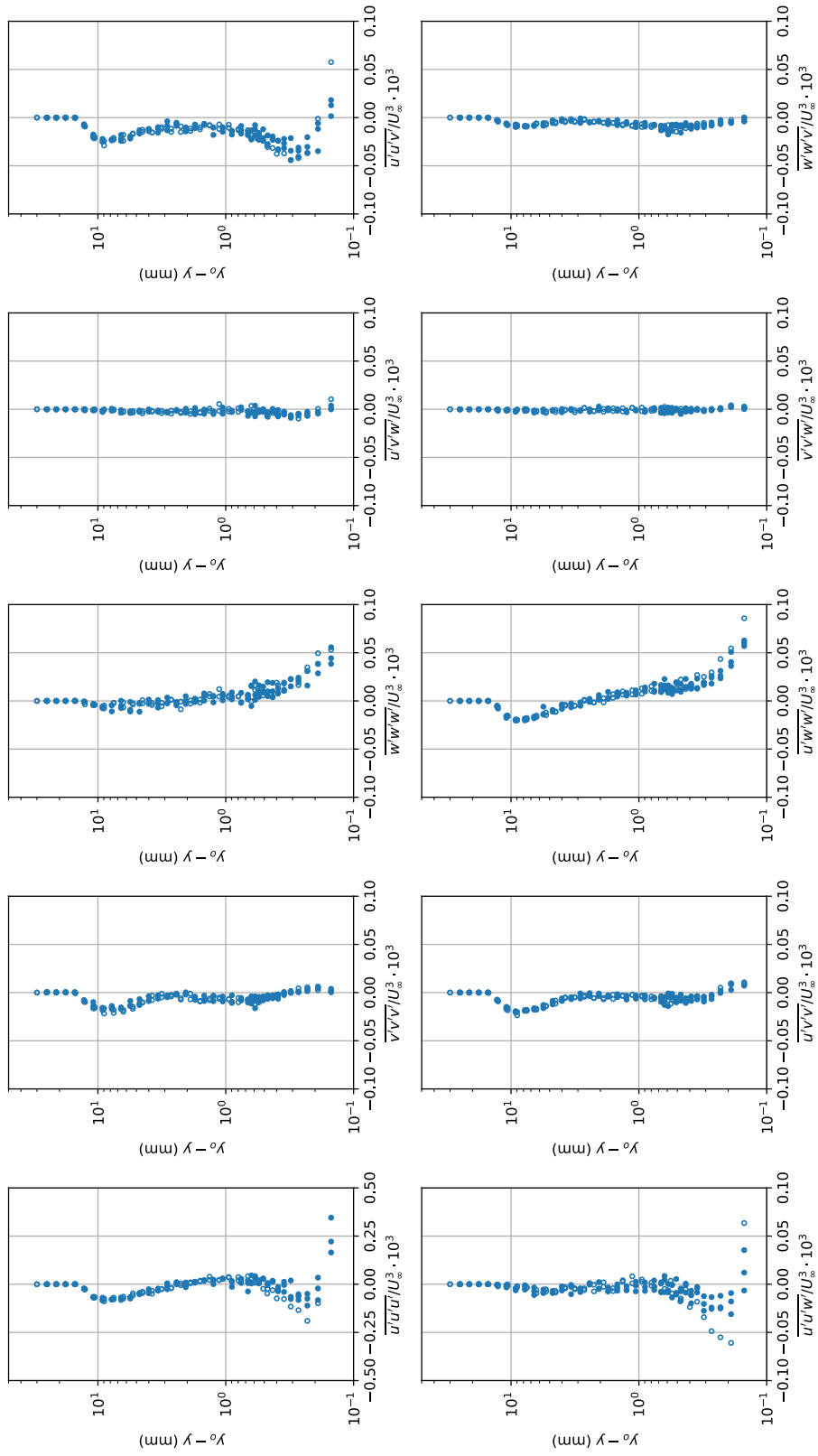
Figure 61: Triple products of the velocity components on the fuselage nose section of the junction model at $x = 1168.4$ mm, $z = 0$ mm, and $\alpha = 5°$. Open symbols denote profiles for the model configured with F6 wing and closed symbols denote profiles for the model configured with F6 wing with leading-edge extension.
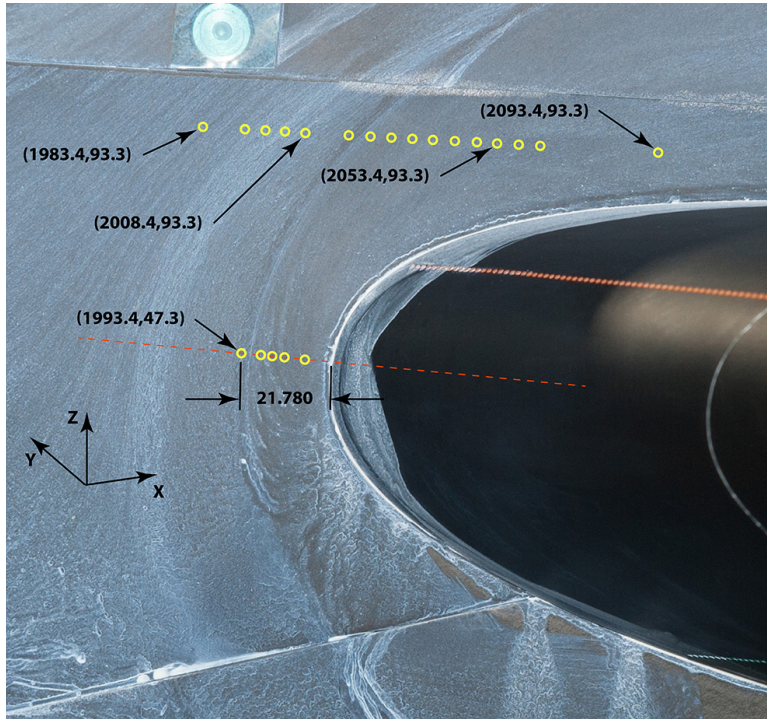
Figure 62: Schematic of the LDV measurement locations in the leading-edge region of the F6 wing at a model pitch angle of $5°$. The yellow circles denote locations where profile measurement were made and the red dashed line denotes the chord line of the wing root section. Dimensions are in millimeters.

(a) Top view, looking down on the wing/fuselage.

(b) End view, looking upstream.
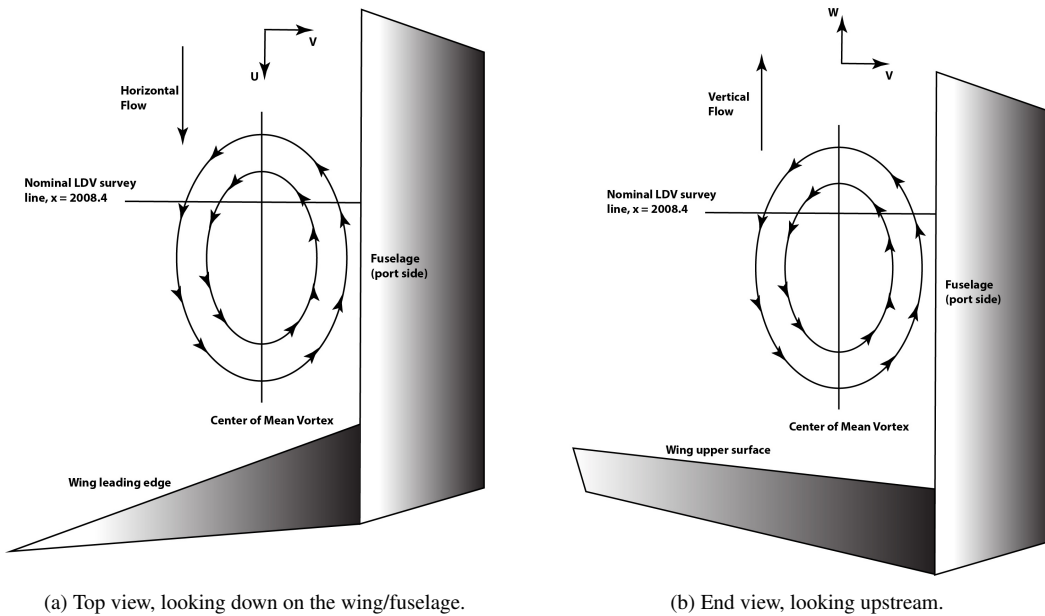
Figure 63: Schematic of hypothesized mean flow in the leading-edge region of the F6 wing. Dimensions are in millimeters.
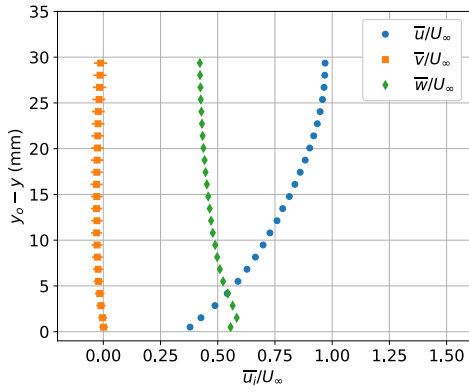
(a) $x = 1983.4$ mm, $z = 93.3$ mm
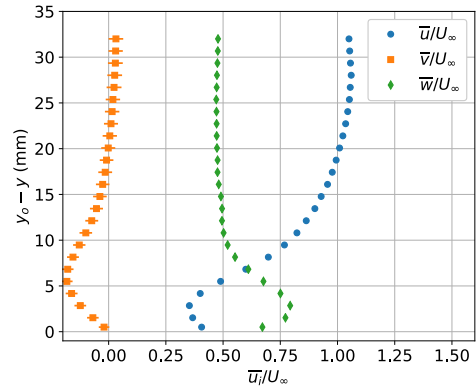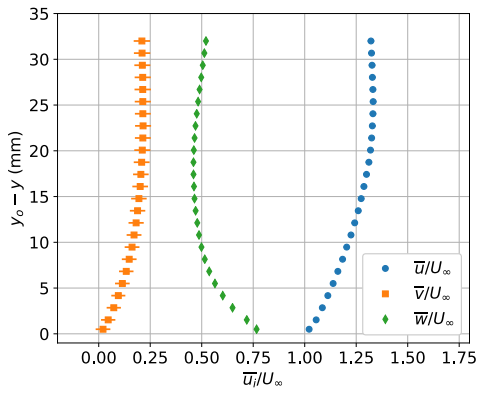
(b) $x = 2008.4$ mm, $z = 93.3$ mm
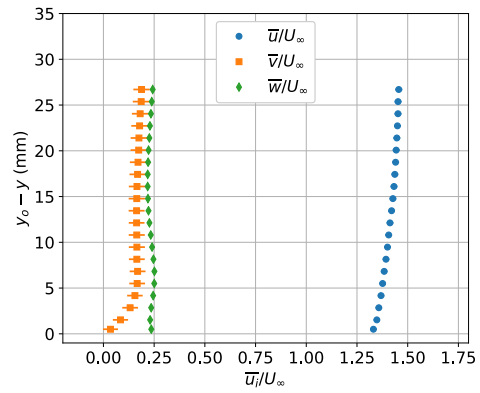
(c) $x = 2053.4$ mm, $z = 93.3$ mm
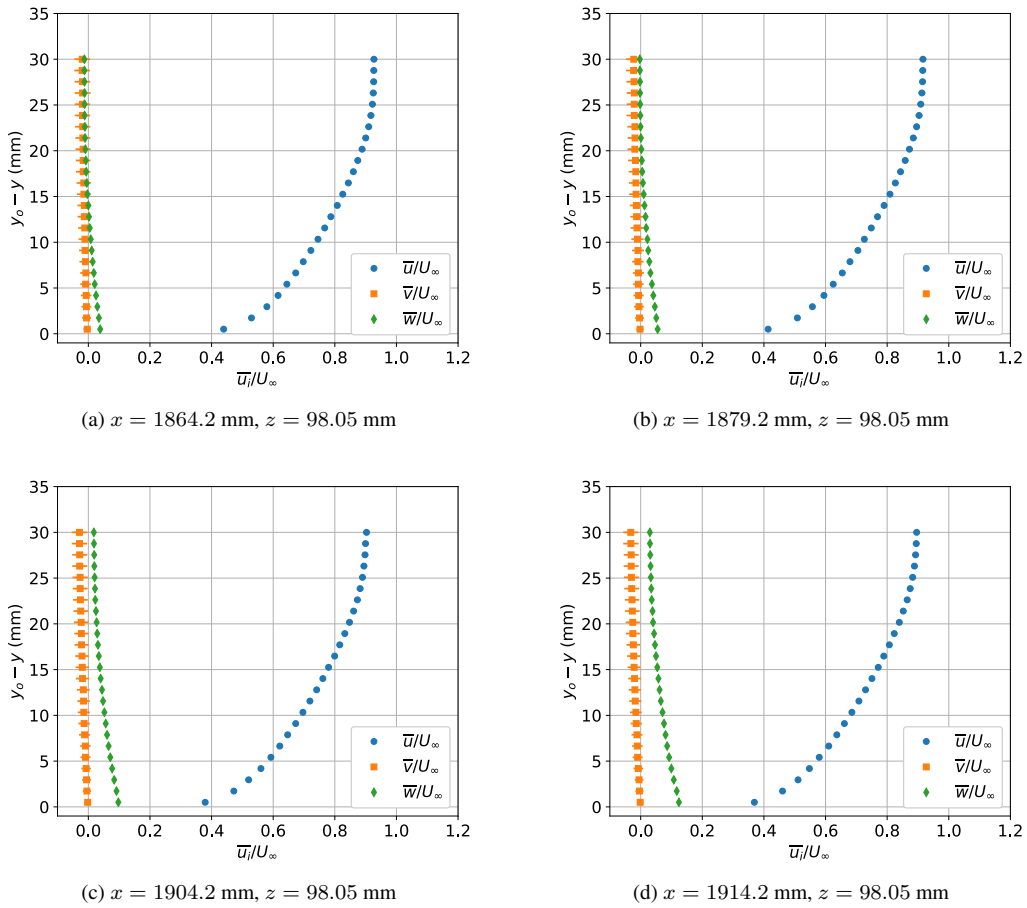
(d) $x = 2093.4$ mm, $z = 93.3$ mm

Figure 64: Mean velocity profiles on the port side of the fuselage near the wing leading edge. The model was configured with the F6 wing and set at a pitch angle of $5°$.
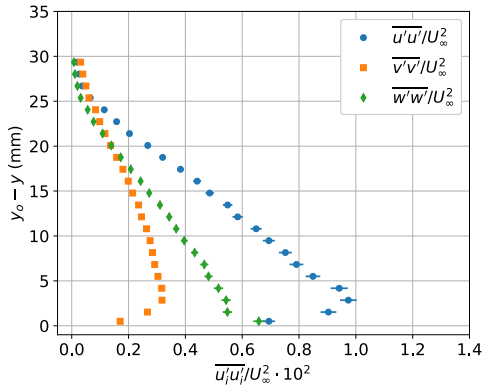
(a) $x = 1983.4$ mm, $z = 93.3$ mm
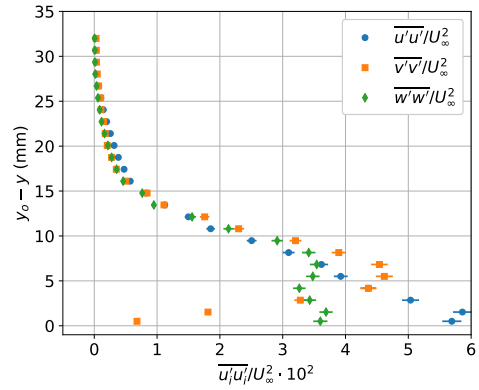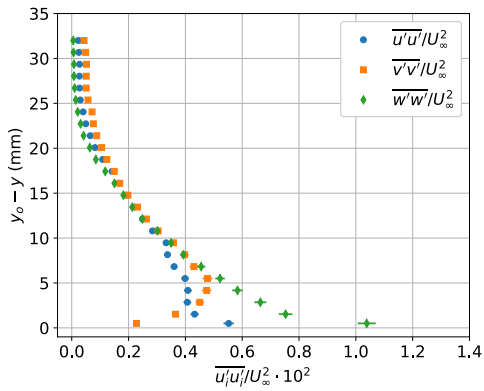
(b) $x = 2008.4$ mm, $z = 93.3$ mm
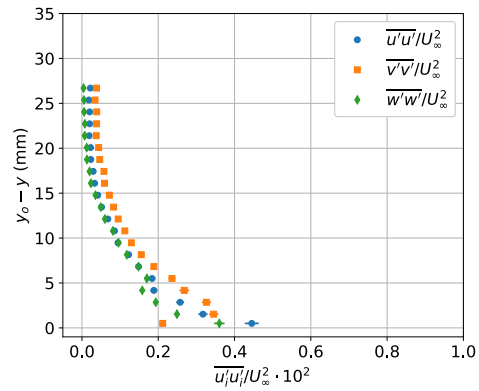
(c) $x = 2053.4$ mm, $z = 93.3$ mm

(d) $x = 2093.4$ mm, $z = 93.3$ mm

Figure 65: Reynolds normal stress profiles on the port side of the fuselage near the wing leading edge. The model was configured with the F6 wing and set at a pitch angle of $5°$.

117
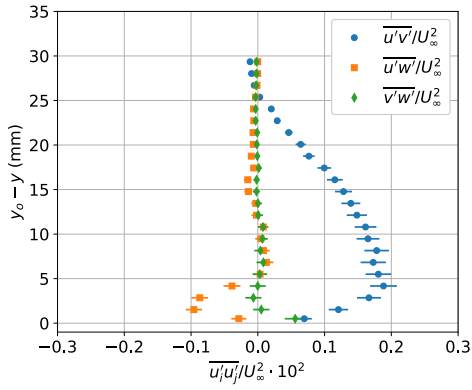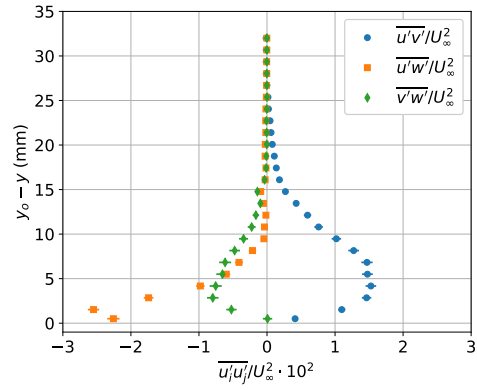
(a) $x = 1983.4$ mm, $z = 93.3$ mm

(b) $x = 2008.4$ mm, $z = 93.3$ mm
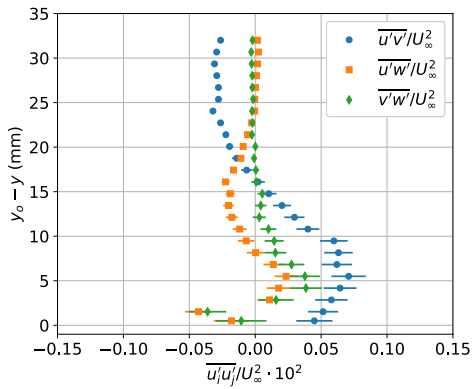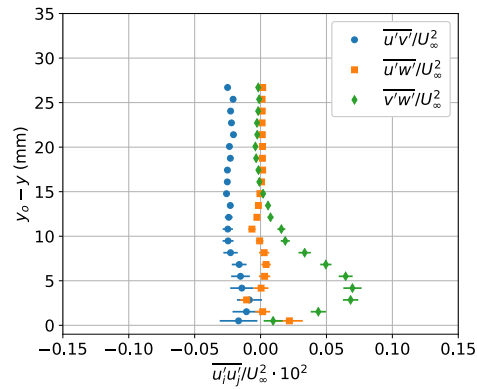
(c) $x = 2053.4$ mm, $z = 93.3$ mm

(d) $x = 2093.4$ mm, $z = 93.3$ mm

Figure 66: Reynolds shear stress profiles on the port side of the fuselage near the wing leading edge. The model was configured with the F6 wing and set at a pitch angle of $5°$.
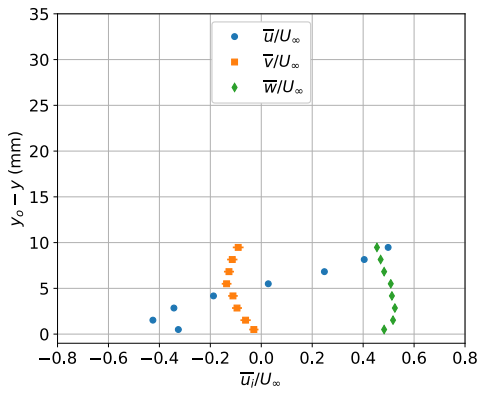
(a) $x = 1993.4$ mm, $z = 47.3$ mm
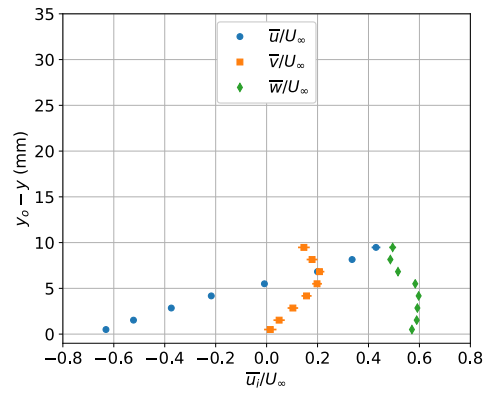
(b) $x = 1998.5$ mm, $z = 46.8$ mm
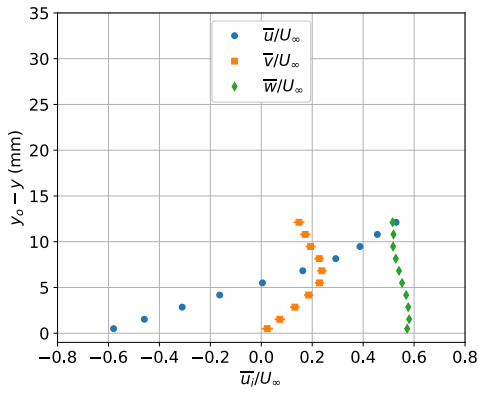
(c) $x = 2001.3$ mm, $z = 46.6$ mm
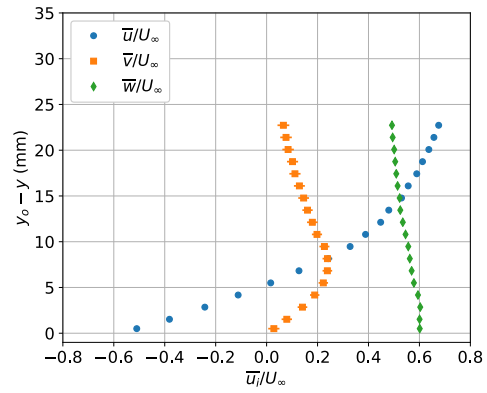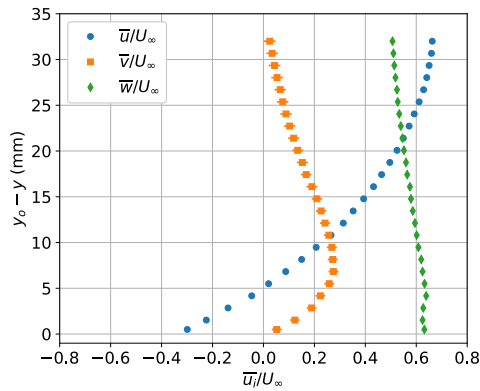
(d) $x = 2004.1$ mm, $z = 46.3$ mm

(e) $x = 2009.1$ mm, $z = 45.8$ mm
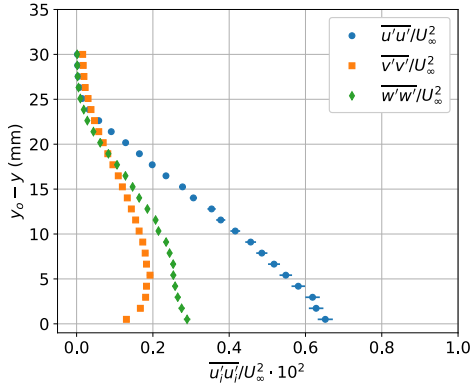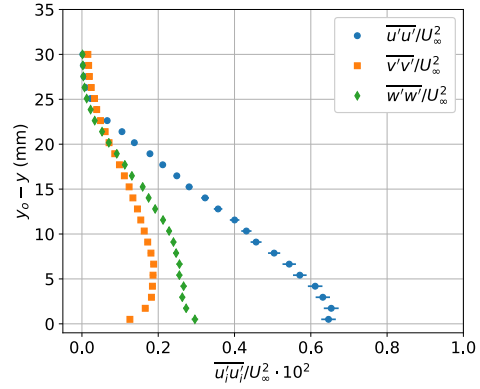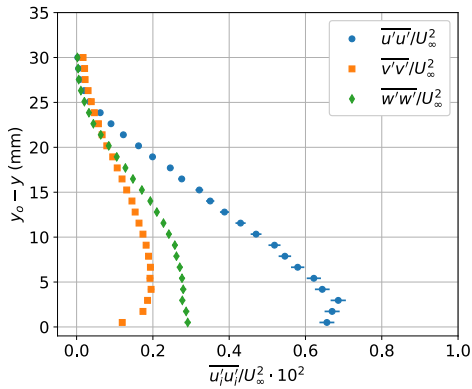
Figure 67: Mean velocity profiles on the port side of the fuselage near the wing leading edge. The model was configured with the F6 wing and set at a pitch angle of $5°$.
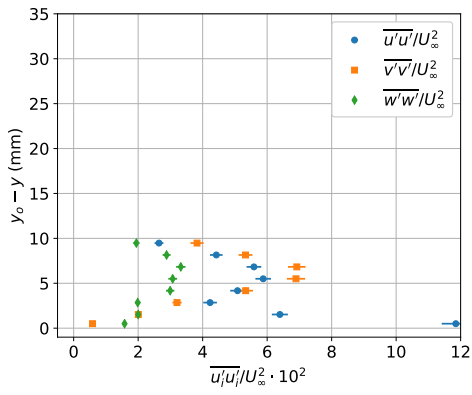
(a) $x = 1993.4$ mm, $z = 47.3$ mm
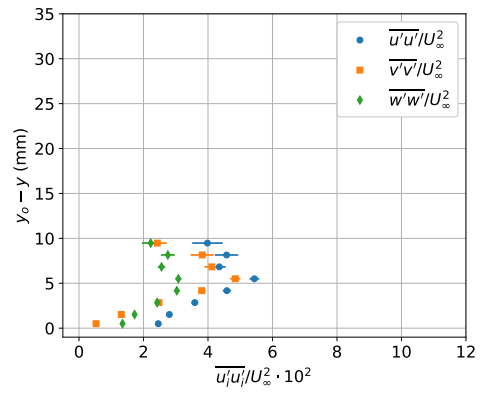
(b) $x = 1998.5$ mm, $z = 46.8$ mm
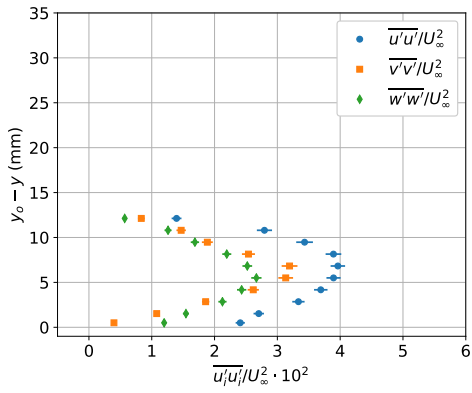
(c) $x = 2001.3$ mm, $z = 46.6$ mm
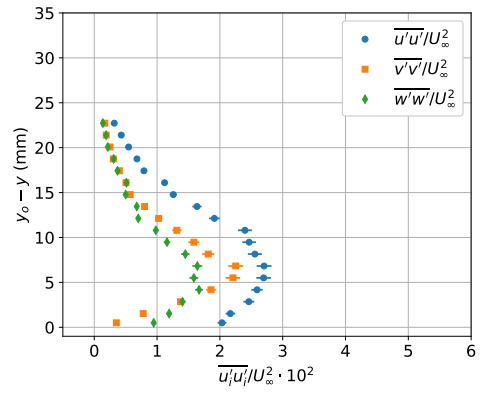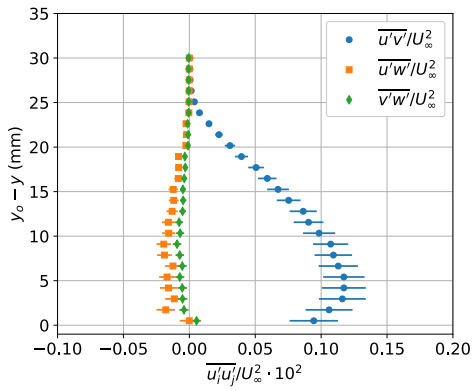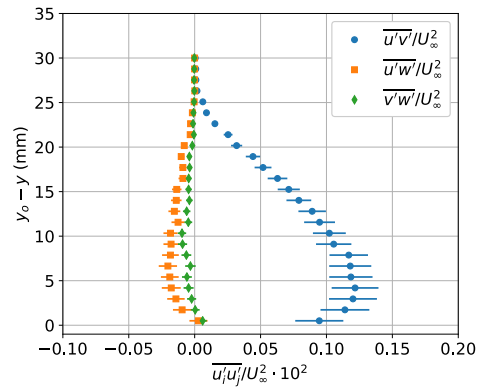
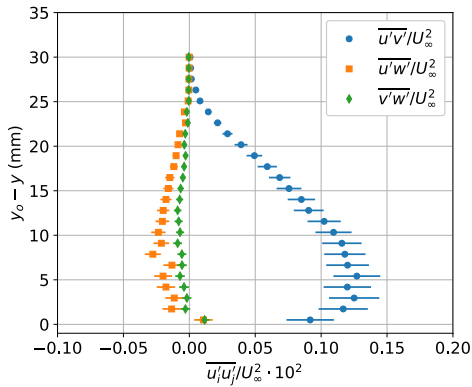(d) $x = 2004.1$ mm, $z = 46.3$ mm
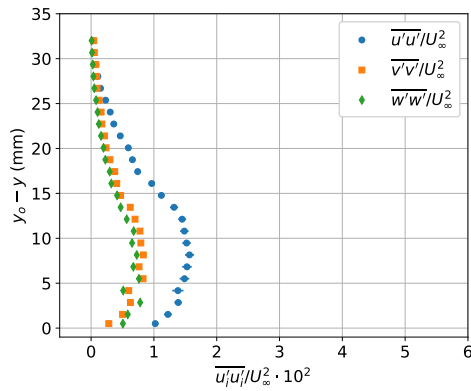
(e) $x = 2009.1$ mm, $z = 45.8$ mm

Figure 68: Reynolds normal stress profiles on the port side of the fuselage near the wing leading edge. The model was configured with the F6 wing and set at a pitch angle of $5°$.
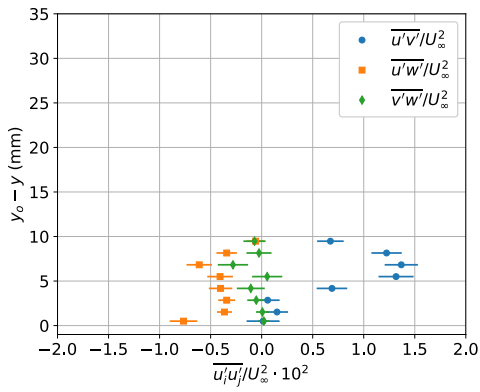
(a) $x = 1993.4$ mm, $z = 47.3$ mm
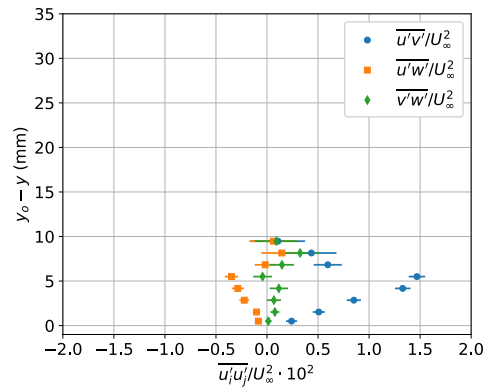
(b) $x = 1998.5$ mm, $z = 46.8$ mm
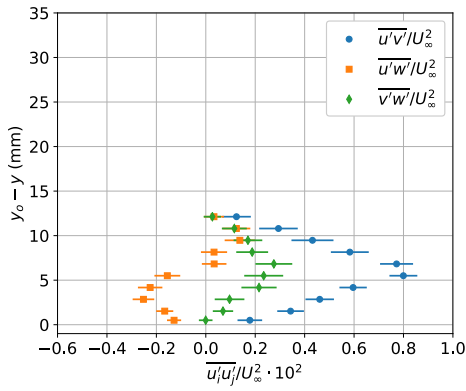
(c) $x = 2001.3$ mm, $z = 46.6$ mm
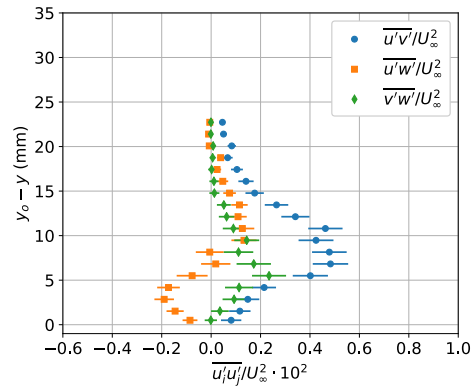
(d) $x = 2004.1$ mm, $z = 46.3$ mm
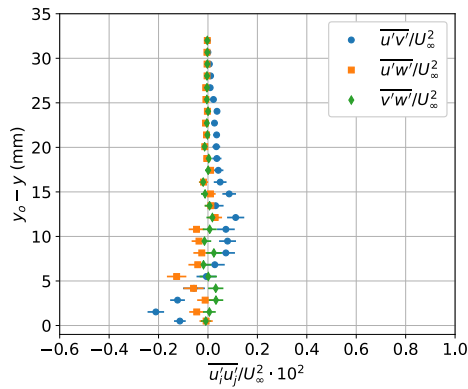
(e) $x = 2009.1$ mm, $z = 45.8$ mm

Figure 69: Reynolds shear stress profiles on the port side of the fuselage near the wing leading edge. The model was configured with the F6 wing and set at a pitch angle of $5°$.
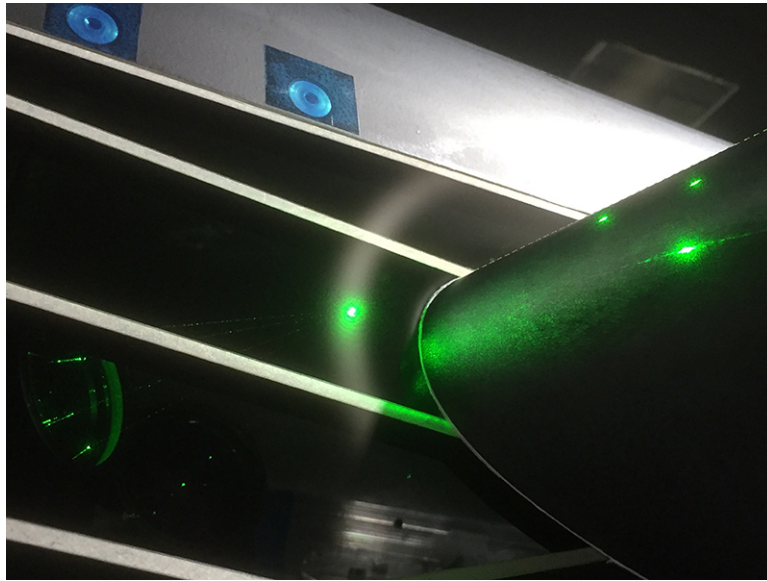
Figure 70: Photograph of seeding material accumulation on the fuselage window.
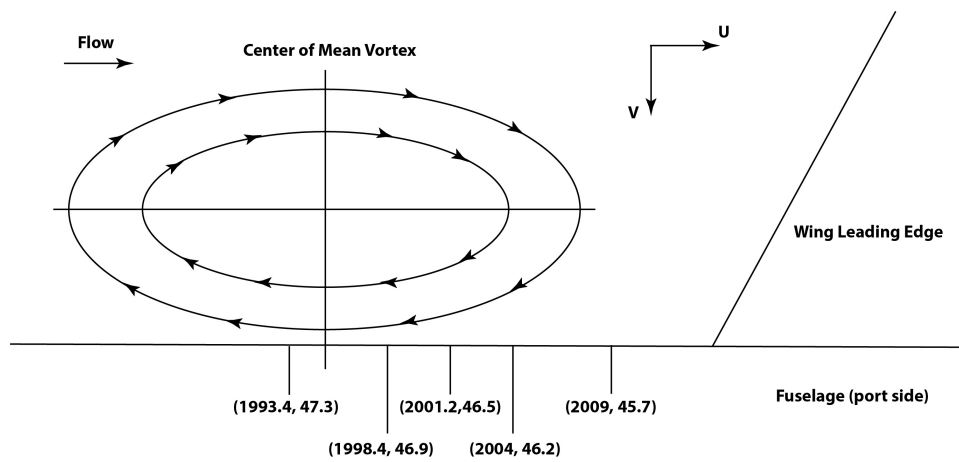
Figure 71: Schematic of hypothesized mean flow in the leading-edge region of the F6 wing. Bottom view, looking up from beneath the model. Dimensions are in millimeters.
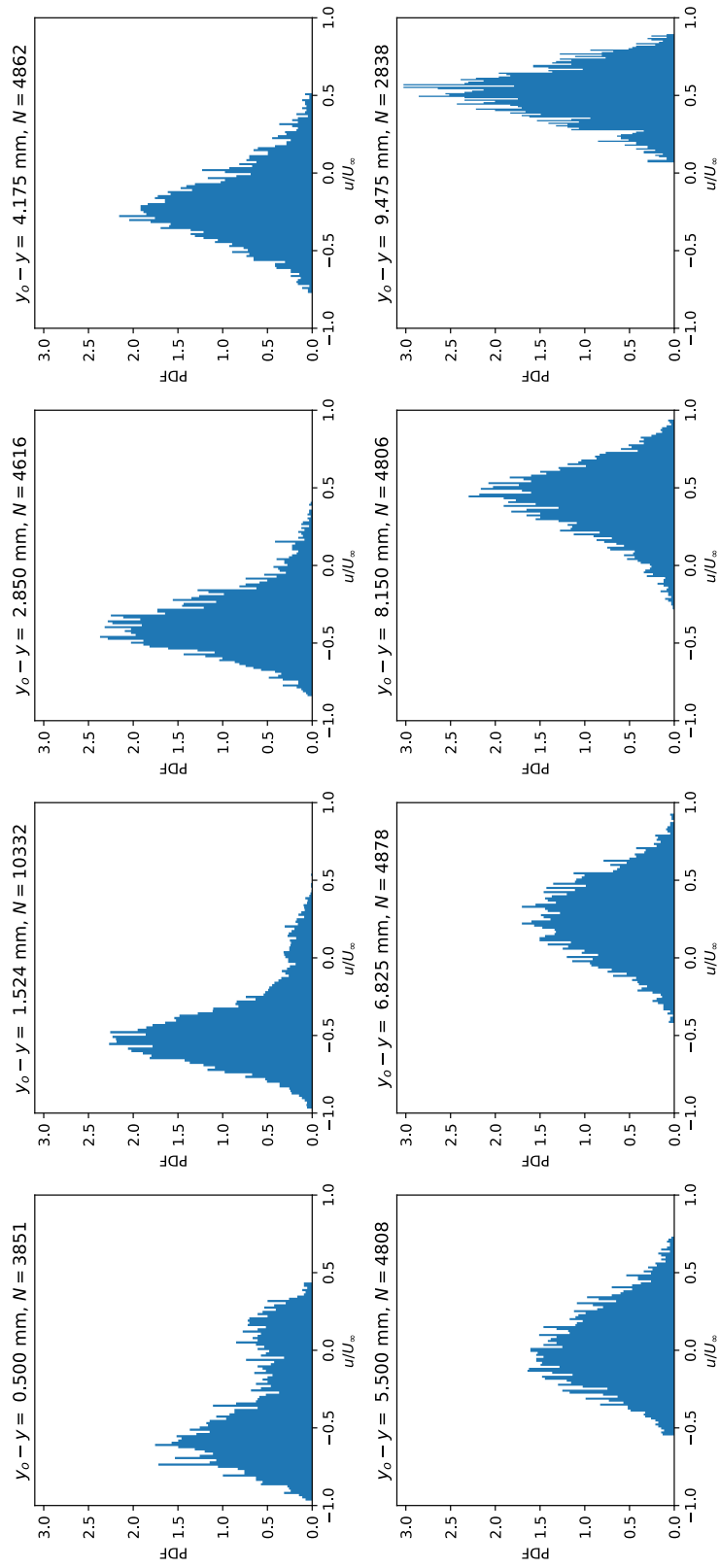
Figure 72: Probability density functions of the x-component of velocity for several y-locations on the port side of the fuselage. The measurements were made at $x = 1993.4$ mm, $z = 47.3$ mm. The model was configured with the F6 wing and set at a pitch angle of $5°$.
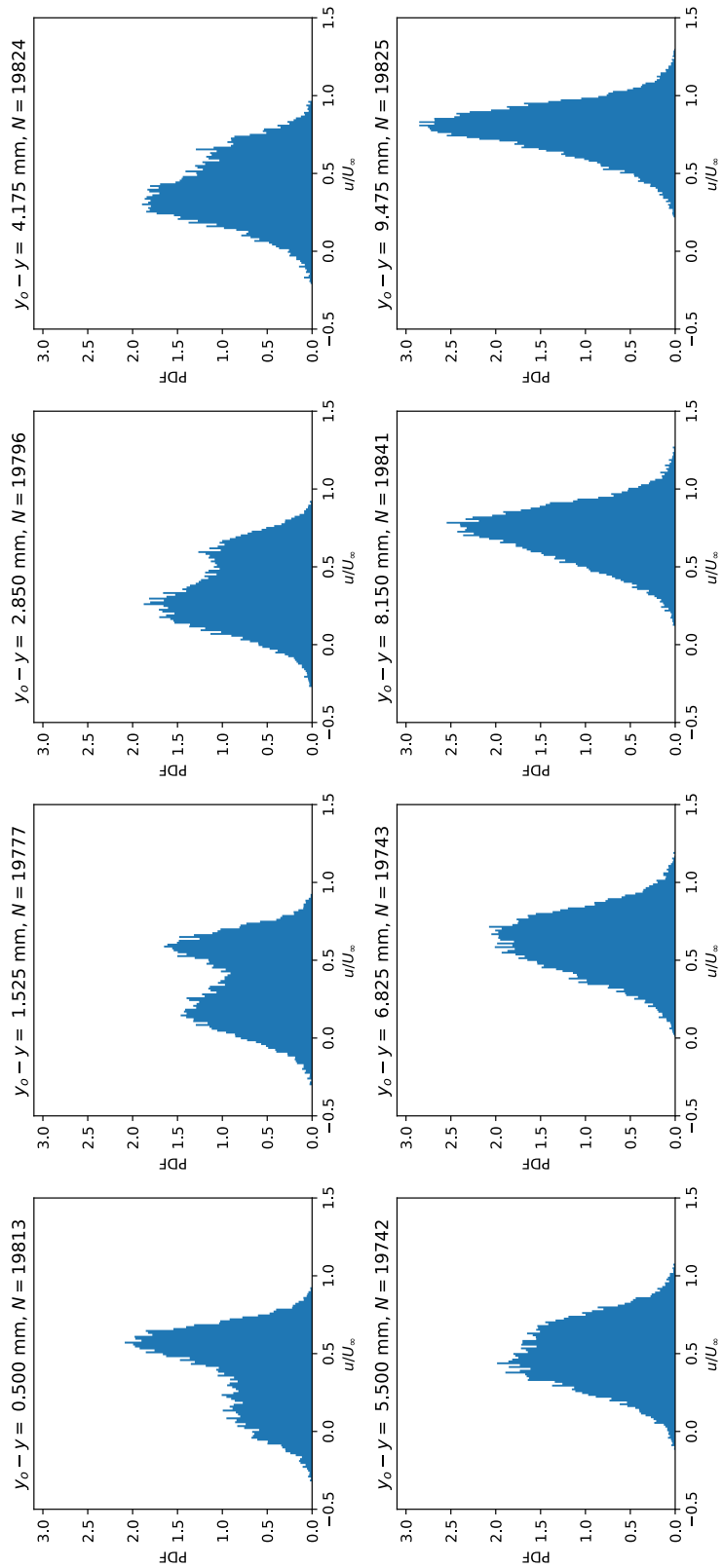
Figure 73: Probability density functions of the x-component of velocity for several y-locations on the port side of the fuselage. The measurements were made at $x = 2008.4$ mm, $z = 93.3$ mm. The model was configured with the F6 wing and set at a pitch angle of $5°$.
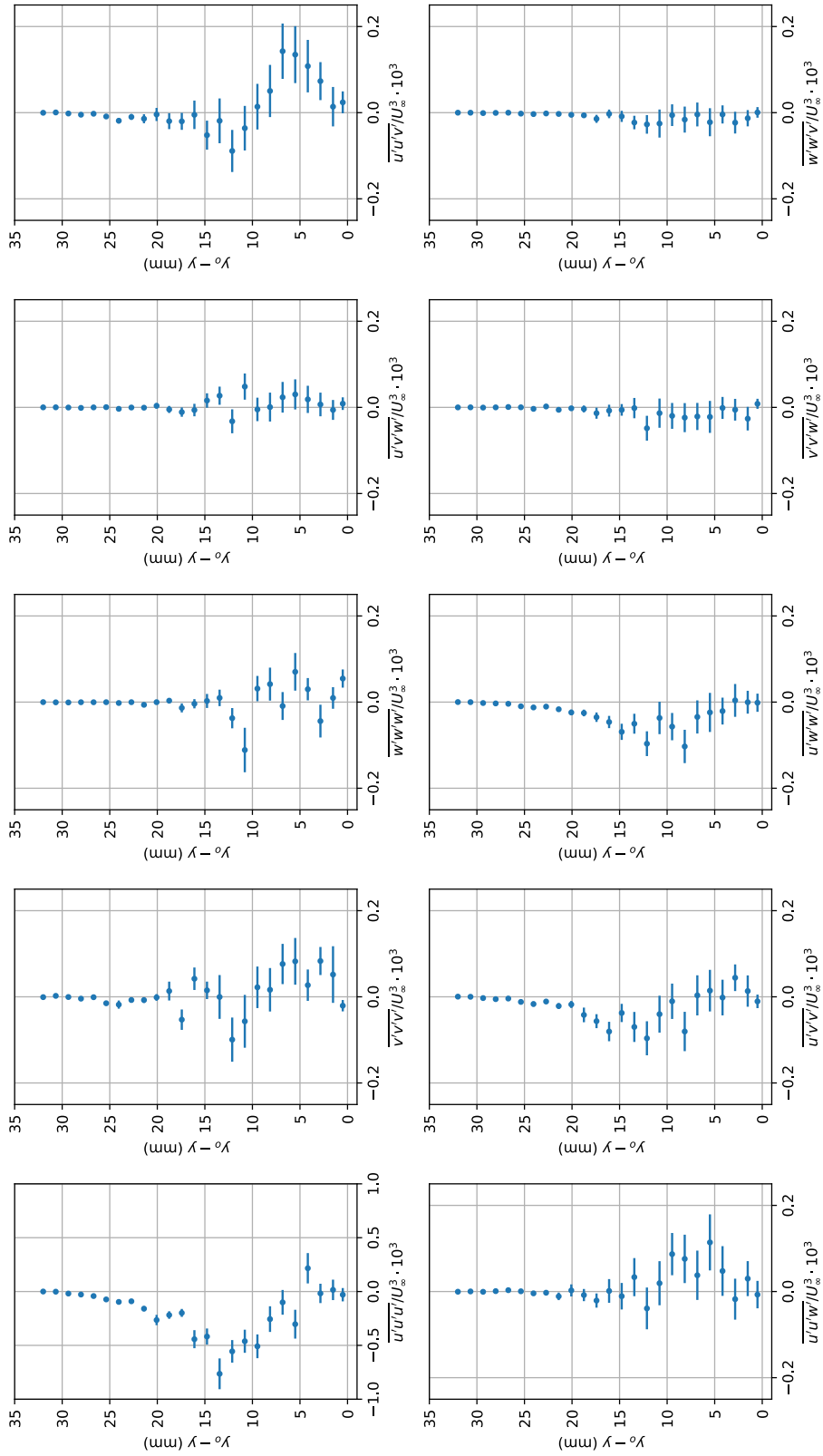
Figure 74: Triple products of the velocity components on the port side of the fuselage at $x = 2009.1$ mm, $z = 45.8$ mm. The model was configured with the F6 wing and set at a pitch angle of $5°$.
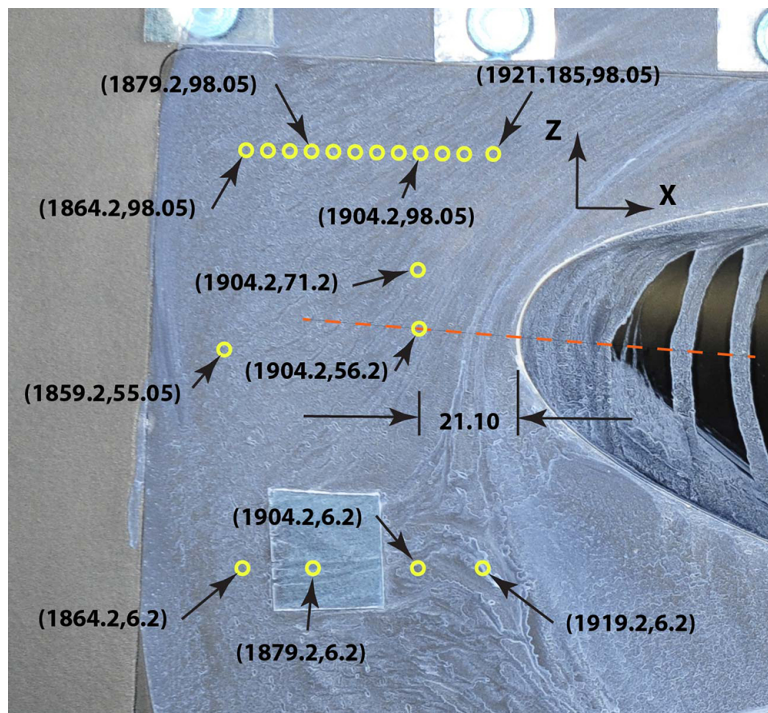
Figure 75: Schematic of the LDV measurement locations in the leading-edge region of the F6 wing with leading-edge extension at a model pitch angle of $5°$. The yellow circles denote locations where profile measurement were made and the red dashed line denotes the chord line of the wing root section. Dimensions are in millimeters.
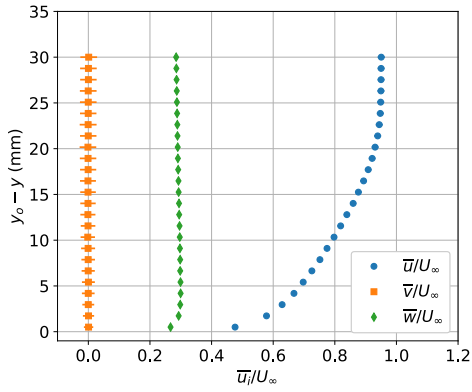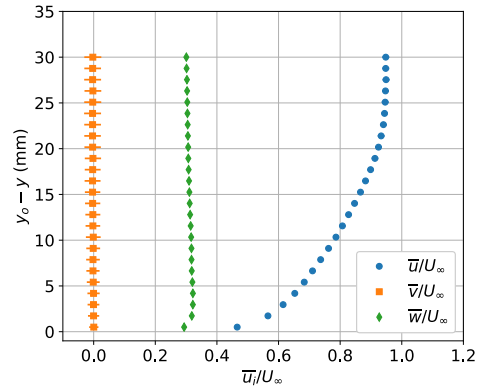
(a) $x = 1864.2$ mm, $z = 98.05$ mm

(b) $x = 1879.2$ mm, $z = 98.05$ mm
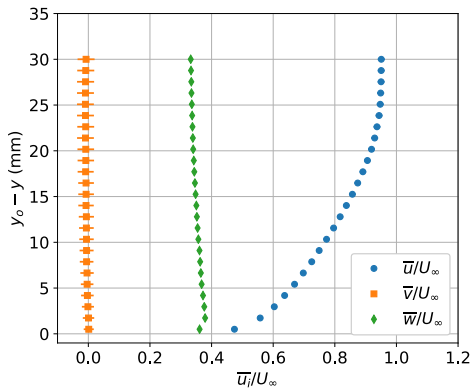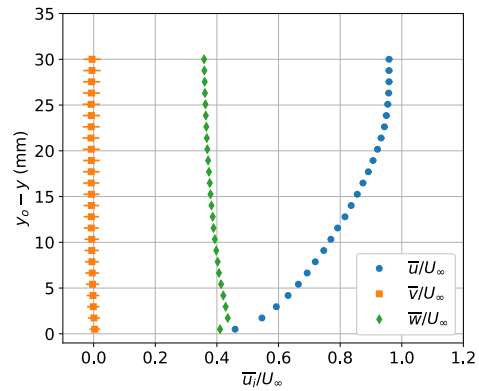
(c) $x = 1904.2$ mm, $z = 98.05$ mm

(d) $x = 1921.2$ mm, $z = 98.05$ mm

Figure 76: Mean velocity profiles on the port side of the fuselage near the wing leading edge. The model was configured with the F6 wing with leading-edge extension and set at a pitch angle of $5°$.
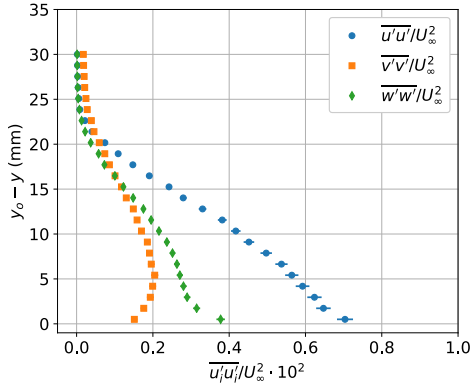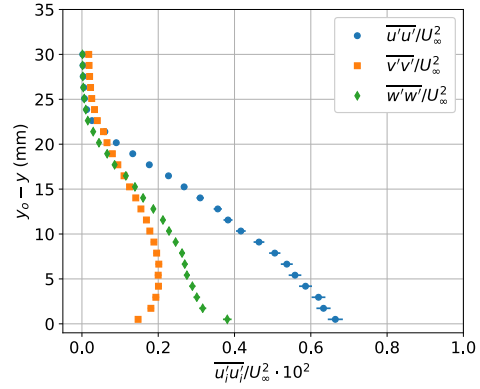
(a) $x = 1864.2$ mm, $z = 98.05$ mm
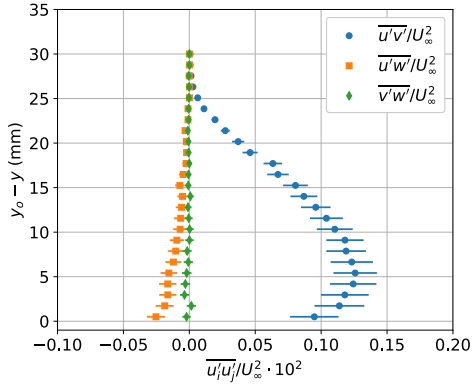
(b) $x = 1879.2$ mm, $z = 98.05$ mm
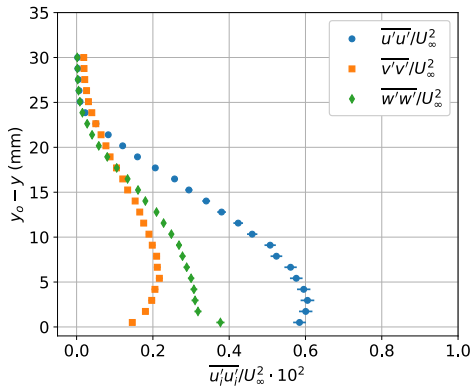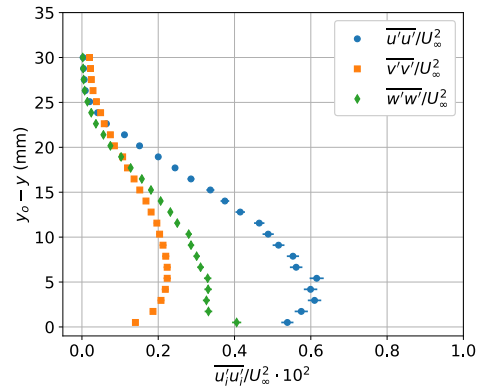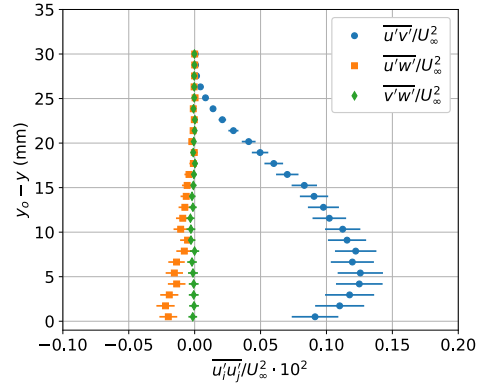
(c) $x = 1904.2$ mm, $z = 98.05$ mm

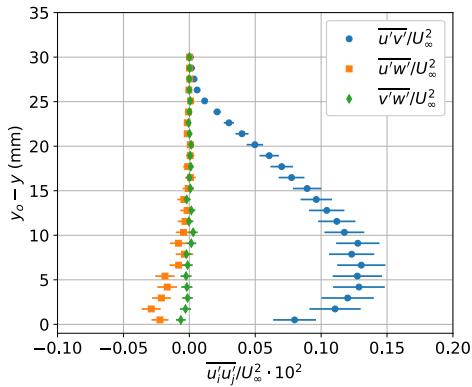(d) $x = 1921.2$ mm, $z = 98.05$ mm

Figure 77: Reynolds normal stress profiles on the port side of the fuselage near the wing leading edge. The model was configured with the F6 wing with leading-edge extension and set at a pitch angle of $5°$.
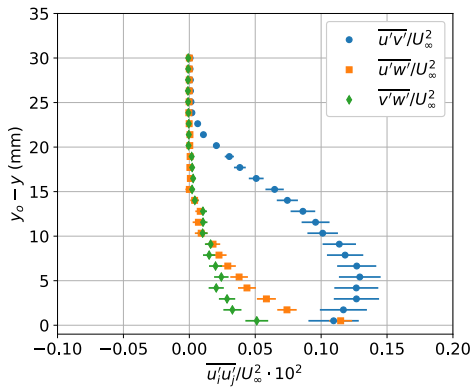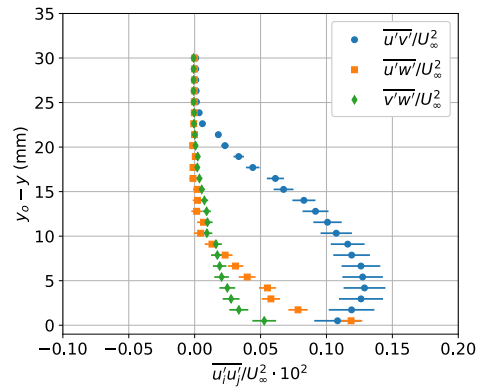
(a) $x = 1864.2$ mm, $z = 98.05$ mm

(b) $x = 1879.2$ mm, $z = 98.05$ mm
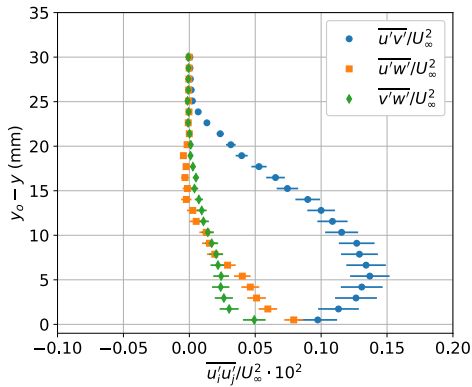
(c) $x = 1904.2$ mm, $z = 98.05$ mm
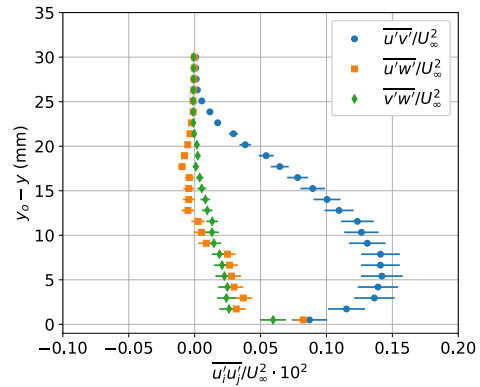
(d) $x = 1921.2$ mm, $z = 98.05$ mm

Figure 78: Reynolds shear stress profiles on the port side of the fuselage near the wing leading edge. The model was configured with the F6 wing with leading-edge extension and set at a pitch angle of $5°$.
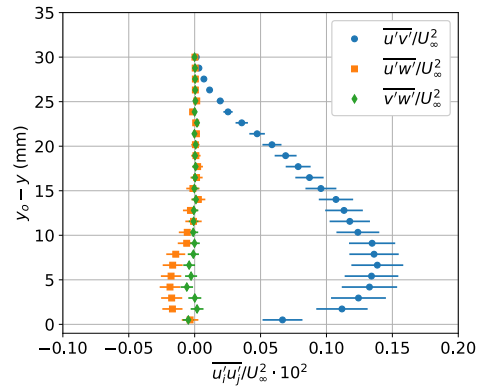
(a) $x = 1864.2$ mm, $z = 6.2$ mm

(b) $x = 1879.2$ mm, $z = 6.2$ mm

(c) $x = 1904.2$ mm, $z = 6.2$ mm

(d) $x = 1919.2$ mm, $z = 6.2$ mm
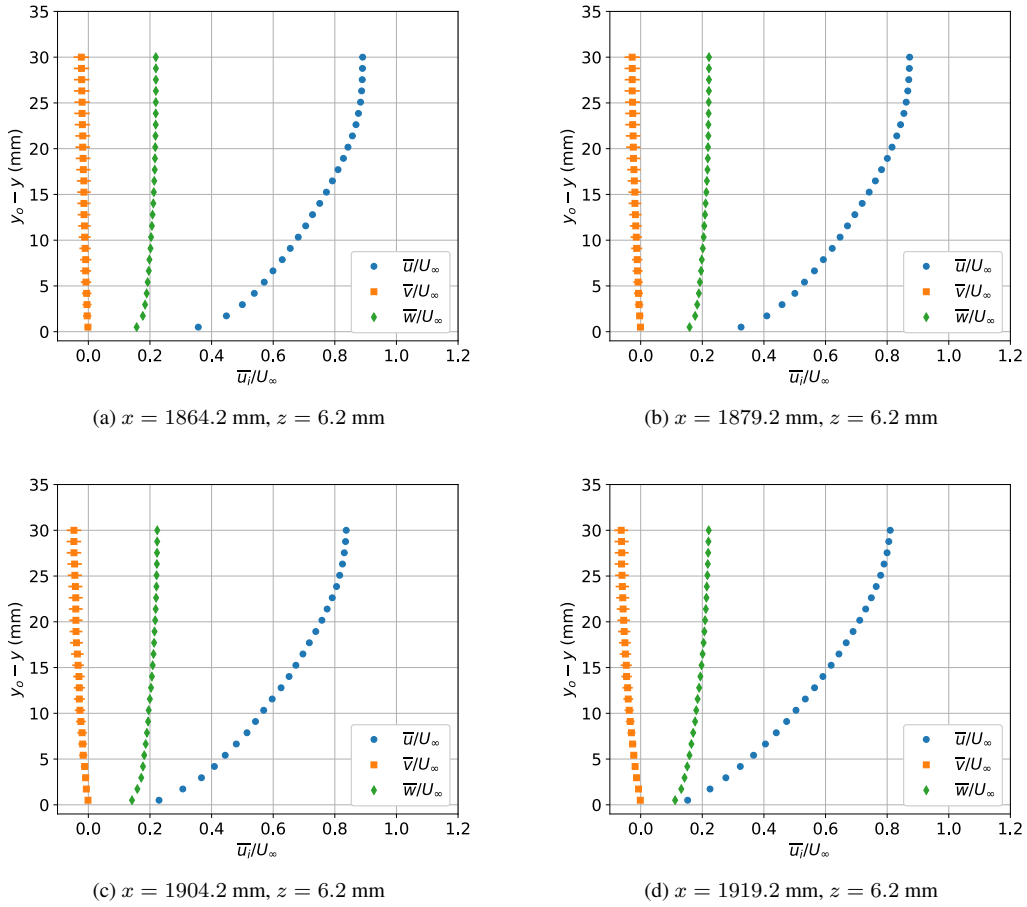
Figure 79: Mean velocity profiles on the port side of the fuselage near the wing leading edge. The model was configured with the F6 wing with leading-edge extension and set at a pitch angle of $5°$.
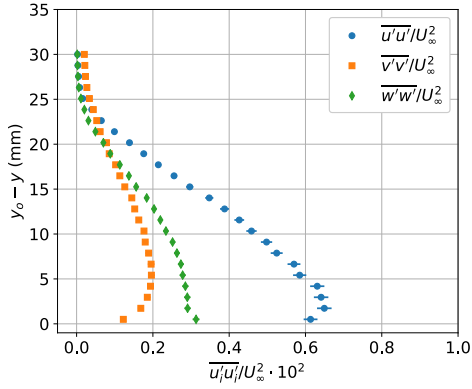
(a) $x = 1864.2$ mm, $z = 6.2$ mm
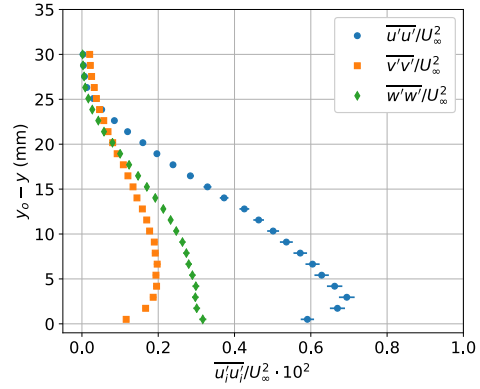
(b) $x = 1879.2$ mm, $z = 6.2$ mm
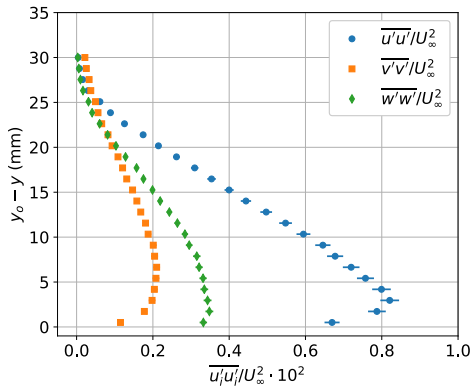
(c) $x = 1904.2$ mm, $z = 6.2$ mm
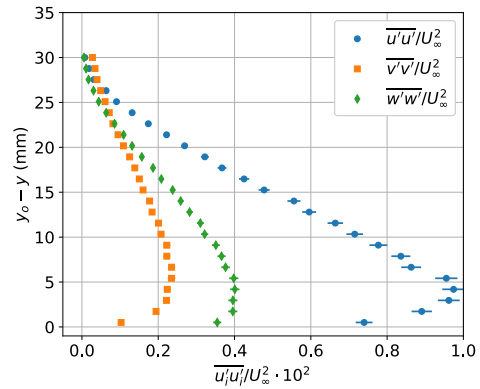
(d) $x = 1919.2$ mm, $z = 6.2$ mm

Figure 80: Reynolds normal stress profiles on the port side of the fuselage near the wing leading edge. The model was configured with the F6 wing with leading-edge extension and set at a pitch angle of $5°$.

131
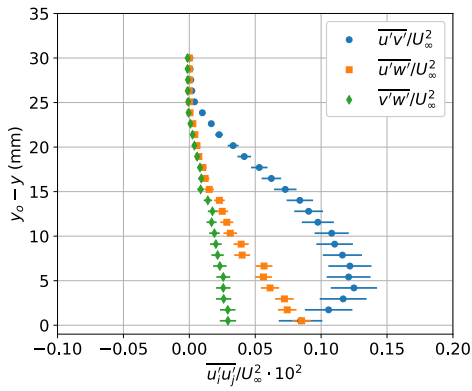
(a) $x = 1864.2$ mm, $z = 6.2$ mm
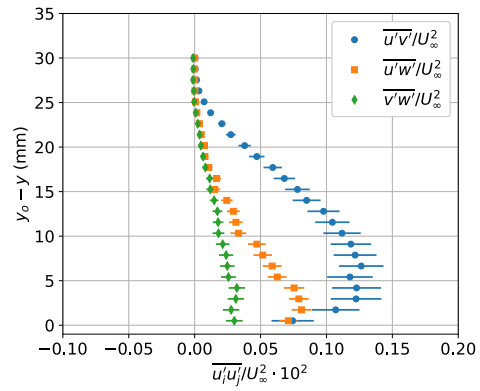
(b) $x = 1879.2$ mm, $z = 6.2$ mm
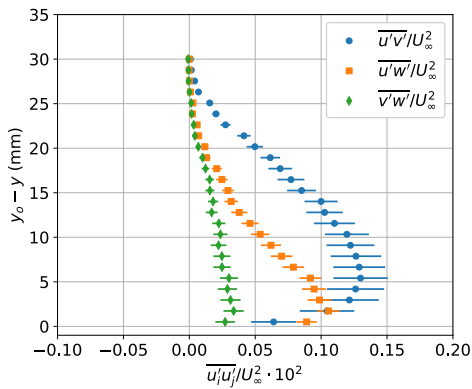
(c) $x = 1904.2$ mm, $z = 6.2$ mm
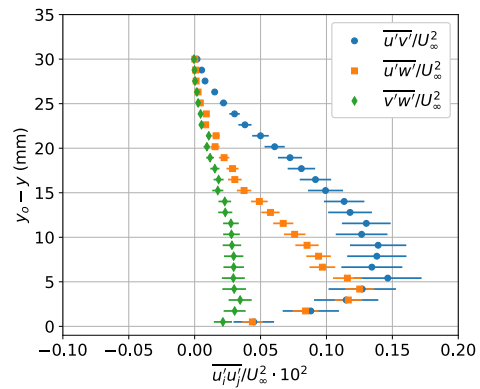
(d) $x = 1919.2$ mm, $z = 6.2$ mm

Figure 81: Reynolds shear stress profiles on the port side of the fuselage near the wing leading edge. The model was configured with the F6 wing with leading-edge extension and set at a pitch angle of $5°$.
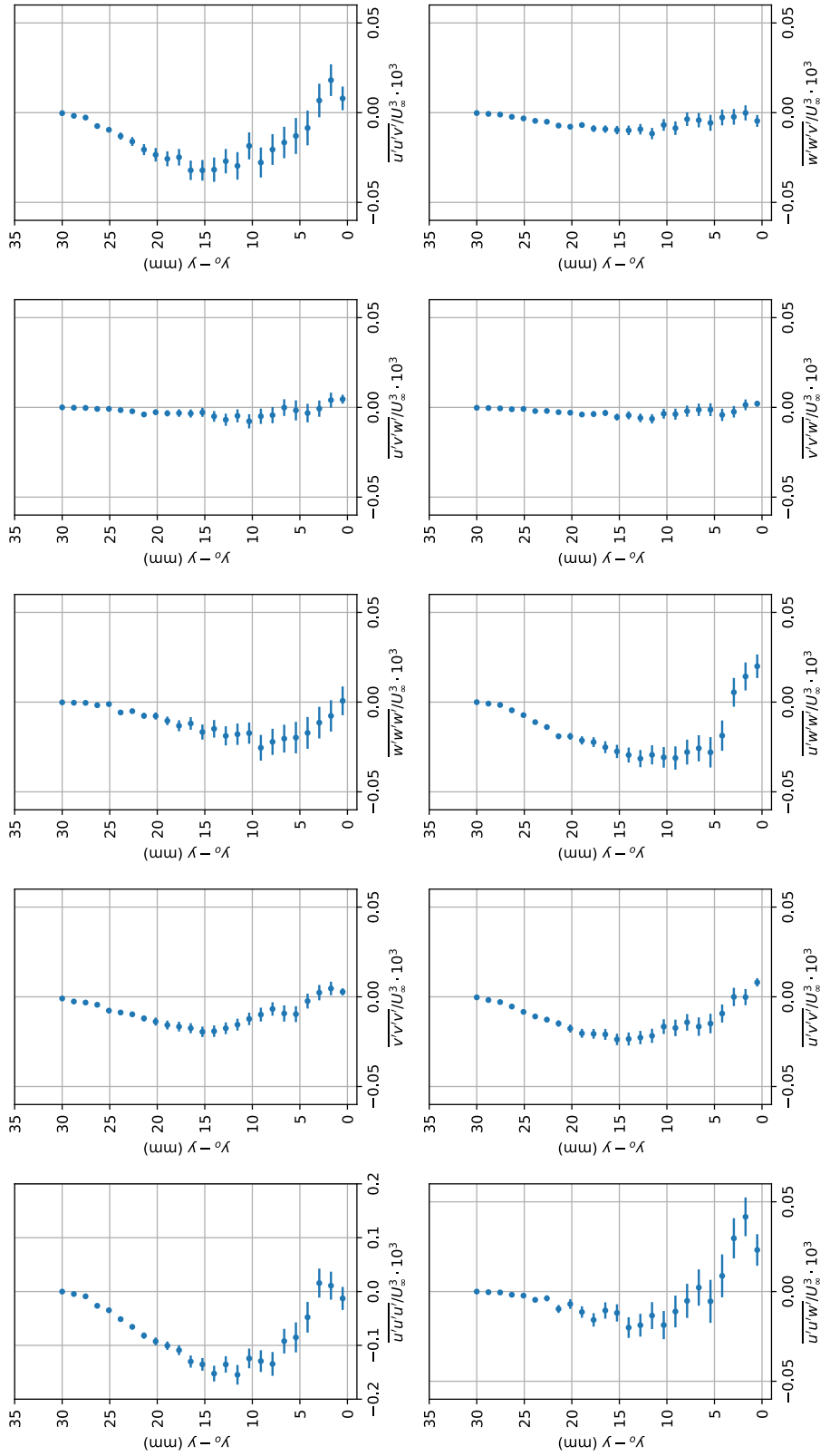
Figure 82: Triple products of the velocity components on the port side of the fuselage at $x = 1919.2$ mm, $z = 6.2$ mm. The model was configured with the F6 wing with leading-edge extension and set at a pitch angle of $5°$.
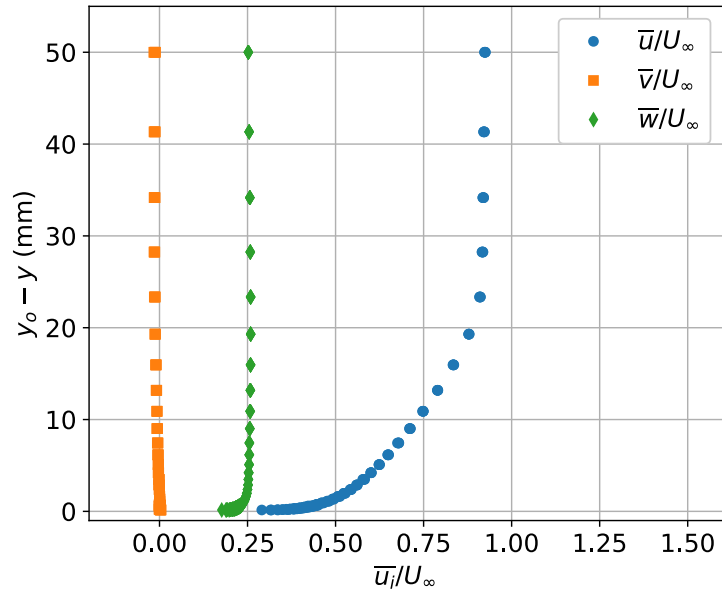
Figure 83: Repeat measurements of the mean velocity profiles at $x = 1859.2$ mm, $z = 55.05$ mm, and $\alpha = 5°$ on the F6 wing with leading-edge extension.
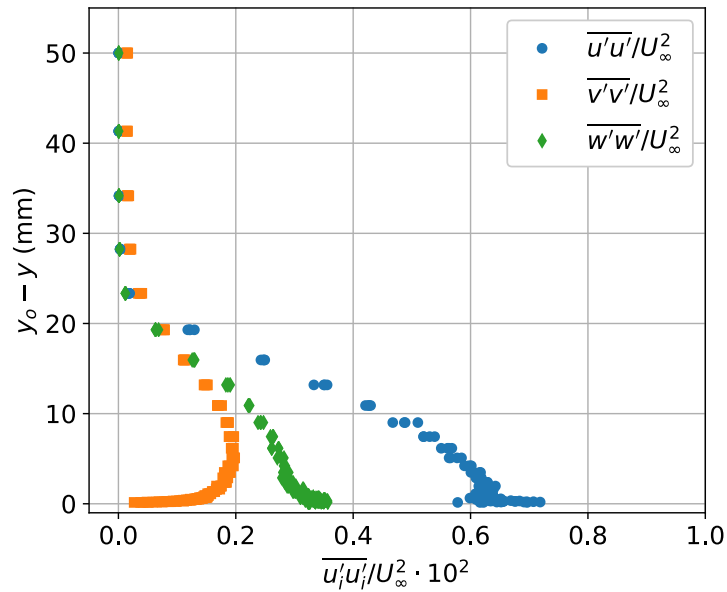
Figure 84: Repeat measurements of the Reynolds normal stress profiles at $x = 1859.2$ mm, $y = 55.05$ mm, and $\alpha = 5°$ on the F6 wing with leading-edge extension.
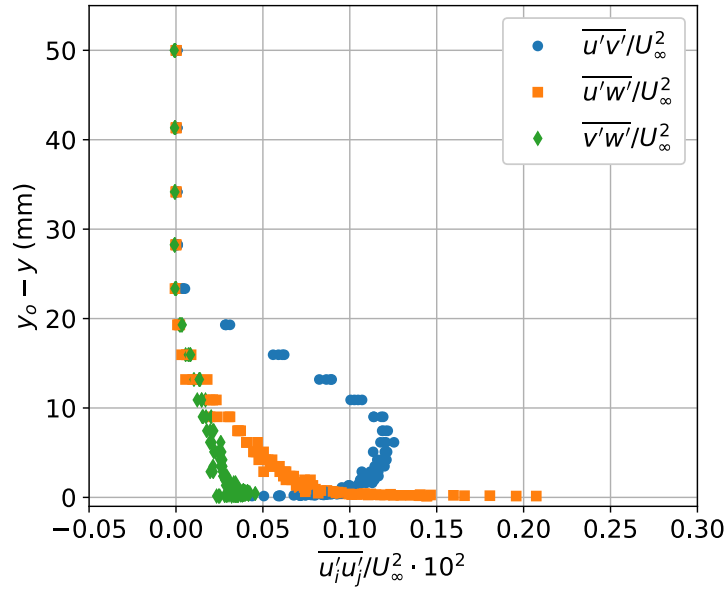
Figure 85: Repeat measurements of the Reynolds shear stress profiles at $x = 1859.2$ mm, $y = 55.05$ mm, and $\alpha = 5°$ on the F6 wing with leading-edge extension.
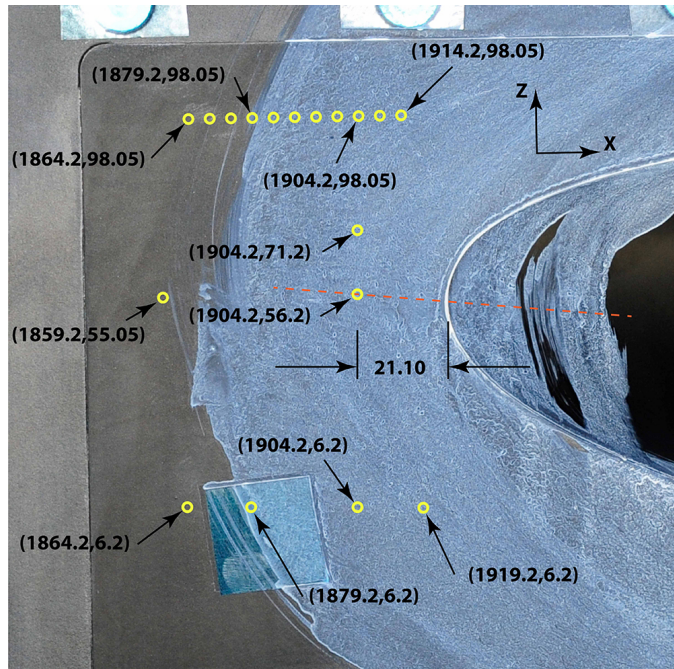
Figure 86: Schematic of the LDV measurement locations in the leading-edge region of the F6 wing with leading-edge extension at a model pitch angle of $-2.5°$. The yellow circles denote locations where profile measurement were made and the red dashed line denotes the chord line of the wing root section. Dimensions are in millimeters.

(a) $x = 1864.2$ mm, $z = 98.05$ mm

(b) $x = 1879.2$ mm, $z = 98.05$ mm

(c) $x = 1904.2$ mm, $z = 98.05$ mm

(d) $x = 1914.2$ mm, $z = 98.05$ mm

Figure 87: Mean velocity profiles on the port side of the fuselage near the wing leading edge. The model was configured with the F6 wing with leading-edge extension and set at a pitch angle of $-2.5°$.

(a) $x = 1864.2$ mm, $z = 98.05$ mm

(b) $x = 1879.2$ mm, $z = 98.05$ mm
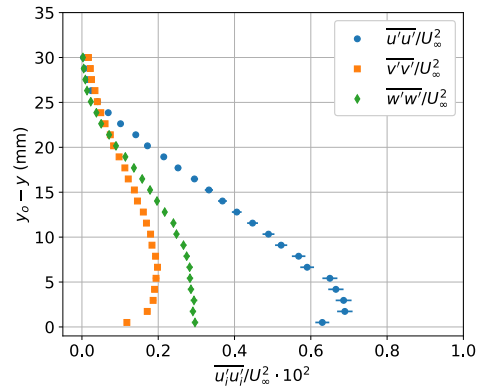
(c) $x = 1904.2$ mm, $z = 98.05$ mm

(d) $x = 1914.2$ mm, $z = 98.05$ mm

Figure 88: Reynolds normal stress profiles on the port side of the fuselage near the wing leading edge. The model was configured with the F6 wing with leading-edge extension and set at a pitch angle of $-2.5°$.

(a) $x = 1864.2$ mm, $z = 98.05$ mm

(b) $x = 1879.2$ mm, $z = 98.05$ mm
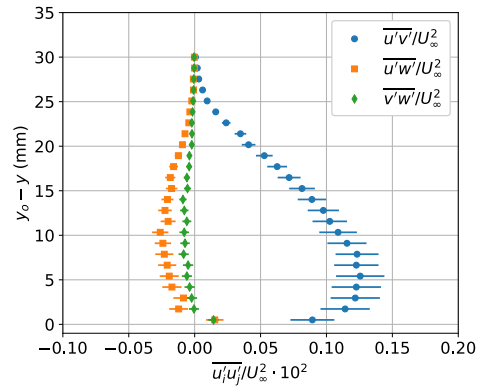
(c) $x = 1904.2$ mm, $z = 98.05$ mm

(d) $x = 1914.2$ mm, $z = 98.05$ mm

Figure 89: Reynolds shear stress profiles on the port side of the fuselage near the wing leading edge. The model was configured with the F6 wing with leading-edge extension and set at a pitch angle of $-2.5°$.

(a) $x = 1864.2$ mm, $z = 6.2$ mm

(b) $x = 1879.2$ mm, $z = 6.2$ mm

(c) $x = 1904.2$ mm, $z = 6.2$ mm

(d) $x = 1919.2$ mm, $z = 6.2$ mm
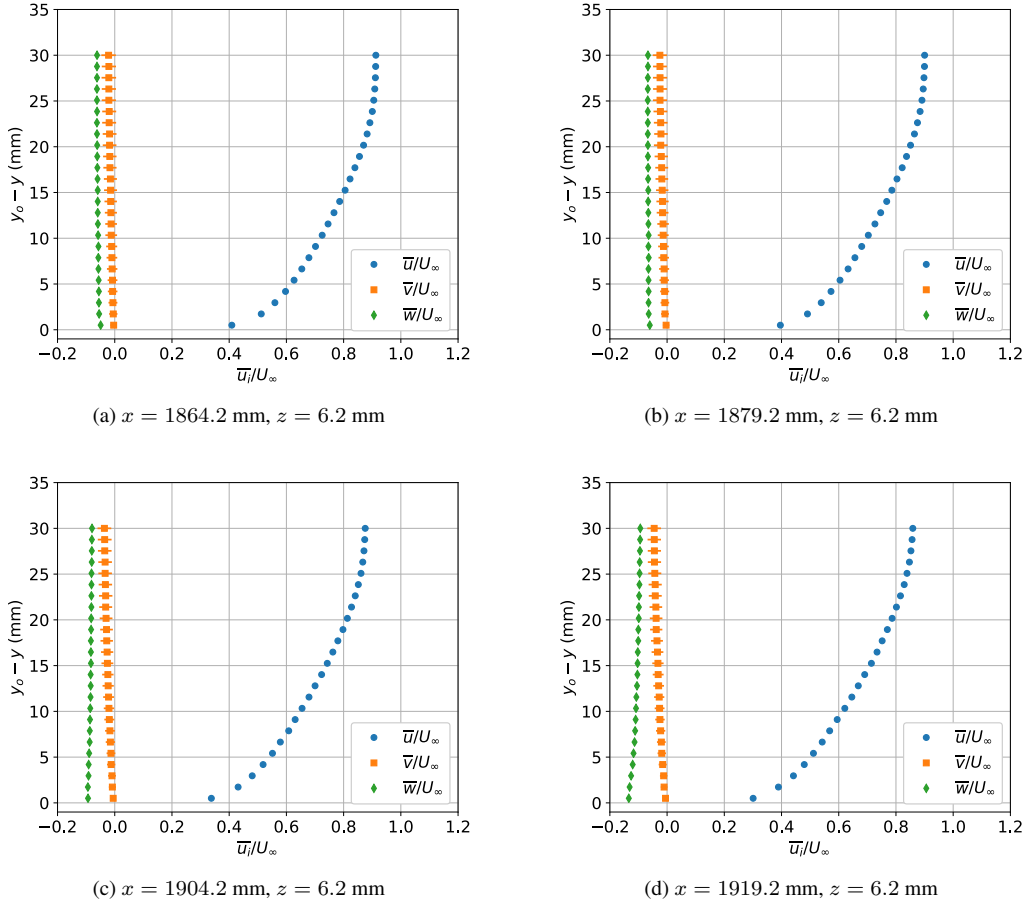
Figure 90: Mean velocity profiles on the port side of the fuselage near the wing leading edge. The model was configured with the F6 wing with leading-edge extension and set at a pitch angle of $-2.5°$.
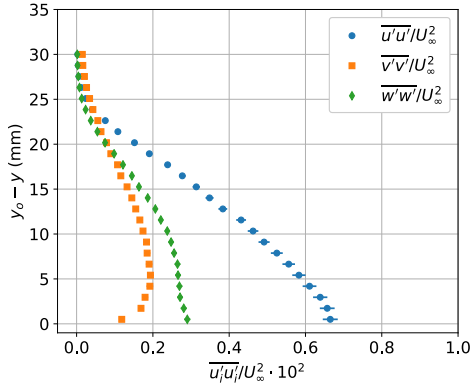
(a) $x = 1864.2$ mm, $z = 6.2$ mm
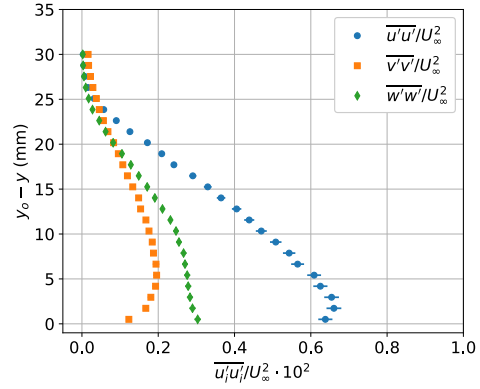
(b) $x = 1879.2$ mm, $z = 6.2$ mm
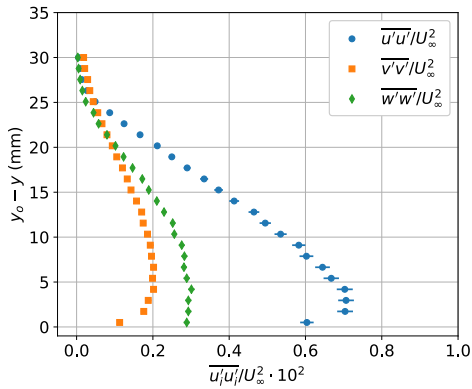
(c) $x = 1904.2$ mm, $z = 6.2$ mm
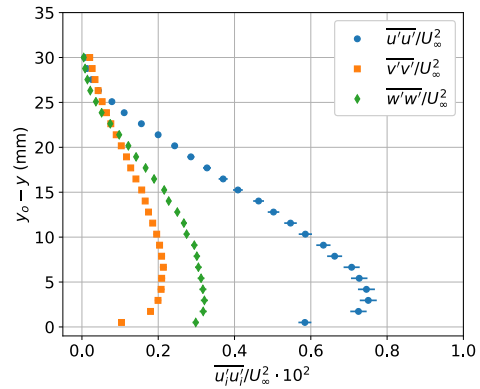
(d) $x = 1919.2$ mm, $z = 6.2$ mm

Figure 91: Reynolds normal stress profiles on the port side of the fuselage near the wing leading edge. The model was configured with the F6 wing with leading-edge extension and set at a pitch angle of $-2.5°$.

(a) $x = 1864.2$ mm, $z = 6.2$ mm

(b) $x = 1879.2$ mm, $z = 6.2$ mm

(c) $x = 1904.2$ mm, $z = 6.2$ mm

(d) $x = 1919.2$ mm, $z = 6.2$ mm

Figure 92: Reynolds shear stress profiles on the port side of the fuselage near the wing leading edge. The model was configured with the F6 wing with leading-edge extension and set at a pitch angle of $-2.5°$.

(a) $y = -236.6$ mm

(b) $y = -237.1$ mm

(c) $y = -239.1$ mm

(d) $y = -246.1$ mm

(e) $y = -256.1$ mm

(f) $y = -286.1$ mm
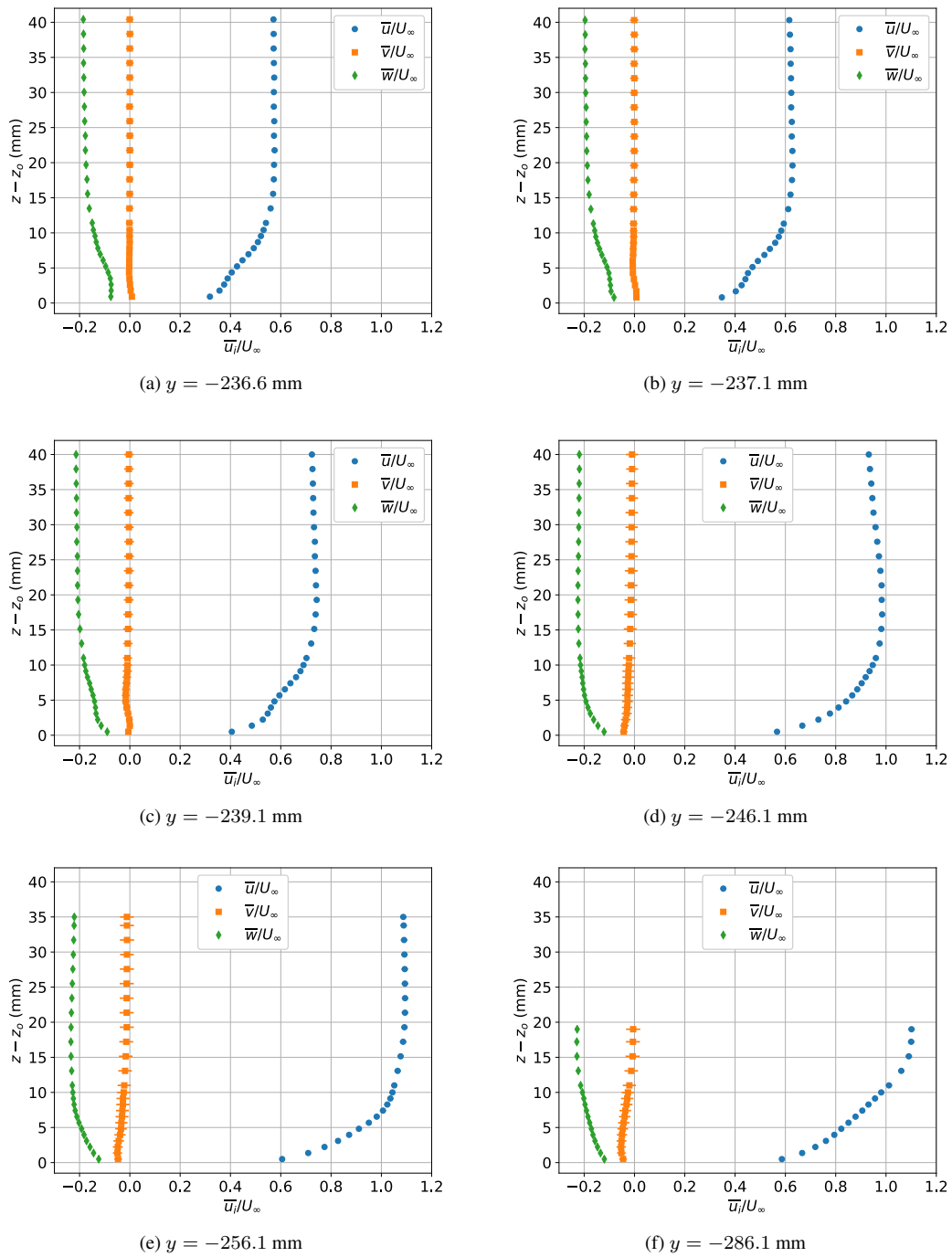
Figure 93: Mean velocity profiles in the corner-flow region of the F6 wing at $x = 2747.6$ mm and $\alpha = 5°$.

(a) $y = -236.6$ mm

(b) $y = -237.1$ mm

(c) $y = -239.1$ mm

(d) $y = -246.1$ mm

(e) $y = -256.1$ mm

(f) $y = -286.1$ mm
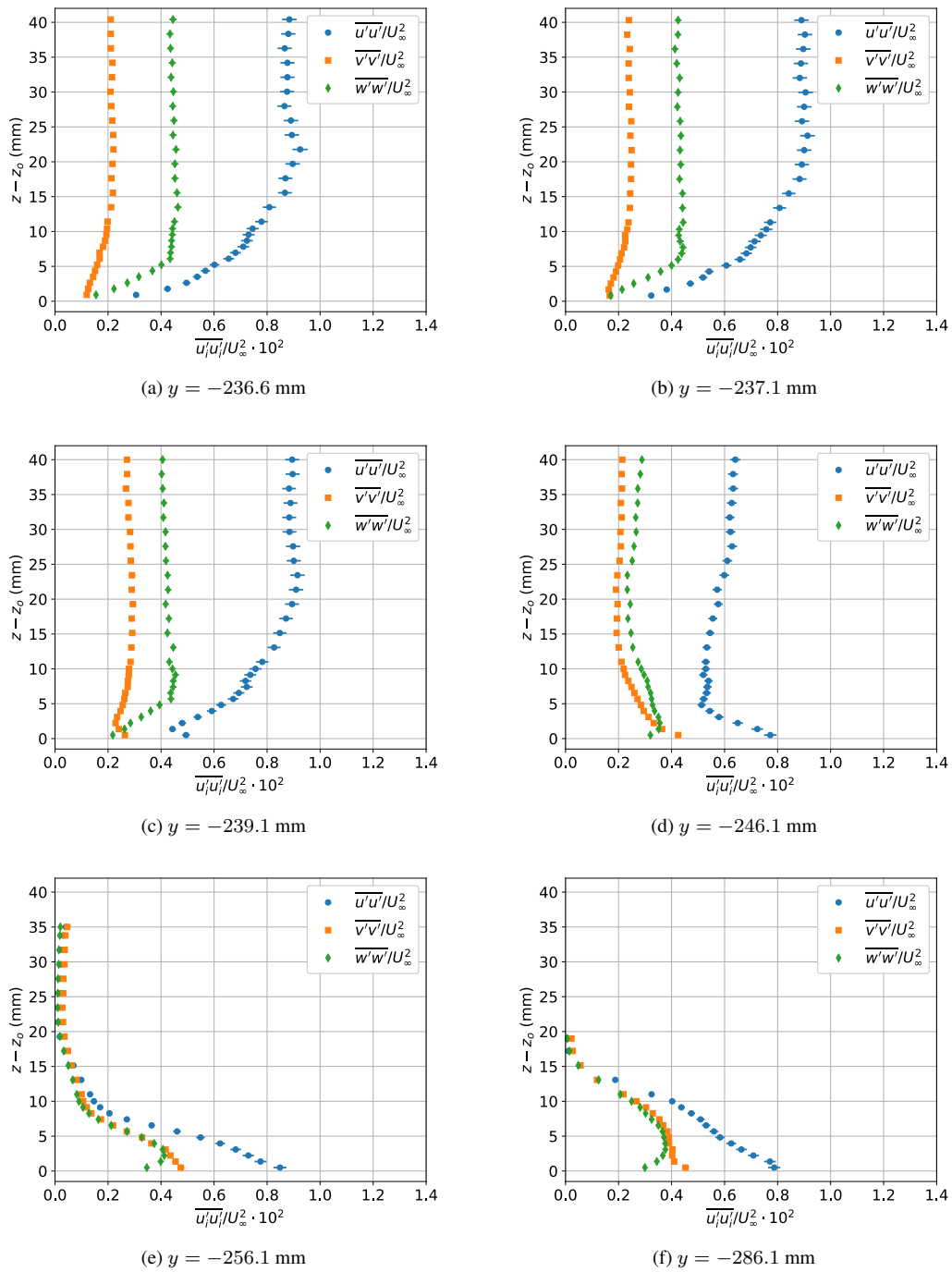
Figure 94: Reynolds normal stress profiles in the corner-flow region of the F6 wing at $x = 2747.6$ mm and $\alpha = 5°$.

(a) $y = -236.6$ mm

(b) $y = -237.1$ mm

(c) $y = -239.1$ mm

(d) $y = -246.1$ mm

(e) $y = -256.1$ mm

(f) $y = -286.1$ mm
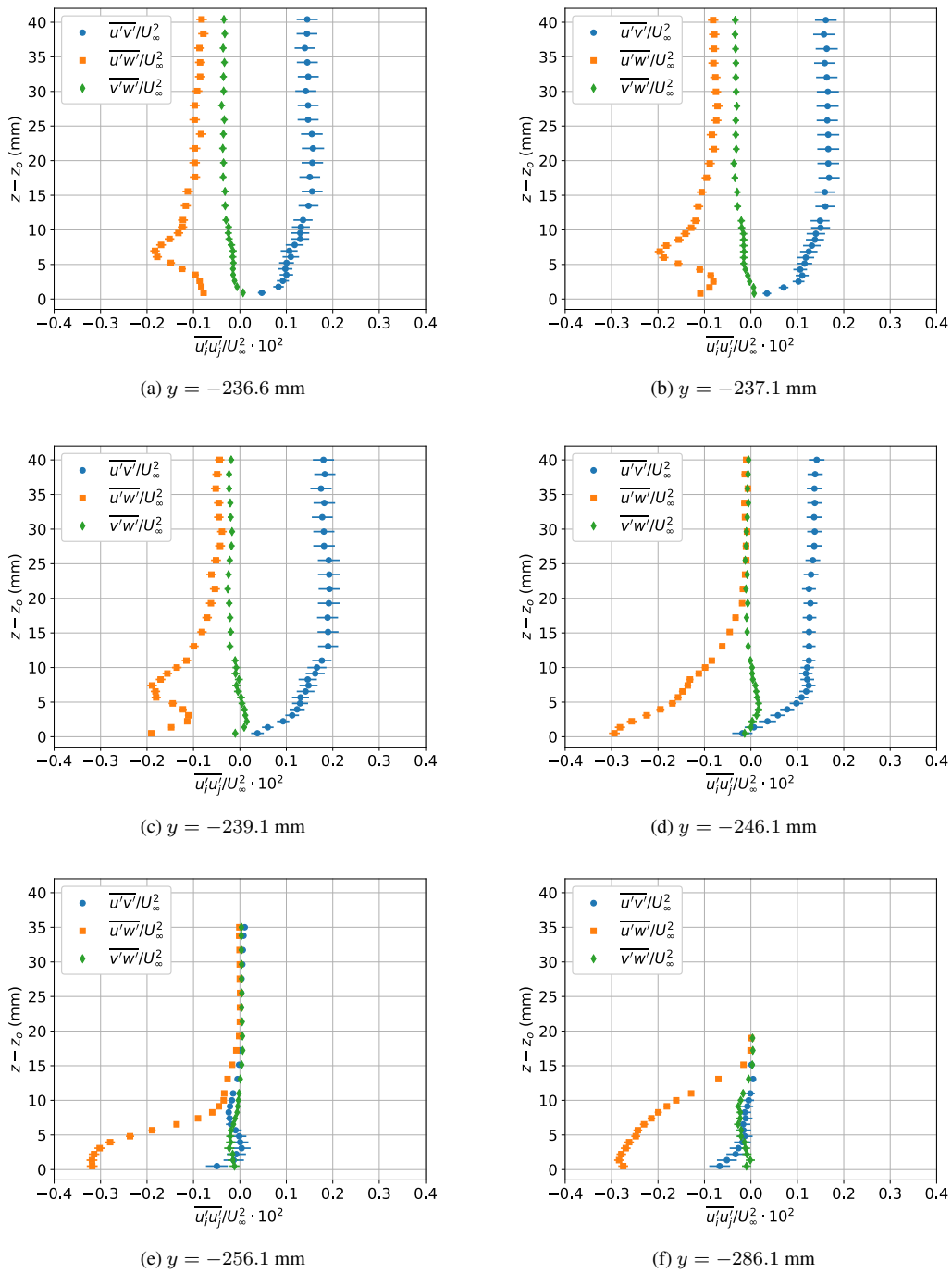
Figure 95: Reynolds shear stress profiles in the corner-flow region of the F6 wing at $x = 2747.6$ mm and $\alpha = 5°$.

(a) $y = -236.6$ mm

(b) $y = -237.1$ mm

(c) $y = -239.1$ mm

(d) $y = -246.1$ mm

(e) $y = -256.1$ mm

(f) $y = -286.1$ mm
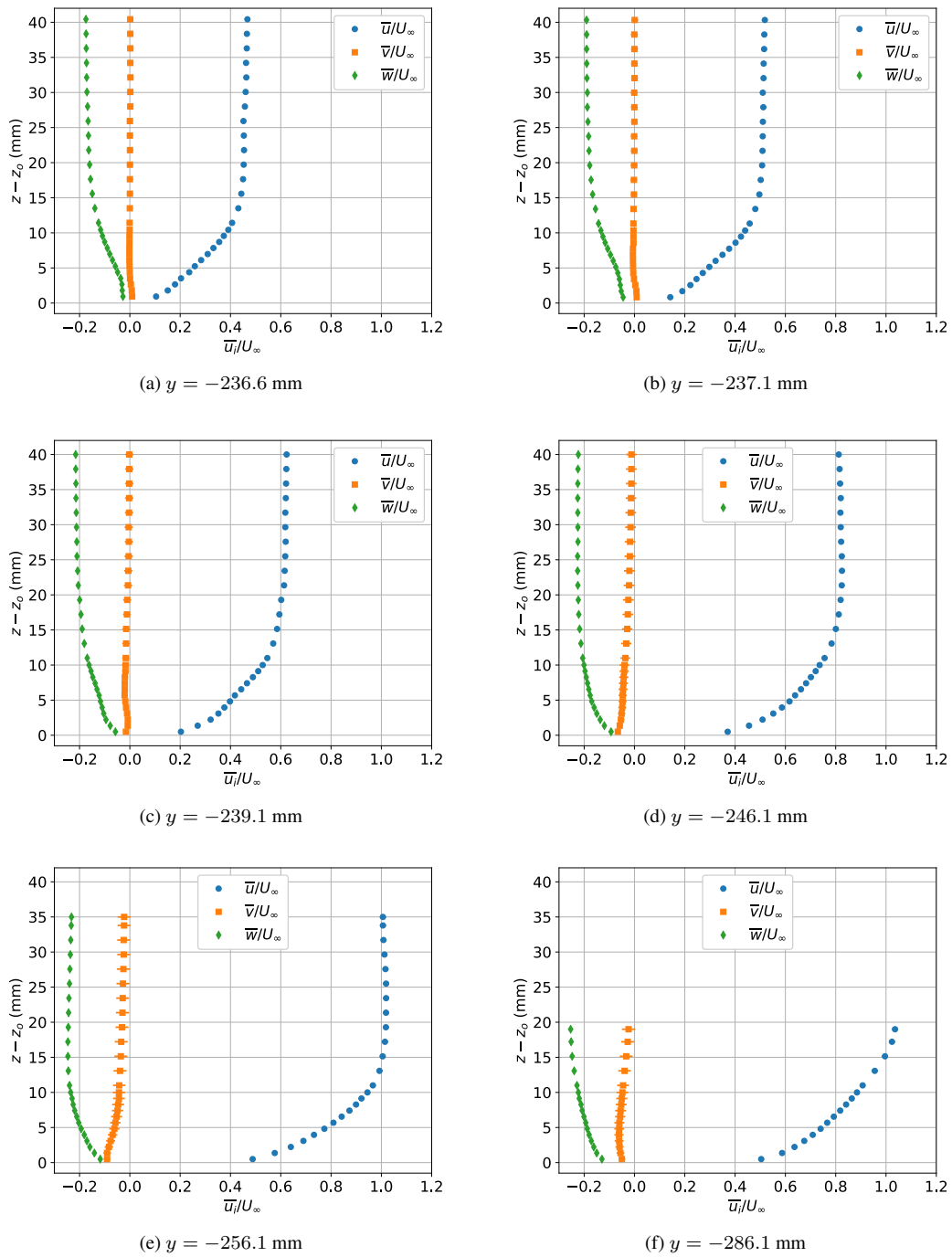
Figure 96: Mean velocity profiles in the corner-flow region of the F6 wing at $x = 2852.6$ mm and $\alpha = 5°$.

(a) $y = -236.6$ mm

(b) $y = -237.1$ mm

(c) $y = -239.1$ mm

(d) $y = -246.1$ mm

(e) $y = -256.1$ mm

(f) $y = -286.1$ mm
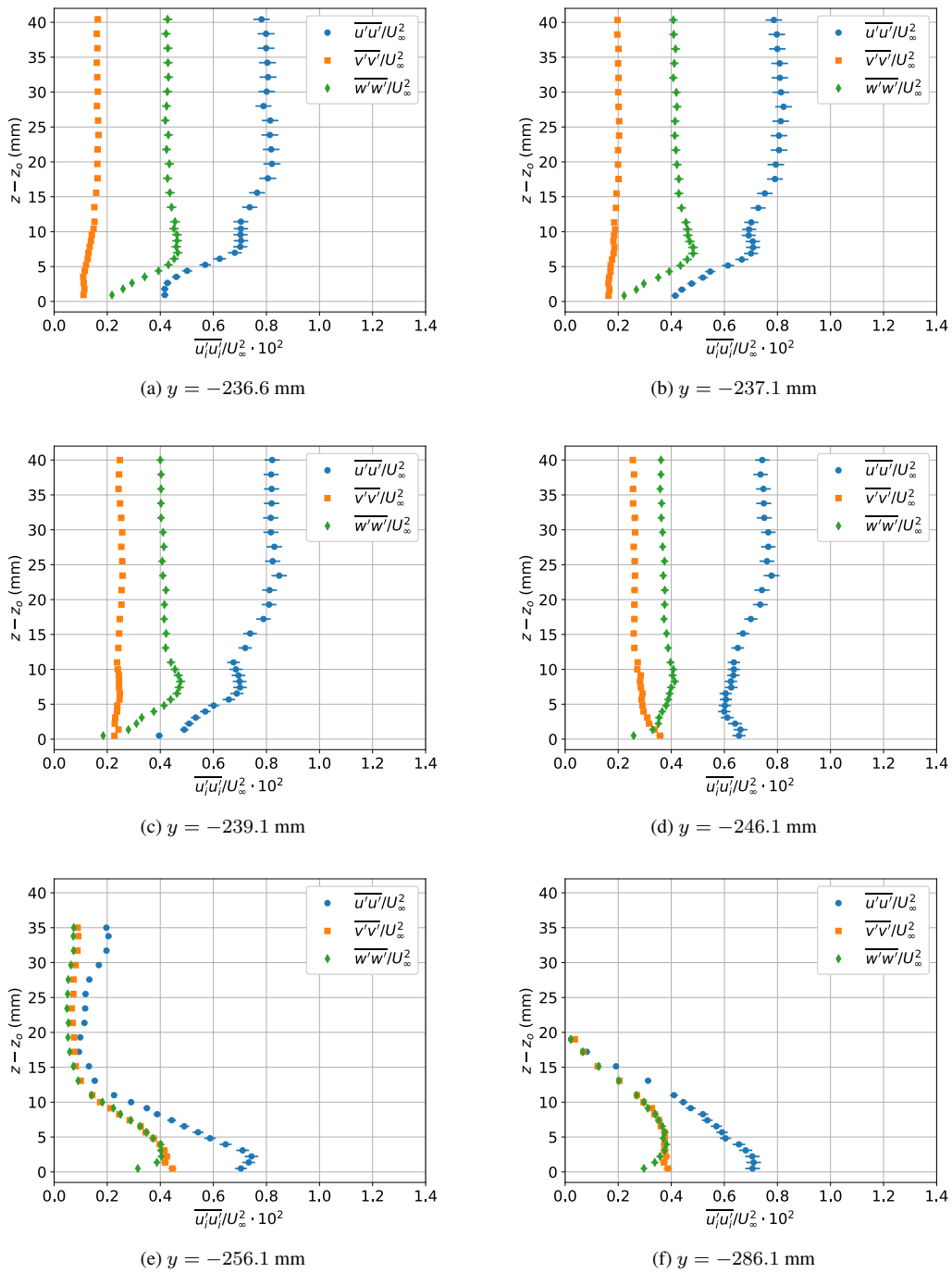
Figure 97: Reynolds normal stress profiles in the corner-flow region of the F6 wing at $x = 2852.6$ mm and $\alpha = 5°$.

146

(a) $y = -236.6$ mm

(b) $y = -237.1$ mm

(c) $y = -239.1$ mm

(d) $y = -246.1$ mm

(e) $y = -256.1$ mm

(f) $y = -286.1$ mm
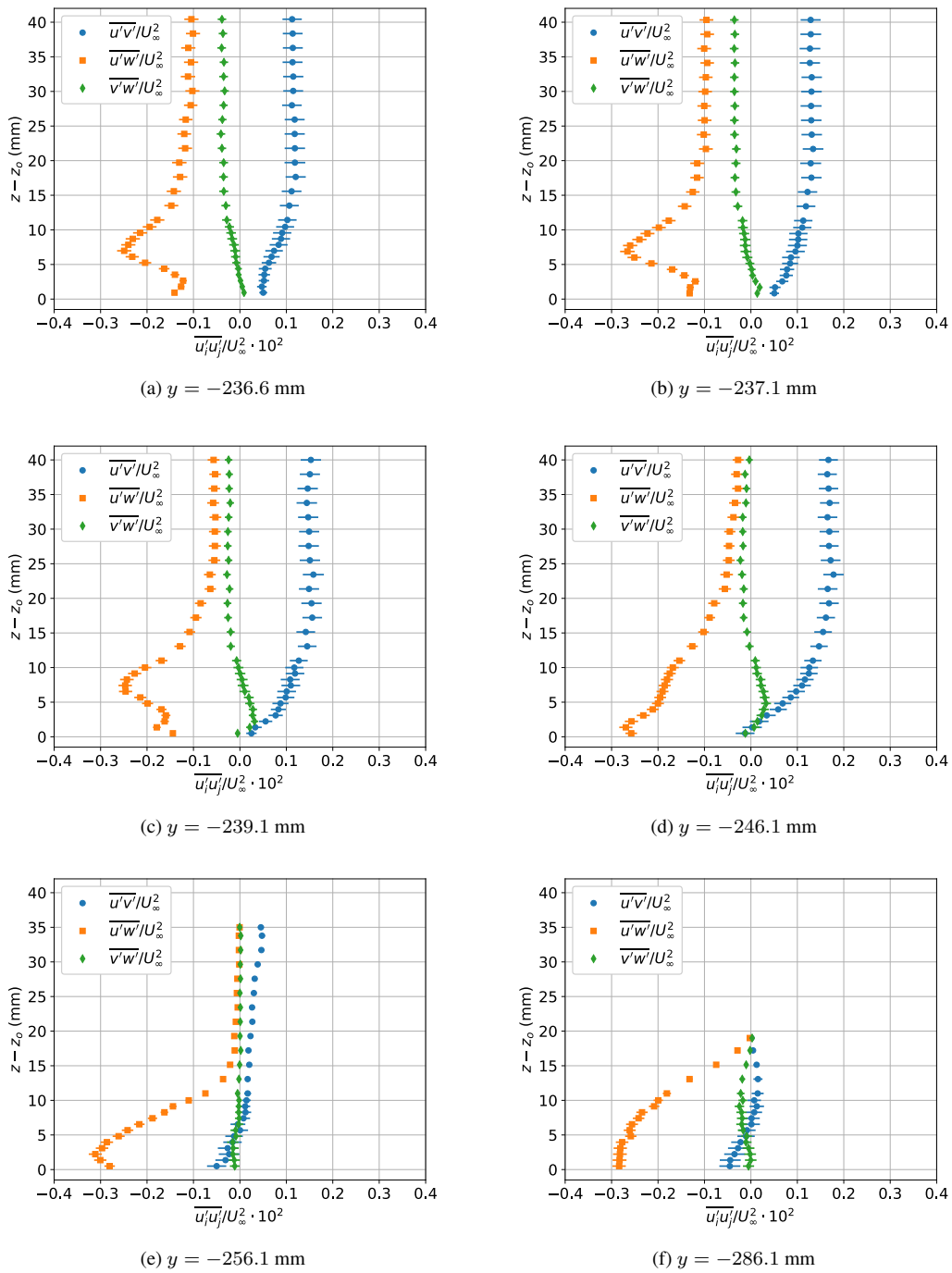
Figure 98: Reynolds shear stress profiles in the corner-flow region of the F6 wing at $x = 2852.6$ mm and $\alpha = 5°$.

(a) $y = -236.6$ mm

(b) $y = -239.1$ mm

(c) $y = -243.1$ mm

(d) $y = -246.1$ mm

(e) $y = -256.1$ mm

(f) $y = -286.1$ mm
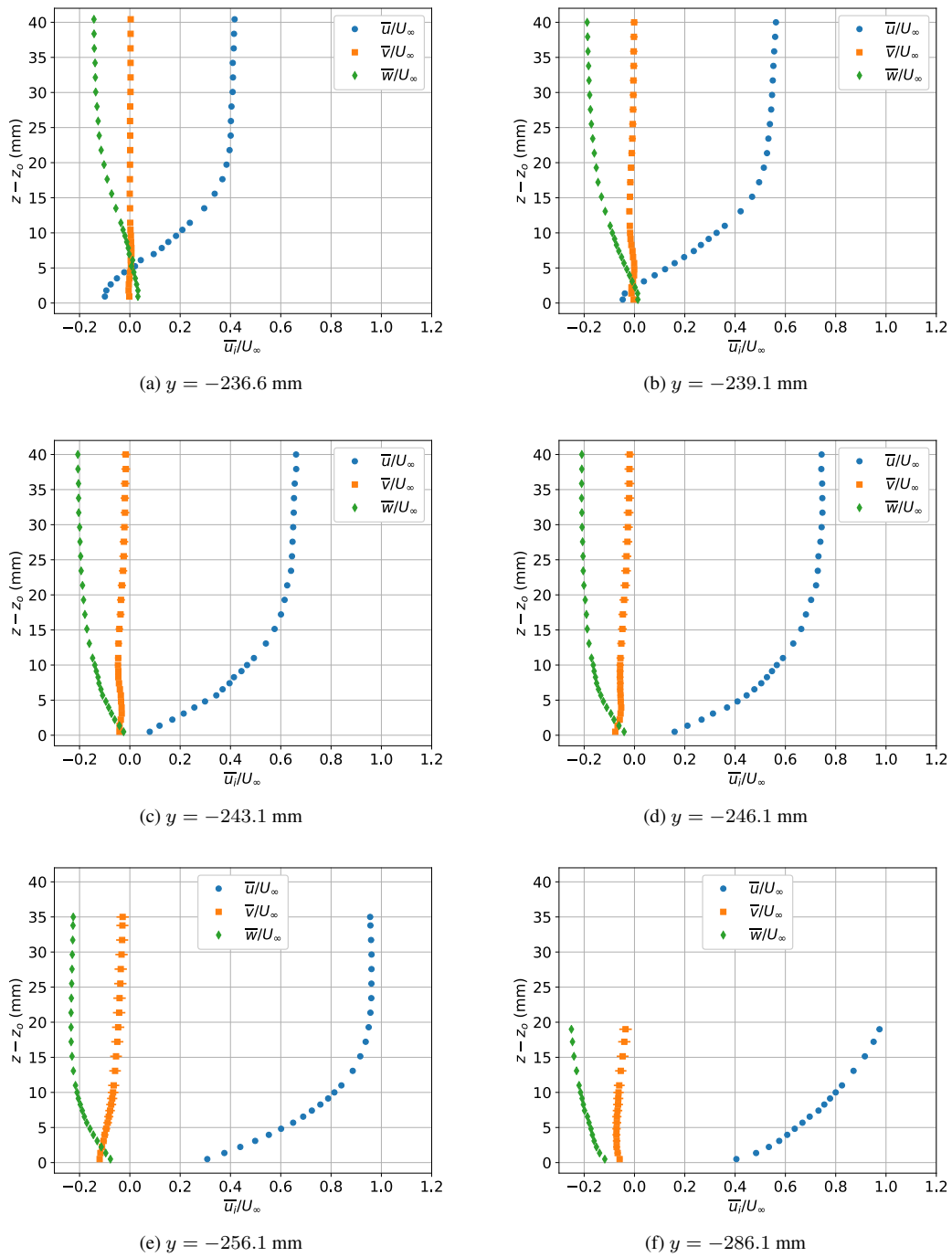
Figure 99: Mean velocity profiles in the corner-flow region of the F6 wing at $x = 2892.6$ mm and $\alpha = 5°$.

(a) $y = -236.6$ mm

(b) $y = -239.1$ mm

(c) $y = -243.1$ mm

(d) $y = -246.1$ mm

(e) $y = -256.1$ mm

(f) $y = -286.1$ mm
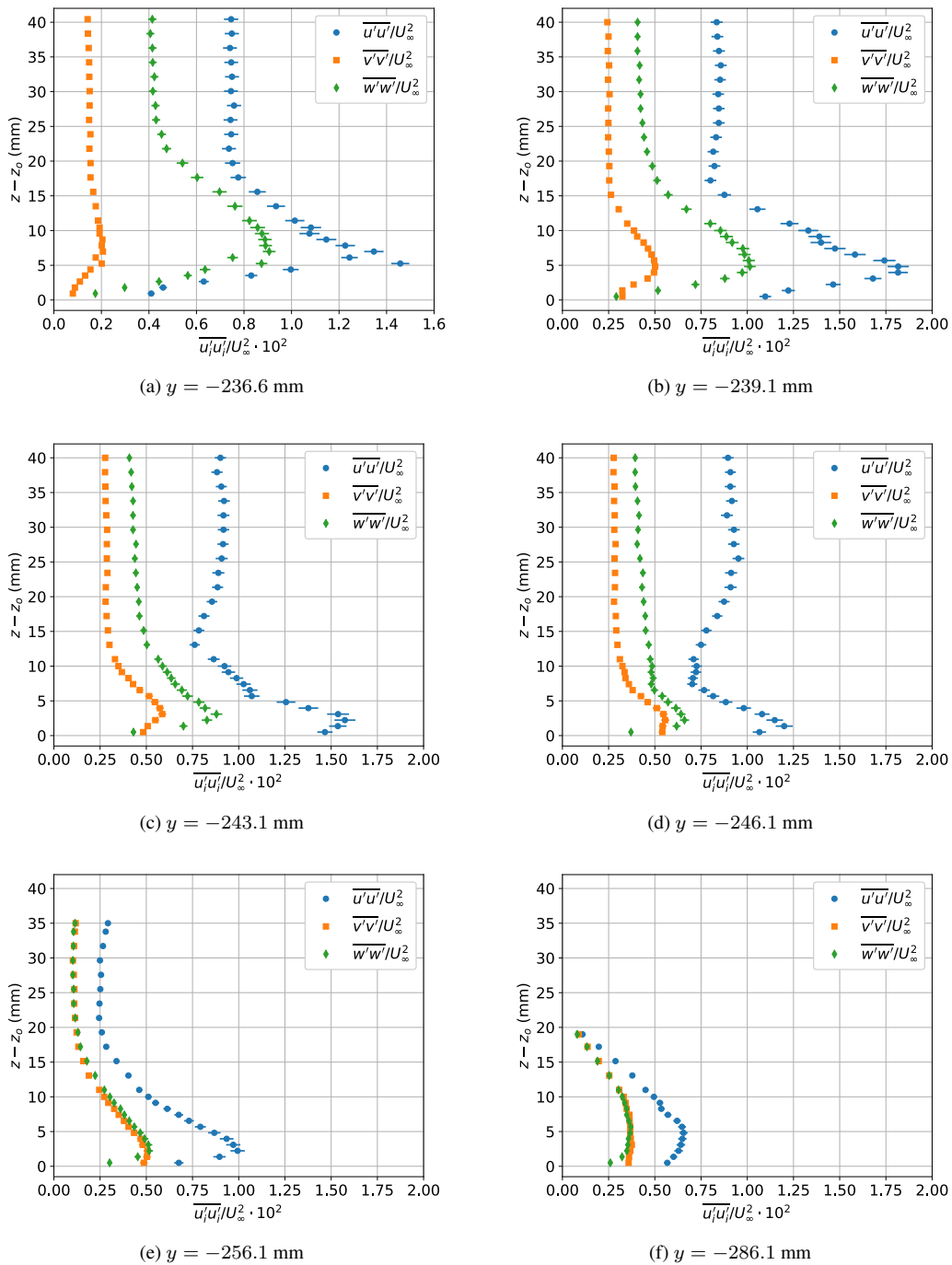
Figure 100: Reynolds normal stress profiles in the corner-flow region of the F6 wing at $x = 2892.6$ mm and $\alpha = 5°$.

(a) $y = -236.6$ mm

(b) $y = -239.1$ mm

(c) $y = -243.1$ mm

(d) $y = -246.1$ mm

(e) $y = -256.1$ mm

(f) $y = -286.1$ mm
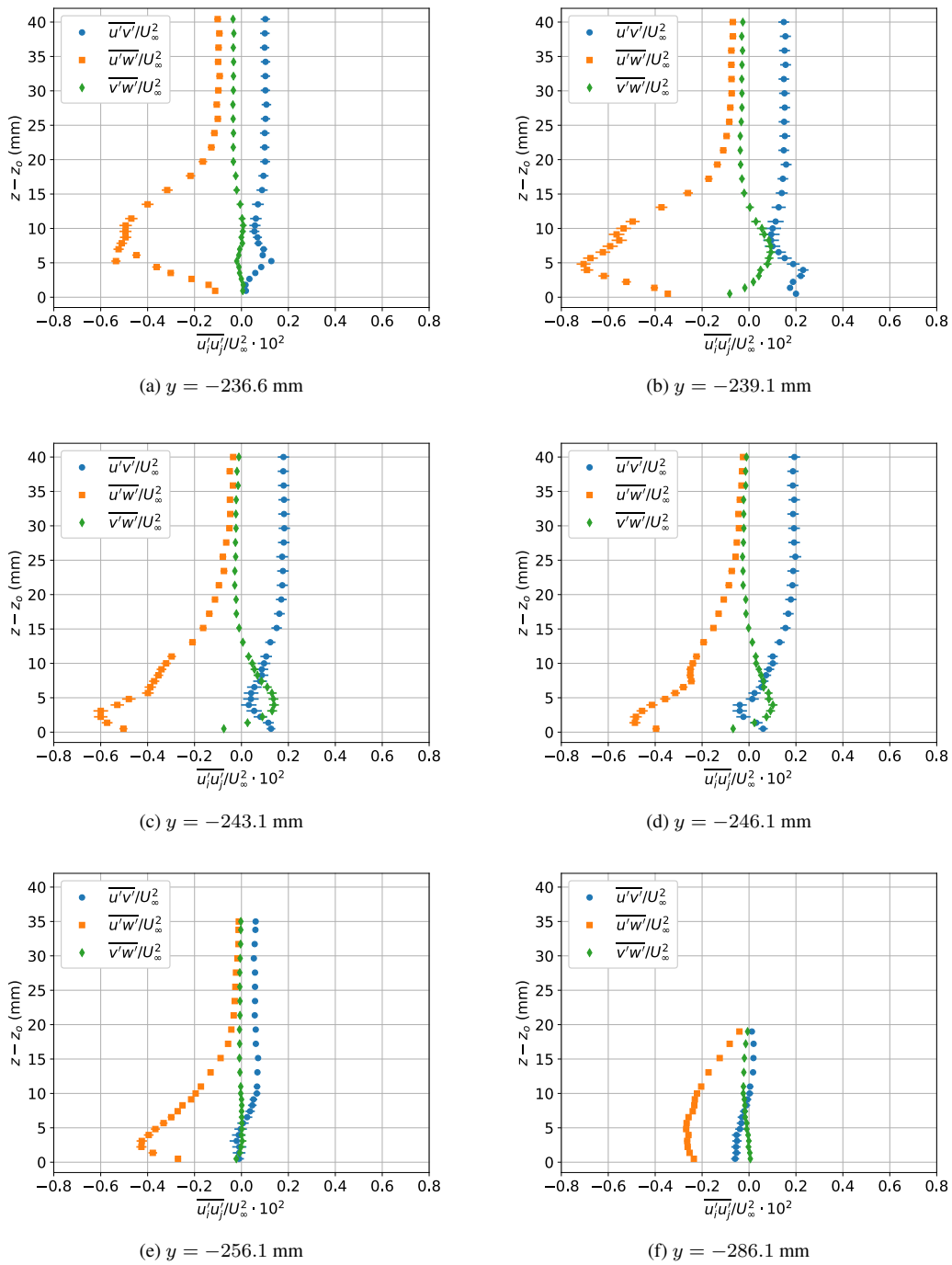
Figure 101: Reynolds shear stress profiles in the corner-flow region of the F6 wing at $x = 2892.6$ mm and $\alpha = 5°$.

(a) $y = -237.1$ mm
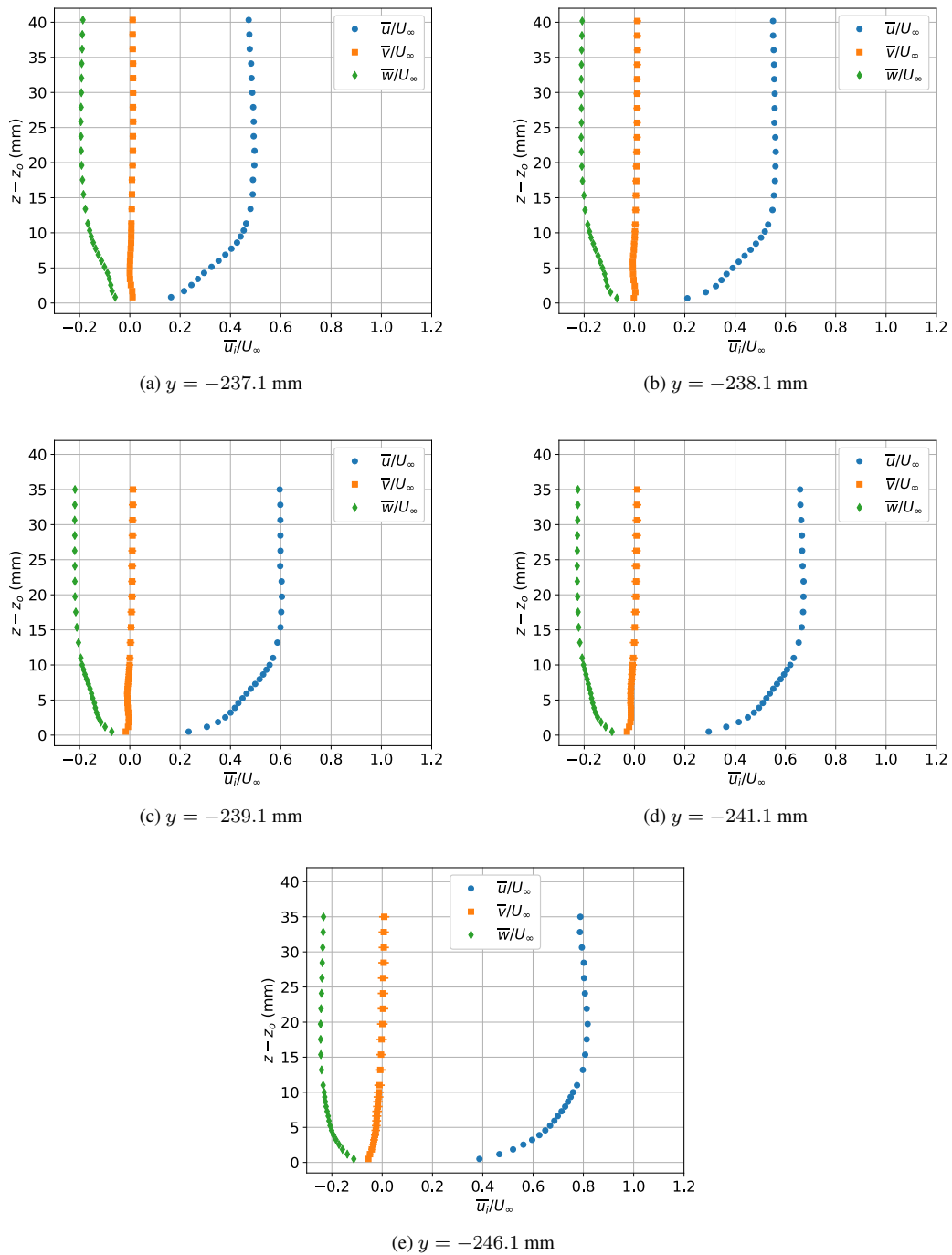
(b) $y = -239.1$ mm

(c) $y = -246.1$ mm

(d) $y = -266.1$ mm
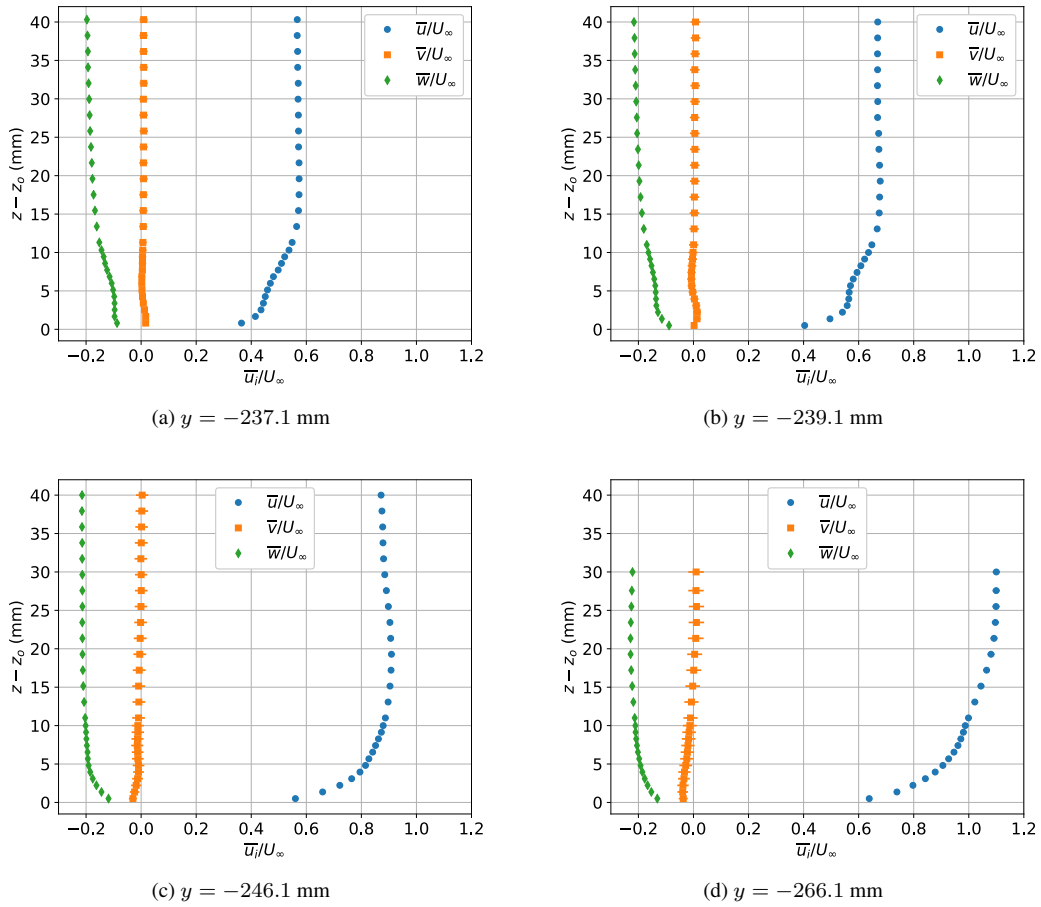
Figure 102: Mean velocity profiles in the corner-flow region of the F6 wing with leading-edge extension at $x = 2747.6$ mm and $\alpha = 5°$.
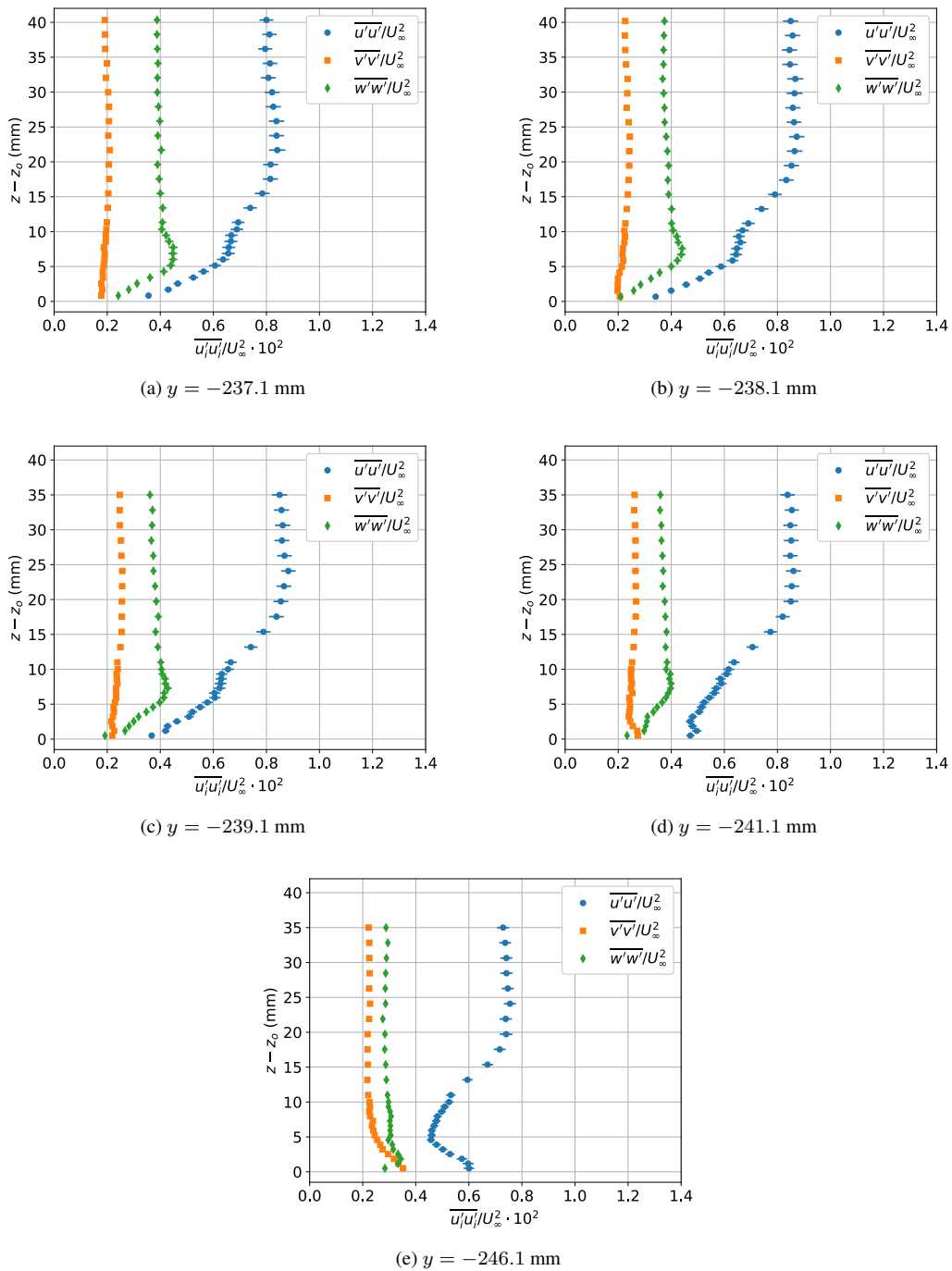
(a) $y = -237.1$ mm

(b) $y = -239.1$ mm
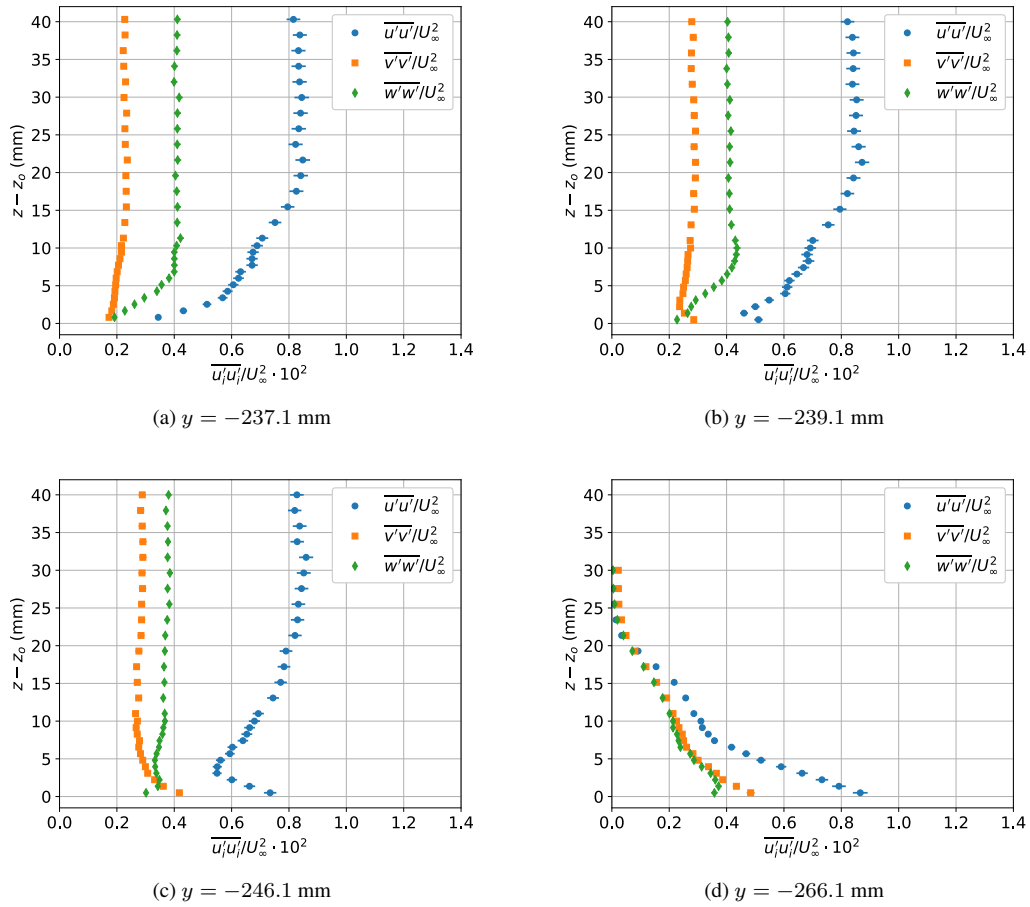
(c) $y = -246.1$ mm

(d) $y = -266.1$ mm

Figure 103: Reynolds normal stress profiles in the corner-flow region of the F6 wing with leading-edge extension at $x = 2747.6$ mm and $\alpha = 5°$.
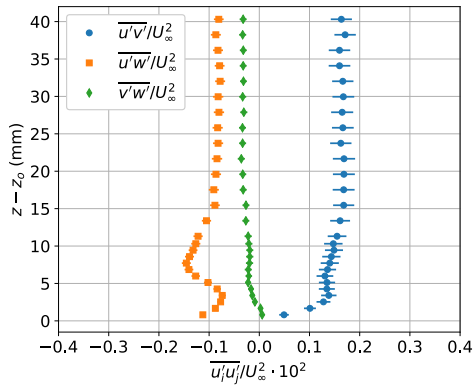
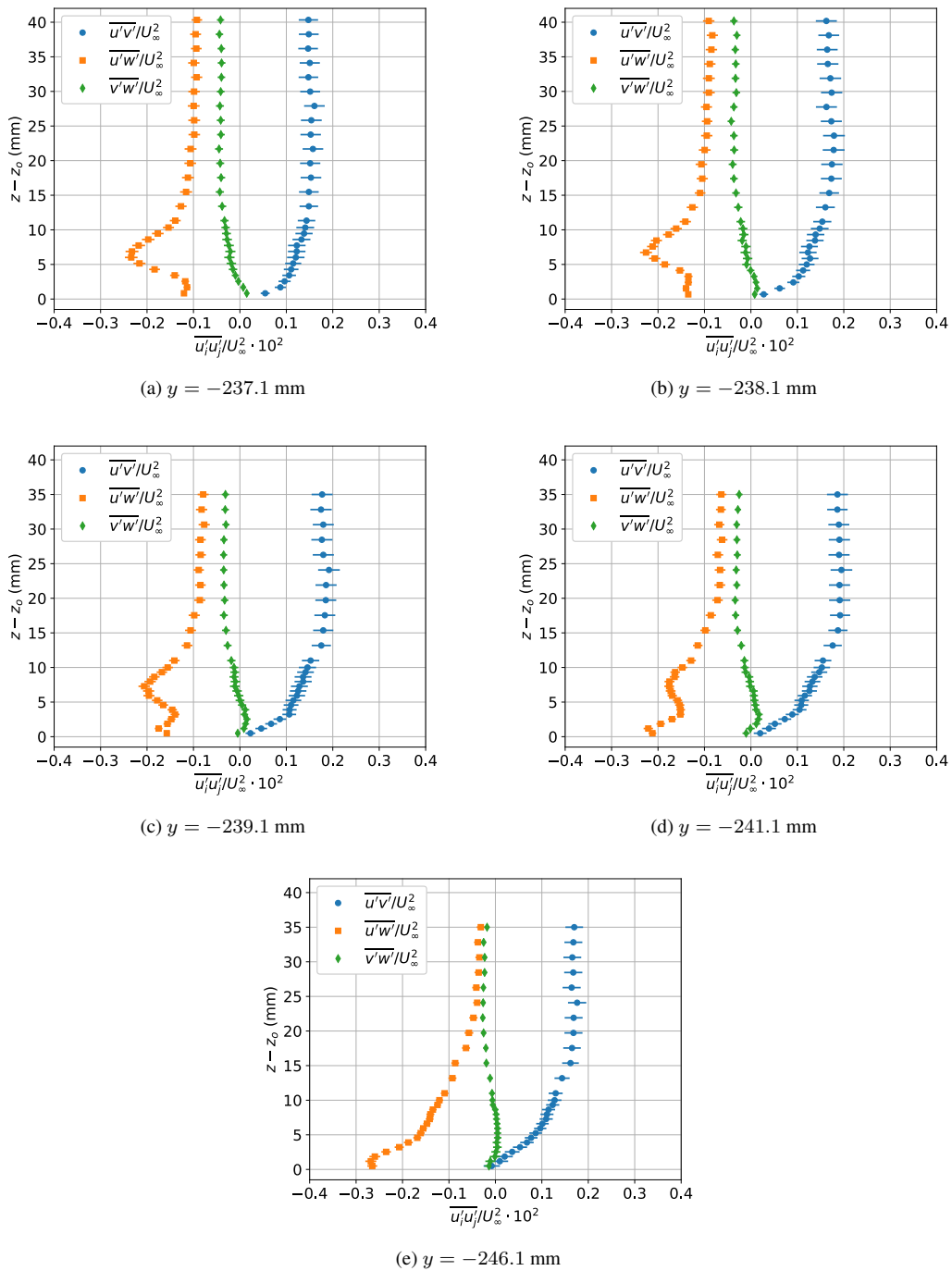(a) $y = -237.1$ mm
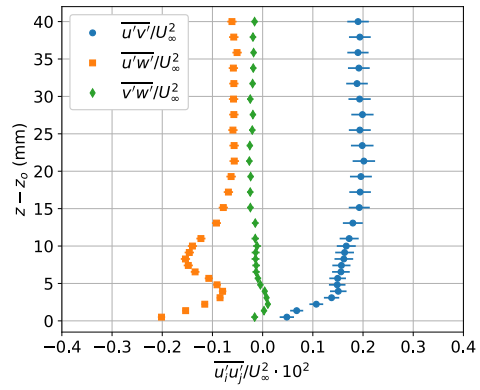
(b) $y = -239.1$ mm
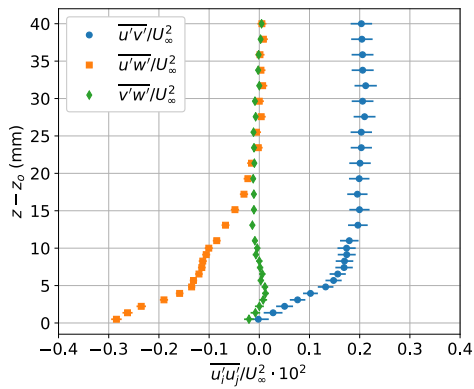
(c) $y = -246.1$ mm
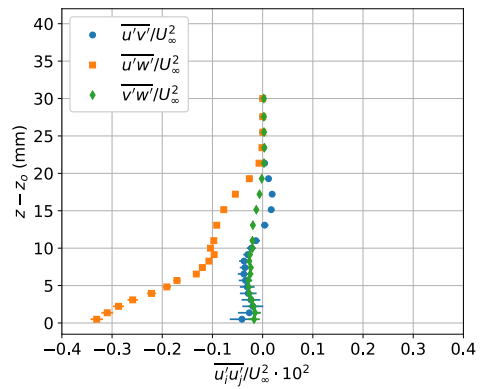
(d) $y = -266.1$ mm

Figure 104: Reynolds shear stress profiles in the corner-flow region of the F6 wing with leading-edge extension at $x = 2747.6$ mm and $\alpha = 5°$.
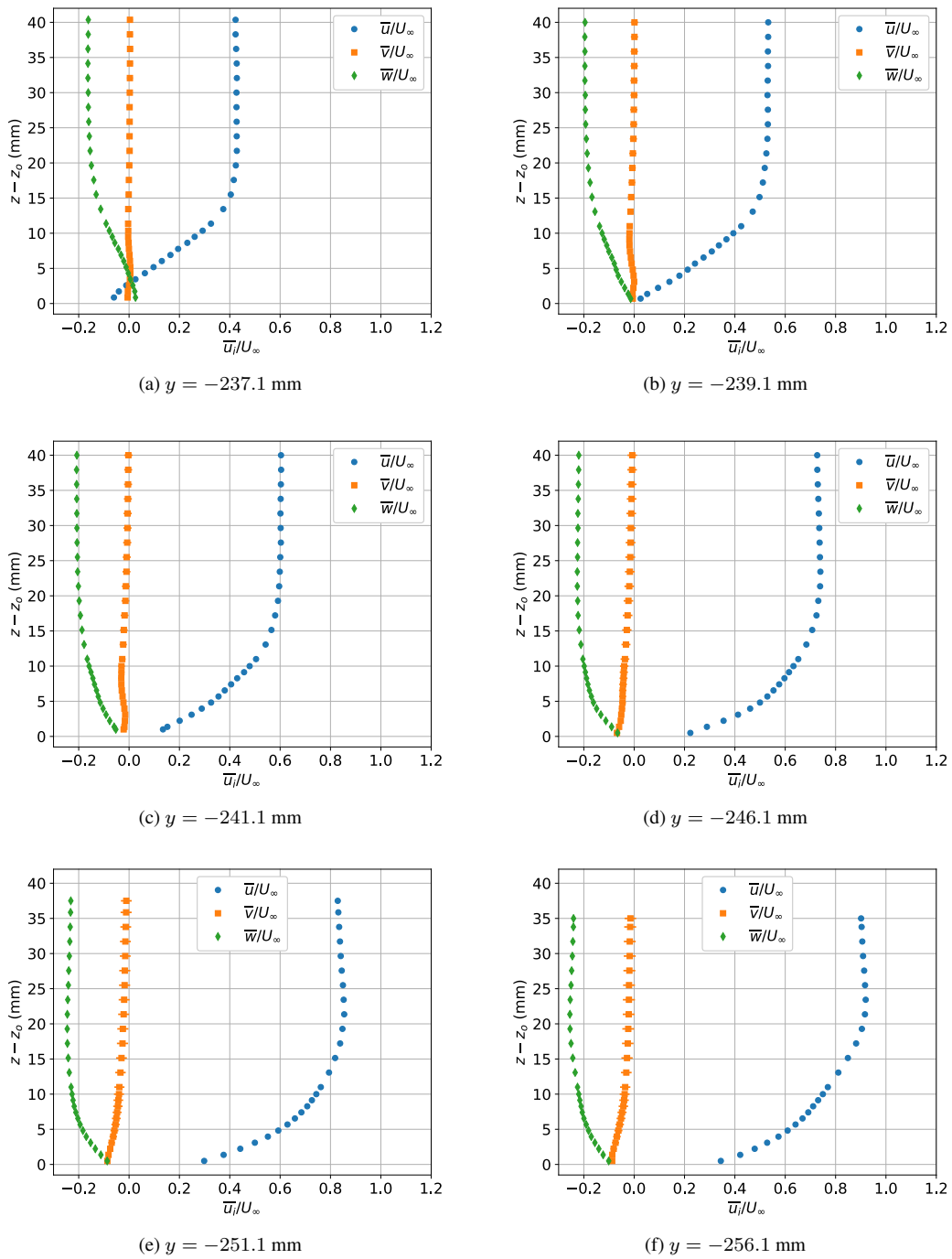
(a) $y = -236.6$ mm

(b) $y = -237.1$ mm

(c) $y = -239.1$ mm

(d) $y = -241.1$ mm

(e) $y = -246.1$ mm

(f) $y = -266.1$ mm
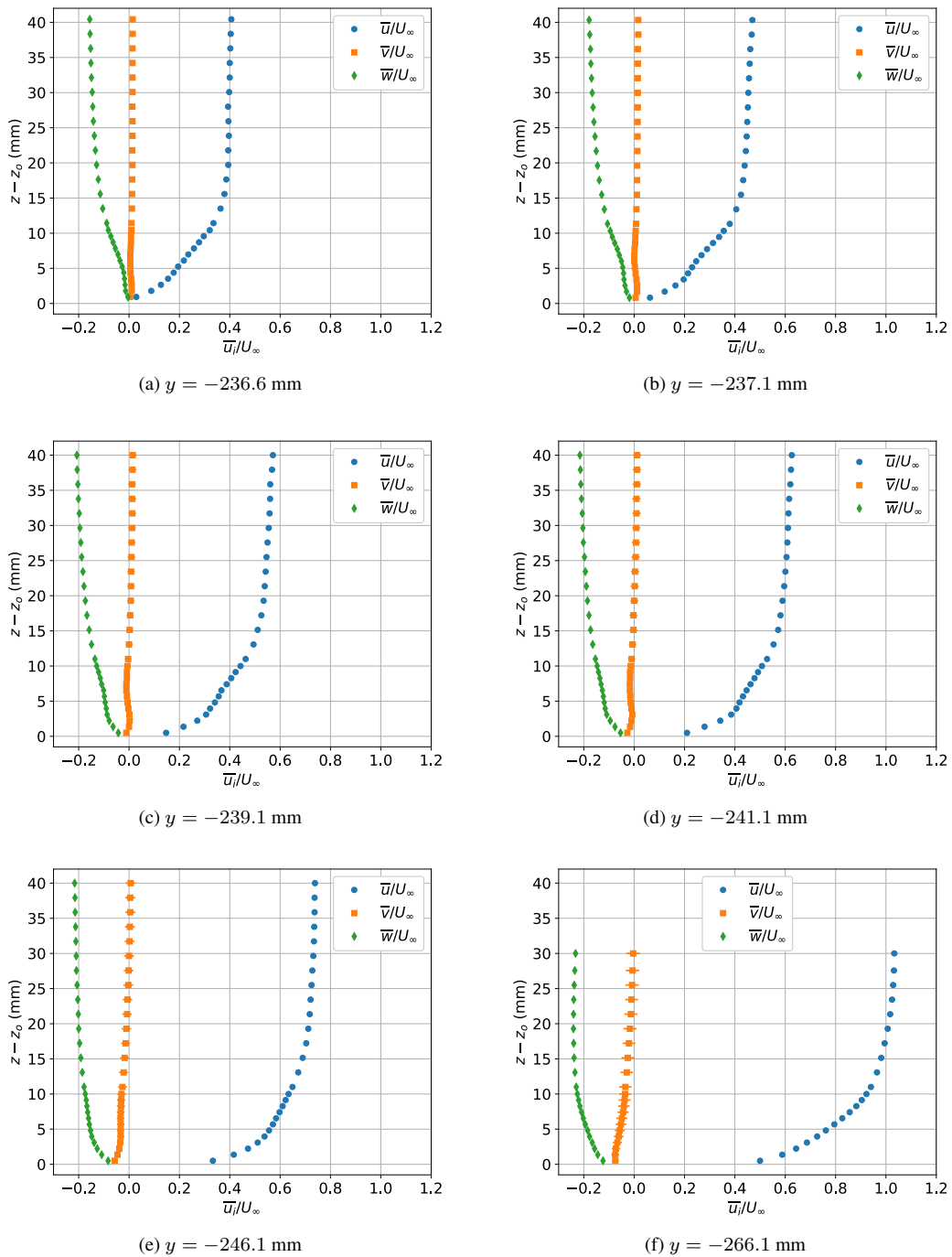
Figure 105: Mean velocity profiles in the corner-flow region of the F6 wing with leading-edge extension at $x = 2852.6$ mm and $\alpha = 5°$.
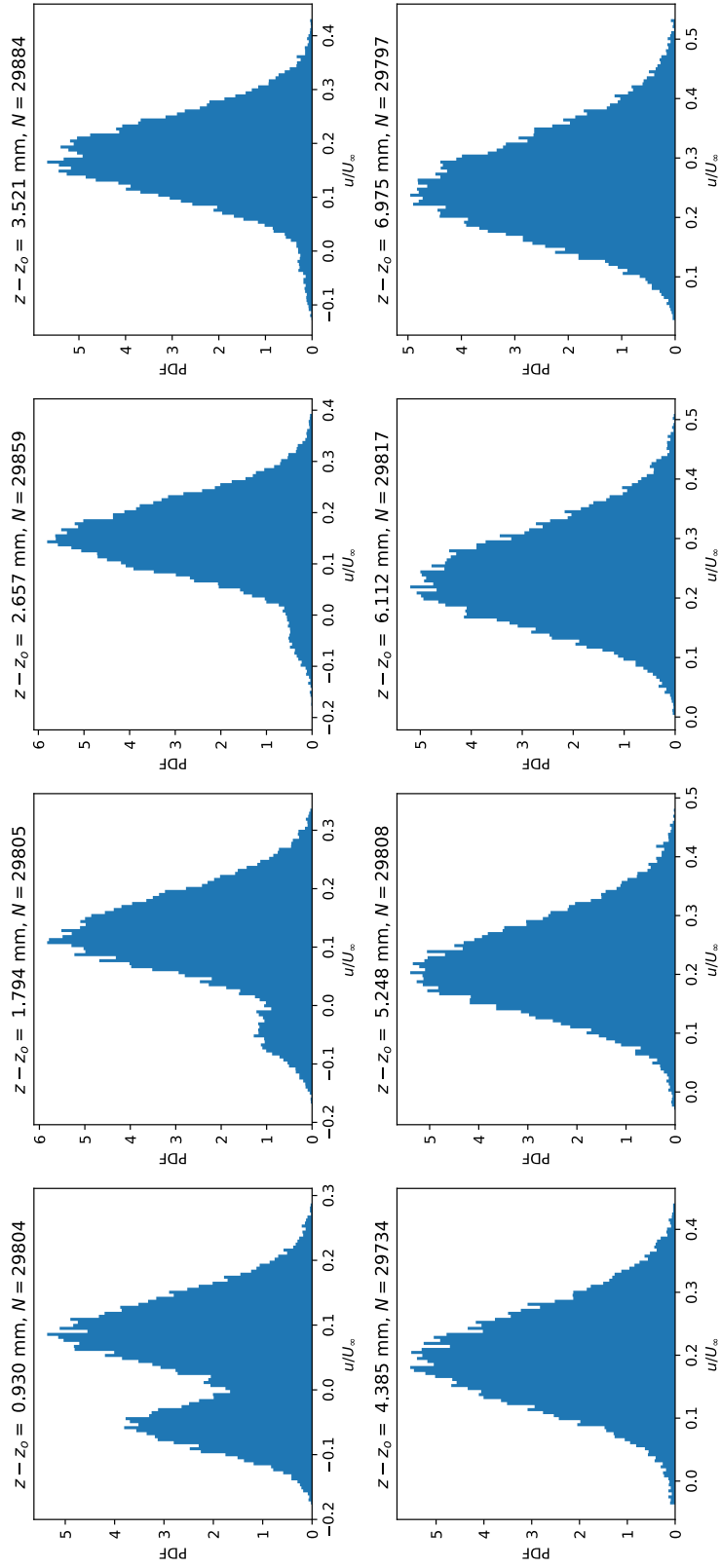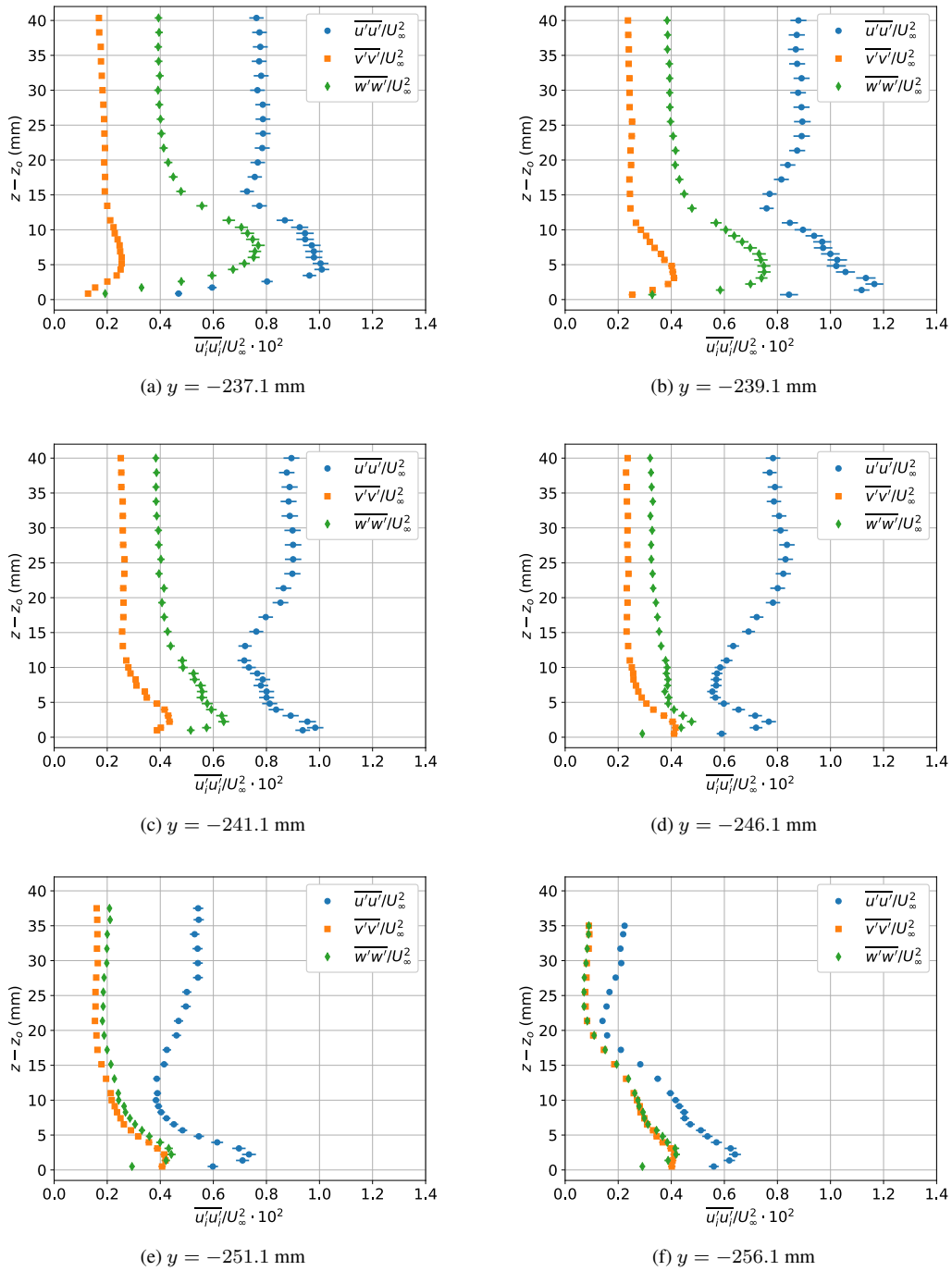
Figure 106: Probability density functions of the x-component of velocity at $x = 2852.6$ mm, $y = -236.6$ mm for several $z - z_o$ locations above the wing surface. The model was configured with the F6 wing with extension and set at a pitch angle of $5°$.

(a) $y = -236.6$ mm

(b) $y = -237.1$ mm

(c) $y = -239.1$ mm

(d) $y = -241.1$ mm

(e) $y = -246.1$ mm

(f) $y = -266.1$ mm
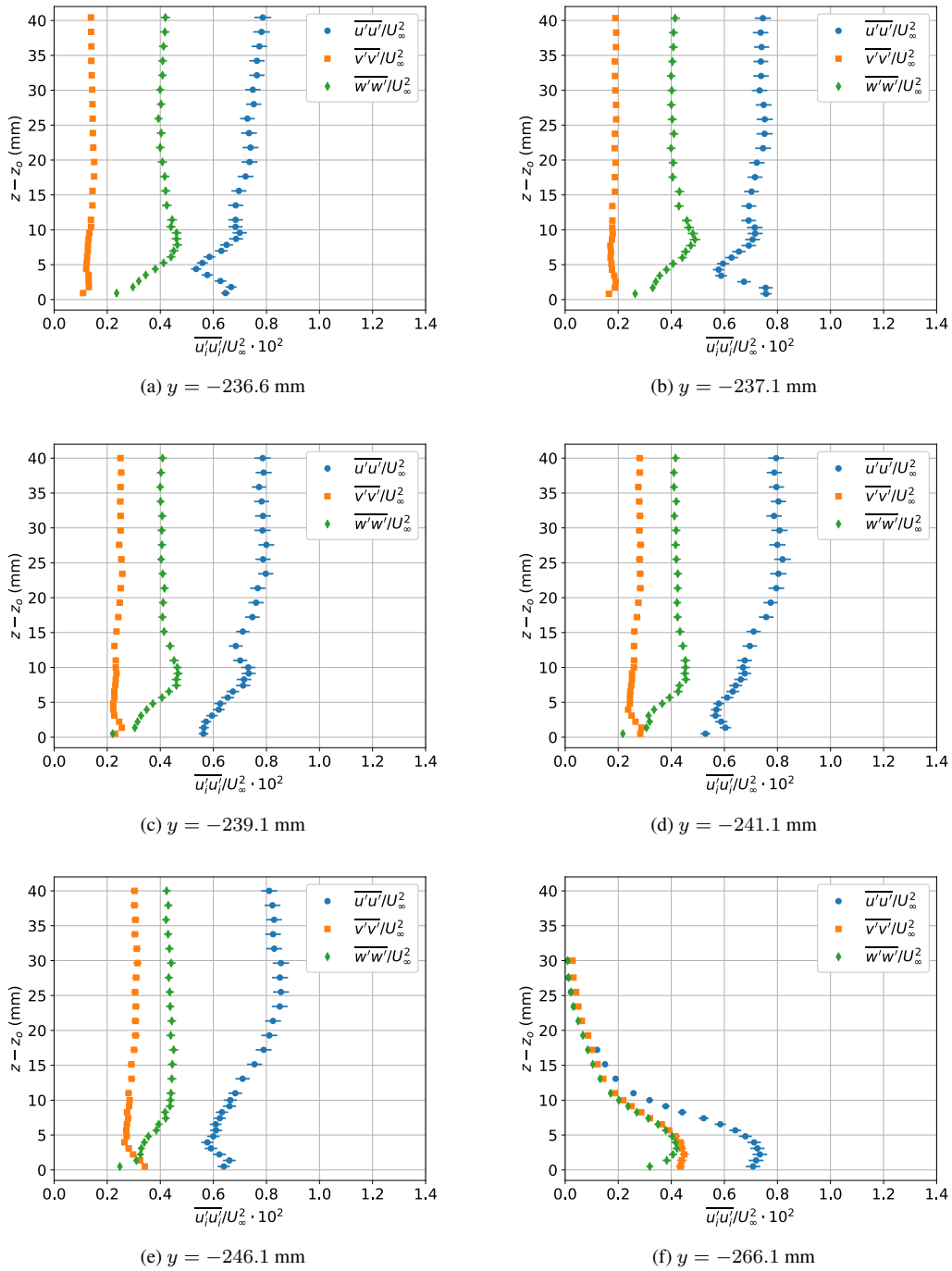
Figure 107: Reynolds normal stress profiles in the corner-flow region of the F6 wing with leading-edge extension at $x = 2852.6$ mm and $\alpha = 5°$.
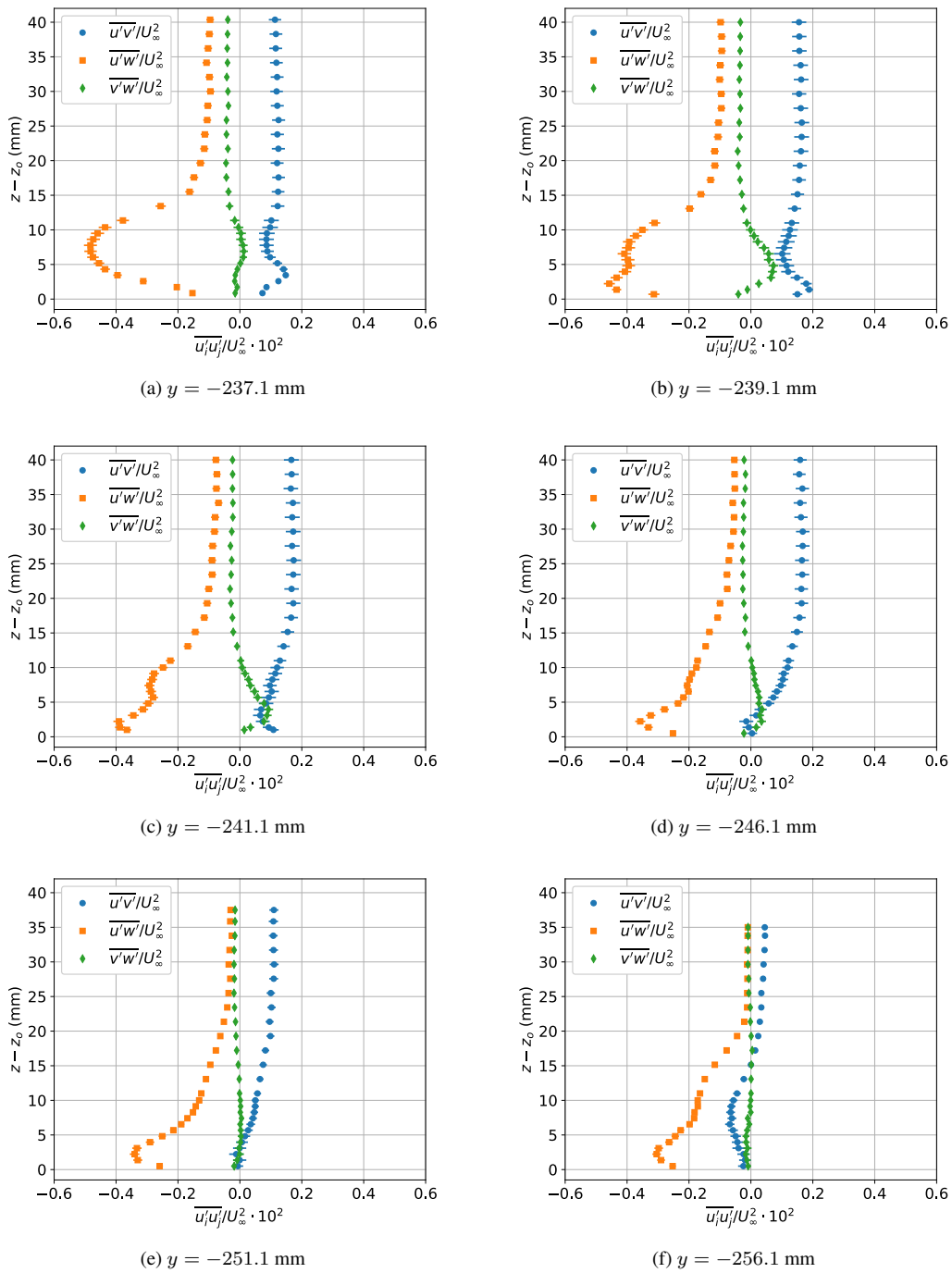
(a) $y = -236.6$ mm

(b) $y = -237.1$ mm

(c) $y = -239.1$ mm

(d) $y = -241.1$ mm

(e) $y = -246.1$ mm

(f) $y = -266.1$ mm
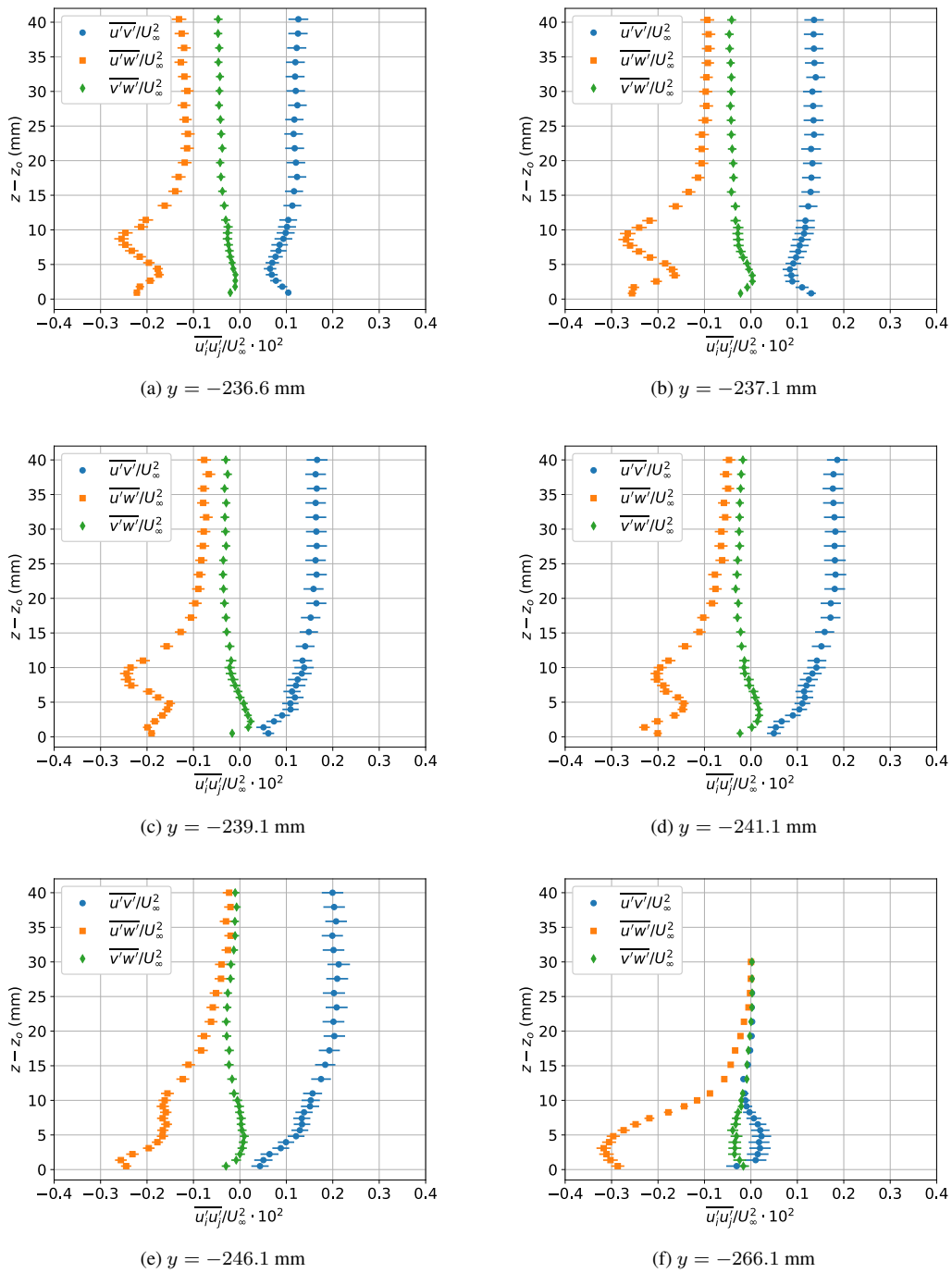
Figure 108: Reynolds shear stress profiles in the corner-flow region of the F6 wing with leading-edge extension at $x = 2852.6$ mm and $\alpha = 5°$.

(a) $y = -237.1$ mm

(b) $y = -239.1$ mm

(c) $y = -246.1$ mm

(d) $y = -251.1$ mm

(e) $y = -256.1$ mm

(f) $y = -266.1$ mm
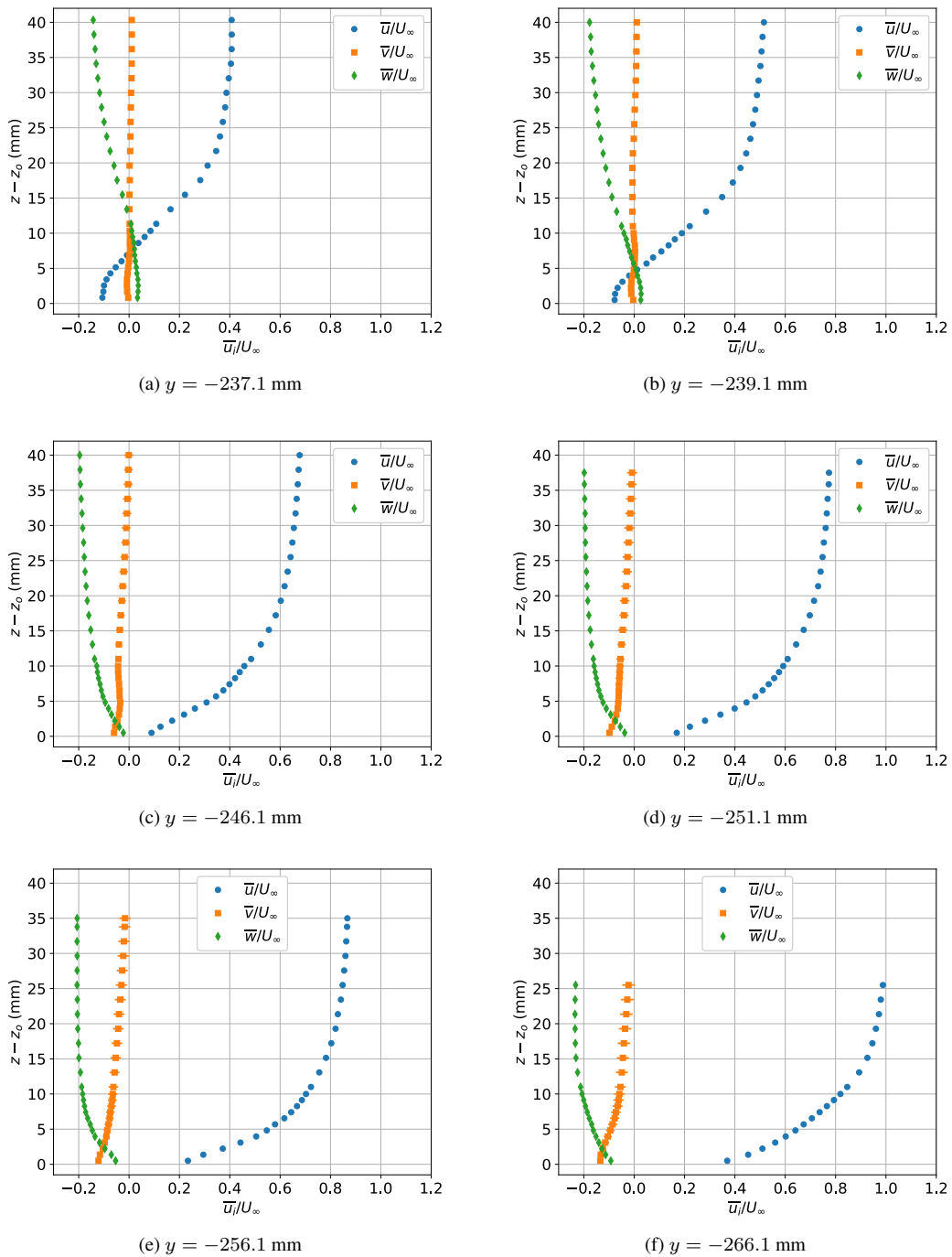
Figure 109: Mean velocity profiles in the corner-flow region of the F6 wing with leading-edge extension at $x = 2892.6$ mm and $\alpha = 5°$.

(a) $y = -237.1$ mm

(b) $y = -239.1$ mm

(c) $y = -246.1$ mm

(d) $y = -251.1$ mm

(e) $y = -256.1$ mm

(f) $y = -266.1$ mm
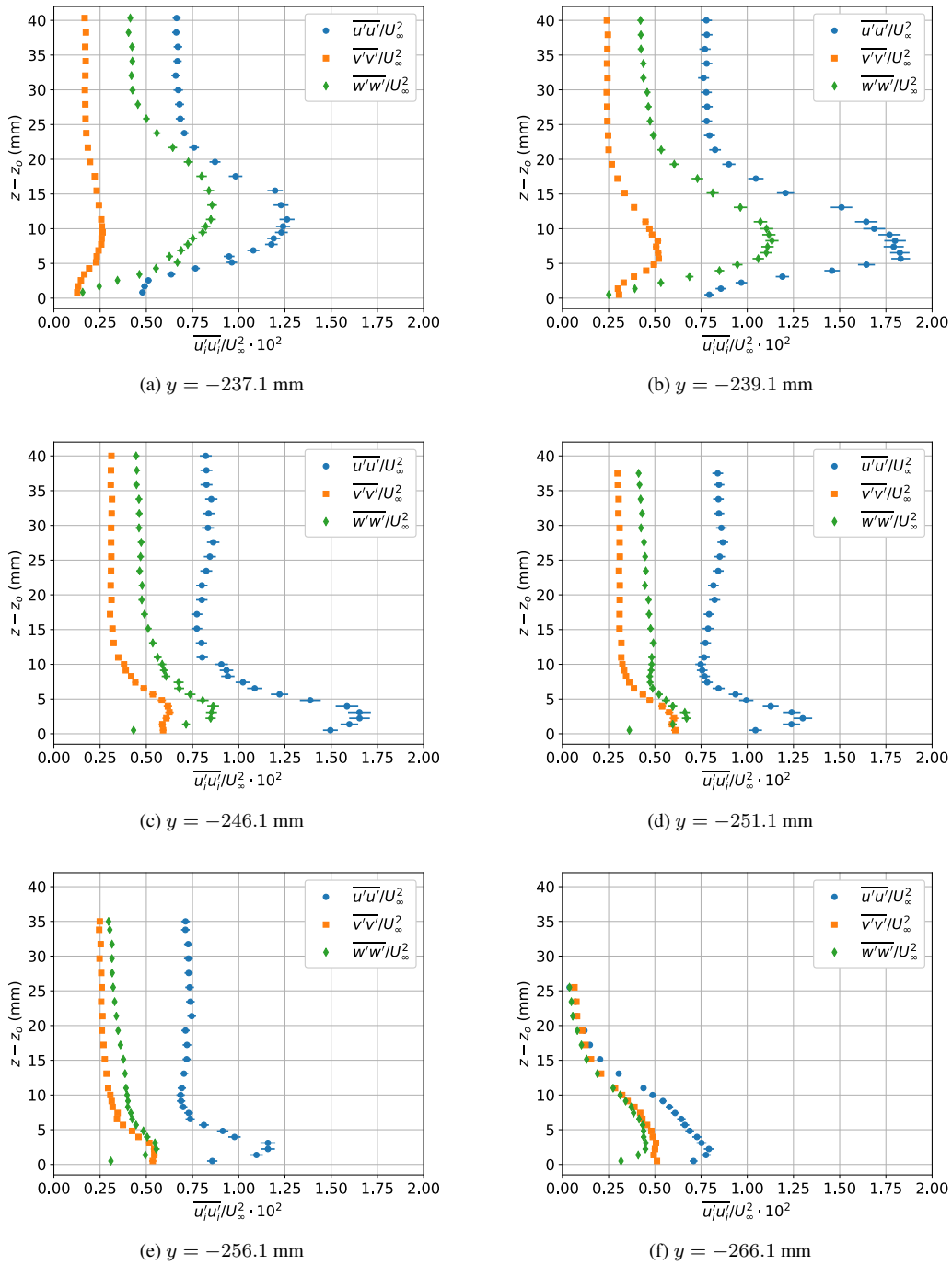
Figure 110: Reynolds normal stress profiles in the corner-flow region of the F6 wing with leading-edge extension at $x = 2892.6$ mm and $\alpha = 5°$.

(a) $y = -237.1$ mm

(b) $y = -239.1$ mm

(c) $y = -246.1$ mm

(d) $y = -251.1$ mm

(e) $y = -256.1$ mm

(f) $y = -266.1$ mm
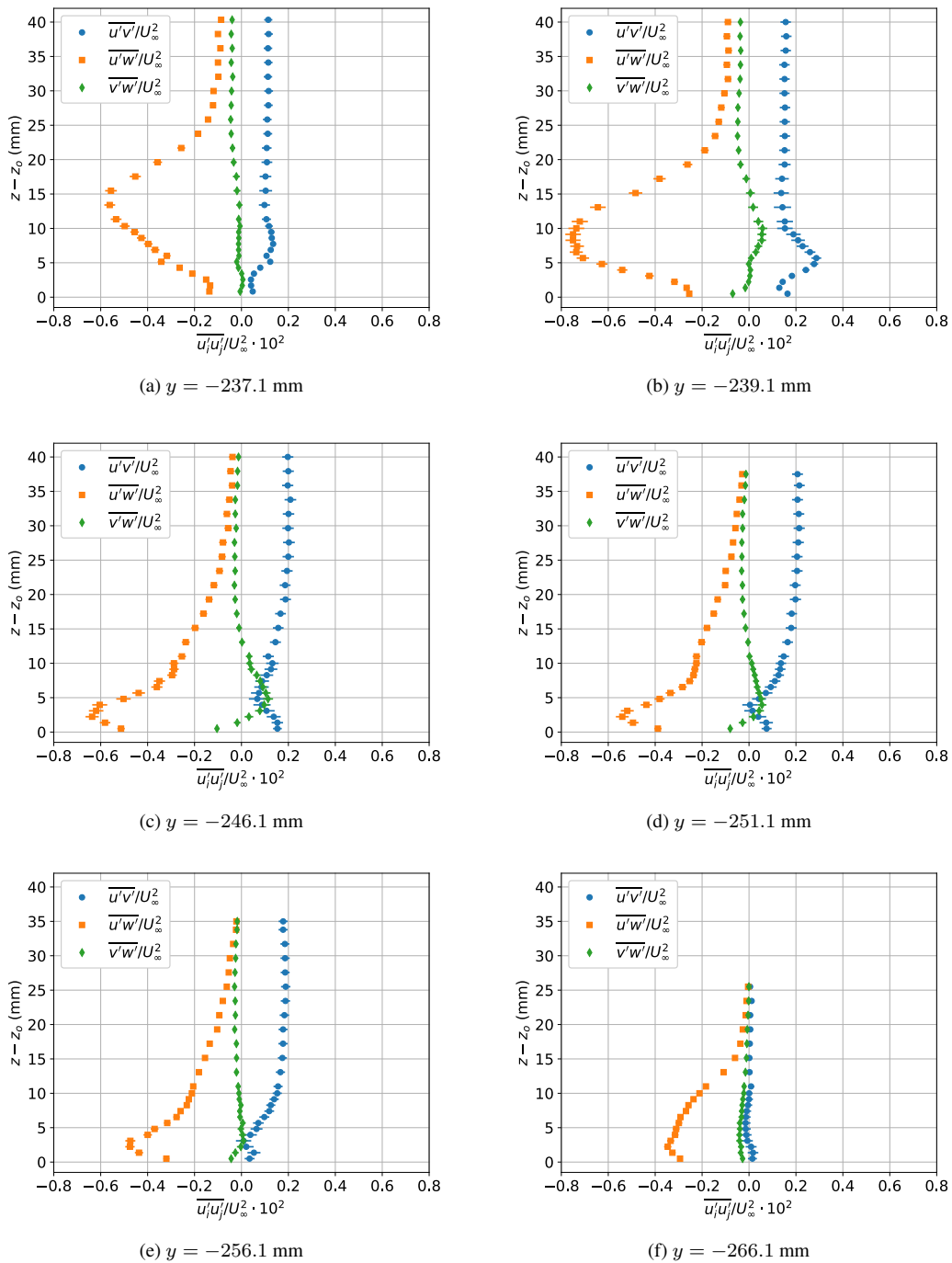
Figure 111: Reynolds shear stress profiles in the corner-flow region of the F6 wing with leading-edge extension at $x = 2892.6$ mm and $\alpha = 5°$.

(a) $y = -237.1$ mm

(b) $y = -239.1$ mm

(c) $y = -241.1$ mm

(d) $y = -246.1$ mm

(e) $y = -266.1$ mm
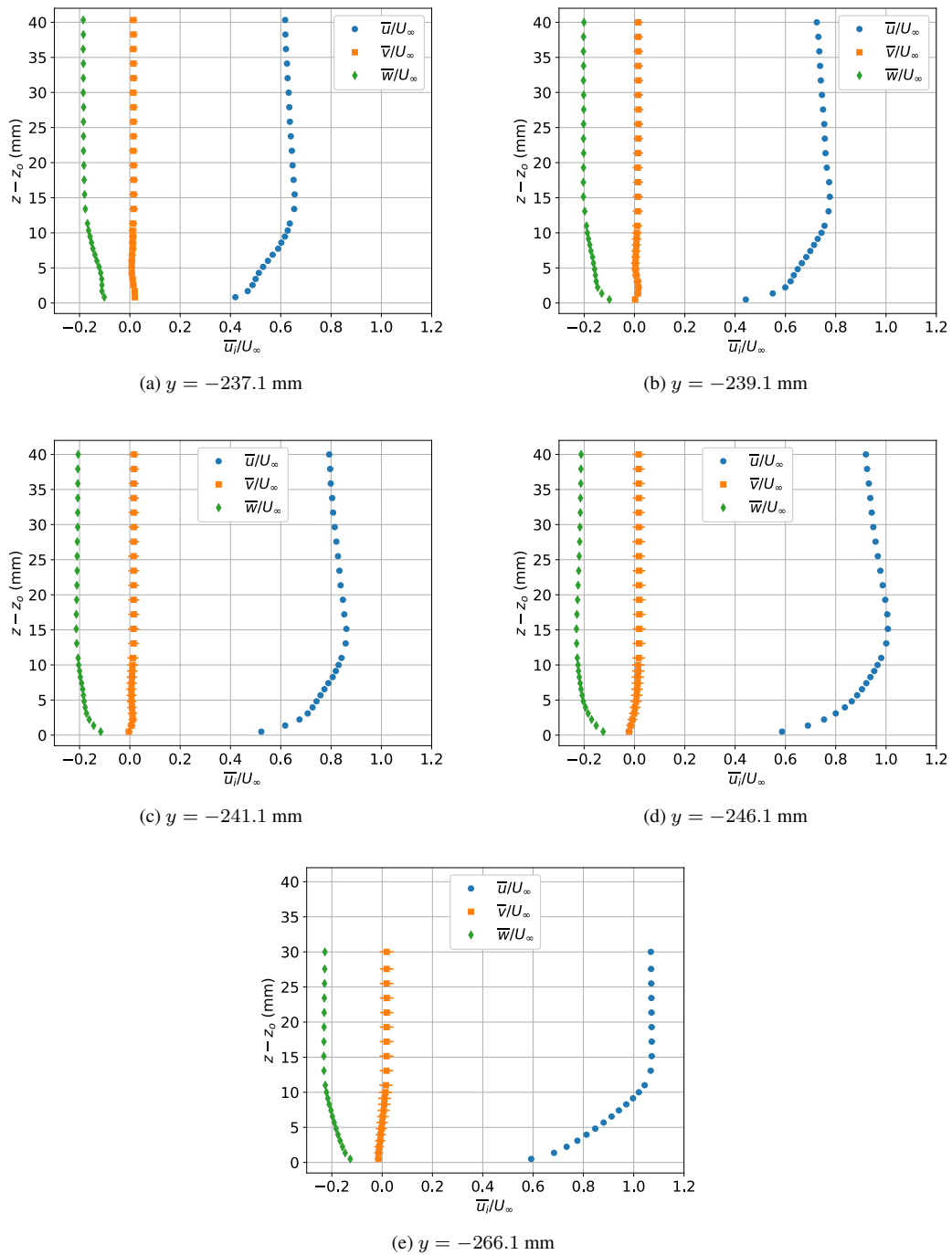
Figure 112: Mean velocity profiles in the corner-flow region of the F6 wing with leading-edge extension at $x = 2757.6$ mm and $\alpha = -2.5°$.

(a) $y = -237.1$ mm

(b) $y = -239.1$ mm

(c) $y = -241.1$ mm

(d) $y = -246.1$ mm

(e) $y = -266.1$ mm
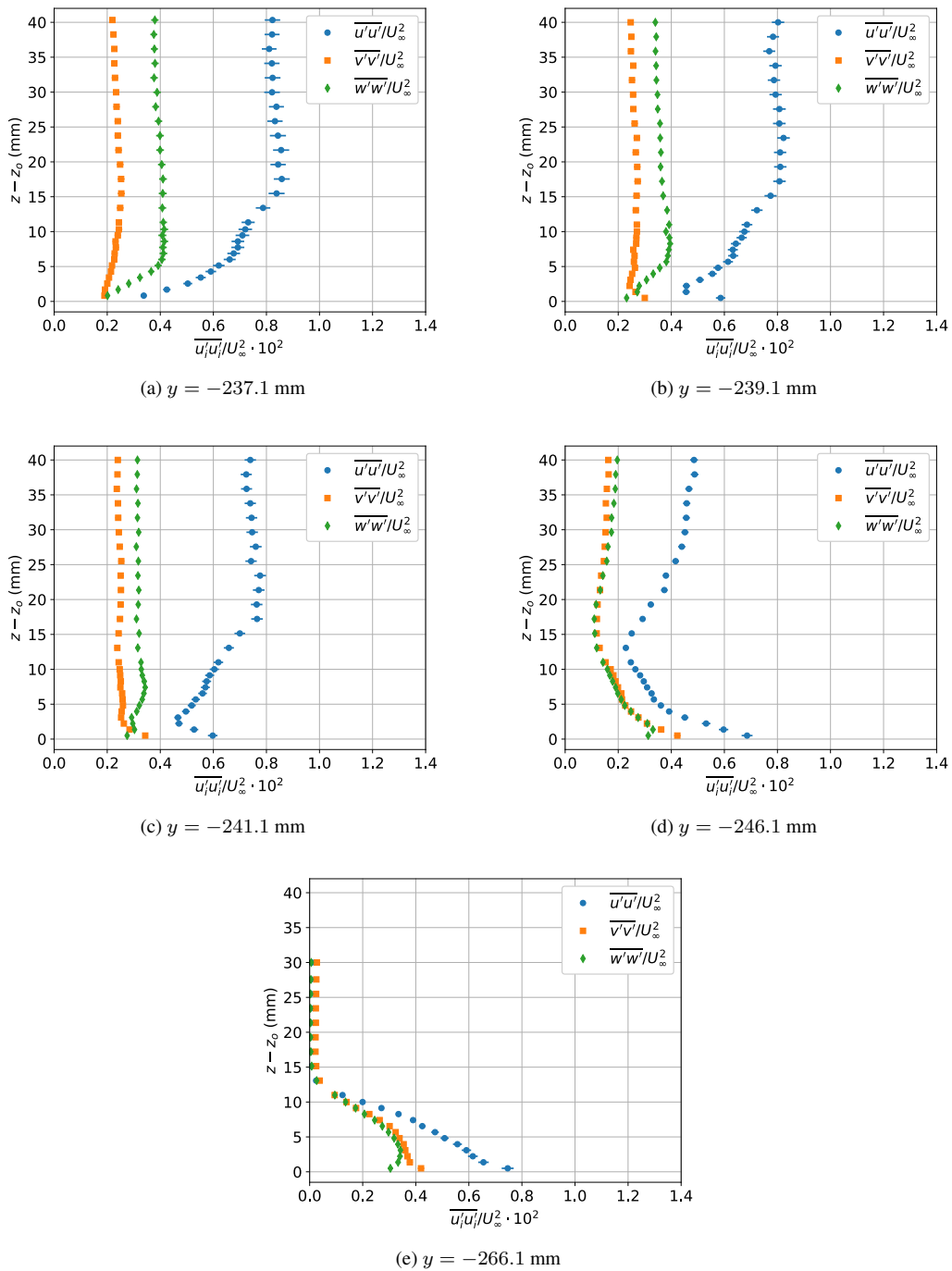
Figure 113: Reynolds normal stress profiles in the corner-flow region of the F6 wing with leading-edge extension at $x = 2757.6$ mm and $\alpha = -2.5°$.

(a) $y = -237.1$ mm

(b) $y = -239.1$ mm

(c) $y = -241.1$ mm

(d) $y = -246.1$ mm

(e) $y = -266.1$ mm
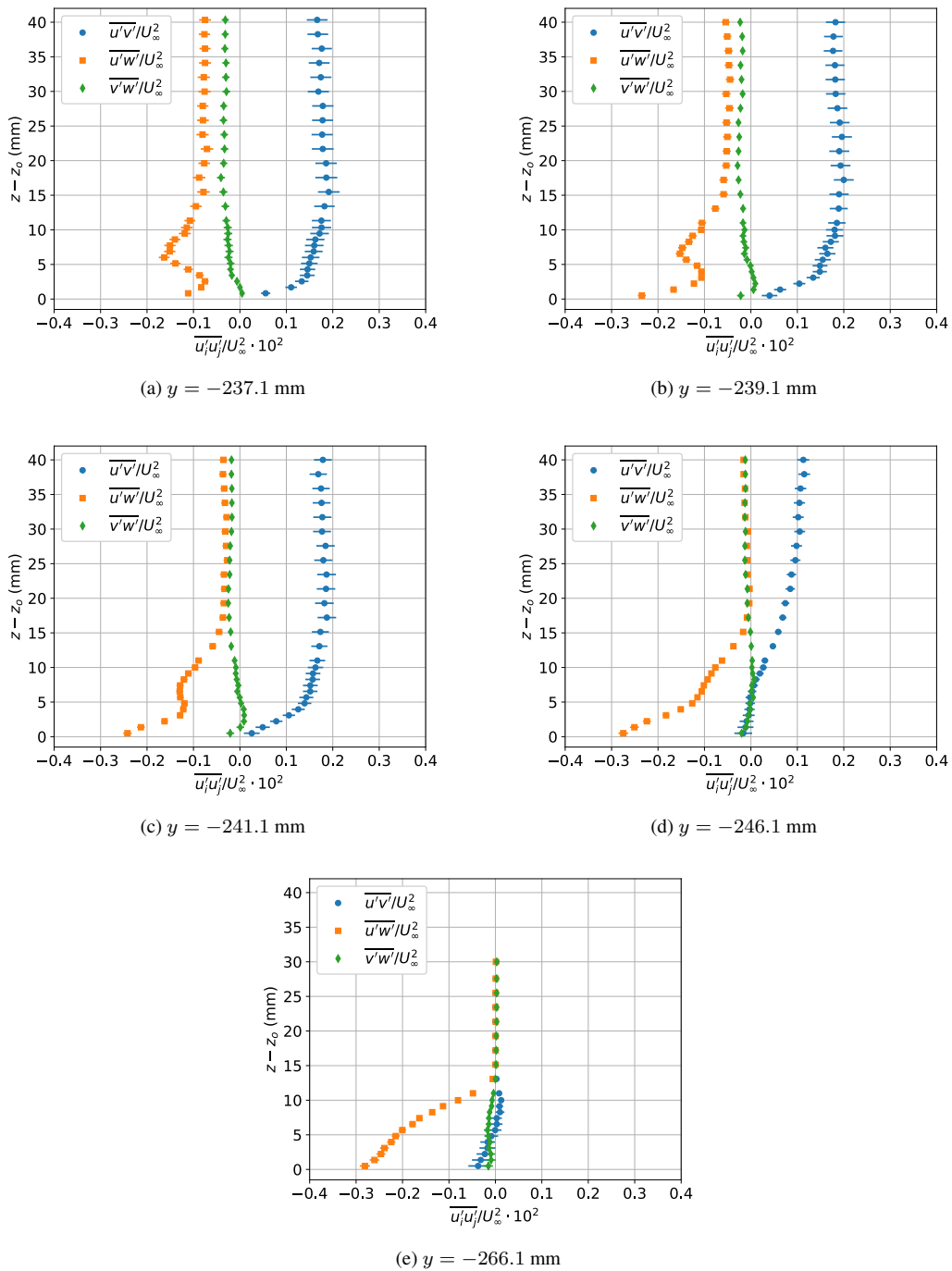
Figure 114: Reynolds shear stress profiles in the corner-flow region of the F6 wing with leading-edge extension at $x = 2757.6$ mm and $\alpha = -2.5°$.

(a) $y = -237.1$ mm

(b) $y = -238.1$ mm

(c) $y = -239.1$ mm

(d) $y = -241.1$ mm

(e) $y = -246.1$ mm

Figure 115: Mean velocity profiles in the corner-flow region of the F6 wing with leading-edge extension at $x = 2887.6$ mm and $\alpha = -2.5°$.

(a) $y = -237.1$ mm

(b) $y = -238.1$ mm

(c) $y = -239.1$ mm

(d) $y = -241.1$ mm

(e) $y = -246.1$ mm

Figure 116: Reynolds normal stress profiles in the corner-flow region of the F6 wing with leading-edge extension at $x = 2887.6$ mm and $\alpha = -2.5°$.

(a) $y = -237.1$ mm

(b) $y = -238.1$ mm

(c) $y = -239.1$ mm

(d) $y = -241.1$ mm

(e) $y = -246.1$ mm

Figure 117: Reynolds shear stress profiles in the corner-flow region of the F6 wing with leading-edge extension at $x = 2887.6$ mm and $\alpha = -2.5°$.

(a) $y = -237.1$ mm

(b) $y = -239.1$ mm

(c) $y = -241.1$ mm

(d) $y = -246.1$ mm

(e) $y = -251.1$ mm

(f) $y = -256.1$ mm

Figure 118: Mean velocity profiles in the corner-flow region of the F6 wing with leading-edge extension at $x = 2922.6$ mm and $\alpha = -2.5°$.

(a) $y = -237.1$ mm

(b) $y = -239.1$ mm

(c) $y = -241.1$ mm

(d) $y = -246.1$ mm

(e) $y = -251.1$ mm

(f) $y = -256.1$ mm

Figure 119: Reynolds normal stress profiles in the corner-flow region of the F6 wing with leading-edge extension at $x = 2922.6$ mm and $\alpha = -2.5°$.

(a) $y = -237.1$ mm

(b) $y = -239.1$ mm

(c) $y = -241.1$ mm

(d) $y = -246.1$ mm

(e) $y = -251.1$ mm

(f) $y = -256.1$ mm

Figure 120: Reynolds shear stress profiles in the corner-flow region of the F6 wing with leading-edge extension at $x = 2922.6$ mm and $\alpha = -2.5°$.
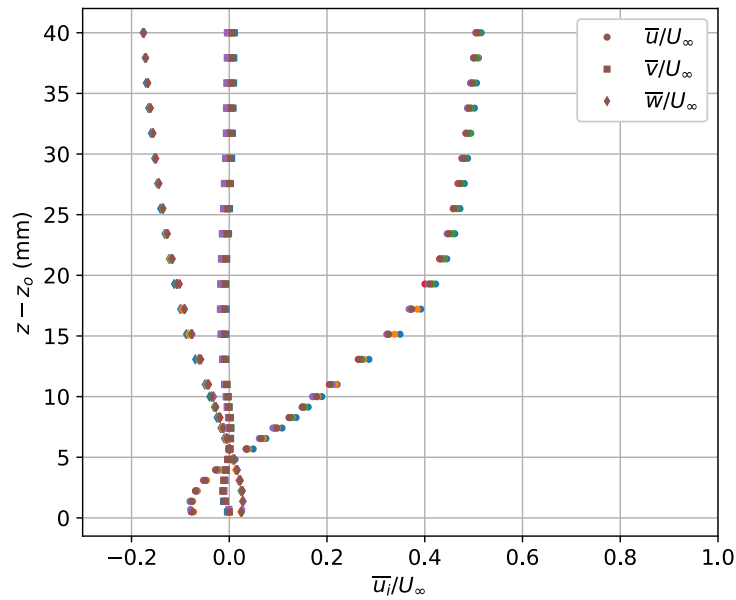
Figure 121: Repeat measurements of the mean velocity profiles at $x = 2892.6$ mm, $y = -239.1$ mm, and $\alpha = 5°$ on the F6 wing with leading-edge extension.
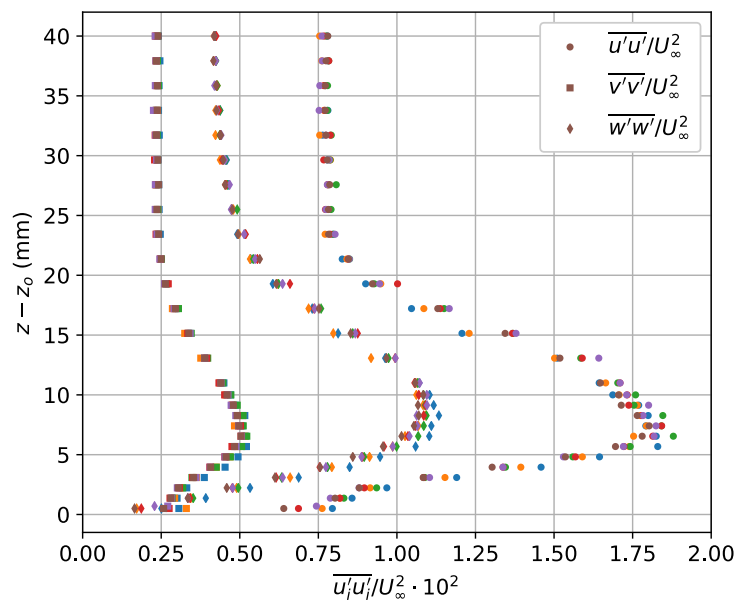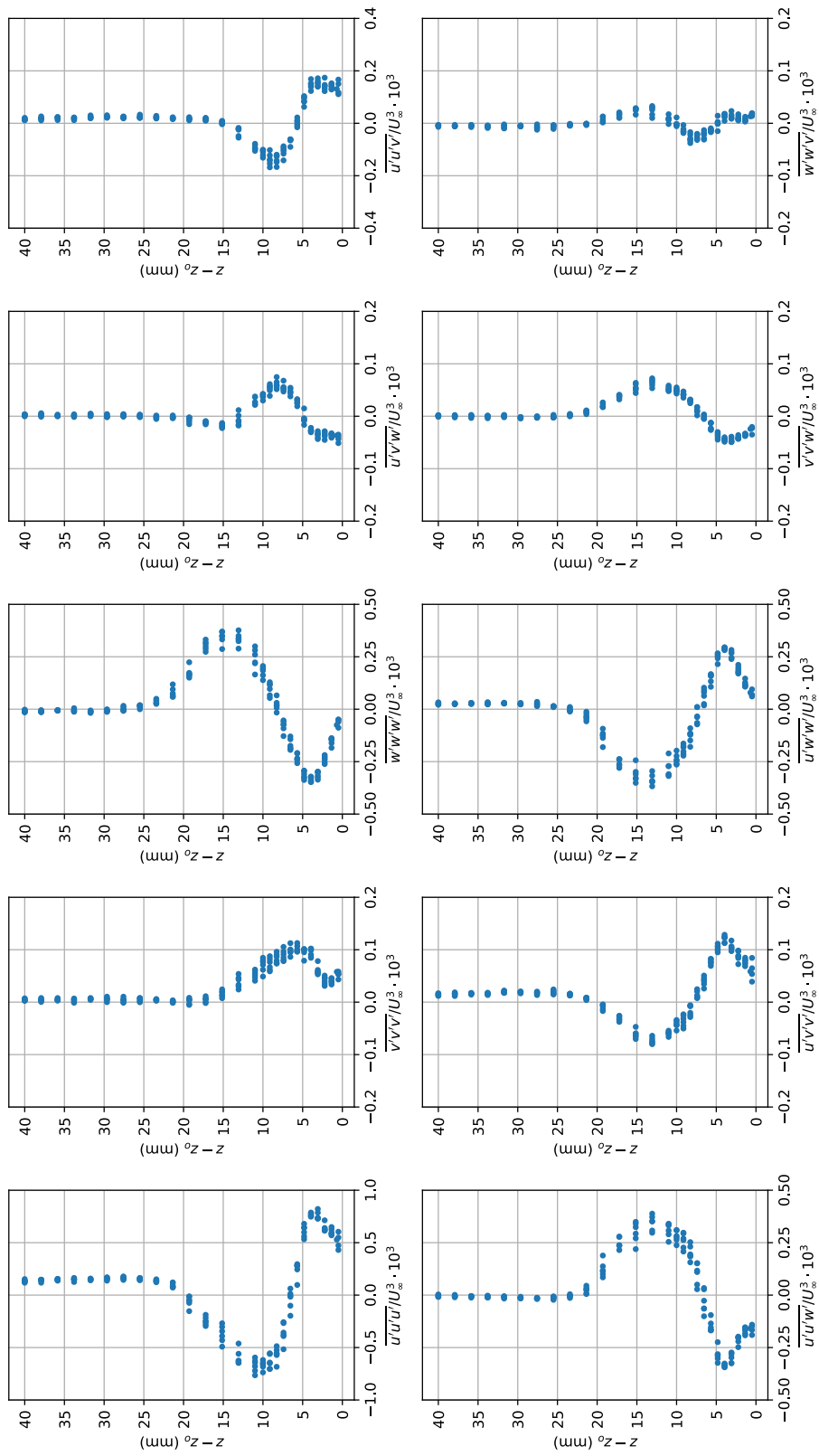

Figure 122: Repeat measurements of the Reynolds normal stress profiles at $x = 2892.6$ mm, $y = -239.1$ mm, and $\alpha = 5°$ on the F6 wing with leading-edge extension.
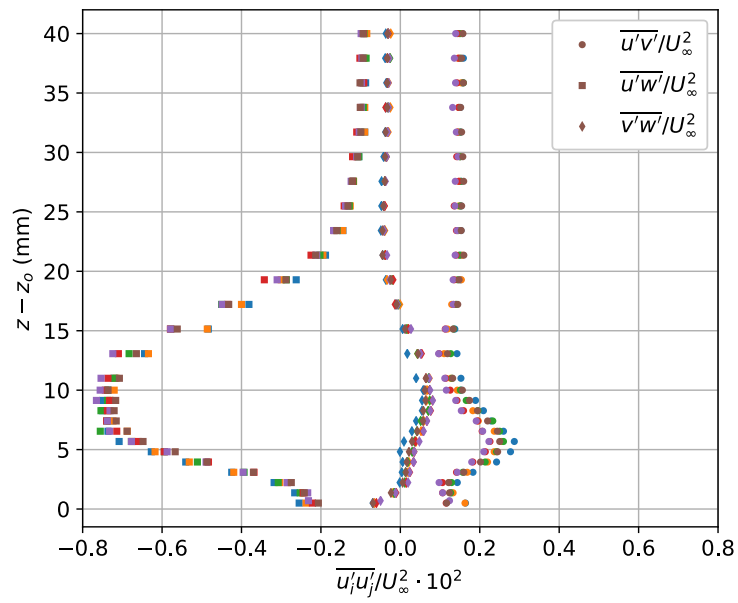
Figure 123: Repeat measurements of the Reynolds shear stress profiles at $x = 2892.6$ mm, $y = -239.1$ mm, and $\alpha = 5°$ on the F6 wing with leading-edge extension.
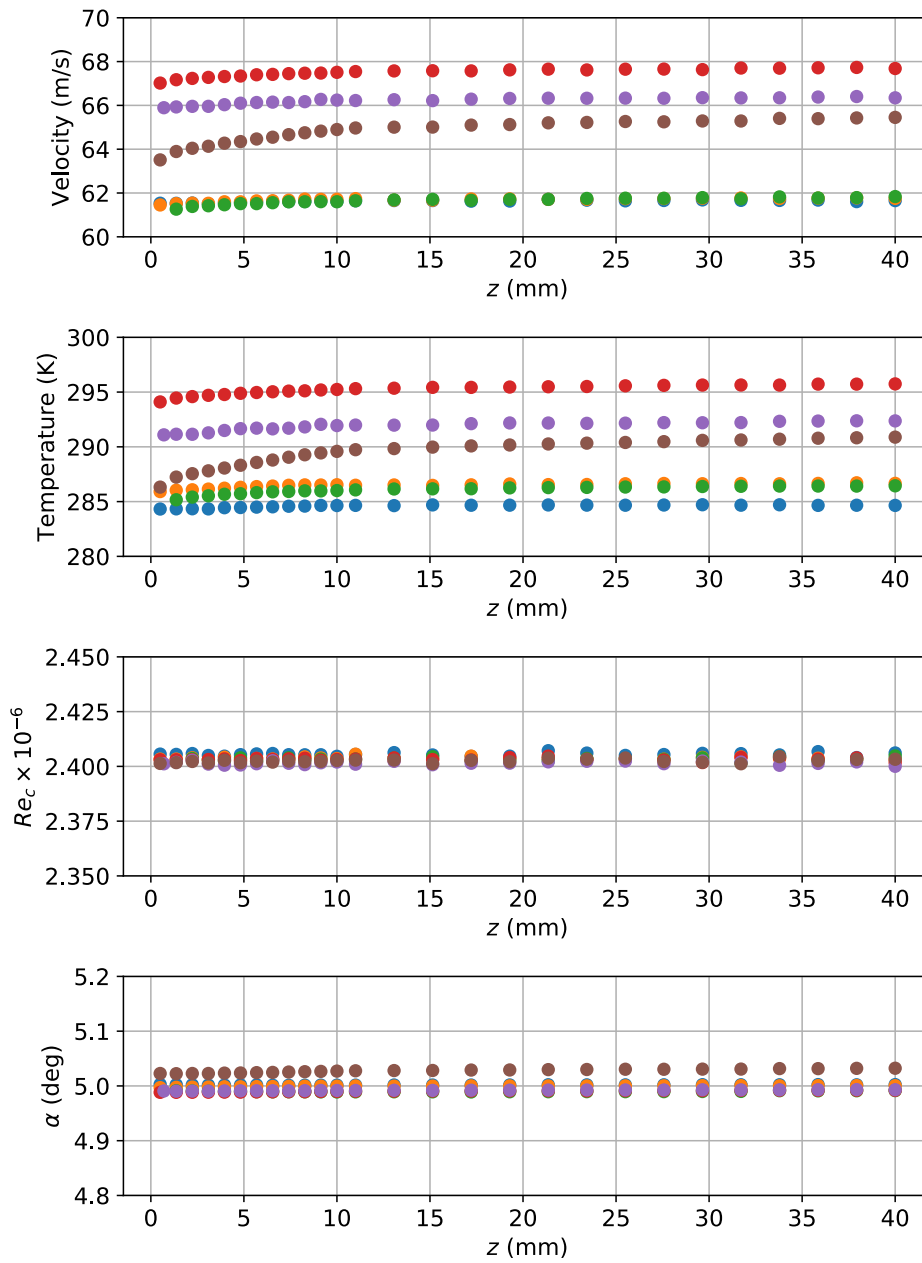
Figure 124: Tunnel conditions during repeat profile measurements at $x = 2892.6$ mm, $y = -239.1$ mm, and $\alpha = 5°$ on the F6 wing with leading-edge extension. Each color represents a different repeat profile at this location on the junction model.
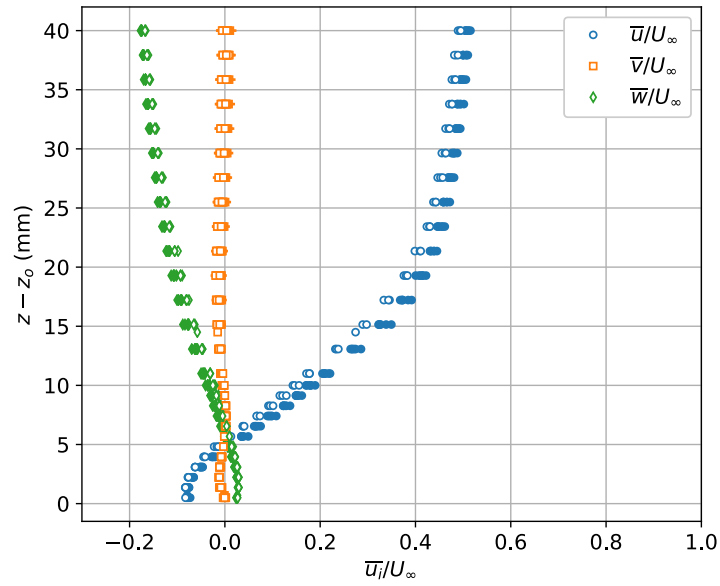
Figure 125: Repeat measurements of the mean velocity profiles at $x = 2892.6$ mm, $y = -239.1$ mm, and $\alpha = 5°$ on the F6 wing with leading-edge extension. The closed symbols denote data acquired at a roll angle of $0°$ while the open symbols denote data acquired at a roll angle of $180°$.
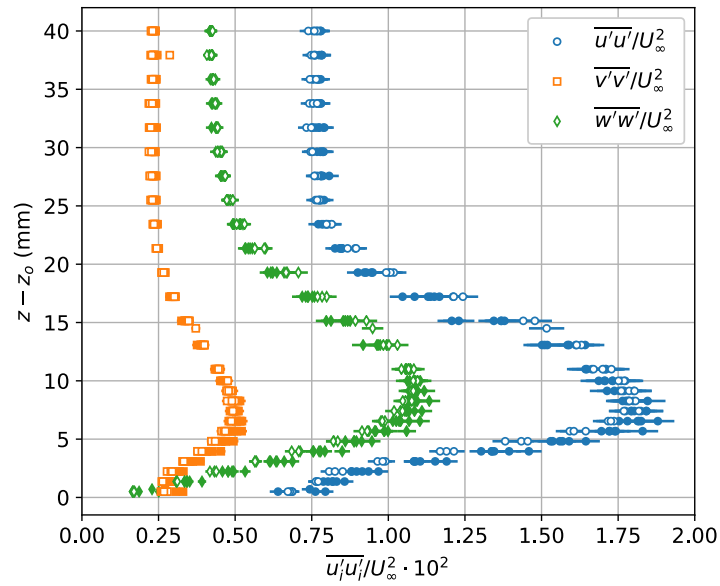
Figure 126: Repeat measurements of the Reynolds normal stress profiles at $x = 2892.6$ mm, $y = -239.1$ mm, and $\alpha = 5°$ on the F6 wing with leading-edge extension. The closed symbols denote data acquired at a roll angle of $0°$ while the open symbols denote data acquired at a roll angle of $180°$.
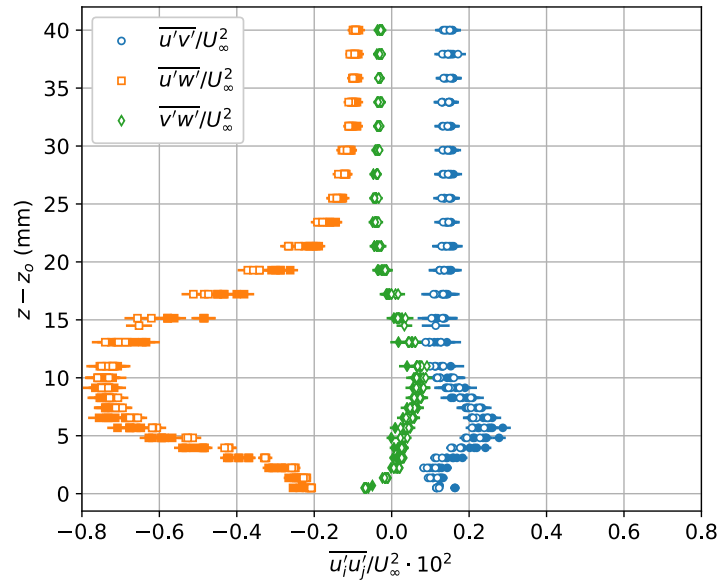
Figure 127: Repeat measurements of the Reynolds shear stress profiles at $x = 2892.6$ mm, $y = -239.1$ mm, and $\alpha = 5°$ on the F6 wing with leading-edge extension. The closed symbols denote data acquired at a roll angle of $0°$ while the open symbols denote data acquired at a roll angle of $180°$.
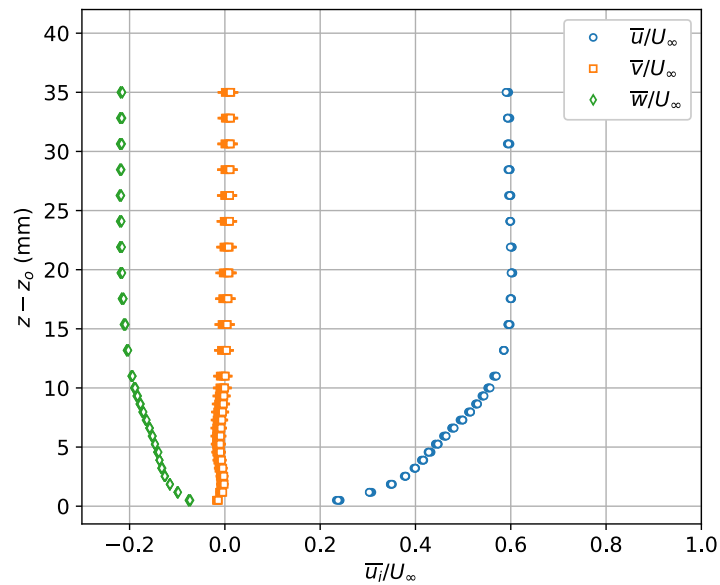
Figure 128: Repeat measurements of the mean velocity profiles at $x = 2887.6$ mm, $y = -239.1$ mm, and $\alpha = -2.5°$ on the F6 wing with leading-edge extension. The closed symbols denote data acquired at a roll angle of $0°$ while the open symbols denote data acquired at a roll angle of $180°$.
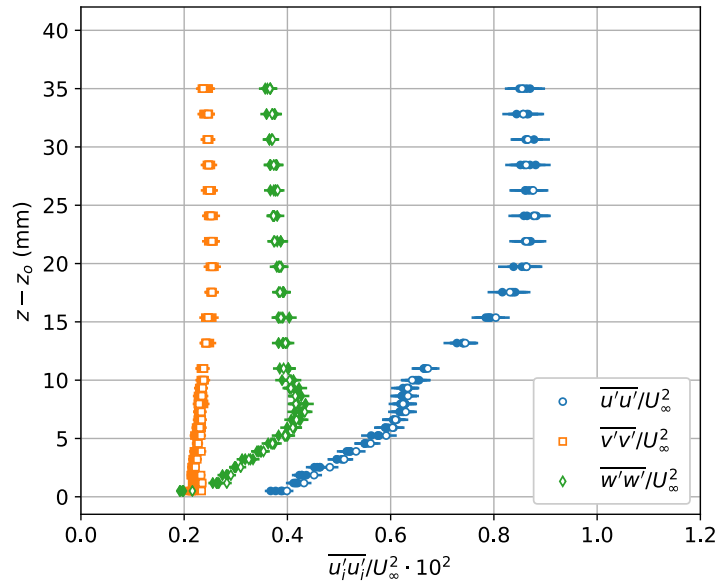
Figure 129: Repeat measurements of the Reynolds normal stress profiles at $x = 2887.6$ mm, $y = -239.1$ mm, and $\alpha = -2.5°$ on the F6 wing with leading-edge extension. The closed symbols denote data acquired at a roll angle of $0°$ while the open symbols denote data acquired at a roll angle of $180°$.
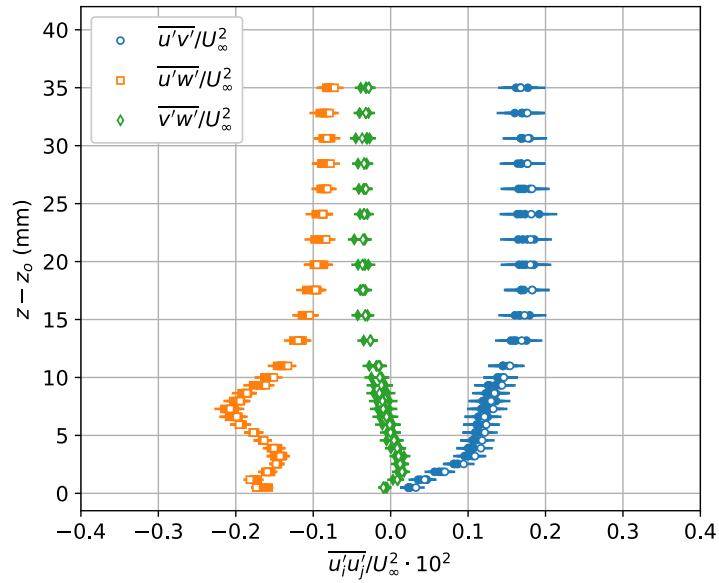
Figure 130: Repeat measurements of the Reynolds shear stress profiles at $x = 2887.6$ mm, $y = -239.1$ mm, and $\alpha = -2.5°$ on the F6 wing with leading-edge extension. The closed symbols denote data acquired at a roll angle of $0°$ while the open symbols denote data acquired at a roll angle of $180°$.
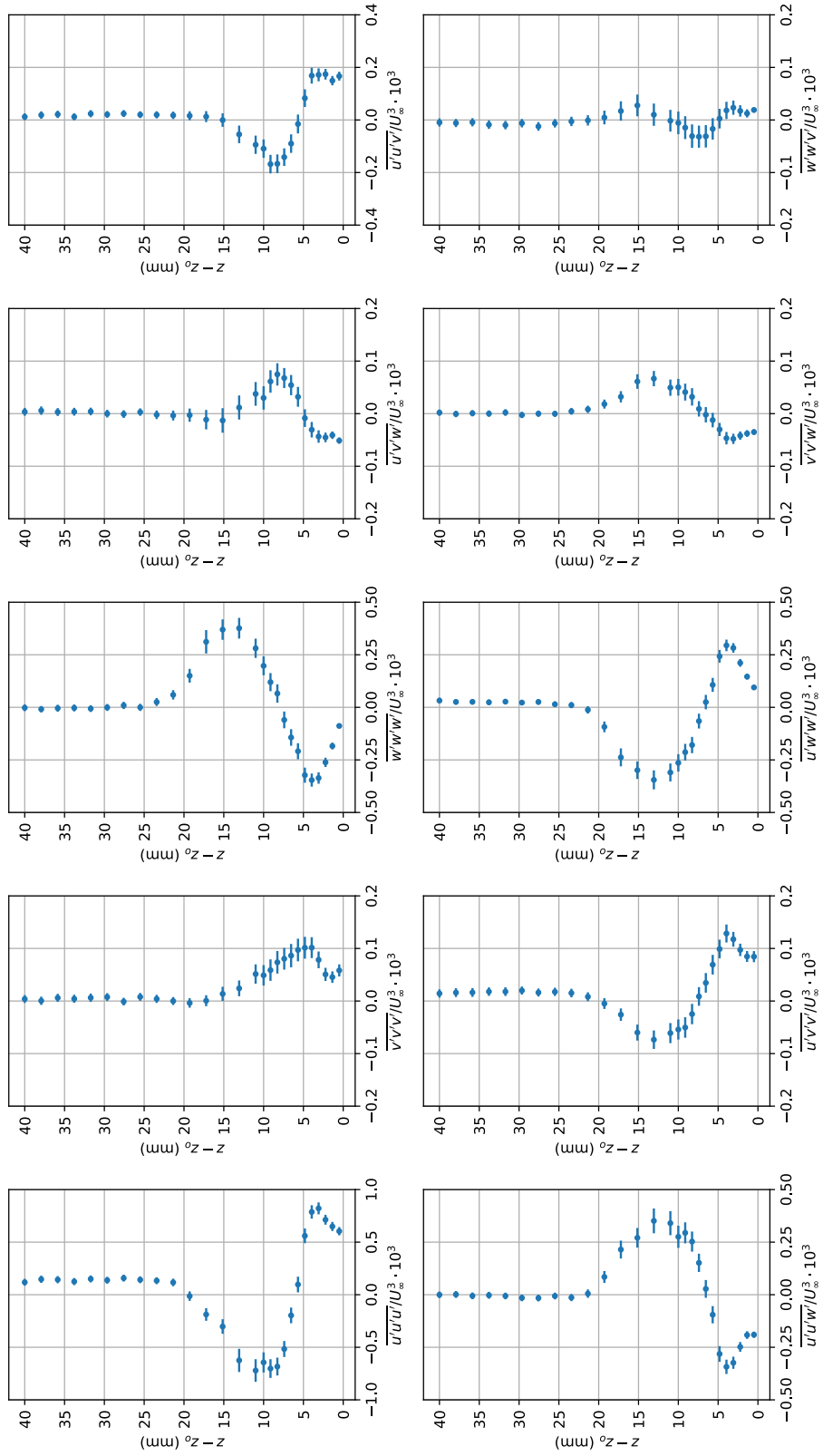
Figure 131: Triple products of the velocity components at $x = 2892.6$ mm, $y = -239.1$ mm, and $\alpha = 5°$ on the F6 wing with leading-edge extension.

176

Figure 132: Repeat measurements of the triple-product of the profiles at $x = 2892.6$ mm, $y = -239.1$ mm, and $\alpha = 5°$ on the F6 wing with leading-edge extension.
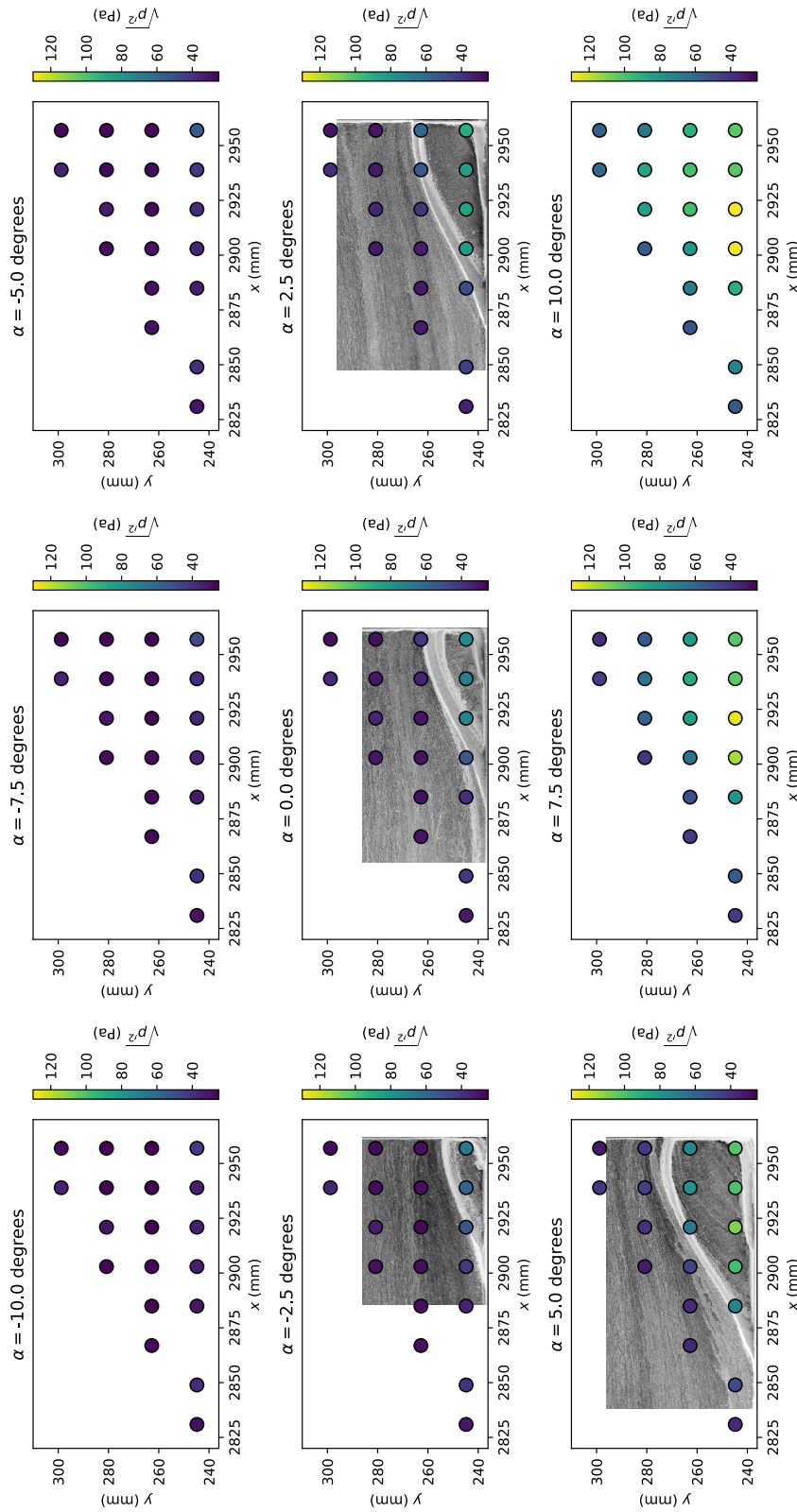
Figure 133: Broadband RMS pressures in the trailing-edge region of the starboard F6 wing versus model pitch angle. For each subplot, the symbols denote the (x, y)-locations of the unsteady pressure sensors and they are color coded according to the broadband RMS pressure. In specific cases, the RMS pressures are overlaid on an oil-flow visualization (mirror imaged from the port wing of the model) for spatial reference.
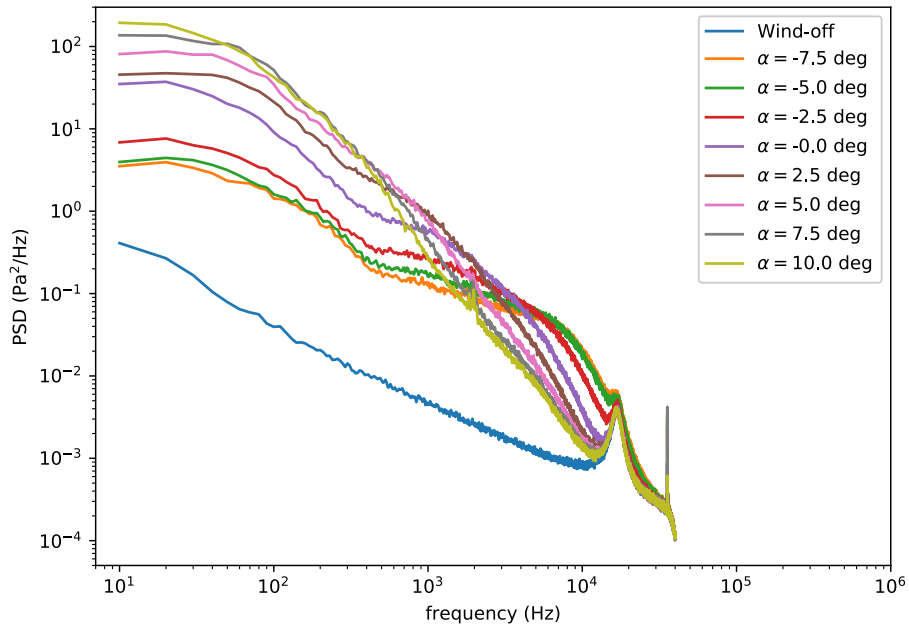
178
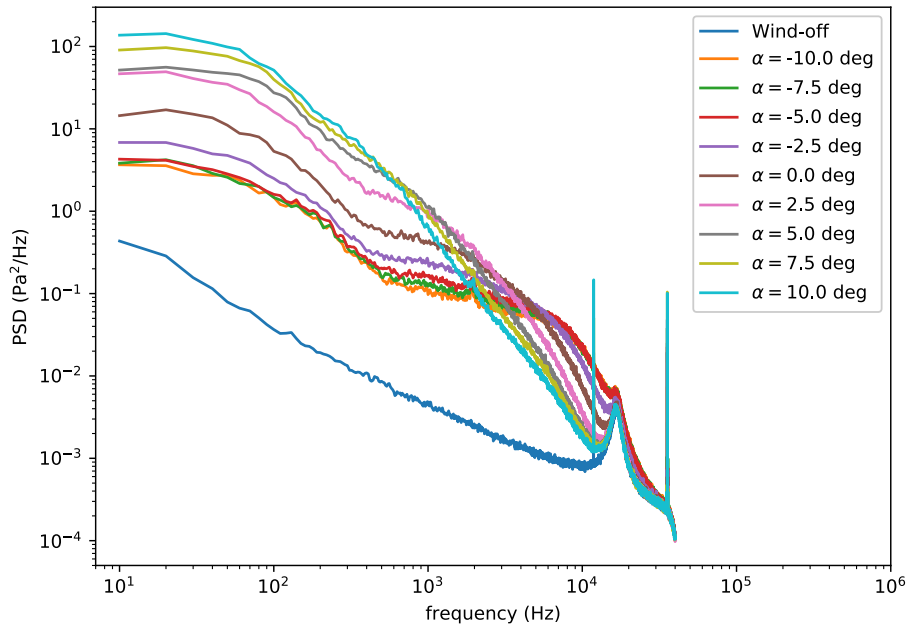
Figure 134: Power spectral densities of unsteady pressures measured at $x = 2902.94$ mm, $y = 244.81$ mm (Sensor 4) for a range of model pitch angles. The model was configured with the F6 wing.
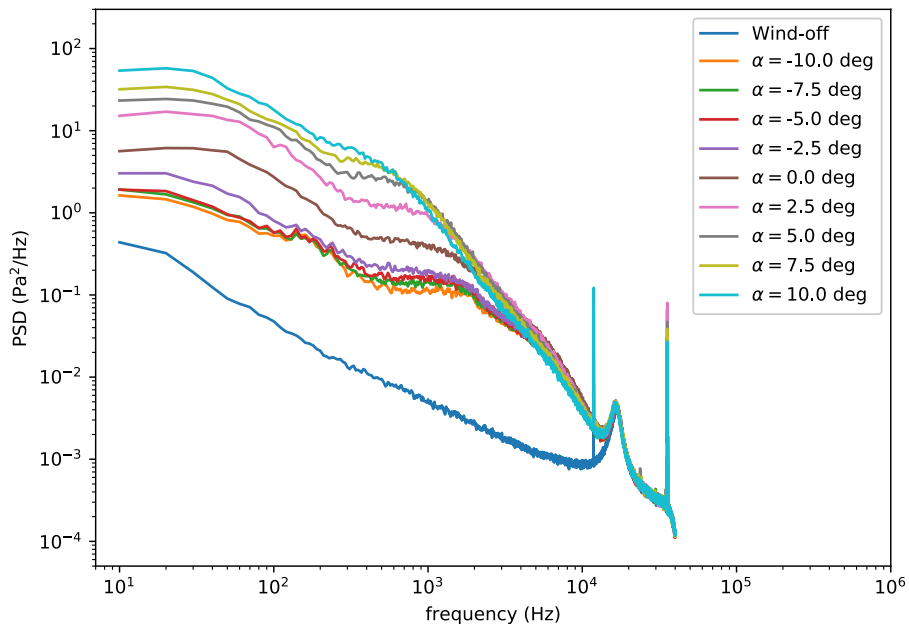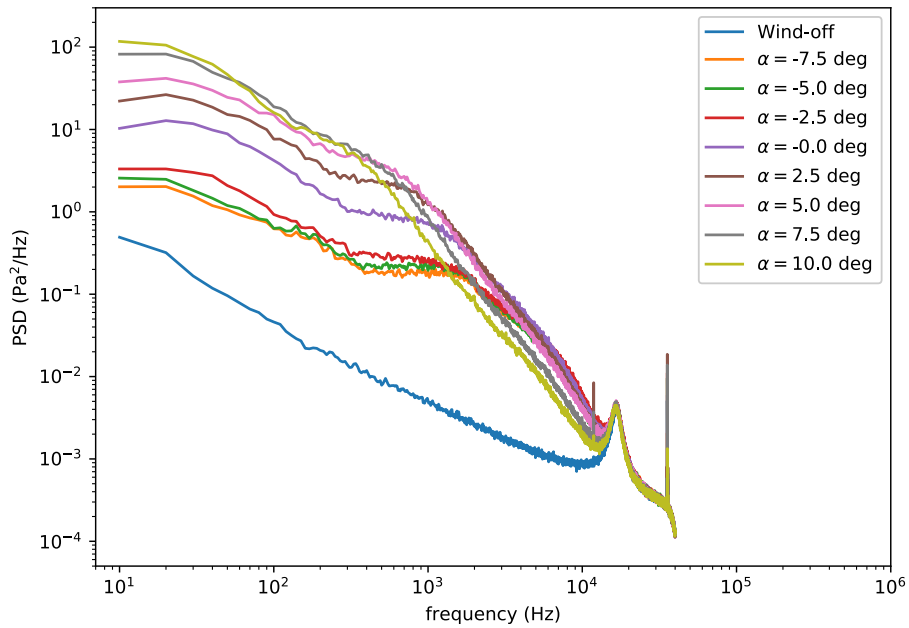

Figure 135: Power spectral densities of unsteady pressures measured at $x = 2956.94$ mm, $y = 262.79$ mm (Sensor 13) for a range of model pitch angles. The model was configured with the F6 wing.
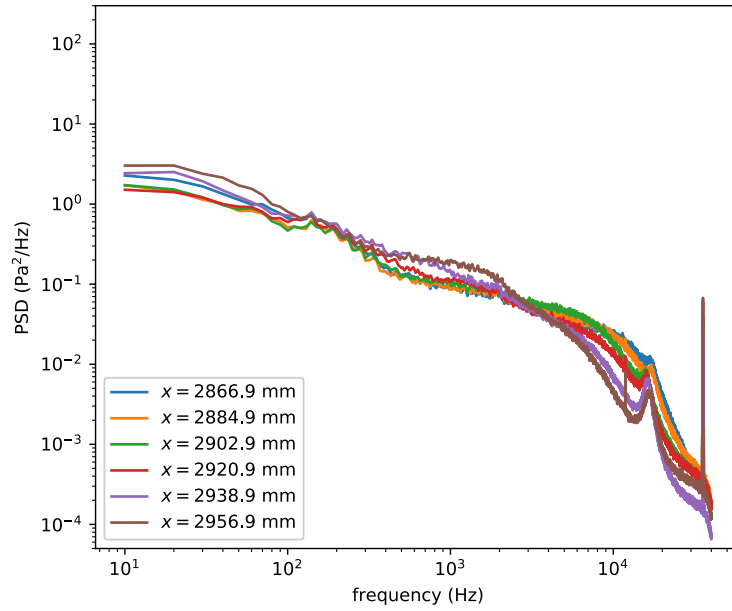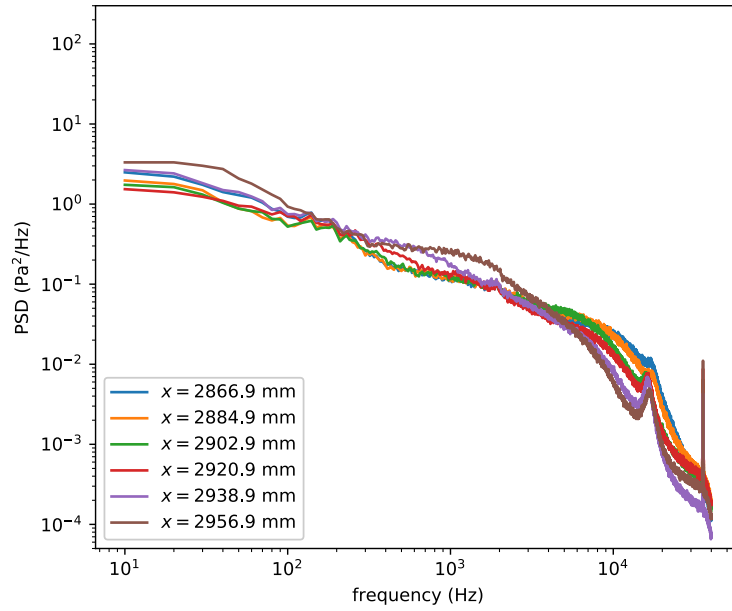
Figure 136: Power spectral densities of unsteady pressures measured along a line a sensors (Sensors 8–13) located at $y = 262.79$ mm. The model was configured with the F6 wing and set at a pitch angle of $-2.5°$.
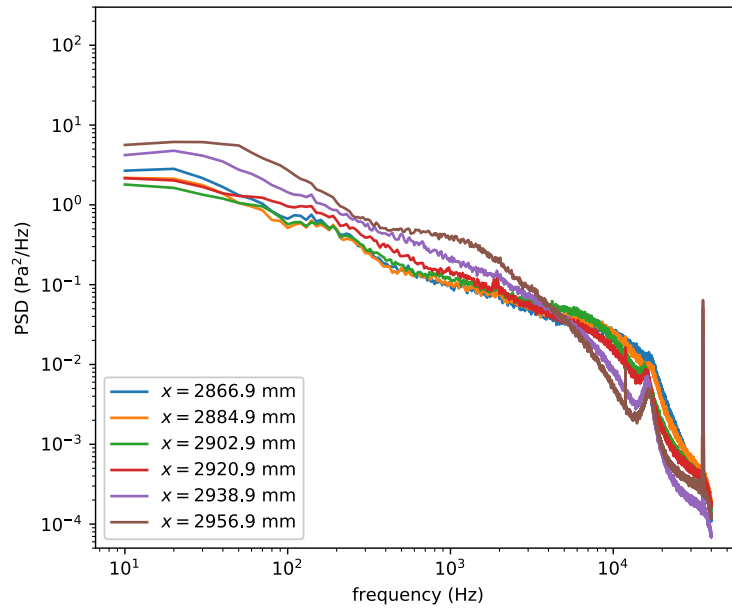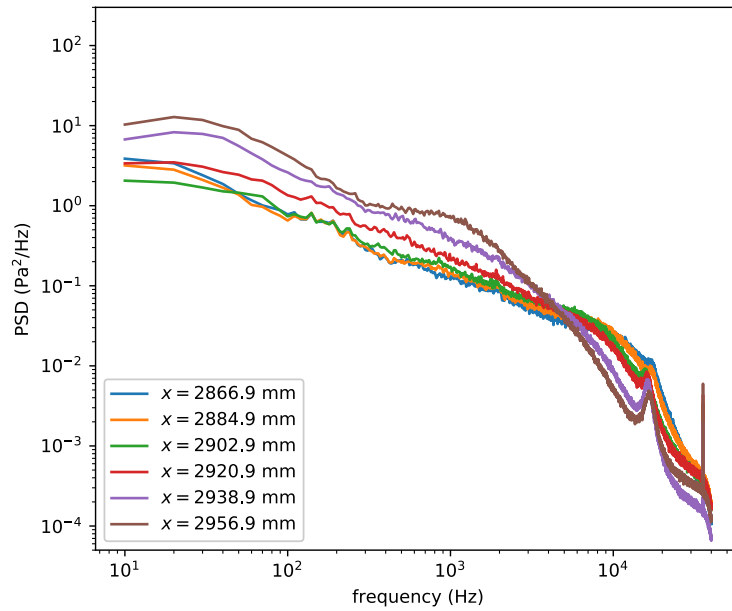

Figure 137: Power spectral densities of unsteady pressures measured along a line a sensors (Sensors 8–13) located at $y = 262.79$ mm. The model was configured with the F6 wing and set at a pitch angle of $0°$.
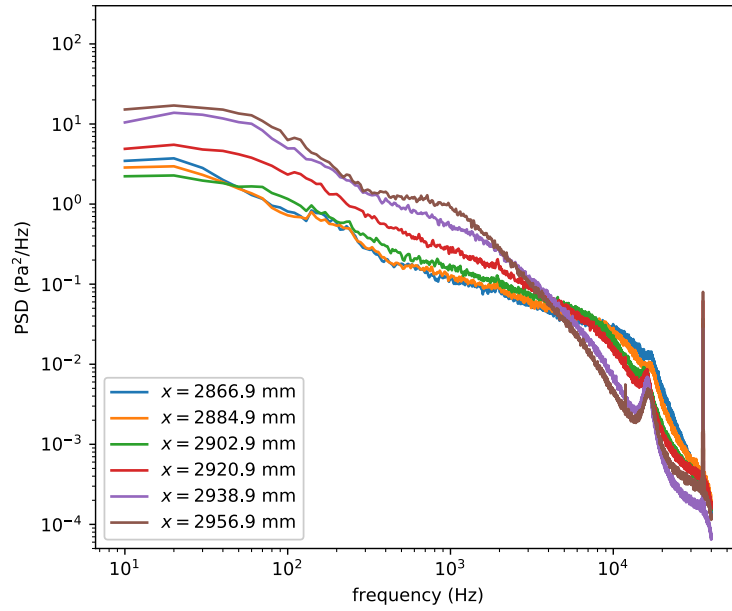
Figure 138: Power spectral densities of unsteady pressures measured along a line a sensors (Sensors 8–13) located at $y = 262.79$ mm. The model was configured with the F6 wing and set at a pitch angle of $2.5°$.
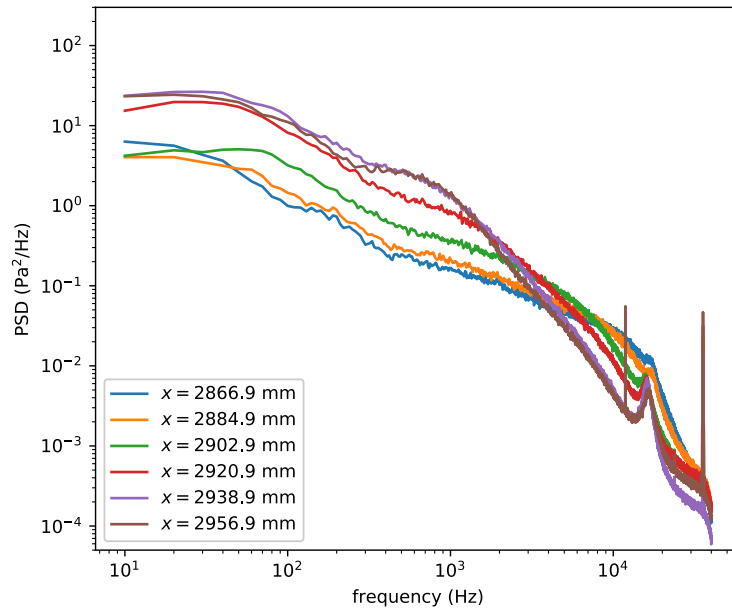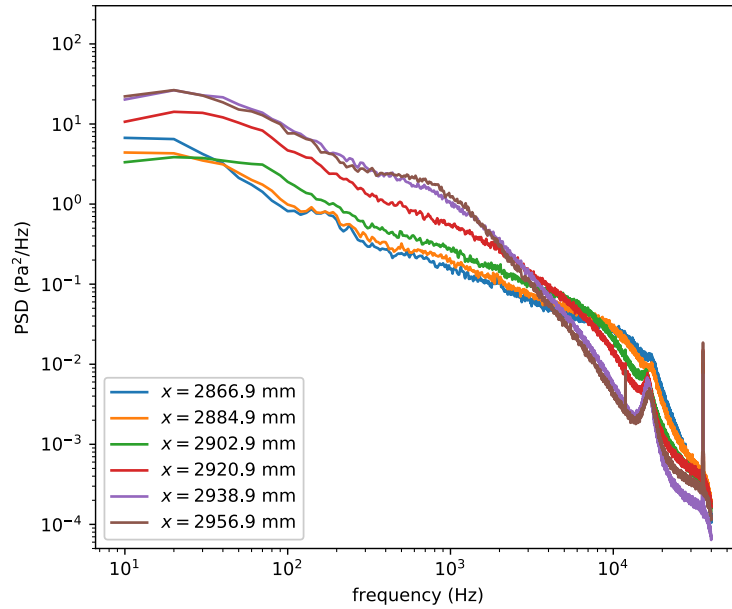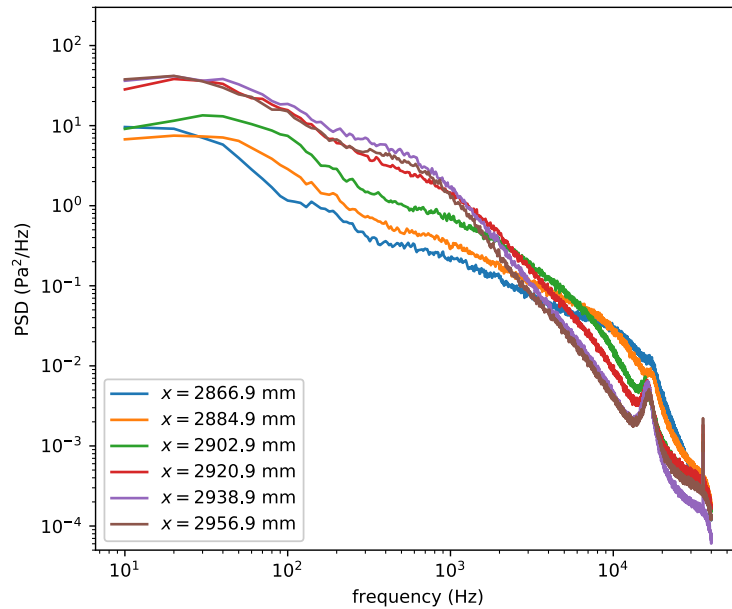

Figure 139: Power spectral densities of unsteady pressures measured along a line a sensors (Sensors 8–13) located at $y = 262.79$ mm. The model was configured with the F6 wing and set at a pitch angle of $5°$.
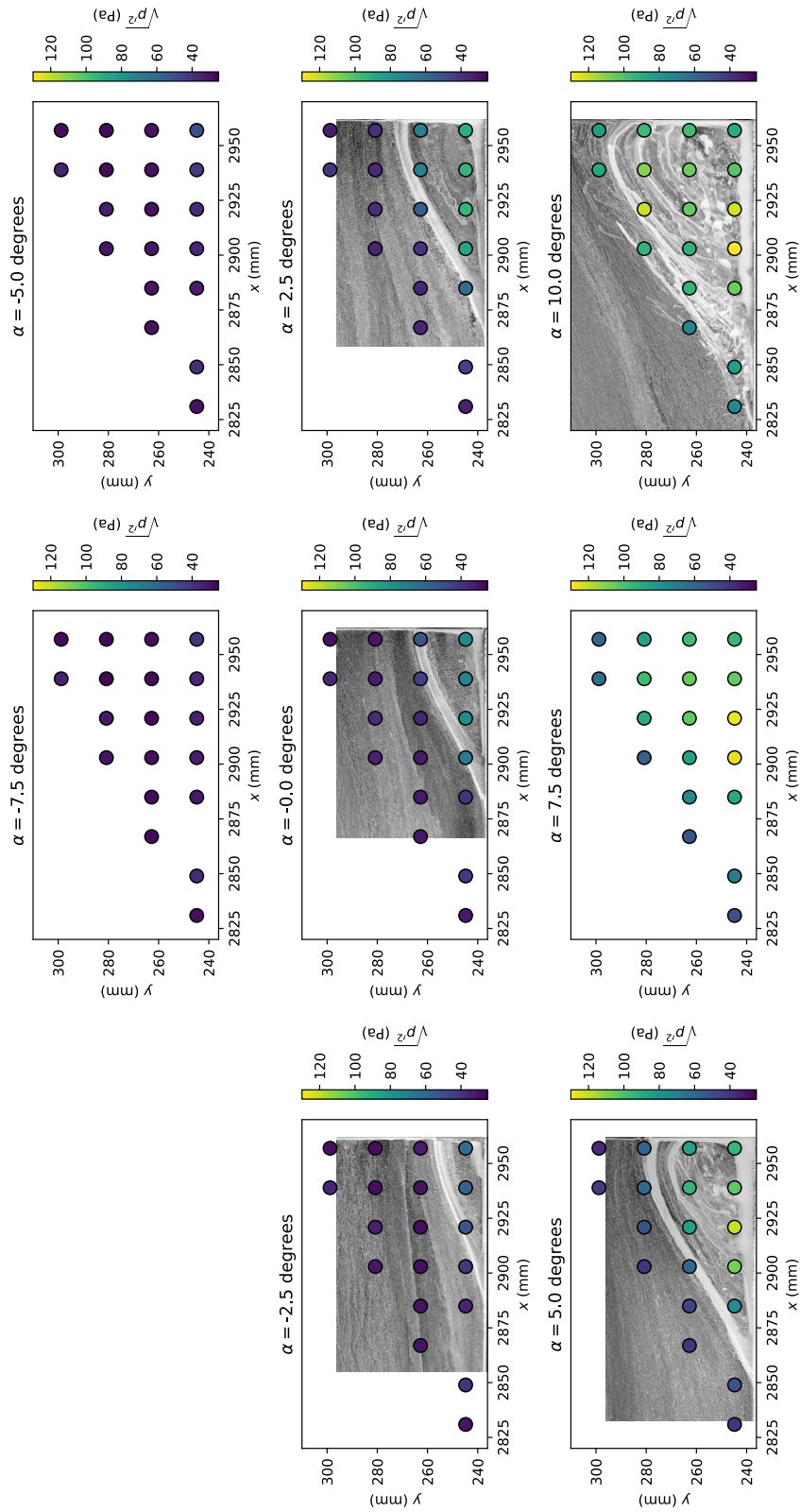
Figure 140: Broadband RMS pressures in the trailing-edge region of the starboard F6 wing with leading-edge extension versus model pitch angle. For each subplot, the symbols denote the (x, y)-locations of the unsteady pressure sensors and they are color coded according to the broadband RMS pressure. In specific cases, the RMS pressures are overlaid on an oil-flow visualization (mirror-imaged from the port wing of the model) for spatial reference.
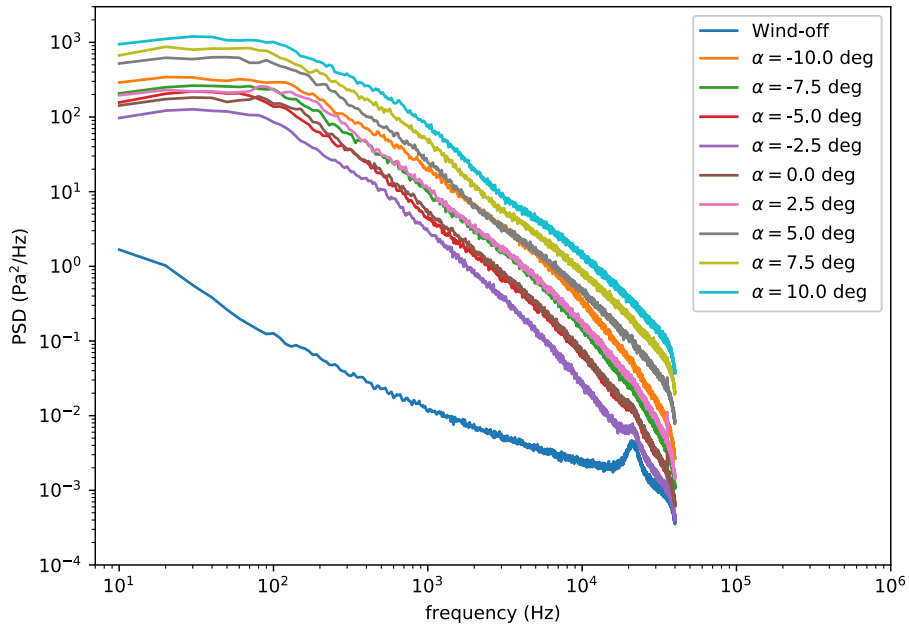
182

Figure 141: Power spectral densities of unsteady pressures measured at $x = 2902.94$ mm, $y = 244.81$ mm (Sensor 4) for a range of model pitch angles. The model was configured with the F6 wing with leading-edge extension.

Figure 142: Power spectral densities of unsteady pressures measured at $x = 2956.94$ mm, $y = 262.79$ mm (Sensor 13) for a range of model pitch angles. The model was configured with the F6 wing with leading-edge extension.
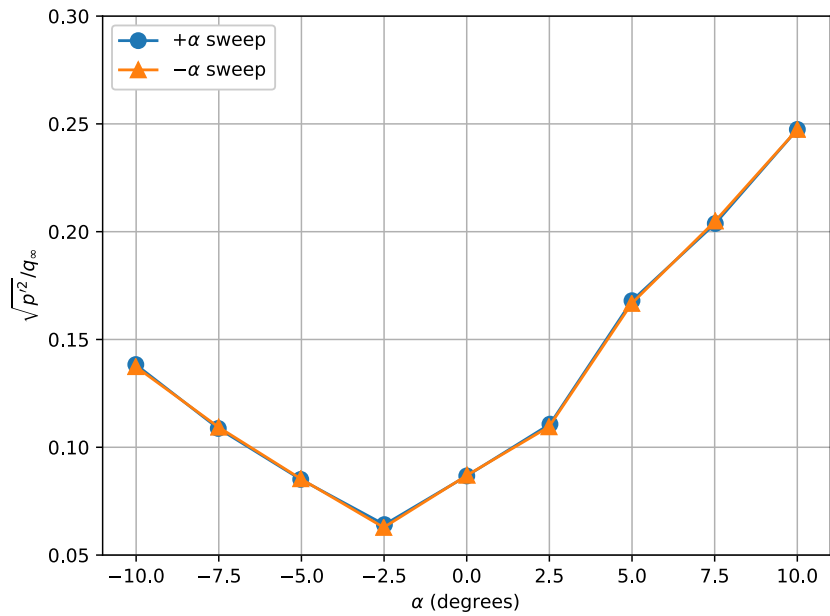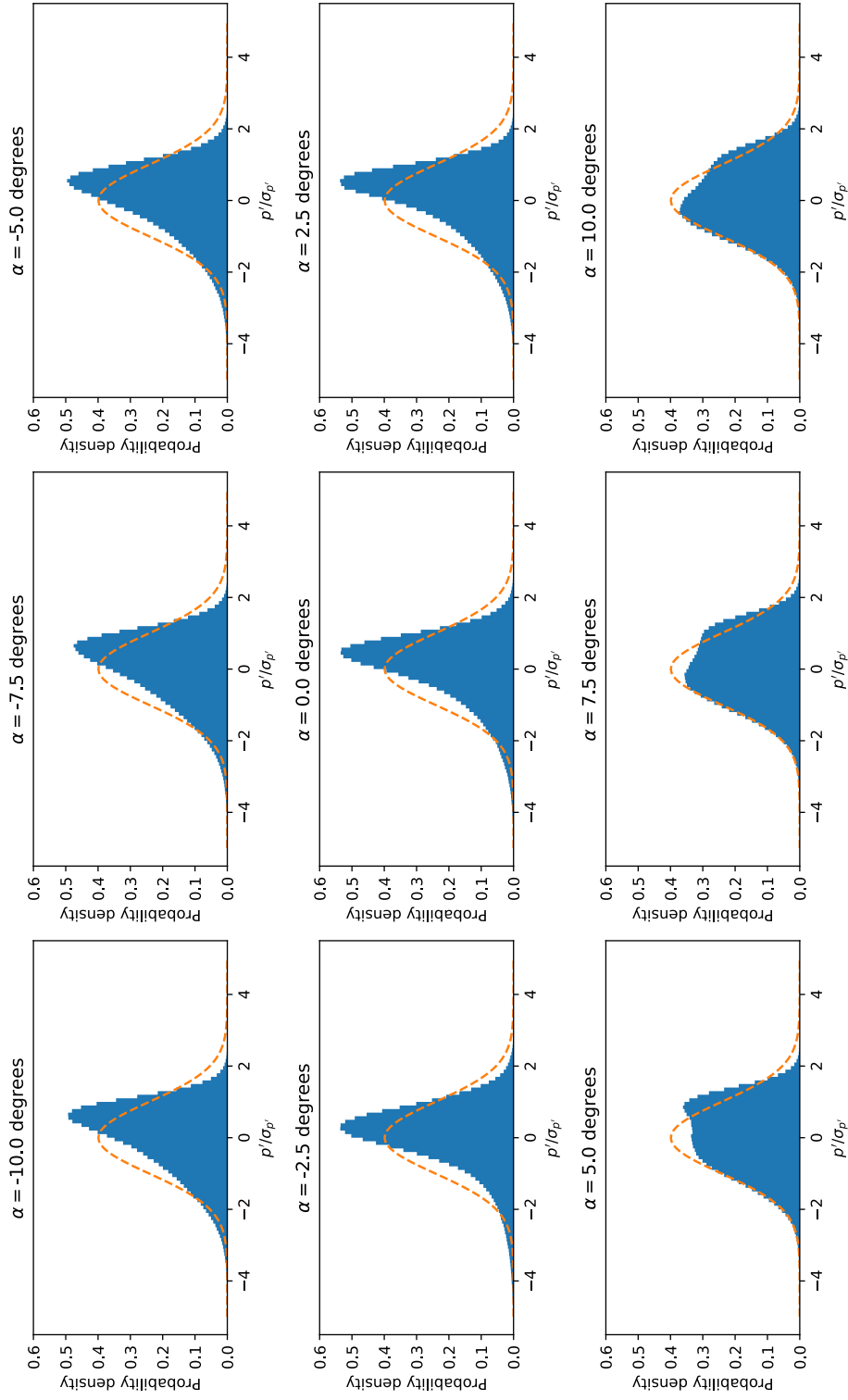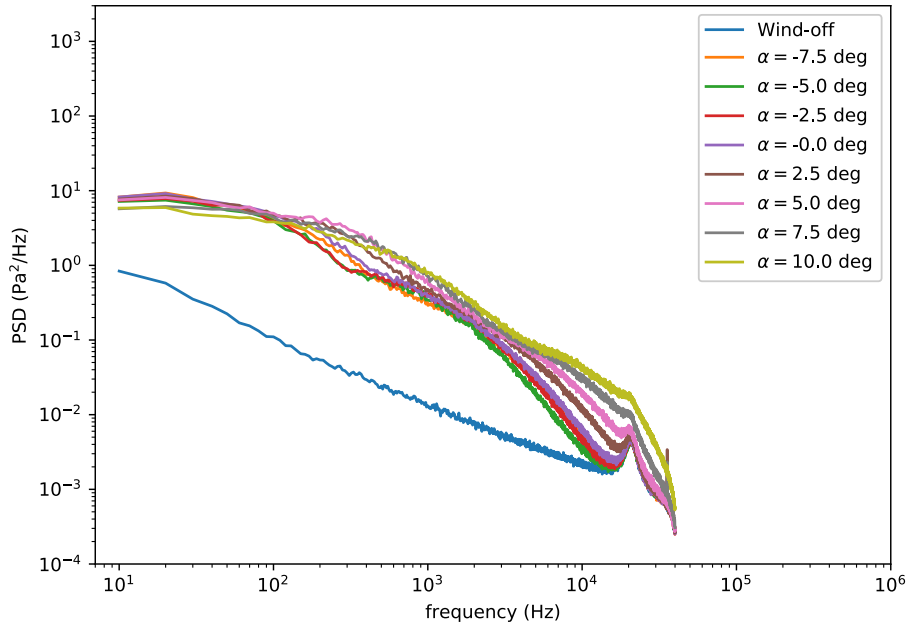
Figure 143: Power spectral densities of unsteady pressures measured along a line a sensors (Sensors 8–13) located at $y = 262.79$ mm. The model was configured with the F6 wing with leading-edge extension and set at a pitch angle of $-2.5°$.

Figure 144: Power spectral densities of unsteady pressures measured along a line a sensors (Sensors 8–13) located at $y = 262.79$ mm. The model was configured with the F6 wing with leading-edge extension and set at a pitch angle of $0°$.

Figure 145: Power spectral densities of unsteady pressures measured along a line a sensors (Sensors 8–13) located at $y = 262.79$ mm. The model was configured with the F6 wing with leading-edge extension and set at a pitch angle of $2.5°$.

Figure 146: Power spectral densities of unsteady pressures measured along a line a sensors (Sensors 8–13) located at $y = 262.79$ mm. The model was configured with the F6 wing with leading-edge extension and set at a pitch angle of $5°$.

Figure 147: Power spectral densities of unsteady pressures measured at $x = 1993.44$ mm, $z = 47.32$ mm (Sensor 27) for a range of model pitch angles. The model was configured with the F6 wing.
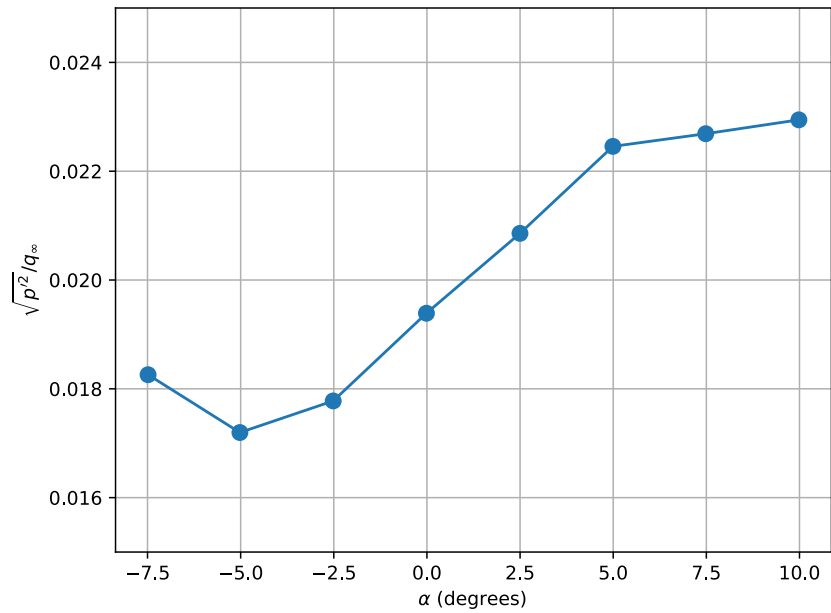

Figure 148: RMS pressure measured at $x = 1993.44$ mm, $z = 47.32$ mm (Sensor 27) for a range of model pitch angles. The model was configured with the F6 wing.
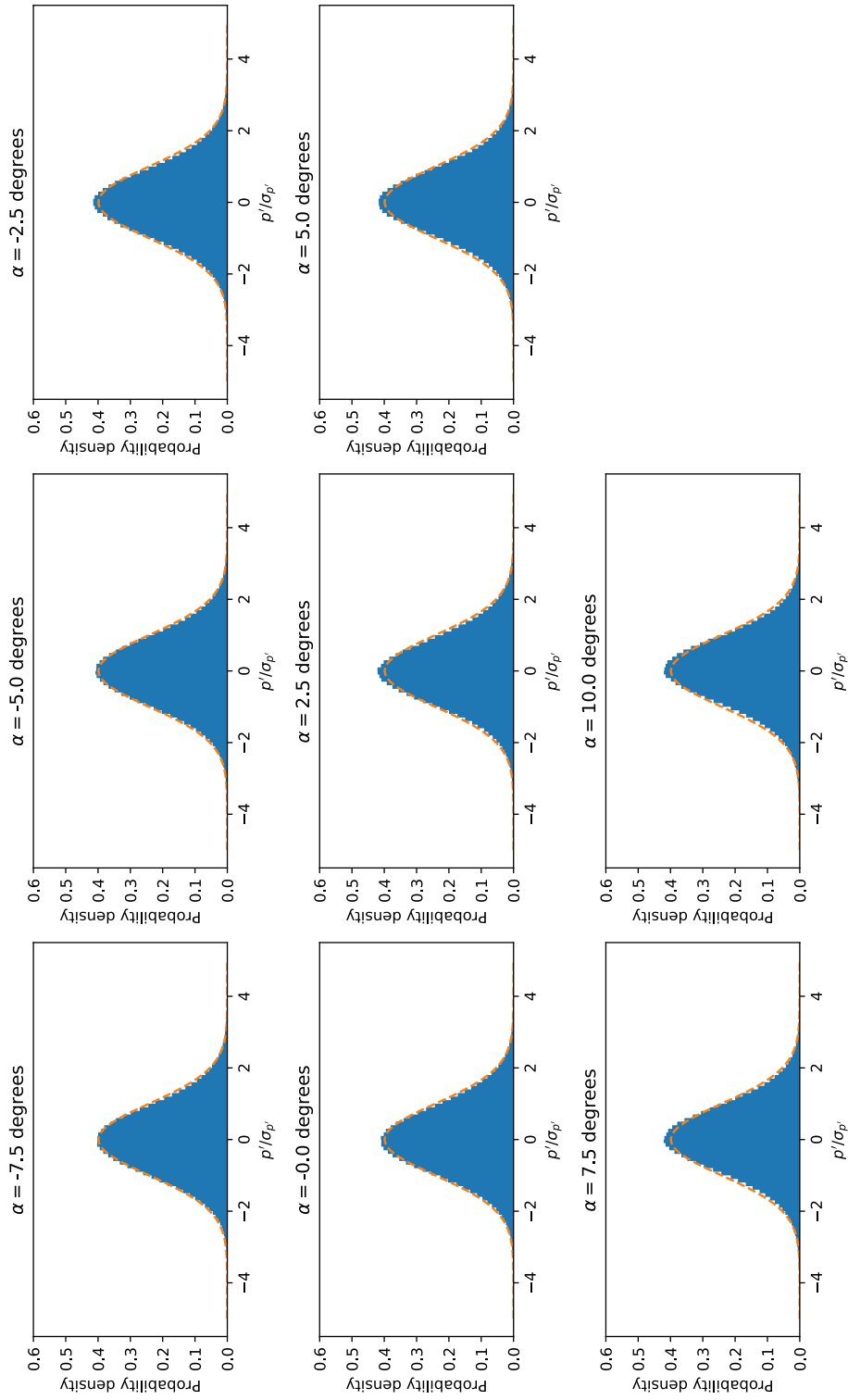
Figure 149: Probability densities of unsteady pressure measured at $x = 1993.44$ mm, $z = 47.32$ mm (Sensor 27) for a range of model pitch angles. The model was configured with the F6 wing. The dashed orange lines in each subplot correspond to a Gaussian probability density function.
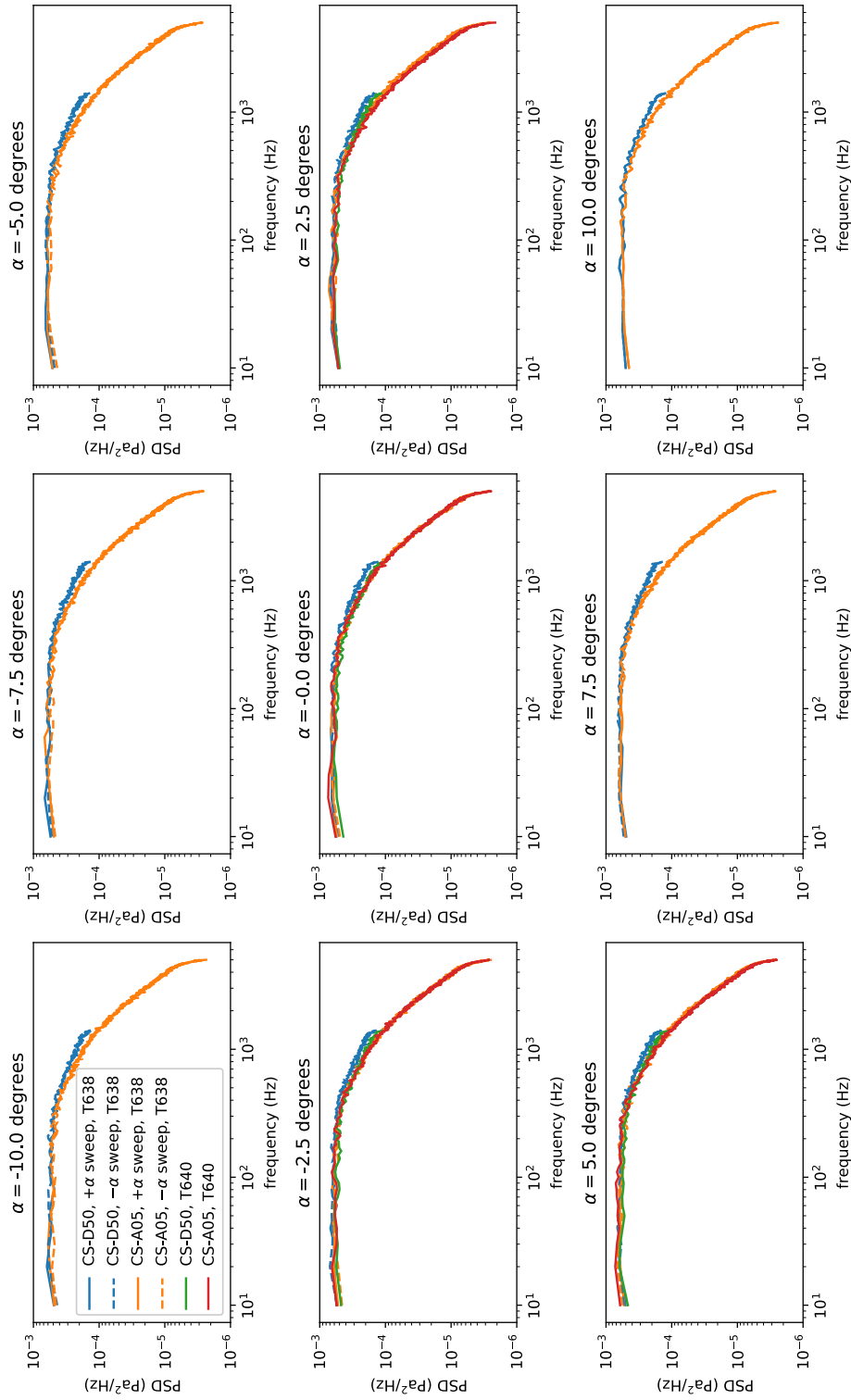
Figure 150: Power spectral densities of unsteady pressures measured at $x = 1921.89$ mm, $z = 54.46$ mm (Sensor 24) for a range of model pitch angles. The model was configured with the F6 wing with leading-edge extension.

Figure 151: RMS pressure measured at $x = 1921.89$ mm, $z = 54.46$ mm (Sensor 24) for a range of model pitch angles. The model was configured with the F6 wing with leading-edge extension.

Figure 152: Probability densities of unsteady pressure measured at $x = 1921.89$ mm, $z = 54.46$ mm (Sensor 24) for a range of model pitch angles. The model was configured with the F6 wing with leading-edge extension. The dashed orange lines in each subplot correspond to a Gaussian probability density function.

Figure 153: Power spectral densities of the x component of shear stress measured at $x = 1168.4$ mm, $y = -236.1$ mm, $z = 0$ mm for a range of model pitch angles.
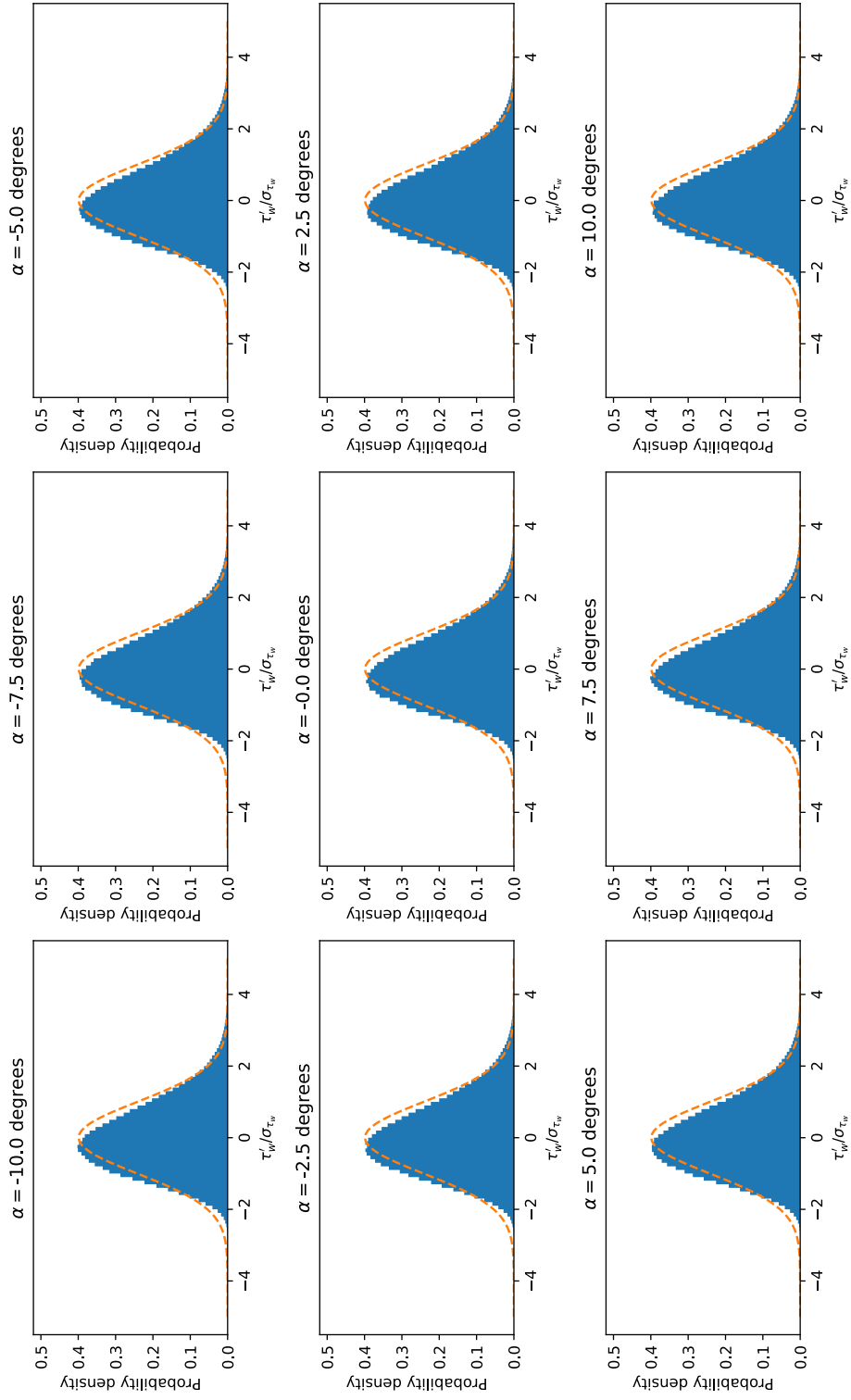
Figure 154: Probability densities of the x component of shear stress measured at $x = 1168.4$ mm, $y = -236.1$ mm, $z = 0$ mm for a range of model pitch angles. For this data set, the shear stress sensor bandwidth was 5 kHz. The dashed line in the figures denotes a Gaussian distribution.
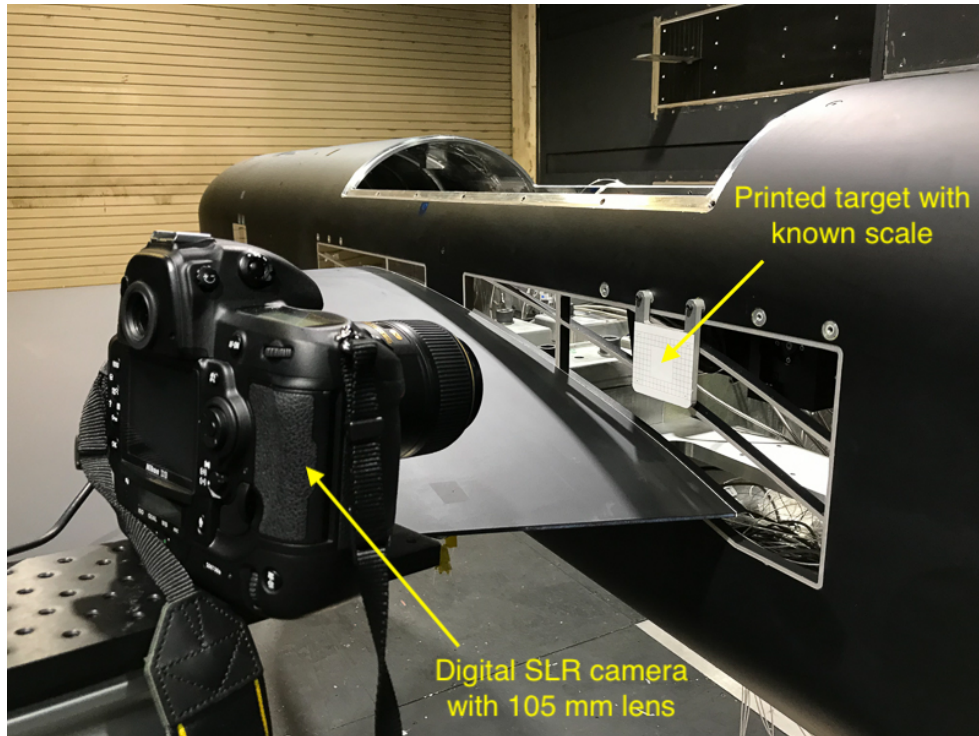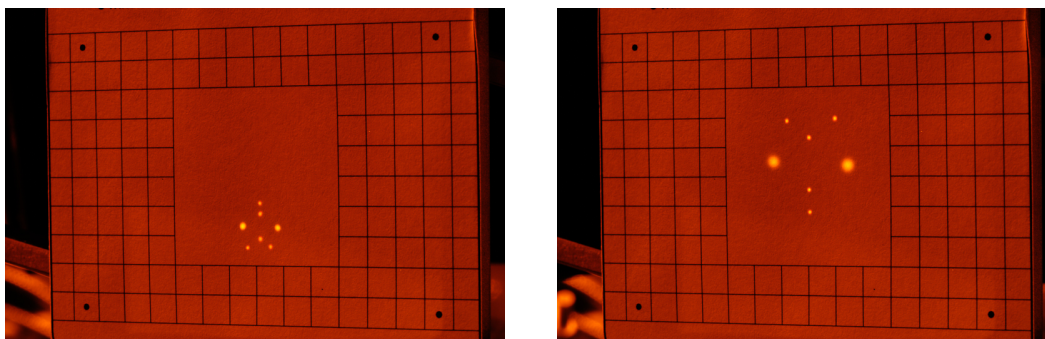
Figure 155: Photograph of setup used to measure the probe laser beam unit vectors.

(a) LDV measurement volume located inside the model, 10 mm from the outer surface of the window.

(b) LDV measurement volume located outside the model, 50 mm from the outer surface of the window.

Figure 156: Photographs of the laser-beam pattern projected onto the calibration target with the measurement volume positioned at two different y locations.
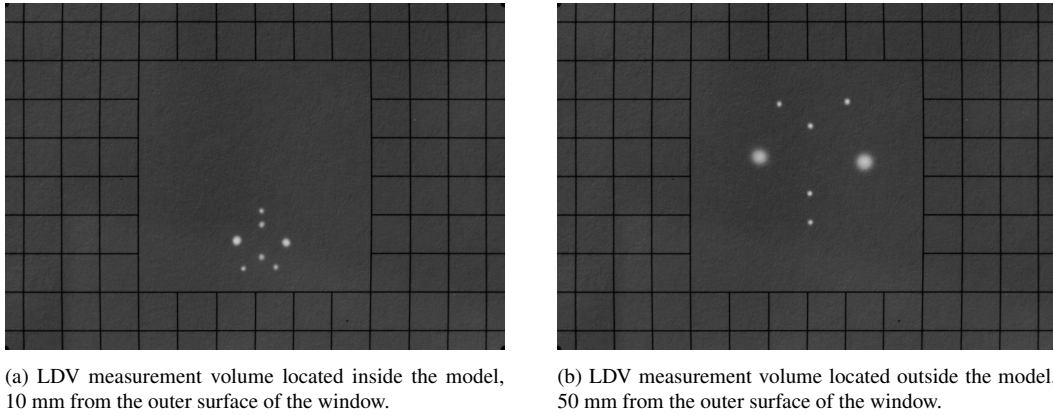
(a) LDV measurement volume located inside the model, 10 mm from the outer surface of the window.

(b) LDV measurement volume located outside the model, 50 mm from the outer surface of the window.

Figure 157: Preprocessed images of the laser-beam pattern projected onto the calibration target with the measurement volume positioned at two different y locations.
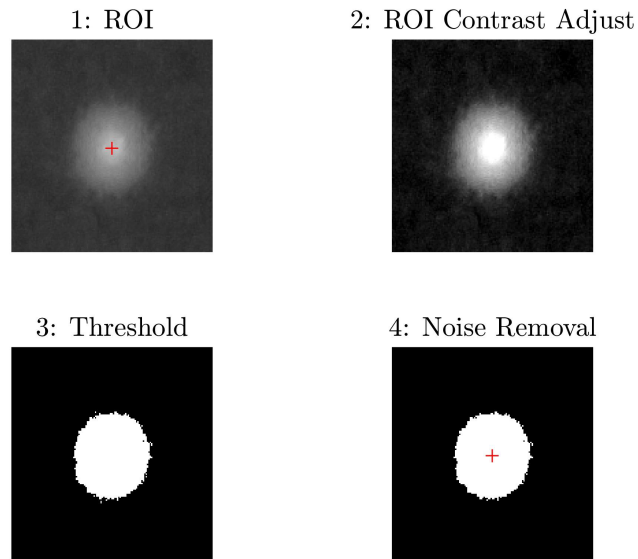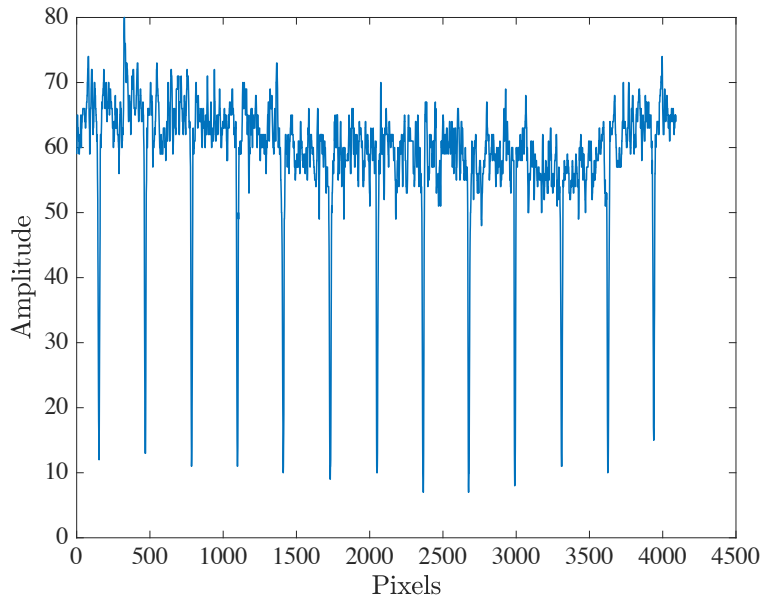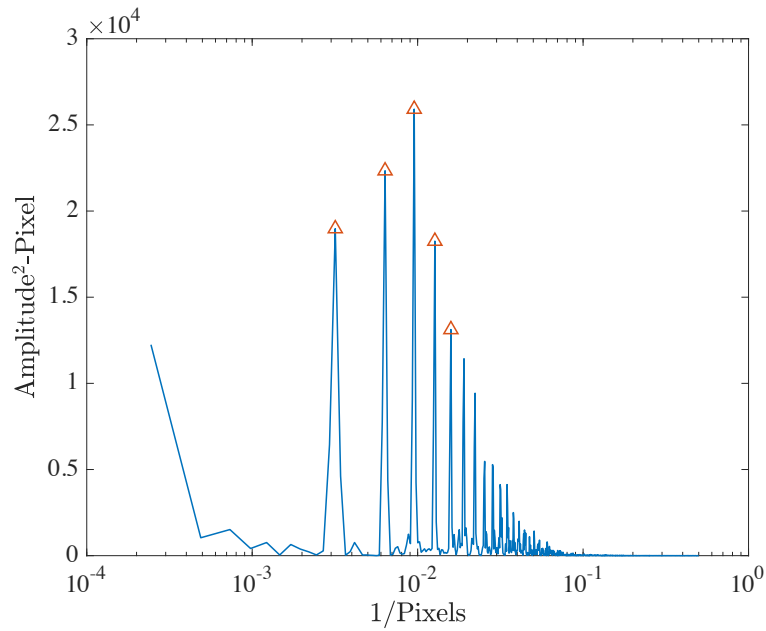

Figure 158: Example of processing steps on a region of interest (ROI) around an image of a laser beam on the calibration target.

(a) Pixel intensity values for a line passing through the grid on an image of the calibration target.

(b) Spectrum for the line of pixel intensity values passing through the grid on an image of the calibration target.

Figure 159: Example of pixel intensity values for a line passing through the grid on an image of the calibration target and the corresponding spectrum for that line of pixels.
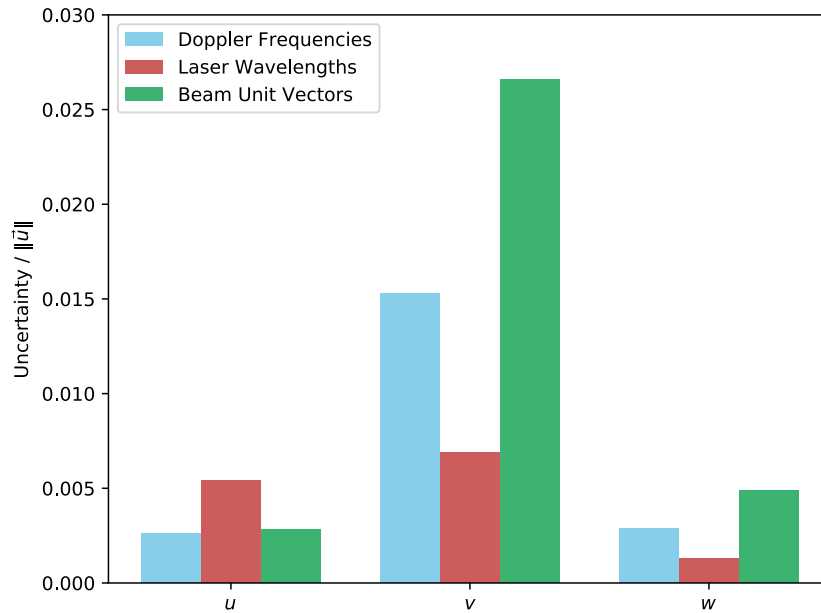
Figure 160: Breakdown of uncertainty sources for a single, instantaneous velocity measurement with LDV probe 1.
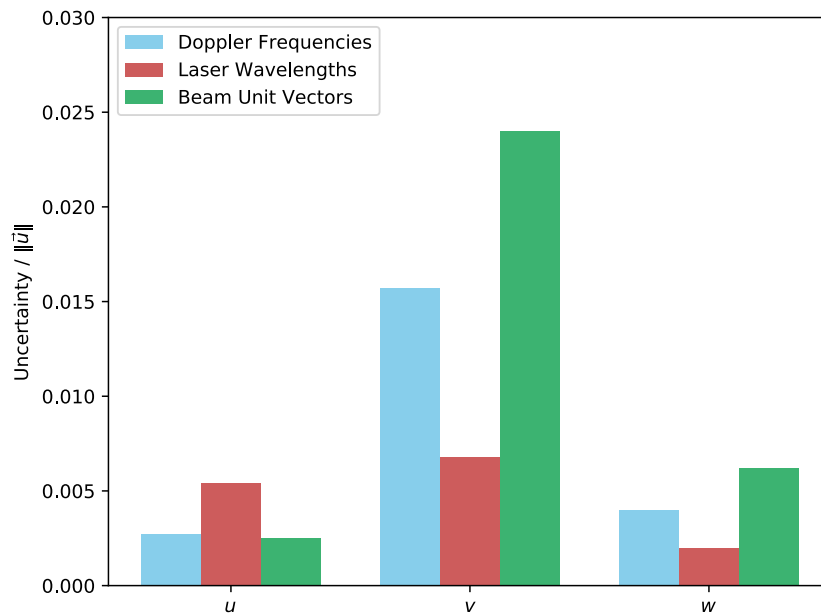

Figure 161: Breakdown of uncertainty sources for a single, instantaneous velocity measurement with LDV probe 2.

REPORT DOCUMENTATION PAGE

1. REPORT DATE *(DD-MM-YYYY)*	2. REPORT TYPE	3. DATES COVERED *(From - To)*
1-06-2019	Technical Memorandum	

4. TITLE AND SUBTITLE	5a. CONTRACT NUMBER
An Experimental Investigation of a Wing-Fuselage Model in the NASA Langley 14- by 22-Foot Subsonic Tunnel	
	5b. GRANT NUMBER
	5c. PROGRAM ELEMENT NUMBER
6. AUTHOR(S)	5d. PROJECT NUMBER
Michael A. Kegerise and Dan H. Neuhart	
Langley Research Center, Hampton, Virginia	5e. TASK NUMBER
	5f. WORK UNIT NUMBER
	109492.02.07.01.01

7. PERFORMING ORGANIZATION NAME(S) AND ADDRESS(ES)	8. PERFORMING ORGANIZATION REPORT NUMBER
NASA Langley Research Center Hampton, VA 23681-2199	L-21030

9. SPONSORING/MONITORING AGENCY NAME(S) AND ADDRESS(ES)	10. SPONSOR/MONITOR'S ACRONYM(S)
National Aeronautics and Space Administration Washington, DC 20546-0001	NASA
	11. SPONSOR/MONITOR'S REPORT NUMBER(S)
	NASA-TM-2019-220286

12. DISTRIBUTION/AVAILABILITY STATEMENT

Unclassified
Subject Category 34
Availability: NASA STI Program (757) 864-9658

13. SUPPLEMENTARY NOTES

14. ABSTRACT

Current turbulence models, such as those employed in Reynolds-averaged Navier-Stokes CFD, are unable to reliably predict the onset and extent of the three-dimensional separated flow that typically occurs in wing-fuselage junctions. To critically assess, as well as to improve upon, existing turbulence models, experimental validation-quality flow-field data in the junction region is needed. In this report, we present an overview of experimental measurements on a wing-fuselage junction model that addresses this need. Sample results from the measurement techniques employed during the test are presented and discussed.

15. SUBJECT TERMS

16. SECURITY CLASSIFICATION OF:			17. LIMITATION OF ABSTRACT	18. NUMBER OF PAGES	19a. NAME OF RESPONSIBLE PERSON
a. REPORT	b. ABSTRACT	c. THIS PAGE			STI Help Desk (email: help@sti.nasa.gov)
U	U	U	UU	200	19b. TELEPHONE NUMBER *(Include area code)* (757) 864-9658